Mechanisms and Mitigation of Agglomeration During Fluidized Bed Combustion of Biomass

Jonathan Morris

A thesis submitted in partial fulfilment of the requirements for the degree of Doctor of Engineering (EngD)

February 2021

Department of Mechanical Engineering
Faculty of Engineering
The University of Sheffield

Redaction Notice

Content has been redacted in the online version of this thesis for commercial confidentiality reasons. The redacted content includes the entirety of Chapter 7 and related supplementary Appendices E-K.

Where content has been redacted, it has been made clearly apparent with a notice.

The overall pagination of this redacted version of the thesis remains identical to the unredacted copy.

This page is intentionally left blank in the unredacted version of the thesis, and therefore remains intentionally unnumbered in this redacted version of the thesis.

Abstract

Fluidized bed combustion technology is increasingly used for biomass fuels, due to the high variability of their energy density and composition. However, this technology is still susceptible to ash-related issues. Agglomeration is caused by ash melting onto or reacting with bed material to form alkali silicate melts, allowing bed particles to adhere together. Accumulation of agglomerates causes bed defluidization, and consequently unscheduled downtime. This thesis investigates agglomeration mechanisms and mitigation measures at the pilot-scale, focusing on agricultural fuels that have received less attention in literature and may be of interest for boiler operators.

When burning wheat straw, the magnesium-iron silicate bed material olivine lengthened defluidization times versus silica sand, though this was not sufficient to make the fuel viable. The additives kaolin and dolomite prevented bed defluidization entirely when burning miscanthus, but had no effect with wheat straw, despite chemically reacting with both fuel ashes. In combination with thermochemical modelling, it was proposed that the poor breakdown of wheat straw pellet sand release of ash to their surface allows the pellet to act as a seed for agglomerate formation, hence additives proving ineffective.

Agglomeration mechanisms were studied with different fuels, bed materials and additives. This included a novel analysis of agglomerates from different bed locations, and a spatially defined study of agglomerates from tests with additives, both of which revealed mechanisms in greater detail than previously reported. A novel thermochemical modelling approach using FactSage was applied to agglomerate compositional data, together with an appraisal of the software for agglomeration studies.

Through collaboration with project sponsor Sembcorp Energy UK on their "Wilton 10" bubbling fluidized bed boiler, a 5-year fuel data set was studied to determine fuel quality improvement potential. Several analytical methods were applied, including a machine learning algorithm. Recommendations were made regarding fuel quality and sampling.

Declaration of Authorship

The candidate confirms that they are aware of the University of Sheffield guidance on the use of unfair means (www.sheffield.ac.uk/ssid/unfair-means). This work has not previously been presented for an award at this, or any other, university. The candidate confirms that the work submitted is their own, except where work that has formed part of jointly authored publications has been included. The contribution of the candidate and the other authors to this work has been explicitly indicated below. The candidate confirms that appropriate credit has been given within the thesis where reference has been made to the work of others.

Paper I: Mechanisms and mitigation of agglomeration during fluidized bed combustion of biomass: A review. **Morris, J.D.**, Daood, S.S., Chilton, S., Nimmo, W. 2018. Fuel, Vol. 230, pp. 452-473.

> This paper forms part of Chapter 2. J.D. Morris was lead author, responsible for carrying out the literature review and writing the manuscript. S.S. Daood as second supervisor provided feedback on the manuscript and project guidance. As an industrial contributor, S. Chilton supplied some further sections of the manuscript, which have been removed in this thesis, and provided feedback on the manuscript. W. Nimmo as first supervisor provided feedback on the manuscript and project guidance.

Paper II: Agglomeration and the effect of process conditions on fluidized bed combustion of biomasses with olivine and silica sand as bed materials: Pilot-scale investigation. **Morris, J.D.**, Daood, S.S., Nimmo, W. 2020. Biomass and Bioenergy, Vol. 142, Article No. 105806.

> This paper forms part of Chapter 4. J.D. Morris was lead author, responsible for performing testing and sample analysis, analysing data, and writing the manuscript. S.S. Daood as second supervisor assisted with pilot-scale combustion tests and provided feedback on the manuscript and project guidance. W. Nimmo as first supervisor provided feedback on the manuscript and project guidance.

Paper III: The effect of using kaolin and dolomite additives to mitigate agglomeration with challenging agricultural biomass fuels. **Morris, J.D.**, Daood, S.S., Nimmo, W. Unpublished manuscript under submission.

This paper forms parts of Chapter 5 and Chapter 6. J.D. Morris was lead author, responsible for performing testing and sample analysis, analysing data, and writing the manuscript. S.S. Daood as second supervisor assisted with pilot-scale combustion tests and provided feedback on the manuscript and project guidance. W. Nimmo as first supervisor provided feedback on the manuscript and project guidance.

For a list of all other dissemination activities in relation to this project see Appendix A.

Acknowledgements

I would first like to thank my supervisors, Prof. Bill Nimmo and Dr. Sheraz Daood. Bill and Sheraz provided expert guidance and supervision to develop me into a researcher over the last four years. They both enabled my success throughout the process: providing ideas and encouragement, ensuring experimental and modelling work was fruitful, securing additional resources when needed, and providing opportunities to publish and present findings. For their continued support I am incredibly grateful.

Experimental work made up a large part of the research and would not have been possible without the training and support of various technical staff. At the Low Carbon Combustion Centre (LCCC), I think everyone helped at some point to run (or frequently, fix) the pilot-scale fluidized bed. Special thanks in alphabetical order to Sam Chapman, Dave Dunstan, Andy Hemstock, and Ashley Thornton, all of whom spent many hours providing dedicated technical support. For the analysis work, particularly SEM/EDX, thanks are due for Tes Monaghan, Dr. Cheryl Shaw, and Stuart Micklethwaite (Leeds University).

A major benefit of the EngD is the training programme and cohort structure. I would like to thank all staff and students, past and present, at the Centre for Doctoral Training in Carbon Capture, Storage & Cleaner Fossil Energy for making the journey enjoyable, for the development opportunities, and of course for the funding. On a similar note, I would also like to thank the entire Energy 2050 group at Sheffield, as well as the wider academic and industrial community, for the many useful discussions over the years.

A significant chunk of my time was spent with project sponsors Sembcorp Energy UK in Middlesbrough. A big thanks goes to the performance engineering team, past and present, during my time at Sembcorp: Howard Sutton, Nick Tann, Graeme Lewis, Jonathan Scroggie, Nicholas Chen, and Dr. Stephen Chilton. The team welcomed me, gave me interesting projects, valued my inputs, took me on many in-depth tours of the site, and contributed significantly to my development as an engineer. Many others at Sembcorp contributed to various projects over the years, and all have my gratitude.

I also of course must thank my family for their support and encouragement. They are probably relieved that they will never have to hear about fluidized beds, biomass, and/or agglomeration again (or will they?).

…And finally, one of the fun(?) things about writing a thesis is that it will sit around in a dusty corner of the ~~library~~ internet for a very long time. Allow me then to share a couple of anecdotes from the research process with future readers:

- In March 2018, during the UCU strikes, students barricaded themselves inside the Arts Tower in Sheffield. Samples that I *needed* to analyse for my first conference (overseas, six weeks later) were inside my office cupboard. In the Arts Tower. Luckily, after a few stressful days rebooking carefully planned analysis, the students ended their occupation.
- Towards the end of 2019, I had a few remaining pilot-scale tests planned and plenty of samples stored at the LCCC facility in Beighton. I had a test planned for the 8th of November. In the early hours of the 8th of November, the River Rother flooded the labs, destroying all my equipment and washing away most of my samples. Fortunately, I had enough results to write up, some modelling work to finish, and some samples in the office to analyse *at the start of 2020…*

For the one person that does read this in the distant future, if you give me the answer to any of the below questions, I will answer any questions you may have (if you find me!):

- 2025: Has Robert Caro finished writing LBJ book #5?
- 2035: Are there any large-scale CCS plants in the UK yet?
- 2050: Has the UK achieved net-zero CO_2 emissions?

Contents

List of Figures

List of Tables

List of Equations

Nomenclature

Abbreviations

Abbreviation	Description
%RW	Percentage recycled wood. Feed fraction of recycled wood into the Wilton 10 boiler (energy basis).
AFBC	Atmospheric fluidized bed combustion
ANN	Artificial neural networks
Backpass	The ducting following the exit of flue gas from a BFB boiler. Contains heat exchange equipment (e.g. economizers and air pre-heaters for heat recovery from the flue gas).
BAT	Best available technique
BFB	Bubbling fluidized bed
BFW	Boiler feed water
Boiler efficiency	A measure of energy input to a boiler versus energy output.
BREF	BAT reference documents
BtB	Blend to boiler
CALPHAD	CALculation of PHAse Diagrams
CEMS	Continuous emissions monitoring system
CFB	Circulating fluidized bed
CHP	Combined heat & power
CHPQA	CHP Quality Assurance
COP21	21st United Nations Climate Change Conference
CRE	British Coal Research Establishment
DDGS	Distillers dried grain using wheat and solubles
DP	Differential pressure
EDX	Energy Dispersive X-ray Spectroscopy
EfW	Energy from waste
ELV	Emission limit values
FBC	Fluidized bed combustion
GT2	Gas turbine 2
HRSG	Heat recovery steam generator
IACM	in-situ alkali chloride monitor
ICDD	International Centre for Diffraction Data
ICP-MS	Inductively coupled plasma mass spectrometry
IDT	Initial deformation temperature
IEA	International Energy Agency
IED	Industrial emissions directive
LCCC	Low Carbon Combustion Centre
LCOE	Levelized cost of electricity
LCP	Large combustion plant
MAE	Mean absolute error
MAPE	Mean absolute percentage error
MSE	Mean square error
MSW	Municipal solid waste
NDIR	Non-dispersive infrared

Abbreviation	Description
OOB	Out-of-bag error
PCA	Principal component analysis
PF	Pulverized fuel
PFB	Pressurized fluidized bed
PFBC	Pressurized fluidized bed combustion
Phyllis2	Biomass composition database maintained by Energy Research Centre of the Netherlands (ECN).
RDF	Refuse derived fuels
RHI	Renewable Heat Incentive
RMSE	Root mean squared error
RO	Renewable Obligation
ROC	Renewable Obligation certificate
SCE	Sembcorp Energy UK
SEM/EDX	Scanning electron microscopy with energy dispersive X-ray spectroscopy
SNCR	Selective non-catalytic reduction
SS 304	Stainless steel 304
UKAS	United Kingdom Accreditation Service
W10	Wilton 10
WI	Waste incineration
XRD	X-ray diffraction

Roman Alphabet

Symbol	Units	Description
A	%	Agglomeration ratio
CHP_{QHO}	MWh_{th}	Total use heat output per year from CHP plant (i.e. that which would have displaced heat generation from other sources).
CHP_{TFI}	MWh	Gross calorific value of total fuel input per year to CHP plant.
CHP_{TPO}	MWh_e	Total power output per year from CHP plant.
cps		Counts per second. Unit for X-ray count rate during EDX analysis.
D_A	%	Additive dosage
d_{bed}	m	Bed diameter
d_p	m	Bed particle diameter. Typically quoted as either an average value or range.
g	m/s^2	Gravitational constant
GCV	MJ/kg	Gross calorific value
h_{bed}	m	Static bed height
i		Data feature under evaluation when calculating permutation importance
k		Number of times to random shuffle data when calculating permutation importance.
M_A	kg	Mass of additive
m_a	kg	Mass of agglomerated bed material
M_{FA}	kg	Calculated mass of fuel ash
m_i	kg	Mass of initial/fresh bed material
n		Number of data points predicted by random forest model.
QI		Quality Index. Used to determine the energy efficiency and environmental performance of a CHP scheme.

Symbol	Units	Description
R^2		Coefficient of determination
Re_p	*None*	Reynolds number
s		Value of the score criteria when calculating permutation importance.
T		Temperature
T_{aggl}	°C	Agglomerating temperature. During combustion, the fluidized bed undergoes controlled, progressive, heating until agglomeration and defluidization occurs. This temperature is thus T_{aggl}.
t_{def}	Minutes	Defluidization time. Recorded from first addition of biomass fuel until bed defluidizes, unless otherwise noted.
U	m/s	Superficial gas velocity (fluidizing gas velocity)
U/U_{mf}	*None*	Fluidization number
U_{mf}	m/s	Minimum fluidization velocity
X_{QI}		Coefficient specific to different fuel and electricity supply options for QI calculation.
y		"Real" data value when evaluating prediction error for random forest model.
$\hat{y}$		"Predicted" data value when evaluating prediction error for random forest model.
Y_{QI}		Coefficient specific to different fuel and electricity supply options for QI calculation.

Greek Alphabet

Symbol	Units	Description
μ	kg/m.s	Dynamic viscosity of the fluidizing gas
ε_{mf}	*None*	Void fraction of bulk particles
η_{Heat}	%	Heat output efficiency
η_{Power}	%	Power output efficiency
ρ_g	kg/m^3	Density of the fluidizing gas
ρ_s	kg/m^3	Density of the solid
φ_s	*None*	Particle sphericity
ΔG		Change in Gibbs free energy
ΔH		Change in enthalpy
ΔS		Change in entropy

This page intentionally left blank.

This page intentionally left blank.

Chapter 1

Introduction

1.1   Introduction

In recent decades, an increased importance has been placed on fuel sources and power generation technologies that emit reduced amounts of carbon dioxide, a key contributor to anthropogenic climate change [1, pp. 12-19, 2]. With the "Paris Agreement" [3], approved at the 21st United Nations Climate Change Conference (COP21) in 2015, many countries have since signed into law a commitment to keep the increase in global average temperature to "well-below" 2°C, with an aim to limit this to 1.5°C, versus pre-industrial levels. Achieving this aim will necessitate large scale decarbonisation. One fuel type that has captured the interest of researchers, policymakers, and industry in pursuit of these targets is biomass.

Biomass is a broad classification for organic materials that can be used as a fuel source, such as wood or straws [4, pp. 7-9]. Biomass has been termed a "carbon neutral" fuel source, as the CO_2 emitted during the combustion of biomass is equal to that absorbed by the material during its growth cycle, albeit with a small net emission of CO_2 due to processing and transport [5] which may not themselves be CO_2 neutral. The combustion of biomass comes with several technological challenges for traditional pulverized fuel (PF) burners [6]. For example, fuels may not be particularly dense, contain non-combustible contaminants, or may otherwise need large amounts of pre-processing or pre-treatment to be a viable fuel stock for a PF burner. Furthermore, there may be a desire to co-fire biomass with coal, or to use several types of biomass dependent on seasonal availability or cost, all of which would add significant complexity if used with a PF burner.

These challenges have encouraged the use of fluidized bed combustion (FBC) boilers when using biomass fuels. These have the advantage of being able to handle a variety of fuel types, blends, and qualities; a concept termed "fuel flexibility". However, FBC of biomass is not without its own challenges [7]. The primary ash-related issues are

1

fouling and slagging, corrosion, and bed agglomeration. The latter of these, bed agglomeration, is the focus of this thesis. This chapter introduces fluidized bed combustion technology, its use with biomass fuels, and the commercial context surrounding the use of FBC technology with biomass fuels. The chapter ends by stating the aims, objectives, and structure of this thesis.

1.2 Fluidization Theory

Fluidized bed combustion is the application of particle fluidization to the combustion of solid fuels. When a sufficient upwards flow of gas is applied to a bed of particles, the bed will first expand and then become suspended by the gas. In doing so, a fluidized bed is created, as the suspended bed of particles will behave as if it were a fluid [8]. By heating the fluidized bed, it can be used for combustion of solid fuels. The exothermic release of heat during combustion will maintain a bed temperature sufficient for further combustion, thus negating the need for continued heating of the bed by other means.

To fluidize a bed of particles, the 'minimum fluidization velocity', U_{mf}, of the fluidizing gas must be achieved. As Kunii & Levenspiel [8, p. 72] describe, this point of incipient fluidization occurs when:

$$Drag\ force\ by\ upward\ moving\ gas = Weight\ of\ particles$$

The specific equation for U_{mf} differs for different Reynolds numbers (Re_p), though Kunii & Levenspiel [8, p. 73] present two common derivations, with numerous others existing in the literature:

$$U_{mf} = \frac{(\phi_s d_p)^2}{150} \cdot \frac{\rho_s - \rho_g}{\mu} g \left(\frac{\varepsilon_{mf}^3}{1 - \varepsilon_{mf}} \right) \quad Re_p < 20$$

Equation 1.1

$$U_{mf} = \frac{\phi_s d_p}{1.75} \cdot \frac{\rho_s - \rho_g}{\rho_g} g \varepsilon_{mf}^3 \quad Re_p > 1000$$

Equation 1.2

Where:

   φs is particle sphericity, empirically determined

   d_p is particle diameter

ρ_s is particle density of the solid

ρ_g is density of the fluidizing gas

μ is dynamic viscosity of the fluidizing gas

g is gravitational constant

ε_{mf} is the void fraction of the solid

The minimum fluidization velocity is the minimum superficial velocity required to achieve fluidization. The interstitial velocity is that of the gas flowing between the particles in the bed and is higher than U_{mf} [9, pp. 68-71]. Once a bed of particles has been fluidized, gas flow rates are adjusted to achieve the desired 'fluidization regime'. In order of increasing gas velocity, fluidization regimes include: fixed bed (not fluidized), bubbling regime, slug flow, turbulent regime, fast fluidization, and pneumatic conveying (Figure 1.1). As can be deduced from both Equation 1.1 and Equation 1.2, density of the fluidizing gas has an impact on the value of U_{mf}, therefore in the context of FBC, pre-heating of the fluidizing air can impact the value of U_{mf}. Moreover, as the fluidizing air flow enters the hot bed it will further heat up, again changing its density and the relative ratio of the superficial gas velocity to U_{mf}. A fluidized bed undergoes bed defluidization if changes to the gas or particle parameters in Equation 1.1 or Equation 1.2, such as particle diameter or gas density, mean that the minimum fluidization velocity is no longer achieved. Defluidization is characterised by a rapid decrease in the pressure drop across the bed, as gas begins to channel through the bed instead of suspending it.

For FBC, operational gas flow rates are not defined solely based upon those needed to achieve a specific fluidization regime. The amount of air required for combustion also needs to be considered [10]. In commercial FBC boilers, air is typically staged to control combustion and emissions (e.g. NO_x). A fraction of the air required for combustion is delivered into the bed as the primary (fluidizing) air, whilst the remaining air is delivered above the bed in several secondary and tertiary air input stages [11]. The total amount of air delivered to the boiler typically exceeds what is needed on a stoichiometric basis to allow for complete combustion of the fuel. Therefore, the resultant bed fluidization regime is influenced both by the desired fluidization regime, and the proportion of combustion air that is to be delivered to the bed.
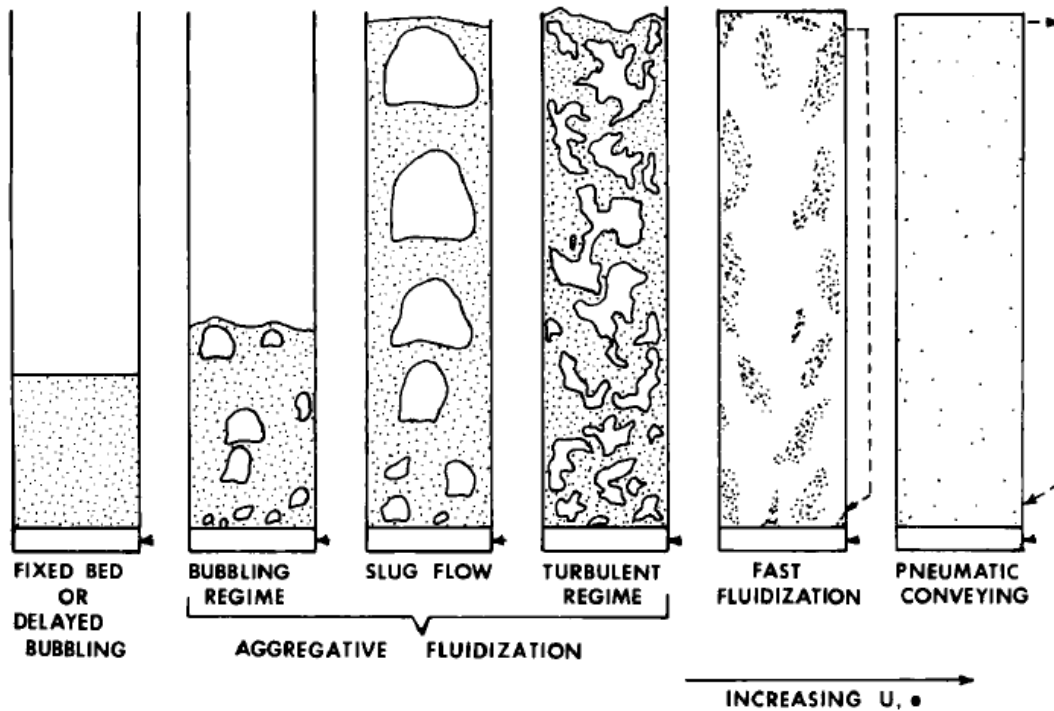
Figure 1.1: *Fluidization regimes. Image reproduced from the work of Grace [12]. Reprinted with approval from copyright holder John Wiley & Sons.*

1.3 Fluidized Bed Combustion Technology

FBC technology has been a topic of research and development since the 1960's [13], with Leckner [14] providing a review of the development of FBC technology over time. Fluidized beds were used for gasification of lignite in the 1920's following a patent by Fritz Winkler [15]. In the 1960's it was identified that FBC could enable better use of low-grade coals and other poor-quality fuels by Douglas Elliott of the British Coal Research Establishment (CRE) [16, p. 192]. Elliott demonstrated that fluidized beds were both suitable for the combustion of coal, and furthermore, that they could offer reduced sulphur emissions via the addition of bed additives and absorbents. In the 1970's interest arose in the Nordic countries in the use of FBC for combusting "difficult fuels" such as peat or paper and pulp waste [16, p. 194]. In 1977, a FBC boiler was commissioned near Stockholm to provide district heating, and utilised several fuels such as coal, peat, and wood biomass [17].

These early FBC boilers were of the "bubbling" bed variety. In the early 1980's Ahlstrom of Finland and Lurgi of Germany began developing "circulating" fluidized bed boilers, with Ahlstrom naming their design "Pyroflow" [18, pp. 19-36]. The late 1980's then saw another variant to FBC technology in the form of the first pressurized

FBC boiler, from a partnership between the International Energy Agency and several countries [19, pp. 120-120].

FBC boilers are now a relatively mature technology, with numerous comprehensive works detailing their design, variants, operation, and scale-up challenges [4, 20, 21, 22, 23]. The three main design options for FBC units that arose from the 1960-1990 period of rapid development remain: bubbling fluidized bed (BFB) designs, circulating fluidized bed (CFB) designs, and pressurized fluidized bed (PFB) designs.

As described by Basu [21, p. 7], a BFB boiler (Figure 1.2) consists of the following primary sections:

> **Bed:** In a BFB, the gas flow rate through the bed is set such that entrainment of bed material is minimized, with a bubbling fluidization regime desired.
>
> **Freeboard:** The open space above the bed where wall tubes are typically placed for raising steam, as well as the input location for secondary and tertiary combustion air streams. The uppermost region is typically where superheater tube banks begin.
>
> **Backpass:** The ducting through which flue gas exits the top of the BFB combustion chamber, and often holds economizers and air pre-heaters for heat recovery from the flue gas.
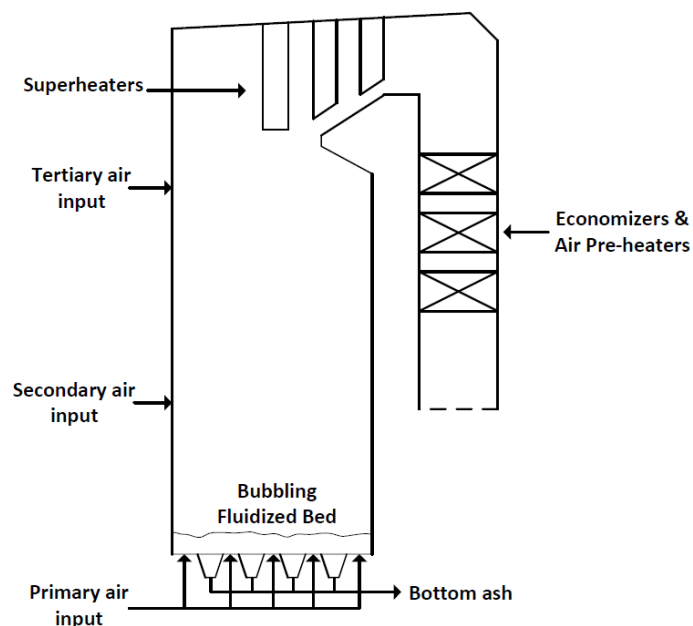
Figure 1.2: *Simplified diagram of a BFB boiler. Adapted and redrawn from the diagram of Basu [21, p. 212].*

Basu [21, p. 8] also details the main characteristics of a CFB boiler (Figure 1.3):

Combustion chamber with bed: Gas flow rates are set such that bed material becomes entrained in the gas flow and will be carried out of the combustion chamber, thus the bed is the full height of the chamber.

Cyclone (or equivalent) for solids removal: On leaving the combustion chamber, the combined stream of gas, bed material, and ash passes into a cyclone (or equivalent) where solids are removed.

Solid recycle loop: Bed material from the cyclone then flows back into the bottom of the combustion chamber, resulting in a continuous loop of bed material from the combustion chamber, into cyclone, and back again. The loop seal design itself is often a bubbling fluidized bed to promote movement of bed material back into the combustion chamber.

Some of the typical key design parameters for BFBs and CFBs are given in Table 1.1 as a point of comparison.
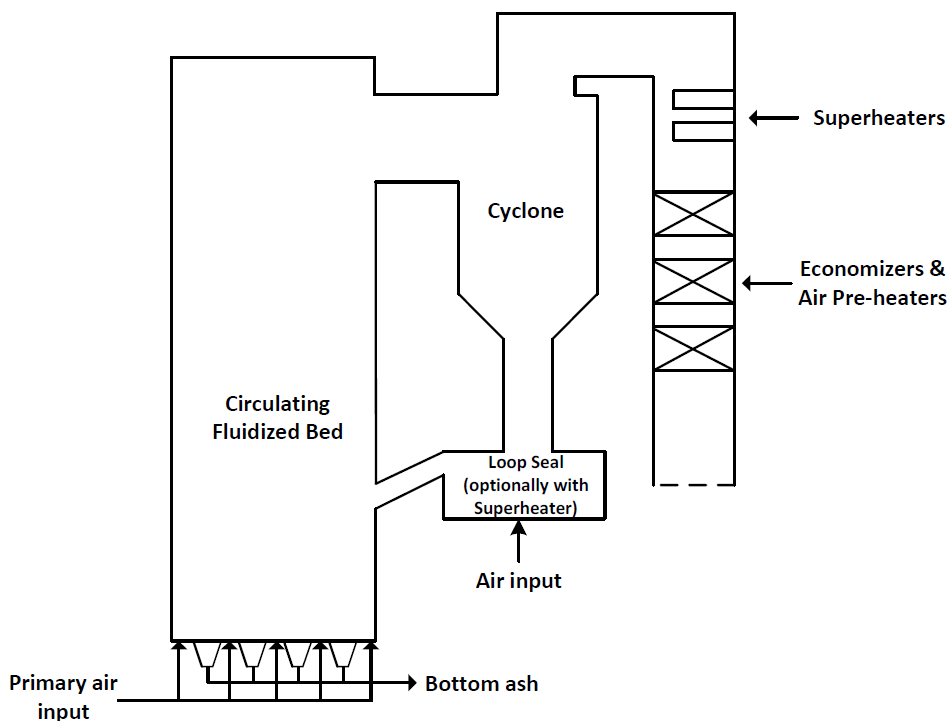
Figure 1.3: *Simplified diagram of a CFB boiler. Adapted and redrawn from the diagram of Basu [21, p. 254].*

Table 1.1: *Typical design parameters for BFBs and CFBs. Data collated from work of Koornneef, et al. [24], and Basu [21, p. 6].*

Parameter	BFB	CFB
Operating Temperature (°C)	760-870	800-900
Operating Pressure	Atmospheric	Atmospheric
Fluidization Velocity (m/s)	1-3	3-10
Boiler Efficiency (%)	90-96	95-99.5
Bed Height (m)	1-2	10-30

Pressurized fluidized beds (PFBs) operate at an elevated pressure, typically 10-15 bar [25], and come in either bubbling PFB or circulating PFB variants, similar to their atmospheric pressure equivalents. However, PFBs are less common, with only six circulating PFB boilers in commercial operation as of 2004 [24], thus will not be discussed in further detail.

Table 1.2 summarises information on the installed capacity of both CFB and BFB type boilers from several of the main manufacturers. CFB installations are both more numerous and, on average, are larger in capacity than BFBs. As Koornneef, et al. [24] describe, this is due to CFB boilers being easier to scale-up. At present, BFB boilers are preferred when burning more challenging high ash fuels or blends, whereas CFB boilers are preferred with lower ash fuels which can be handled at larger thermal capacities [26]. A broad discussion on the difficulties and development of FBC technology over time is given in a review by Bañales-López & Norberg-Bohn [13].

Recent numbers from Sumitomo SHI FW (formerly part of Foster Wheeler) show that they have installed 385 CFB units worldwide as of 2012 [27]. This implies there is continued high demand since installed figures were collated in 2007, as figures in Table 1.2 represent the total of several manufacturers.

Table 1.2: *Total installed capacity, total number of boilers, and total number of installations, for boilers from the following manufacturers as of 2007: Alstom, Babcock and Wilcox, Babcox Borsig, Bharat Heavy Electricals, EPI, Foster Wheeler, Kvaerner Pulping, Lurgi-Lentjes. Data adapted from Koornneef, et al. [24]. (Note that several of these manufacturers have changed names due to mergers or ownership changes. Refer to Table 1.3). More recent equivalent data on the total number installations globally has not been collated. As of 2013, more than 80 supercritical CFB boilers of capacities 350-660MW$_e$ were installed in China, which are in addition to the numbers below [28].*

Type	Installed Capacity (MW$_e$)				No. of boilers	No. of installations
	Min.	Max.	Average Per Boiler	Total		
BFB	<1	142	23.2	4,011	173	146
CFB	<1	520	79.1	23,422	396	311

Table 1.3 highlights the major designers of large scale commercial FBC boilers and the typical fuel/size options for each offering where available. This list is not exhaustive, and designers of smaller scale units are not included. Changes in names and ownership have been reflected where appropriate, as significant amounts of available literature are listed under previous company names. As discussed, it is clear from Table 1.3 that BFBs are offered at smaller sizes for challenging biomass fuels, with CFBs generally offered to larger sizes albeit for better quality biomasses and coals.

Table 1.3: *Major designers of fluidized bed boilers, and their largest boiler thermal capacity offered. Note: where an example of the largest installed capacity is not stated by the manufacturer, the largest capacity offered is instead quoted. In some cases, boiler thermal capacity data is not available and electrical generation output is instead listed.*

Manufacturer	BFB	CFB
Sumitomo SHI FW *(FB boiler business previously part of Foster Wheeler)*	Fuels: Biomass Largest installed capacity: $100MW_{th}$ [29]	Fuels: Coals, biomass, other wastes Largest installed capacity: $1116MW_{th}$ x4 (coal + biomass), $651MW_{th}$ (biomass) [30, 31]
Valmet *(FB boiler business previously part of: Metso, Kvaerner)*	"HYBEX" Fuels: Woody, pulp & paper sludge, peat, some agricultural fuels/wastes Largest installed capacity: $400MW_{th}$ [32]	"CYMIC" Fuels: Coals, biomass, mixed fuels Largest installed capacity: $1200MW_{th}$ [33]
GE *(FB boiler business previously part of Alstom)*	*Not available*	Fuels: Coals, biomass, other waste fuels Largest installed capacity: $330MW_e$ x2 (coal) [34, 35]
Andritz	"ECOFLUID" Fuels: Biomass, refuse derived fuel (RDF), residues Largest capacity offered: approx. $400MW_{th}$ [36, 37]	"POWERFLUID" Fuels: Coals, biomass Largest capacity offered: approx. $800MW_{th}$ [37, 38]
Babcock & Wilcox	Fuels: Biomass Largest capacity offered: approx. $430MW_{th}$ [39]	"IR-CFB" Fuels: Coals, biomass Largest capacity offered: approx. $960MW_{th}$+ [40]
Doosan Lentjes	*Not available*	Fuels: Biomass, Coals, others wastes. Largest installed capacity: $700MW_{th}$ [41]
Dongfang	*Not available*	Fuel: Coals Largest installed capacity: $660MW_e$ supercritical CFB [28]

1.4   Biomass

As seen in section 1.3, biomass fuels are a common option for fluidized bed boilers. Biomass fuels are chiefly divided into one of four categories, as Jenkins, et al. [42] list:

1. Wood & woody materials.
2. Herbaceous & other annual growth materials (e.g. straws, grasses & leaves).
3. Agricultural by-products & residues (e.g. shells, hulls, pits, animal manure).
4. Refuse derived fuels (RDF), wastes & other non-recyclables.

Proximate analyses performed by Jenkins, et al. [42] across a broad range of biomass fuels reveal that on a dry fuel basis, fixed carbon values are between 12-20wt.%, volatile matter contents are between 70-85wt.%, and ash contents are between 2-8wt.%. The high quantity of volatiles, plus the large moisture contents of biomass (frequently 30-60wt.%) have similarly been shown in the works of others [43, 42, 44, 45]. Typical ultimate analyses data from the work of Jenkins, et al. [42] is shown in Table 1.4 as a point of reference. A recent extensive review and study by Vassilev, et al. [46] examined ash compositions and behaviours during combustion for a wide range of biomass fuels, including the potential effects of biomass blends. This work illustrated the high complexity and variation in biomass ash, with silica, alkali and alkaline earth metals featuring as significant components of biomass ash (20wt.%+), as well as the high amounts of chlorine and heavy metals for some fuels.

Table 1.4: *Typical ultimate analyses data for the biomass fuels examined by Jenkins, et al. [42].*

Component	Typical Range (wt.%)
Carbon	38.00-50.00
Hydrogen	4.50-6.00
Oxygen (diff.)	35.00-40.00
Nitrogen	0.50-1.50
Sulphur	0.05-0.20
Chlorine	0.10-0.50
Ash	2.00-8.00

Saidur, et al. [43] placed biomass fuels into one of three different categories based upon their fuel ash composition:

- Ca- & K-rich, Si-lean. Typically woody biomass.
- Si- & Ca-rich, K-lean. Typically herbaceous or agricultural.
- Ca-, K-, & P-rich, e.g. sunflower stalk ash or rapeseed expeller ash.

The variability of biomass makes its combustion more challenging, particularly for pulverized fuel (PF) combustion technology (e.g. differing energy densities, variable composition by source/season, and non-combustible contaminants). These factors necessitate significant amounts of processing (e.g. pelletization) to effectively use biomass fuels in PF burners [4, 6, 20]. These are challenges that FBC technology can overcome, as fuel can burn over longer timescales and be delivered in larger physical sizes. Fuel does not need to be delivered to the burner in the form of a fine, homogeneous powder for near instantaneous combustion as is needed in a PF burner [6].

This variety of forms that biomass comes in offers a level of security and dependability to the fuel supply [47, 48]. The International Energy Agency's (IEA) 2020 World Energy Balances Report [49, p. 9] stated that biomass accounted for 9% of the total global energy supply of 14,282Mtoe. Biomass as a fuel is frequently used as a fuel in combustion and gasification systems due to its wide availability [50, 51]. In 2016, the UK Government reported on the estimated levelized cost of electricity (LCOE) for several fuels and generation technologies [52, p. 29]. This report gave an estimated LCOE of £87/MWh for a biomass power station deployed in 2020, compared to values of £66/MWh for combined cycle gas turbines (CCGTs), £63/MWh for on-shore wind, and £106/MWh for off-shore wind. Whilst these figures show that biomass is unlikely to become a dominant fuel source in the UK on a cost basis, they do show that it remains a viable option. One further advantage to biomass versus renewable sources such as wind and solar is that it can also be used for dispatchable or baseload power generation as it does not depend on weather conditions, ensuring security of generation. These cost and technical benefits have led to biomass becoming a part of the UK power generation fuel mix.

1.5   Biomass Power Generation in the UK

The UK Government's National Renewable Energy Action Plan [53], released in 2010, identified that biomass would be a key renewable energy source for power and heat moving forward. In particular, the report highlighted the likelihood that wood would become a commonly traded resource within Europe and elsewhere for power generation, that there was potential in the UK to further utilise waste wood for power generation, and that there was the opportunity for wider growth and use of energy crops

such as miscanthus and straw. The 2020 Digest of United Kingdom Energy Statistics (DUKES) [54] quotes a value of 25TWh of energy generation from biomass in 2019, a 9.2% increase over the previous year, out of a total UK electricity generation of 325TWh. In total, 28% of the UK's renewable electricity generation was from biomass. This is slightly greater than onshore wind and offshore wind which each accounted for 27% of renewable electricity generation, but when combined accounted for a total of 52% of the UK's renewable electricity generation.

Clearly, biomass has become a key segment of UK renewable energy generation. This uptake been stimulated by financial incentives available to biomass users, such as the Renewable Obligation (RO) scheme, and the non-domestic Renewable Heat Incentive (RHI) scheme, which increased revenue for generators [55]. However, the RO scheme was closed to new applicants of March 2017, with the RHI scheme set to close in 2021. This has introduced uncertainty in industry around the viability of constructing new, large-scale biomass energy facilities. As an example, the Port Clarence Biomass Power Plant was mothballed late into construction at of the end of 2018, due to missing contractually required commissioning deadlines that would have enrolled it into the RO scheme [56].

At present, there are numerous large biomass energy facilities in the UK. As of the end of 2017, there were 22 power or combined heat & power (CHP) stations using biomass fuels in the UK with outputs $>15MW_e$, with 8 more having received planning approval and being in various stages of construction and commissioning [57]. These use a mixture of combustion technology types, such as pulverized fuel burners, fluidized beds, and moving grates. Large biomass-firing fluidized bed boilers in the UK are listed in Table 1.5, and are shown on a map of the UK in Figure 1.4. As is evident from Table 1.5, the entire UK fleet of FBC units primarily use wood fuels, with the only exceptions being those associated with paper mills, which burn paper sludge waste in addition to wood. This use of wood as a biomass fuel is common elsewhere around the world, largely because wood presents less severe ash related issues in comparison to other biomass fuels [7].

Table 1.5: *Table listing large (>20MW$_e$) biomass-firing fluidized bed power/CHP stations in the UK and key details (ordered by start-up date).*

Name	Operator	Nameplate Capacity	Fuel	Boiler Design	Start-up year	Ref.
Wilton 10 Power Station	Sembcorp Energy UK	35MW$_e$ (CHP)	Wood & waste wood	BFB, Sumitomo SHI FW	2007	[58]
UPM Shotton Paper Mill Boiler	UPM	20MW$_e$	Wood & paper sludge	"HYBEX" BFB, Valmet	2007	[59]
Steven's Croft Biomass Power Station	E.ON	44MW$_e$	Wood & waste wood	"HYBEX" BFB, Valmet	2008	[60]
UPM Caledonian Paper Mill Boiler	UPM	26MW$_e$ (CHP)	Wood & paper sludge	"HYBEX" BFB, Valmet	2009	[61]
Iggesund Paperboard Biomass Power Station	Iggesund	44MW$_e$	Wood	"EcoFluid" BFB, ANDRTIZ	2013	[62]
Blackburn Meadows Power Station	E.ON	29MW$_e$ (CHP)	Wood & waste wood	"EcoFluid" BFB, ANDRTIZ	2014	[36]
Markinch Biomass Power Station	RWE	50MW$_e$ (CHP)	Wood & waste wood	"CYMIC" CFB, Valmet	2014	[63]
Tansterne Biomass Gasification Plant	Solar 21	22MW$_e$	Waste wood	2x "STABB" BFB, HRS Energy	2018	[64]
Tees Renewable Energy Plant (REP) (MGT Teesside)	Fortum	299MW$_e$	Wood pellets	CFB, Sumitomo SHI FW	2021 (expected)	[65]

The demand for woody biomass fuels has led to the UK becoming Europe's biggest importer of biomass fuels [66]. As of 2016, virgin wood supply for power generation in the UK was 3.2Mt from a total harvest of 10.7Mt, whilst demand was estimated at 3.3Mt [57]. It is a similar situation for recycled wood, with a total supply estimate of 5Mt for all users, but a power generation demand of 1.6Mt [57]. Further expansion of power generation from woody biomass in the UK will necessitate increased importing, virgin wood harvesting, and/or a reduction in demand from other wood users. The UK Government identified that it was necessary to move away from woody fuels towards greater use of agricultural fuels such as straws and miscanthus in 2010 [53]. Recent presentations at the Fuel and Energy Research Forum in the UK by professionals in the biomass power industry have also highlighted this strain on UK wood supply, and

active efforts to investigate the viability of alternative biomass fuels for biomass power generation [67, 68]. The combined pressures of a limited UK wood supply and uncertainty surrounding government subsidises such as the RO and RHI have created a commercial environment in which biomass power station operators in the UK will increasingly have to consider use of non-woody fuels as a part of their fuel blend. In the context of FBC units, this would principally require overcoming ash related issues, as these are typically worse when using non-woody biomass fuels.
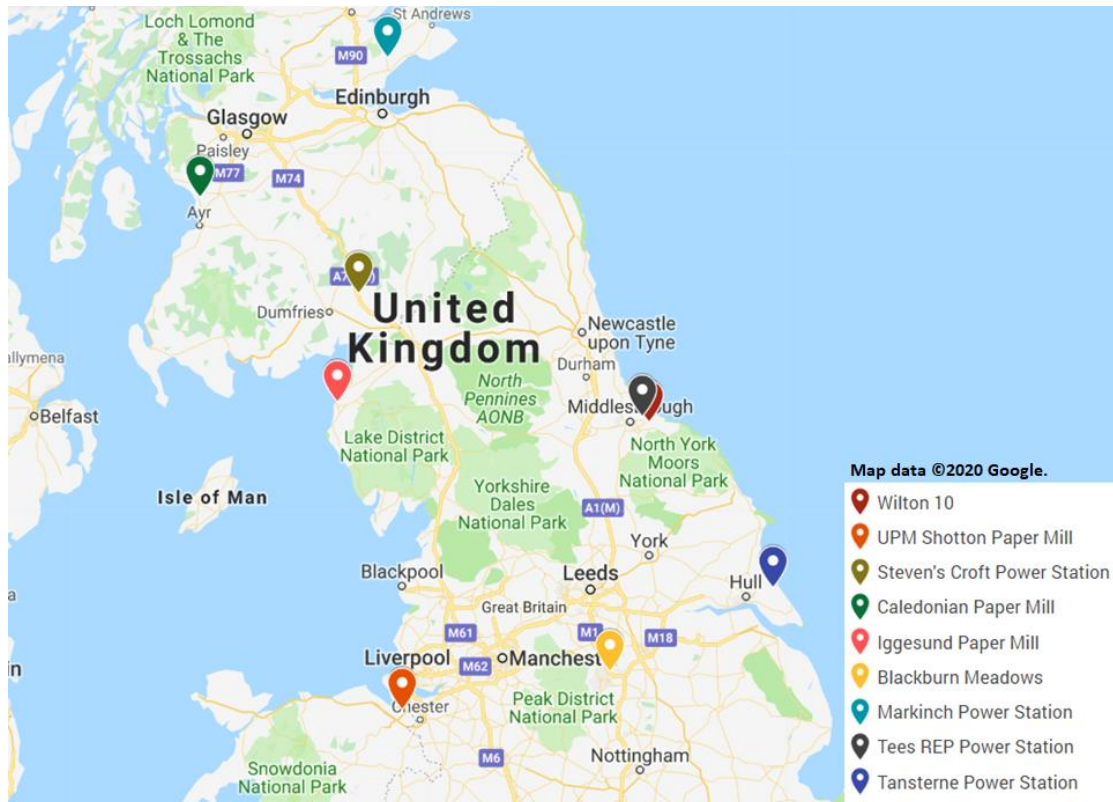
Figure 1.4: *Map showing the large-scale (>20MW$_e$) biomass fluidized bed power stations in the UK, as detailed in Table 1.5. Map created using Google Maps. Map data ©2020 Google.*

1.6 Ash Related Issues During Biomass Combustion

There are four principal ash related issues during fluidized bed combustion of biomass: agglomeration of the bed, slagging and fouling of heat transfer surfaces, and corrosion of boiler metalwork [7]. Figure 1.5 shows where these issues arise within a simple BFB boiler design.

Agglomeration occurs within the bed itself and is where bed particles begin to group together into larger particles [69] (Figure 1.6). In the case of biomass combustion on a silica sand bed, this is due to the formation of sticky alkali silicate melts of low melting temperature. These agglomerates may be further strengthened by sintering, in which

high localised temperatures leads to the melting and fusing of particles into large, hardened structures. The accumulation of agglomerates eventually leads to defluidization of the bed. This is the point at which the bed particles no longer move and behave as a fluid in response to the fluidizing gas, as the mean bed particle size will have increased meaning that the minimum fluidization velocity, U_{mf}, is no longer achieved [8].
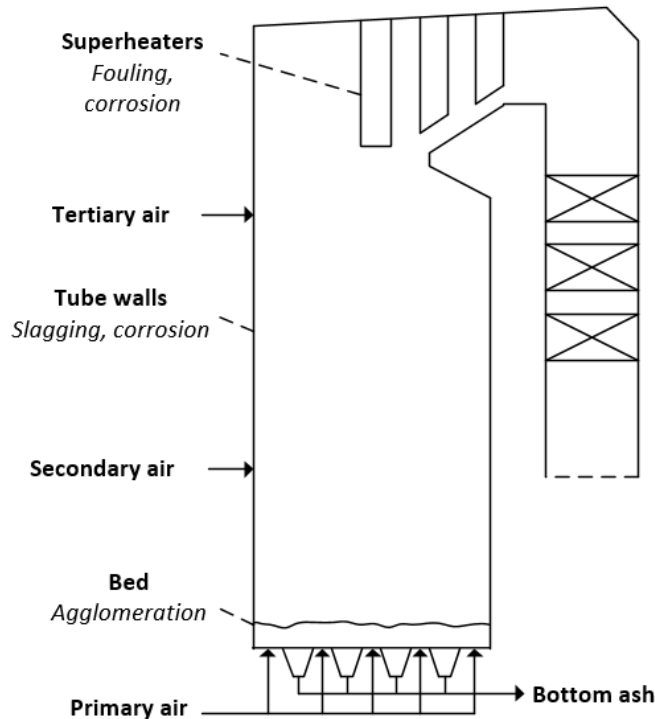
Figure 1.5: *Simplified diagram of a BFB boiler highlighting areas where biomass ash contents (alkali and alkaline earth metals, silica, and chlorine) cause issues. Adapted from the diagram of Hupa, et al. [70].*

In a commercial FBC boiler, operators may control agglomeration by varying fuel feed-rates or blends, using alternative bed materials and/or additives, moderating combustion temperatures and combustion distribution, altering and moderating airflows, or varying rates of bottom ash removal and bed replenishment [71, 72]. A full bed defluidization event would necessitate an unscheduled plant outage, as the bed is cooled, replenished, and started up again [73]. This process would take upwards of 48 hours and would be accompanied by a significant loss of revenue. Moreover, frequent start-up and shutdown cycles may reduce the working lifespan of plant equipment [74, pp. 38-42]. As such, considerable efforts have been made towards methods to predict or prevent agglomeration issues [75].

Figure 1.6: *Image of several agglomerate samples collected from 50kW$_{th}$ fluidized bed combusting wheat straw pellets on a quartz sand bed. Image from experimental work performed as part of this project. Scale is in cm.*

Moving from the bed to the upper sections of the boiler, slagging of the tube walls and fouling of the superheater tubes [76, 77, 78, 79] are processes driven by similar chemical components to agglomeration: alkali silicates, alkali chlorides, and alkali sulphates. Here, alkali silicate melts form deposits, or in some cases alkali chlorides or alkali sulphates, with slagging structures often becoming comprised of multiple layers. Slag deposits may fall off wall tubes and into the bed as they develop, or during on-line soot-blowing. When in the bed, they have the same effect as agglomerates on bed fluidization. Corrosion [77, 80, 81, 82, 83] is caused mainly by chloride species, such as alkali chlorides, hydrogen chloride, or metal chlorides ($PbCl_2$, $ZnCl_2$). Alkali chloride species can also form part of slagging or fouling deposits to further worsen corrosion.

As all these ash related issues are inter-related, it is important to consider the effect on the whole boiler system when evaluating possible countermeasures to one of these issues. For example, countermeasures to agglomeration such as replacing a silica sand bed material with an alternative bed material may free up alkali metal species to then increase the severity of slagging and fouling. Countermeasures that react directly with alkali metals, such as kaolin, may cause chlorine to form HCl instead of alkali chlorides, thereby changing the type of corrosion that proceeds [84], which may necessitate changes to boiler metals or anti-corrosive coatings.

It is for these reasons then that each of these ash related issues receives continued investigative research work, despite the existence of countermeasures to each issue in isolation. The interests of commercial boiler operators also motivate this continued

research activity, as they must manage ash issues whilst maximising plant uptime and profitability.

1.7   Sembcorp Energy UK

Sembcorp Energy UK (SCE) were the industrial partner for this project. SCE own the 2000 acre Wilton International site in Middlesbrough, UK, where they supply electricity, steam and water treatment services to chemicals and manufacturing clients on the site [85]. To provide these services, SCE operate a broad mix of assets [86] including gas turbines, an energy from waste (EfW) plant, and Wilton 10 (W10): a 35MW$_e$ CHP station that uses a bubbling fluidizing boiler designed by Sumitomo SHI FW [58] (see Table 1.5). W10 was the UK's first large scale biomass power station when opened in 2007 and was later converted to CHP in 2010. A mixture of virgin wood and recycled wood is used for fuel. Over the course of the project, process engineering work has been performed with SCE to improve the performance of W10, which forms Chapter 7 of this thesis.

1.8   Aims and Objectives

The aim of this project was as follows:

> To broaden and deepen knowledge surrounding the mechanisms and mitigation of agglomeration when varying operational conditions, changing bed materials, or using additives. A particular focus is to be placed on the use of non-woody biomass fuels, which are less explored in the literature, but do attract interest from researchers and industry as a means to widen FBC fuel envelopes.

To fulfil this aim, objectives were defined as follows:

1. Perform exploratory work across a range of fuels, bed materials and operational conditions, to both clarify the existing literature and deepen the knowledgebase. Determine the relative performance of each fuel, of different bed materials, and the differences in agglomeration mechanisms when varying these factors.

2. Investigate the effects of varying dosages of kaolin and dolomite bed additives with agricultural biomass fuels (wheat straw and miscanthus). Determine the best additive for each fuel, the fundamental agglomeration mechanisms with each fuel/additive combination, and the impact of dosage variations.

3. Perform thermochemical modelling of the fuel and additive combinations tested experimentally in fulfilment of objective 2. Determine if the predicted performance aligns with that seen experimentally and use this to evaluate the overall usefulness of thermochemical modelling tools for agglomeration studies.

4. Perform mixed process engineering and performance improvement activities with industrial sponsor Sembcorp Energy UK on the "Wilton 10" CHP station. A focus is to be placed on a study of the existing blend-to-boiler fuel mixture, and how this may be altered or improved to increase plant performance.

1.9 Thesis Structure

This thesis is divided into 8 chapters. Chapter 1 is this introductory chapter to fluidized bed combustion, biomass usage for power generation, and associated issues.

Chapter 2 is an extensive literature review on the mechanisms of agglomeration during fluidized bed combustion of biomass, studies into agglomeration mitigation, and the use of thermochemical modelling software for biomass ash models and advanced analytical techniques for fuel studies.

Chapter 3 details the experimental methods and materials that were used across the course of the project, along with the approach to thermochemical modelling and industrial fuel data analysis. A discussion on the strengths and weaknesses of the methods is given where appropriate.

Chapter 4 covers the fulfilment of objective 1. Four different biomass fuels were tested, along with sand and olivine bed materials of varying particle sizes. Bed height and bed particle size were also varied. The effects of these materials and operational conditions on emissions and agglomeration were evaluated to clarify inconsistencies in the existing literature and expand existing knowledge, particularly with use of wheat straw and olivine. A novel spatial study of agglomerate composition in different bed regions was also performed.

Chapter 5 explores the impact of varying dosage rates of kaolin and dolomite with miscanthus and wheat straw fuels, in fulfilment of objective 2. The effect of varying additive dosage has been considered for each fuel. A thorough study of agglomerate structure and composition has been performed, across common agglomerate features

and locations, to fully elucidate the mechanisms by which each additive mitigates agglomeration.

Chapter 6 investigates thermochemical modelling of biomass ash with the software package FactSage, in fulfilment of objective 3. The additive scenarios tested experimentally in Chapter 5 are modelled from both a "ground up" basis, using fuel ash, additives, and gas environments as model inputs, along with modelling experimental agglomerate composition data from Chapter 5. Each approach is compared. Following this is a discussion of accuracy and usefulness of FactSage for agglomeration studies.

Chapter 7 is in fulfilment of objective 4 and discusses a study of the Wilton 10 blend-to-boiler fuel mixture. This comprises an in-depth analysis of the current fuel contaminants in terms of change over time and the application of advanced data analytical techniques, including a machine learning approach (random forest regression), to attempt to find underlying fuel relationships. Consideration is also given to the viability of increasing the proportion of waste wood in the fuel blend.

Chapter 8 contains the final conclusions and recommendations for future work, collating the key findings of the research performed across Chapter 4-Chapter 7.

Several appendices are included at the end of this document. Appendix A lists all publications and dissemination arising from this work. Appendix B lists the taught modules completed in fulfilment of the EngD programme requirements. Appendix C and Appendix D contain supplementary information regarding the FactSage modelling work which is the subject of Chapter 6. Appendix E-Appendix K contain supplementary information regarding the industrial fuel data study in Chapter 7 and the work with Sembcorp Energy UK.

Chapter 2

Literature Review

A version of this chapter has been published by the author in the form of a journal article [87]:

> *Mechanisms and mitigation of agglomeration during fluidized bed combustion of biomass: A review.* ***Morris, J.D.***, *Daood, S.S., Chilton, S., Nimmo, W. 2018. Fuel, Vol. 230, pp. 452-473.*

Within this chapter, content has been expanded or abridged in different areas as required to be commensurate with normal thesis formatting. New literature published in subsequent years has been incorporated where appropriate.

2.1 Introduction

This chapter provides a comprehensive review of the current literature on mechanisms and mitigation of agglomeration when using biomass fuels in a fluidized bed combustor. Prior reviews in the field have looked broadly at all ash challenges (agglomeration, slagging, fouling, corrosion) [7, 77], or focused on modelling [88] or the prediction of agglomeration [75]. Reviews specific to agglomeration have only briefly considered the mitigating effects of operational parameters on agglomeration [89, 90].

2.1.1 Review Scope

This chapter is divided into three review sections:

- The mechanisms of agglomeration.
- The effects of process variables on agglomeration severity.
- Use of FactSage for thermochemical modelling in agglomeration studies, and the random forest machine learning algorithm for biomass fuel studies.

Summaries are provided at the end of each section to highlight key findings, note the important critiques, and list key areas for further work. The end of chapter summary highlights the main areas where further work is needed.

2.2   Mechanisms of Agglomeration

2.2.1   Fundamental Agglomeration Chemistry

As noted in Chapter 1 section 1.6, the fundamental chemistry driving agglomeration is the formation of alkali silicate eutectics. This is from the interaction of SiO_2 in the bed material or ash together with alkali metal oxides in the fuel ash, such as K_2O or Na_2O. For example [91]:

$$K_2O + nSiO_2 \rightarrow K_2O \cdot nSiO_2$$
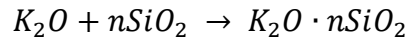
Equation 2.1

The value of 'n' may range from 1-4. In the case of potassium silicates, higher values of 'n' generally reduce the eutectic melting point: with $K_2O \cdot SiO_2$ this is 976°C, whilst for $K_2O \cdot 4SiO_2$ the melting point is 764°C [91]. These low melting points allow for the formation of a melt in the typical FBC bed temperature range of 800-900°C [92], which can then cause adhesion of the bed particles and agglomeration. Other chemical components are also important to biomass ash melting behaviours. For example, increases to the calcium content of an ash melt system raises its melting point, as per the K_2O-CaO-SiO_2 ternary system [93]. The K_2O-CaO-SiO_2 ternary liquidus projection phase diagram, as investigated by Morey, et al. [93], is shown in Figure 2.1 as a point of reference. The behaviour with changes to CaO content is clear in Figure 2.1. Increases in isotherm temperature values occur with increases to CaO content when moving up the right-most axis, and general increases in isotherm temperature values are seen when reducing the K_2O content of the system. Fuels with high phosphorous content add further complexity and challenge to biomass ash melting [94, 95, 96, 97]. Calcium reacts with phosphorous instead of silica to form more stable calcium phosphates. This reduces the CaO content of the K_2O-CaO-SiO_2 ternary system, reducing melting temperatures. Potassium also reacts with phosphorous to form low melting point potassium phosphates, with these also reacting with silica (e.g. in bed material) to form potassium silicates.

The accumulation of agglomerates within the bed will eventually cause bed defluidization [75], hence the interest in minimizing agglomerate formation. Early works into agglomeration with biomass fuels identified eutectic melts as key drivers of agglomeration [98, 99, 100]. Sintering (Figure 2.2) had been identified as a key driver of agglomeration in coal research [101]. This is the process by which bridges between

particles are formed or strengthened by the diffusion of surface matter across particle boundaries, resulting in particles being fused together. Skrifvars, et al. [102] looked at this phenomenon when combusting biomass, and found that the presence of a >15% molten phase in ash would lead to elevated amounts of sintering. Skrifvars, et al. [103] then applied standardised ash testing methods to predict sintering and agglomeration temperatures in biomass. However, there was limited success with either of these methods at predicting agglomeration severity. Subsequent work has led to the definition of two different agglomeration mechanisms: coating-induced agglomeration and melt-induced agglomeration. These will be discussed in detail over the following sections.
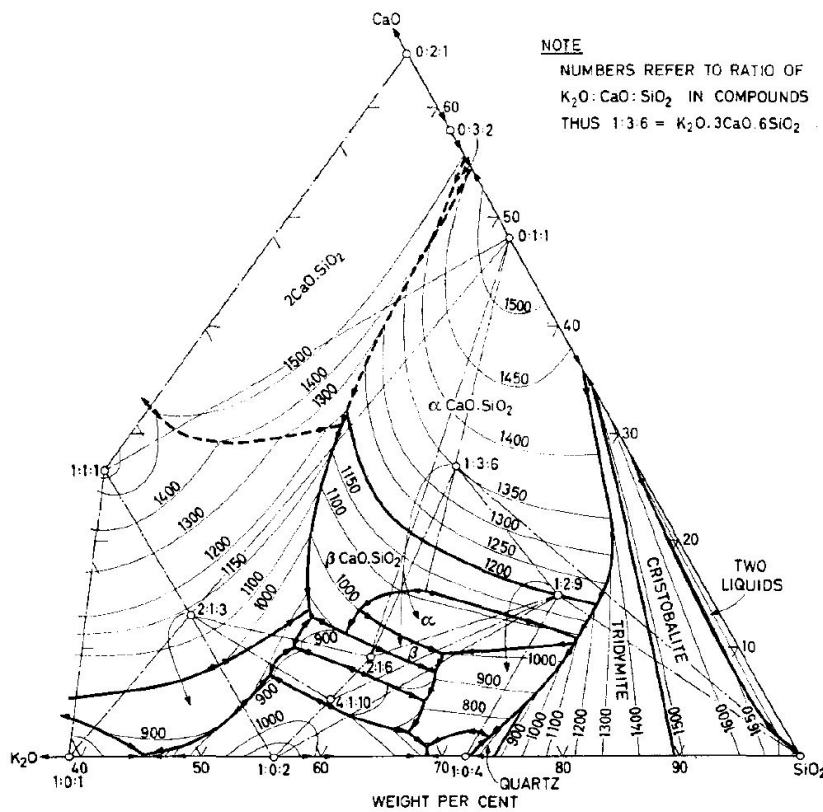
Figure 2.1: *K_2O-CaO-SiO_2 ternary liquidus projection diagram. Reproduced from the work of Roedder [104] with the permission of copyright holder Elsevier. Originally presented by Morey, et al. [93].*
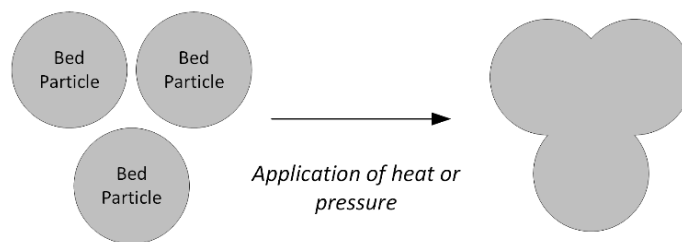
Figure 2.2: *Generalised diagram showing the progression of sintering. Within an atmospheric fluidized bed, particles may be fused together under high temperatures. Diagram adapted from Hosford [105, p. 144].*

2.2.2   Coating-induced Agglomeration

In the work of Öhman, et al. [106], combustion experiments for several different woody and agricultural biomass fuels were performed at lab-scale, using the "Controlled Fluidized Bed Agglomeration" methodology put forth in their earlier work [107]. Here, controlled incremental heating was applied to the bed until agglomeration was detected by principal component analysis (PCA) of temperature and pressure fluctuations within the bed. This was followed by scanning electron microscopy with energy dispersive X-ray spectroscopy (SEM/EDX) analysis of the resulting agglomerates, which focused on the "neck" between two joined particles.

The most abundant non-silica components in the agglomerates were alkali metals or alkaline earth metals – primarily either potassium or calcium – which accounted for between 20-70wt.% across the different fuels. For some fuels, aluminium and iron featured in amounts of up to 20wt.%. Öhman, et al. [106] then proposed the following mechanism for agglomeration:

1. Ash is deposited on bed particles creating a coating, through a mixture of small particles attaching to bed material, gaseous alkali molecules condensing, and reactions involving gaseous alkali molecules on the surface of the bed material.
2. Sintering occurs on this bed particle coating, homogenizing and strengthening it.
3. Melting of this silicate coating layer controls adhesive forces, which influence the severity of the agglomeration process. This is temperature-driven.

The work of Silvennoinen [108] also describes a coating mechanism similar to that of Öhman, et al. [106] with woody fuels, and states that whilst potassium silicates are the primary chemical basis for coating layers, in some cases sodium silicates are instead present. This highlights that other alkali-silicates can be the basis of coating layers.

The works of Nuutinen, et al. [109], Visser [110], Brus, et al. [111], and Öhman, et al. [112] are closely related, in that they further investigated bed particle coatings, all finding compositional and structural differences through the layers, indicating the presence of multiple layers. These works took samples from woody fuels, typically using quartz sand beds, at scales from lab-scale FBC units to full-scale installations.

The presence of multiple layers appears to be a factor of the potassium content of the fuel, with an example from the work of Visser [110] shown diagrammatically in Figure 2.3. Fuels that are lean in potassium produce two layers: an "inner" homogeneous layer

with significant calcium content, and an outer heterogeneous layer more similar in composition to that of the fuel ash. Fuel that are rich in potassium produce an additional "inner-inner" layer with notable amounts of potassium. The relative compositions of the inner and outer layers remain similar regardless of if the fuel is potassium-rich or lean. The difference in the relative compositions across the outer, inner, and inner-inner layers are shown in Figure 2.3.

Three-layer coating: K-rich system

Two-layer coating: K-lean system

Element	Outer Layer wt%	Inner Layer wt%	Inner-Inner Layer wt%
Si	3	14-18	34
P	6	-	-
S	4	-	-
K	7	-	10
Ca	29	44	4-5

Element	Outer Layer wt%	Inner Layer wt%
Si	3	14
P	5	-
S	4	-
K	7	-
Ca	28	41
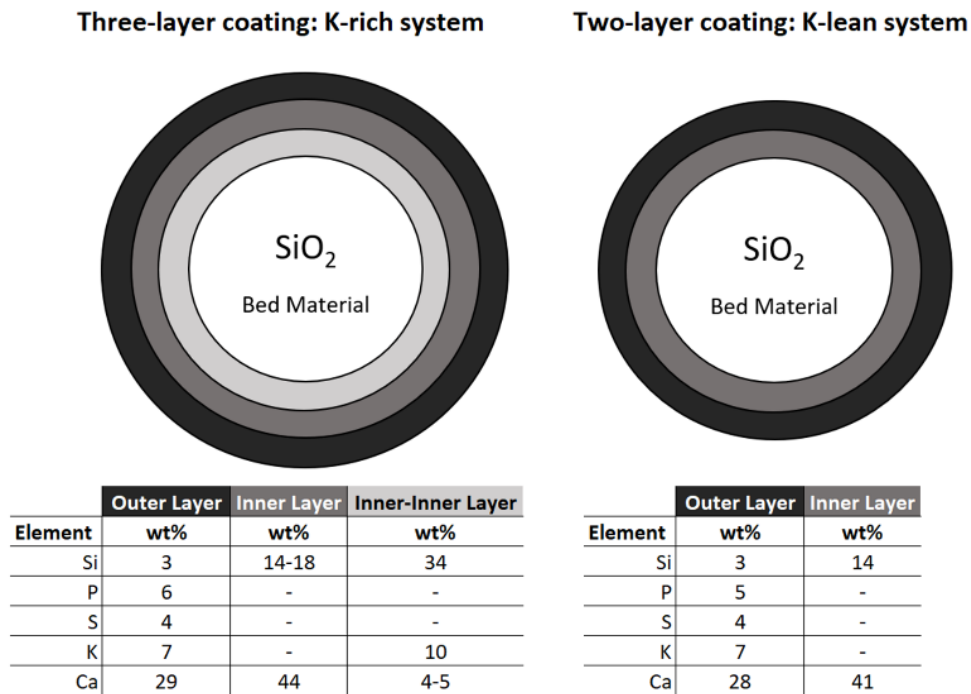
Figure 2.3: *Diagram showing the compositional differences between two- and three-layer coating systems, as described by Visser [110]. Based on the diagram of Visser [110].*

Some different observations can be seen between the works of Nuutinen, et al. [109], Visser [110], Brus, et al. [111], and Öhman, et al. [112].

Nuutinen, et al. [109] noted that for the combustion of peat the "inner" layer was absent, leaving only the outer ash layer. This could perhaps be a result of the operational time, conditions, or a behaviour unique to peat as a fuel. Nuutinen, et al. [109] also trialled a proprietary magnesium-based bed particle named "GR Granule", which had two coating layers present: an inner layer of ~60% calcium and 15-20% silicon, and outer layer with notable amounts of magnesium, possibly from abrasion of the bed material.

Visser [110] proposed a coating mechanism similar to that of Öhman, et al. [106], again with woody fuels, albeit without mention of interactions with gaseous alkali compounds. It was described as a build-up of small ash particles on bed material or

larger ash particles to create a coating, followed by neck formation between two coated particles, which can be followed agglomeration and/or sintering. If agglomeration leads to localised defluidization, an increase in localised bed temperatures may occur, triggering melt-induced agglomeration (see section 2.2.3).

Brus, et al. [111] examined agglomerate samples produced from commercial-scale CFB and BFB boilers ranging from 30-122MW$_{th}$, and those from a lab-scale BFB rig. "Inward chemical attack" by potassium or calcium silicates on the original quartz sand bed particle was observed. This conclusion was drawn through using quartz sand of a homogeneous particle size distribution of 106-125µm, taking 200 SEM images of particles before and after experimentation had occurred, and then comparing the mean cross-sectional area of the sand particles before and after experimentation. This is an adequate method, given the alternative of tracking and comparing a specific particle and the challenges which that would entail. SEM/EDX imaging of sand particles that had been in boilers for upwards of 33 days showed the diffusion of potassium into cracks in the sand particle and the formation of potassium silicate veins within the sand particle. This adds support to their conclusion of inward chemical attack occurring. Brus, et al. [111] also noted that the calcium-silicate dominated "inner" coating layer is replaced by potassium-silicates or other alkali-silicates in locations where calcium is not as available, such as cracks in sand particles, or when the fuel ash contains less calcium.

Öhman, et al. [112] examined coating distribution across the particles examined with SEM/EDX, as summarised in Table 2.1. To obtain their SEM/EDX data, Öhman, et al. [112] selected 3-5 particles per fuel. All the fuels tested led to bed agglomeration, yet, as per Table 2.1, the quantity of coated particles to cause agglomeration varied from <10% of particles examined to being the "majority", which can be assumed as greater than 50%. This raises questions around the methods by which agglomeration occurred: for example, whether these differences are down to sampling methods or are the result of other mechanisms. Therefore, it may be worthwhile investigating the differences coating composition and the frequency of coated particles across the whole bed. This may indicate if certain zones are more susceptible to agglomeration and help provide a better understanding of bed-scale agglomeration and defluidization mechanisms and would be valuable for full-scale installations with bed cross-sectional areas in the tens of square metres scale.

Table 2.1: *Table summarising fuel and relative presence of coating on the particles examined with SEM/EDX by Öhman, et al. [112]. Note that this percentage presence of coating was found to be identical for both combustion and gasification environments.*

Fuel	Percentage of particles examined where coating was present
Bark	"Majority"
Reed canary grass	10%
Lucerne	10%
Olive flesh	"Majority"
Cane trash	10-30%
Bagasse	<10%

Zevenhoven-Onderwater, et al. [113] investigated the ash compositions of five different woody fuels: bark, two forest residues, construction residue wood, and sawdust. From analysis of bed material and fuel ash compositions, the coating layer thickness observed, and the weight of the bed before and after experimentation, the source of coating elements was determined. Roughly 50wt.% of potassium from the fuel remained in the bed, along with 8-30wt.% of the calcium and 30-65wt.% of fuel derived silicon, all of which could contribute to agglomeration. Coating layers were homogeneous, with a formation method suggested: potassium-silicates begin forming a "first layer" on bed particles at around 750°C, which then captures other ash components, leading to the formation of a sticky layer of melting point <800°C.

Grimm, et al. [114] investigated agglomeration behaviour when using olivine as a bed material. Experiments were performed for willow, logging residue, wheat straw, and distillers dried grain using wheat and solubles (DDGS) fuels, on both olivine and quartz sand beds, with a 5kW$_{th}$ BFB reactor. An olivine bed resulted in reduced agglomeration tendency for willow and logging residue, with no change noticed for wheat straw or DDGS. The outer coating layer with olivine was similar in composition to the fuel ash, as it was with quartz sand. A key difference versus quartz sand was the composition of the homogeneous inner coating layer for willow and logging residue, which comprised of Mg, Si and Ca as opposed to K, Si and Ca. This may have been due to the methodology used: fuels were combusted at around 800°C for 8 hours before the temperature was incrementally increased until agglomeration occurred or the maximum temperature of 1060°C was reached. Temperatures in excess of 1000°C, as were reached with willow and logging residue, may have allowed some fraction of the magnesium in olivine to partake in melt formation. Such temperatures would not be reached in the bed typical FBC operation; therefore, this result may not be wholly

representative of a full-scale facility. Wheat straw and DDGS did not reach such high temperatures and did not exhibit differences in ash coating composition when using olivine compared to quartz sand.

More recently, several groups have observed calcium layering when using olivine in fluidized bed gasifiers, mostly when using woody fuels [115, 116, 117, 118]. For example, Kirnbauer & Hofbauer [117] investigated use of olivine with a wood fuel in an industrial-scale dual fluidized bed gasification. They observed the formation of two distinct layers: an inner calcium silicate-rich layer, and an outer layer of similar composition to the fuel ash. The formation of these layers was in part due to the use of calcium additives such as dolomite for increased catalytic performance in the gasification process. However, it was noted that the inner calcium silicate-rich layer arose due to incorporation of calcium into the outer olivine crystal structure, hence why it was of similar thickness across the perimeter of the bed particles examined.

He, et al. [119] analysed the effect of operational time on quartz sand bed particles for a $5kW_{th}$ BFB, $30MW_{th}$ BFB, and $122MW_{th}$ CFB. Samples were taken after the addition of a fresh bed, and at intervals of several hours for the lab-scale $5kW_{th}$ unit or every few days for the full-scale plants. The bed material was replenished at the standard operational rate for the two full-scale units: <3wt.% of the bed per day for the $30MW_{th}$ BFB unit, and 50wt.% of the bed per day for the $122MW_{th}$ CFB unit. He, et al. [119] noted similar multilayer composition findings to others [109, 110], though there was a time dependency for their formation.

In the case of the $5kW_{th}$ BFB, a single coating layer was found on bed particles. For the $30MW_{th}$ BFB, a single layer was found on 1 day old particles, whereas older particles displayed an inner homogeneous layer and outer non-homogeneous layer. For the $122MW_{th}$ CFB, 3 day old samples displayed two coating layers, equivalent in composition to the "inner-inner" and "inner" layers observed by others [109, 110]. An outer layer was found only on 4 and 6 day old particles. Only the $122MW_{th}$ CFB presented an "inner-inner" Si-K-Ca layer. The fuel used in the CFB had higher ash content than the $30MW_{th}$ BFB (3.1wt.% dry, versus 1.8wt.% dry) and higher potassium content (0.18wt.% dry, versus 0.11wt.% dry). This adds further support to the theory that an inner-inner layer of Si-K-Ca is only present with sufficient availability of potassium in the fuel [109, 110].
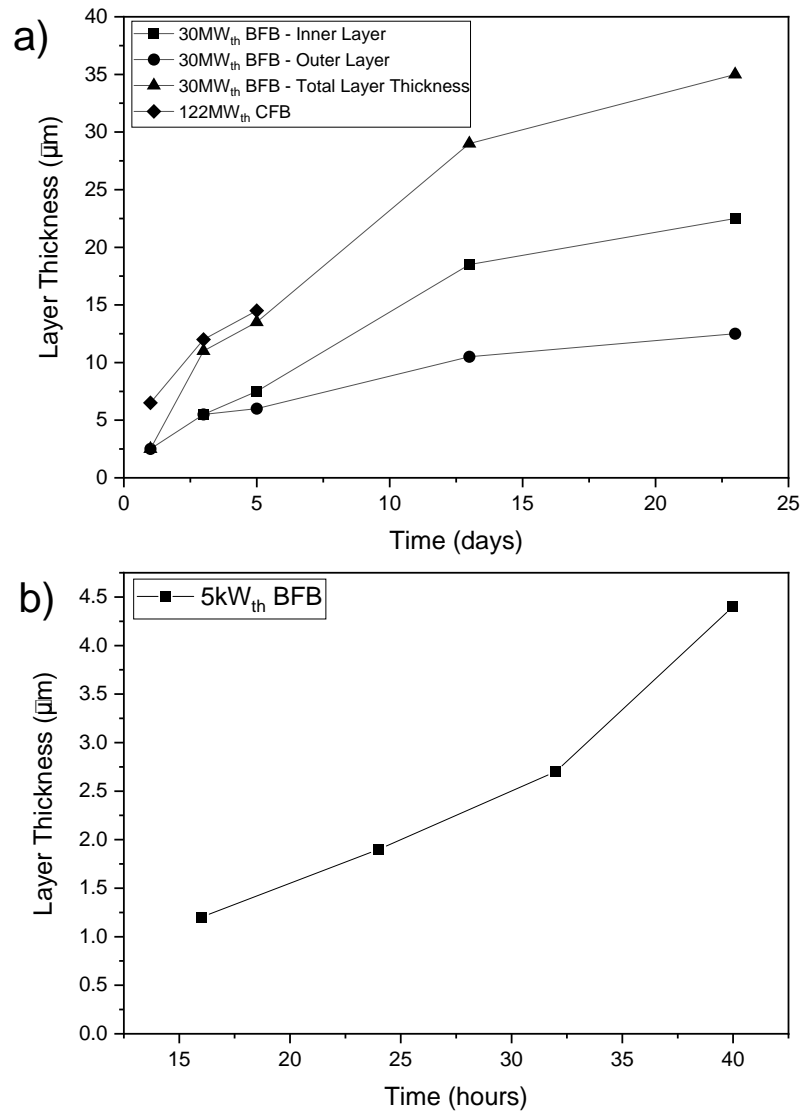
Figure 2.4: *Coating layer growth over time for a) full-scale BFB and CFB units and b) a lab-scale BFB. Based on the data of He, et al. [119].*

Layer growth was tracked over time by He, et al. [119], the results of which are reproduced in Figure 2.4. XRD analysis on $30MW_{th}$ BFB samples from 3-23 days old revealed that initially K-based compounds formed the majority of the mass of the layer. This then progressed to the layers primarily comprising of calcium based compounds such as $Ca_3Mg(SiO_4)_2$, Ca_2SiO_4 and Ca_3SiO_5. SEM images showing the structural changes in coating layers over time have been reproduced in Figure 2.5.

He et al. [119] then gave the following theory for agglomerate formation: Potassium species first react with the bed particle to form low-melting point potassium-silicates. Layer growth proceeds with the addition of calcium to this melt, causing precipitation of stable calcium-silicates with high melting points. The increase in calcium concentration within the layer, and loss of potassium, results in a weaker driving force

for calcium diffusion and reaction, thus a reduced layer growth rate over time. A higher amount of melt in this inner layer would influence diffusion and reaction of calcium into the layer, thus influence layer growth rate.
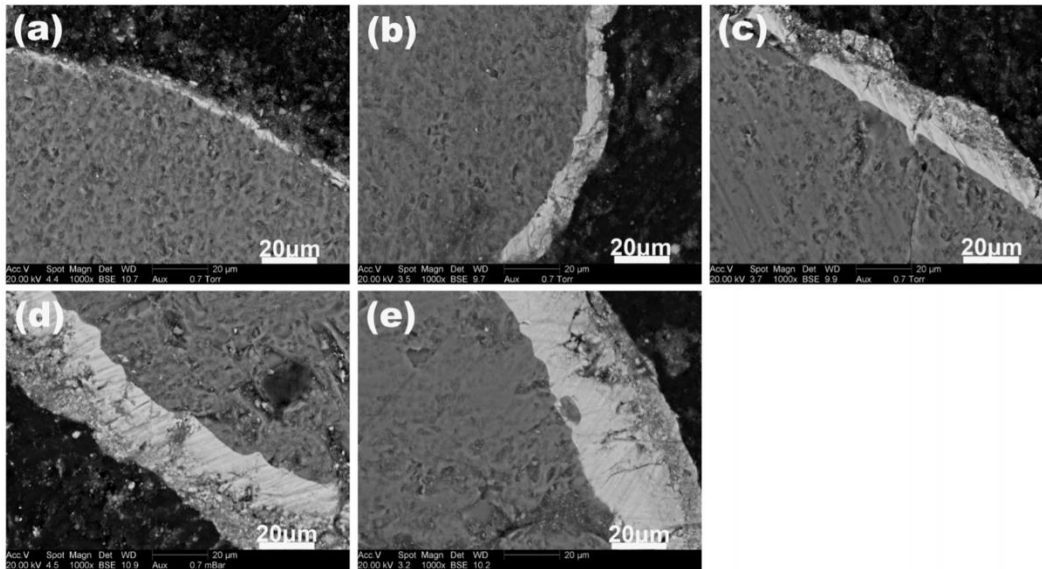
Figure 2.5: Example SEM images of coating layers (lighter grey) resulting from the combustion of wood on a sand bed in a 30MW$_{th}$ Bubbling FBC unit. Images 'a' through 'e' are of particles 1, 3, 5, 13, and 23 days after initial bed start-up. Differences in layer homogeneity moving outward can be clearly seen in images 'c' through 'e'. Images reproduced with copyright holders' permission from the work of He, et al. [119]. Further permission enquiries related to this material should be forwarded to the American Chemical Society.

Gatternig & Karl [120] have further explored coating-induced mechanisms. Experiments were first performed with a progressively heated bed, and multiple coating layers were observed aligning with the findings of others [109, 110]. Building on the inward coating growth theory suggested by Brus, et al. [111], Gatternig and Karl [120] suggested that collisions between two coated particles allows for capillary action to draw coating melts inwards into the particle. Additionally, from SEM/EDX imaging, visible remains of the heterogeneous outer coating shell were seen in agglomerate necks/joins. Gatternig & Karl [120] concluded that the outer coating layer is dry and powdery, a feature observed by others [112], and that it increases in melt fraction towards the centre. On collision, this shell fractures, allowing for the inner melt to form a liquid bridge, with remnants of the outer shell being present within it. Such a theory diverges from previous suggestions that bridges between coated particles form during the initial melt layer phase [110].

Gatternig & Karl [120] also performed experiments with a fluidized bed of sand above a fixed bed into which fuel was added, to detect the effects of gaseous phase alkali

compounds on agglomeration. No coating layer formation was found, indicating that gaseous or aerosol alkali metals do not contribute to coating formation. Others have speculated this to be the case, such as Scala & Chirone [121]. It should be noted that the methodology employed by Gatternig & Karl [120] does not allow for other bed phenomena to proceed, such as localised defluidization and/or bed temperature hotspots, as there is no direct contact with the fuel. Such phenomena may however provide a temperature gradient over which a vaporization-condensation cycle could occur.

He, et al. [122] have expanded upon their previous work [119] by means of chemical equilibria modelling for ash reactions and the development of a diffusion model, using the FactSage software package. The data used in the model, and for validation, was that of their previous work [119]. Temperature had a large effect on layer growth rate for operation at 850°C. The model predicted layer thicknesses of 10µm at 5 days of operation and 15µm at 16 days, whilst at 900°C, a thickness of about 20µm was predicted at 5 days, and 40µm at 16 days. It was suggested that the additional temperature allowed for increased diffusion of Ca^{2+} into the inner melt layer, hence greater layer growth. The decrease in inner layer growth rate over time is suggested as being due to changes in inner layer composition. Ca^{2+} diffusivity was higher in Ca_2SiO_4 than in Ca_3SiO_5, but it is the latter which increases in concentration within the inner layer over time. Furthermore, the physical growth of the layer would increase the diffusion distance, further impacting calcium diffusion. The agglomerate coating layer growth mechanism thus suggested by He, et al. [122] is reproduced in Table 2.2.

Table 2.2: Coating-induced agglomeration layer growth mechanisms proposed by He, et al. [122]. Table reproduced from He, et al. [122].

Phase	Controlled Process	Main Crystalline Phases	Layer Growth Rate
1 (<1 day)	Reaction	Only K-rich silicate melt	Fast in the presence of enough available calcium
2 (from 1 day to ~2 weeks)	Diffusion	$CaSiO_3$, Ca_2SiO_4	Medium
3 (from ~>2 weeks)	Diffusion	Ca_2SiO_4, Ca_3SiO_5	Quite low

When He, et al. [122] validated the model against experimental data, the model was found to provide a good indication of starting and ending coating layer thickness, though did not match the variations in layer growth rate that happened on smaller timescales. This highlights an area for further work: accurately modelling layer growth

rate over the entirety of coating layer growth periods. This would be of particular use for full-scale FBC units, as bed material is removed and replenished during operation [72, 123]. The ability to accurately model and predict coating layer thicknesses across the bed at any point in time could allow for the optimisation of bed replenishment frequency.

2.2.3 Melt-induced Agglomeration

Olofsson, et al. [91] proposed an agglomeration formation mechanism, "heterogeneous agglomeration", and stated that this arises due to localised "hot-spots" of over 1000°C, versus bed temperatures of ~670-870°C, allowing the creation of a melt phase of alkali-silicate derived from both fuel ash and bed material. The largest agglomerates had a glass-like appearance, indicating prolonged exposure to high temperatures, were 50-60mm in size, and frequently caused defluidization. Olofsson, et al. [91] speculated that the cause of "hot-spots" in the bed was a combination of small fuel feed fluctuations and temporary gas channelling through the bed leading to localized fluidization disturbances.

The later work of Lin, et al. [124] presented an alternative "melt-induced" agglomeration mechanism, from combustion of wheat straw on a quartz sand bed. After two minutes of combustion at a bed temperature of 720°C, weak agglomerates were present in the form of a charred fuel pellet with sand particles weakly attached. After two minutes of combustion at 920°C, the agglomerates were stronger and there was far less of a char core present. After ten minutes of combustion, the char core had fully combusted leaving hollow sand agglomerates in the shape of the fuel pellet.

Lin, et al. [124] proposed a mechanism as follows: Burning char particles had been observed as being at higher temperatures than bed particles, and go from partially to almost completely molten between 750-900°C. When bed particles collide with these molten char particles, they may adhere to them, and become coated with the molten char melt. As the char particle burns away, the sand particles would remain stuck together. Such a conclusion is supported by their results: two minutes of combustion at 920°C versus 720°C resulted in a stronger agglomerate, therefore there could be more of a molten char melt hence a stronger agglomerate forms. Additionally, at this higher temperature sintering may have strengthened the agglomerate.

Visser [110] put forth a melt-induced agglomeration formation mechanism from a comparison between a lab-scale FBC unit and an $80MW_{th}$ FBC plant and described it as the result of collisions between bed particles or larger ash particles, which adhere to one another due to molten ash particles that function as a viscous glue. It is notable that whilst similar in nature to the method of Lin, et al. [124], it does not suggest that larger molten char particles may act as a platform from which agglomerates can grow.

Chirone, et al. [125] examined agglomeration behaviour when combusting pine seed shells, using lab-scale and pilot-scale equipment. Chirone, et al. [125] proposed that bed particles stick to melting char particles which then burn away, leaving behind hollow agglomerates in the shape of fuel particles. Chirone, et al. [125] further suggested that combusting char particles act as a localised temperature "hot-spot". This causes more severe melting and thus more severe agglomeration than coating-induced agglomerates typically display.

Scala & Chirone [121] studied mechanisms of agglomeration with a lab-scale unit using olive husk fuel. A prior examination of the literature revealed that temperature had negligible effects on alkali deposition rate, and experimentation with variable air flow rates to control temperature gave little change in amounts of bed ash. Scala & Chirone [121] concluded that vaporisation and condensation pathways for alkali deposition likely had a negligible effect on agglomeration. Scala & Chirone [121] proposed a mechanism for agglomeration: Ash is transferred to bed particles via collisions with small fine ash or large coarse char particles. Alkali species then physically diffuse through the ash and interact with silica to form a eutectic. From the observations of others [124, 125], Scala and Chirone [121] then stated that the transfer of alkali species by collision and their melting behaviour was likely promoted by high temperature char particles. With sufficient temperature and alkali content in the bed, defluidization will occur. If the bed temperature is not high enough to melt the eutectics, burning char particles may provide a "hot-spot" that can drive melt formation and the accumulation of smaller agglomerates, which can defluidize the bed.

Liu, et al. [126] looked at melt-induced phenomena, when combusting rice straw, and suggested that the presence of K and Na components on the exterior of fuel fragments would allow them to form adhesive alkali-silicates with relative ease. Large ash

fragments (>10µm) may then bind together bed material, as was evidenced by agglomerates being conjoined by necks of similar composition to that of the fuel ash.

Gatternig & Karl [120] provided further evidence in support of the melt-induced agglomeration behaviour seen by Lin et al. [124] and Chirone, et al. [125]. Gatternig & Karl [120] first observed that denser fuel particles, such as wood pellets, were fully submerged in the bed during combustion thus had similar temperatures to the bed itself. When testing less dense hay pellets, the pellet "floated" on top of the bed and reached temperatures up to 400°C higher than the bed. This would be sufficient to produce molten ash fuel pellets to drive the melt-induced agglomeration mechanisms proposed by Lin, et al. [124], and may offer one explanation for temperature "hot-spots". Gatternig & Karl [120] state that lower density fuels, typically herbaceous ones, will likely undergo this behaviour. This aligns with the experiences of Lin, et al. [124], who used low density wheat straw, Chirone, et al. [125] who used pine seed shells, and Olofsson, et al. [91], who recorded the occurrence of "hot-spots" and more severe agglomeration when lower density fuels were used (sawdust, straw, and meat and bone meal).

An aspect not explored within the literature is the relative presence of silica and alkali metals within the ash to drive melt-induced agglomerate formation. The fundamental difference seen between coating-induced and melt-induced agglomeration is that the former involves the interaction of alkali metals with silica in the bed material, whilst the latter relies on the presence of both silica and alkali metals in the ash to form an alkali-silicate ash melt [110, 127]. The fuels used in the majority of the works above where severe melt-induced agglomeration occurred were generally herbaceous with high silica content in the ash [91, 120, 121, 124, 126]. Therefore, there may be a point at which the melt-induced mechanism takes precedence over coating-induced agglomeration as the dominant mechanism for agglomeration, due to the relative availability of silica and alkali metals.

2.2.4 Summary of Agglomeration Mechanisms

The current knowledge of agglomeration mechanisms can be summarised as follows (shown diagrammatically in Figure 2.6 and Figure 2.7):

2.2.4.1 Coating-induced Agglomeration (Figure 2.6)

There is broad agreement that this mechanism is initiated via the formation of a molten adhesive alkali-silicate melt on the surface of silica-rich bed particles, usually potassium-silicate, though in some cases sodium-silicates if sufficient quantities are present in the fuel [108]. The mechanism is commonly seen with woody fuels, with coating layers forming via the accumulation of K-compounds from fuel ash on silica-rich bed particles, at temperatures in excess of 750°C.

This K-silicate layer then grows inwards via reaction with silicate species in the bed material [111]. There may be the effects of capillary action from cracks in the bed particle drawing K-compounds further inwards after collisions with other coated particles [120]. Any silica within the fuel ash may also react together with potassium species on the bed material surface to generate more of a melt. Calcium species from the outer ash layer begin diffusing into the molten K-silicate inner layer and react to form stable species with silicate with melting points in excess of 1000°C, such as Ca_2SiO_4 and Ca_3SiO_5 [119].

At the end of this process, bed particles typically possess two- or three-layer coatings. In the case of a two-layer coating, there is an inner homogeneous layer rich in Ca-silicate compounds, and an outer heterogeneous layer whose composition is broadly in line with that of the fuel ash [114, 119, 120]. In the case of three-layer coating systems, there is an additional "inner-inner" homogeneous layer, rich in silica, K, and Ca [110, 119]. The causation of this inner-inner layer has been speculated as the presence of high amounts of K in the fuel [110], or perhaps the lack of a diffusive driving force for Ca to diffuse and react all the way to the bed particle-coating layer boundary [119, 122]. The outer ash layer appears to prevent formation of further K-silicate melts, by denying K-compounds access to the silicate of the bed material with which it would otherwise form a melt. In particular, magnesium in the outer ash layer has been identified as preventing alkali-silicate melt formation [109].

Agglomeration appears to proceed at any point during layer formation. Bed particles collide, in some cases breaking the outer ash layer [120], and enable that formation of a

K- or Ca-silicate neck conjoining bed particles [106, 110, 125]. Temperature-induced sintering may occur, strengthening the agglomerate [106, 110, 111, 112]. With sufficient accumulation of agglomerates, bed defluidization occurs.
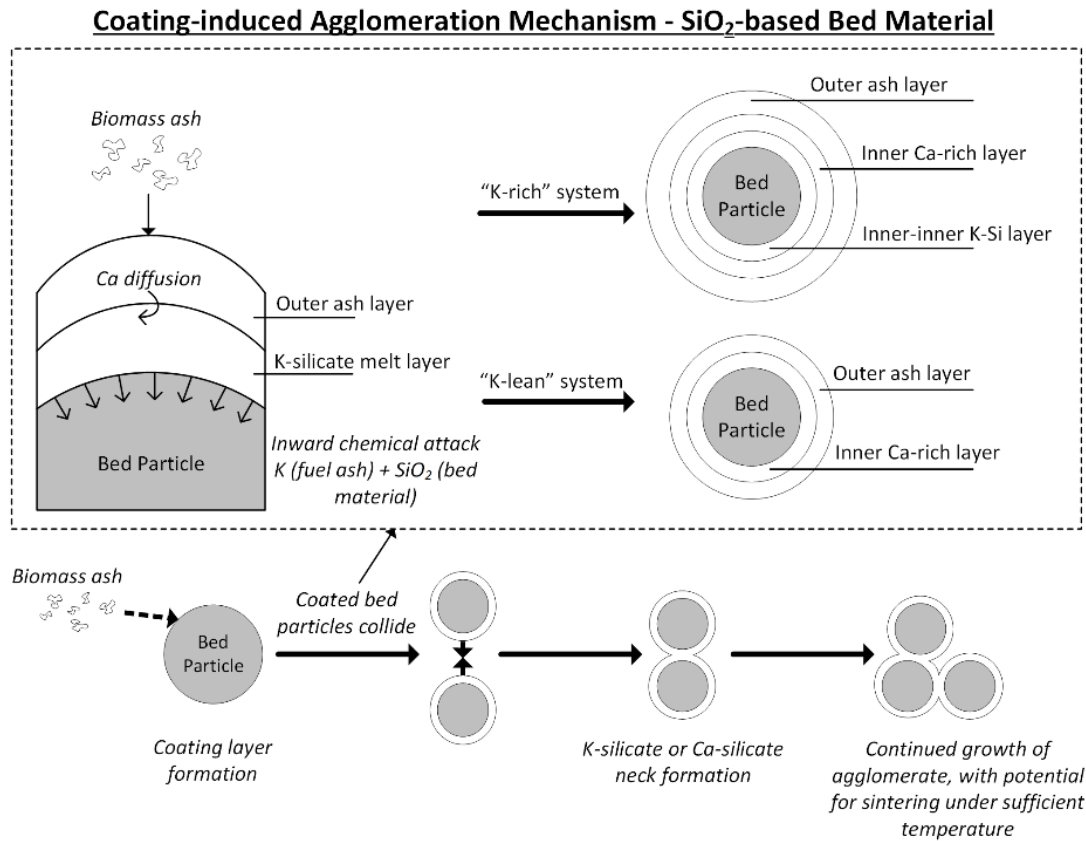
Figure 2.6: *Coating-induced agglomeration mechanism in a system with a SiO$_2$-based bed material, whereby agglomeration proceeds due to potassium presence within the fuel ash. Described within the text of section 2.2.4.1.*

2.2.4.2   Melt-induced Agglomeration (Figure 2.7)

The central idea of melt-induced agglomeration is the collision of molten ash particles with bed particles, where the molten ash particles act as a viscous glue [110, 121, 125]. Scala & Chirone [121] suggest that burning char particles create a localised hotspot that further enhances the adhesive potential of this "viscous glue". The resultant agglomerates are characterized by displaying a more severe melting and agglomeration than traditional coating-induced agglomerates [125].

A notable variant to melt-induced agglomeration is when molten char particles act as a platform for agglomerates to grow, as was first described by Lin, et al. [124]. Combusting char fragments have elevated temperatures in comparison to the bed average, and become almost completely molten at around 900°C. In collisions with bed

particles, the bed particles adhere to the char fragment and the viscous alkali-silicate melt on its surface. This coats the bed particles and propagates further adhesion of bed particles. Eventually, the char fragment fully combusts, typically leaving an agglomerate with a hollow centre in the shape of the initial fuel fragment. The agglomerate retaining the shape of the fuel particle may be due to the ash skeleton of the fuel particle that remains after combustion of the fuel pellet, a topic discussed in the work of Chirone, et al. [128] (further discussed in section 2.3.6.3). Aside from observations of this phenomena, little detailed work has been performed into how or why it arises, or how to prevent it.

Melt-induced Agglomeration Mechanism

Alkali-silicate melt created from fuel ash constituents and released to surface

Combusting fuel surface

Fuel ash skeleton maintains shape of fuel particle as it combusts

Fuel ash skeleton breaks apart

Bed materials adheres to combusting fuel pellet due to presence of alkali-silicate melt

Alkali-silicate melt from fuel ash adheres to bed particles

Hollow agglomerate in shape of fuel particle remains after complete combustion of fuel

Agglomerates form

Figure 2.7: Melt-induced agglomeration mechanism, as described within the text of section 2.2.4.2.

The elevated temperature during char combustion would allow for sintering of the agglomerate, strengthening it. Gatternig & Karl [120] extended this theory, stating that less dense fuels, e.g. straws, were observed to "float" on top of the fluidized bed whilst combusting, as opposed to being submerged within the bed, and were more exposed to higher temperatures of the above-bed region that result from volatiles combustion. Moreover, Olofsson, et al. [91] observed temperature hot-spots whilst utilizing less dense fuels, perhaps also due to this "floating" behaviour.

2.2.4.3   Recommendations for Further Work

Agglomeration mechanisms when using non-SiO_2 based bed materials have not received a great deal of investigation. Both Nuutinen, et al. [109] and Grimm, et al. [114] used Mg-based materials (the former a proprietary material, the latter olivine). Despite these materials not being silica based, layer formation still occurred. Further work may clarify the exact mechanisms under which layer growth is occurring for non-SiO_2 based bed materials.

Use of chemical equilibria modelling software such as FactSage has received increased attention in recent years due to improvements in the accuracy and quality of thermochemical databases. The work of He, et al. [122] resulted in a relatively accurate model of coating layer growth in a silica sand and wood fuel scenario. However, intermediate variances and fluctuations in growth rates weren't fully captured by the model, presenting an opportunity for future improvement. A more comprehensive model of coating growth rate would allow for optimisation of bed replenishment in industrial facilities and allow for minimisation of agglomeration risk through prediction of the coating distribution across the bed inventory. Beyond this, similar coating growth and ash melt models would be of use for different fuels and alternative bed materials, again with the intention of informing agglomeration risk at the industrial scale.

Related to this would be investigations into bed scale variances in coating composition and the relative frequency and distribution of coated bed particles across the bed. If certain zones are found to be particularly problematic with regards to enabling agglomeration, targeted control and prevention methods may be possible.

Melt-induced agglomeration proceeds with sufficient silica and alkali metal content in the fuel ash. However, it appears there has been no work to find a point at which the more severe melt-induced agglomeration becomes the dominant form of agglomeration within the bed, due to fuel ash composition. Such a value would help further inform fuel selection and fuel blending trials. Related is a more general, secondary area for work, on transition points and relationships between melt-induced and coating-induced agglomeration occurrence. There have also been few detailed studies into the occurrence of fuel particle shaped agglomerates, aside from noting their occurrence in agglomeration studies.

2.3   Effect of Operational Variables on Agglomeration

2.3.1   Temperature

The effects of temperature on agglomeration have been extensively researched within the literature. The general trend exhibited is that with increases in temperature, there is an increase in the severity of agglomeration because of the increased presence of liquid melt phases. Ultimately, this leads to a reduction in the defluidization time, t_{def} [124, 129, 130], as shown in Figure 2.8. The elevated temperatures increase the melt fraction within the ash and decrease the viscosity of the melt [124]. This results in a more abundant and more mobile melt, leading to more severe agglomeration. The temperatures at which FBC beds operate (800-900°C) are within the range at which alkali silicate eutectics form melts. Furthermore, the modelling efforts of He, et al. [122] highlighted that increases in temperature of 50°C may lead to a 2-3x increase in coating layer growth rate. This elevated growth rate would make it easier for neck formation between coated particles during collisions, due to the availability of a larger melt layer, thus worsening agglomeration.
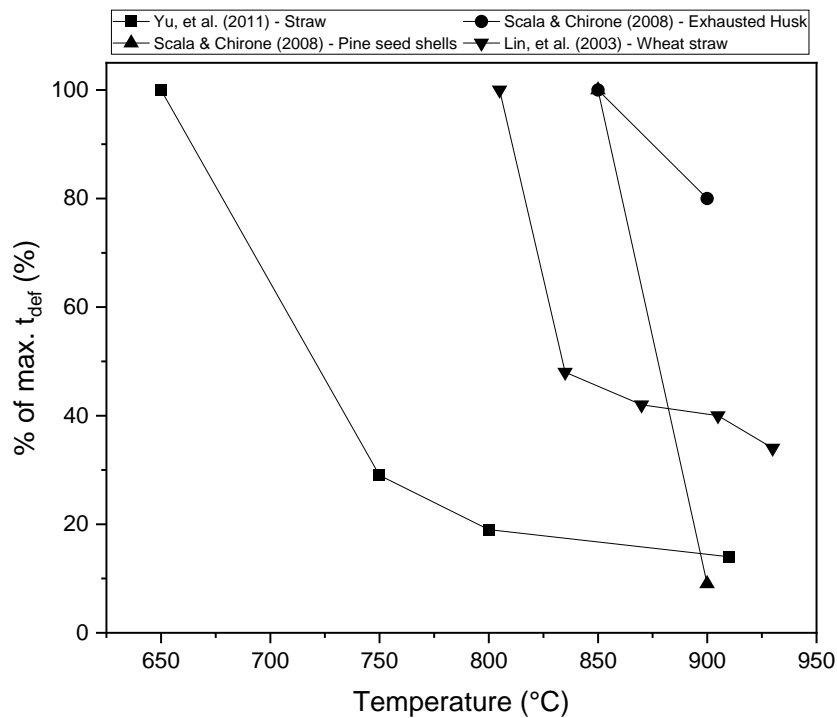
Figure 2.8: *Variations in defluidization time with temperature for several fuels. Data collated from the work of Lin, et al. [124], Scala & Chirone [129], and Yu, et al. [130].*

It is also important to consider that at plant scale, the end goal of combusting biomass is often to raise steam. Lowering combustion temperatures will limit the conditions of the

steam that can be raised, having large impacts downstream of the boiler, such as on turbine efficiency [72]. Therefore, bed temperatures are likely to be constrained by steam requirements.

2.3.2 Pressure

Most literature on agglomeration when using biomass utilises atmospheric FBC (AFBC) units. However, PFBC units have been seen to experience similar agglomeration phenomena to AFBC units. The work of Olofsson, et al. [91] utilised a PFBC unit, showing similar phenomena to later work by others who used AFBC equipment. Recent work by Zhou, et al. [131] examined agglomeration during pressurised fluidized bed gasification of biomass, which appeared to exhibit similar coating-induced phenomena to what would be experienced during AFBC of biomass. However, some caution should be taken when drawing comparisons between AFBC and PFBC agglomeration mechanisms, as whilst the result may be the same, the pathway there may differ.

2.3.3 Fluidizing Gas Velocity

The fluidizing gas velocity, U, has an important role to play in determining the fluidization regime in any FBC system [9, 12]. Over the years, several researchers have looked at the effect of varying U, or the ratio U/U_{mf} known as the fluidization number, on agglomeration and defluidization.

Lin, et al. [124] doubled U whilst maintaining the same combustion conditions through use of N_2. This increased defluidization time by up to 30%. Chaivatamaset, et al. [132] found that increases to U of 28% and 60%, led to average increases of defluidization time for two different fuels of 56% and 95% respectively. Lin, et al. [133] recorded increases in defluidization time with successive increments in U, across four types of particle size distribution (narrow, Gaussian, binary, flat). Yu, et al. [130] observed reduced agglomeration by increasing U/U_{mf} by a factor of 1.6, noting that agglomerates no longer presented themselves as larger clumps, but as a few bed particles attached to an ash fragment.

It is clear then that increases in U or U/U_{mf} will cause an increase in defluidization time. With increases to U, bed particles gain momentum thus are more likely to overcome adhesive forces during collisions with coated bed particles and molten ash particles [124, 133]. Furthermore, higher U values would lead to more vigorous bed mixing. This

would reduce the chance of certain areas experiencing poor fluidization which would otherwise allow for the formation of temperature hotspots; a behaviour suspected to propagate agglomeration.

2.3.4 Gas Distribution Uniformity

An aspect that has received little direct investigation is that of fluidizing gas distribution uniformity on agglomeration. Bubbles will form at the bottom of the fluidized bed as gas is released from the gas distribution plate. These bubbles will coalesce into larger ones as they rise through the bed [9]. This bubble movement drives fluidization, heat transfer, and bed mixing [134], thus if impaired may have significant effects on operation.

Oka [135] suggests that with damaged bubble caps, thermal diffusivity across the bed would be reduced and the bed hydrodynamics would be altered. This would create regions of high and low turbulence, and lead to temperature gradients across the bed that may assist or accelerate the formation of agglomerates. Kuo, et al. [136] trialled a fixed grate furnace with a wood fuel and gave a comparison between sidewall air injection and under-grate air injection. They noted that changing the air distributor configuration had significant effects on flame coverage and led to higher and lower temperature regions within the furnace. These regions of elevated temperature could increase the rate of agglomerate formation (see section 2.3.1). Lin, et al. [133] found that a temporary burst of high velocity air was sufficient to break apart in-situ agglomerates and postpone a defluidization event. This could imply that a region of higher turbulence in the bed may be beneficial for minimizing agglomerate formation.

The work of Chilton [137, pp. 225-291] tested the effects of non-uniform air distribution when using five different biomasses in a 200kW$_{th}$ FBC unit. A uniform air distributor with 30 evenly spaced bubble caps was compared against with one that had 18 slightly larger bubble caps plus an ash chute occupying one corner of the distributor. The ash chute had an air gap around it, allowing for air leakage and further non-uniformity. Use of the non-uniform plate created greater variations in temperatures across the bed and freeboard, and greater variations to emissions. Data on defluidization times was less conclusive. Peanuts and straw experienced reductions in defluidization time of 10% and 40% respectively with the non-uniform air distribution plate, whilst oats experienced an increase of 181% and miscanthus an increase of 73%. Whilst this

does not provide a conclusive result on the effects of gas distribution uniformity on agglomeration, it does indicate that differences in distribution plate design, and the effects of bubble cap or fluidizing air distributor failures or leaks, can be significant on defluidization times. It also shows that it is an area where future work may be useful, albeit challenging to execute, particularly for full-scale installations which may experience localized air distribution grid issues.

2.3.5 Static Bed Height

Lin & Wey [127] examined the effects of static bed height on defluidization time during FBC of waste. Increases in the bed height to diameter ratio (h_{bed}/d_{bed}), produced a non-linear decline in defluidization time (Figure 2.9). The explanation cited was reduced vertical mixing with increasing bed height, allowing for agglomeration to proceed more easily upon release of alkali-metals from ash. However, a reasoning was not proposed for the rate of this decline, particularly from $2.0h_{bed}/d_{bed}$ and $2.3h_{bed}/d_{bed}$. This is perhaps indicative of some larger change in the bed dynamics when moving between these two bed heights, thus allowing for defluidization to occur much sooner. However, this was not explored further. Moreover, the timescales of defluidization time are all below 15 minutes, meaning that smaller irregularities e.g. in fuel feeding, may have a large proportional impact on the results.

Chaivatamaset, et al. [132] examined the effect of static bed height on defluidization time, and observed behaviours that were opposite to those noted by Lin & Wey [127] (Figure 2.9). Doubling h_{bed} whilst maintaining the same fluidizing gas velocity, temperature and bed particle size resulted in increases in defluidization time of between 5-55%, dependent upon the fuel and fluidizing velocity. Corncob typically showed greater percentage increases than Palm Shell in response to increases in static bed height. No further comparison was performed between agglomerates from the two different static bed heights examined.

It may be of interest to further examine the effects of static bed height on agglomeration, defluidization time, and determining any relationships that may exist. A larger static bed height is known to allow the coalescence of bubbles to larger sizes and causes increased turbulence at the top of the bed [138]. This behaviour may also influence that seen through the observations of Gatternig & Karl [120], who noted that low density fuel pellets floating on the bed surface caused severe melt-induced

agglomeration. Therefore, the effects of bubble size and behaviour at the bed surface on agglomeration may be worthy of investigation.
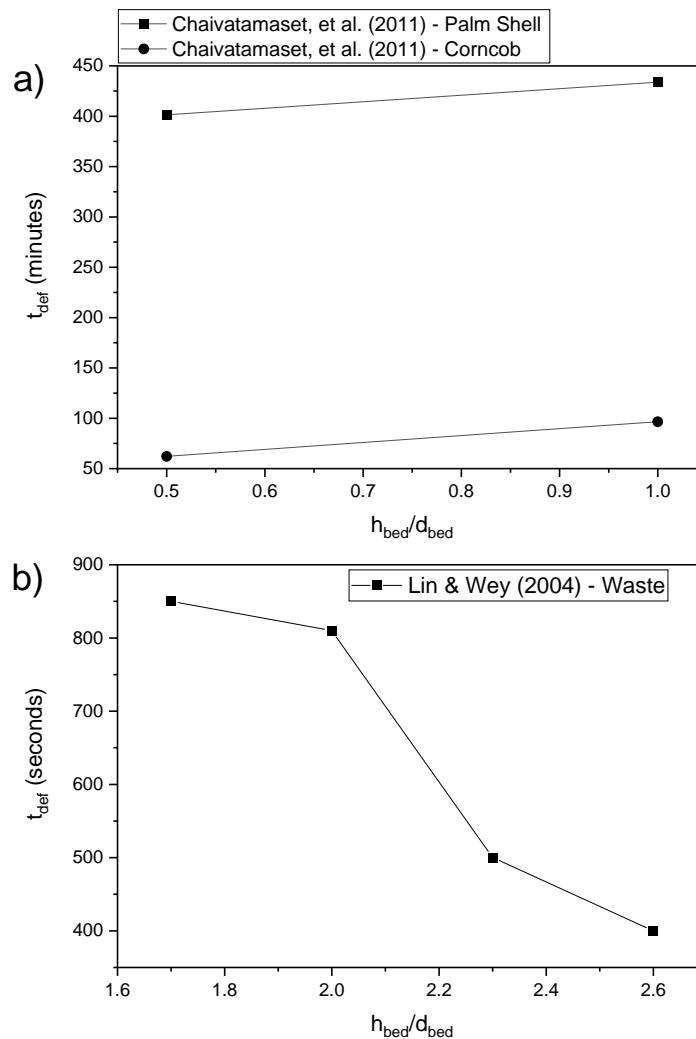
Figure 2.9: *Graph showing the effect of changing the bed height-to-diameter ratio, h_{bed}/d_{bed}, on the defluidization time, t_{def}. Data from the work of (a) Chaivatamaset, et al. [132] and (b) Lin & Wey [127].*

2.3.6   Fuel

2.3.6.1   Fuel Type

The effects of different fuels on agglomeration have been extensively researched. As noted in the introduction, fuel and ash composition can vary massively across different biomass fuels [42, 44]. As illustrated in section 2.2, the presence of alkali metals and alkaline earth metals within fuel ash is a key contributing factor to agglomeration severity. Therefore, both the quantity of ash for a given fuel and the relative amounts of key ash components for melt formation (e.g. potassium) can have a significant impact on agglomeration severity. Likewise, the variability of biomass fuel composition is

apparent even within a singular fuel type as noted in Chapter 1 section 1.4. For example, the composition of a wheat straw and its ash can vary by source, harvest region or rainfall during the harvest season [139], further complicating the use of such fuels and the evaluation of their agglomeration severity.

The agglomeration issues with specific fuels have been discussed in detail across section 2.2 in conjunction with their agglomeration mechanisms. Wood fuels are widely used in industry, and their agglomeration behaviours have been studied in extensive detail; for example, in the works of He, et al. [119, 122] and others. Virgin wood fuels are typically considered to be some of the best available, due to their lower ash contents, with agglomeration mostly occurring via a coating-induced mechanism. Skrifvars, et al. [102], Öhman, et al. [106], and Brus, et al. [111], have looked at fuels across a variety of different biomass categories, such as woods, grasses (e.g. reed canary grass), straws, and other agricultural wastes. The typical observation across these works and others is that fuels with higher amounts of alkali metals within their ash will agglomerate more quickly, and at lower temperatures, usually via a melt-induced agglomeration mechanism. Straws are a fuel that have been particularly noted for their rapid and severe agglomeration, due to their combination of high ash content and high alkali metal content, in the works of Lin, et al. [124] and Yu, et al. [130]. As a general comment, fuels with a combination of high silica content and high alkali content, such as straws, seem predisposed to agglomerating via melt-induced agglomeration, as the fuel ash itself has the necessary material to create an alkali silicate melt. In industrial and plant-scale settings, woody fuels have emerged as the preferred fuel type for FBC of biomass, due to their less severe agglomeration tendencies [72].

2.3.6.2　　Co-firing

Co-firing of biomass fuel blends may be performed due to economic and operational needs, for example balancing usage of a better quality, more expensive fuel with a poorer quality, cheaper one [72, 84, 140]. There is a sizable body of research available on co-firing of coal-biomass blends, as is evident from the reviews by Sami, et al. [141], Agbor, et al. [142], and Sahu, et al. [143]. There is also continued research interest in this area [144, 145, 146, 147]. However, there are fewer systematic studies available on biomass fuel blends and the effects of altering blend ratios. Hupa [140] notes that there was an increasing number of FBC boilers employing co-firing in the 2001-2002 period, some of which using biomass-only fuel blends, and this amount would likely have only

increased with time as there are more FBC units online thus greater competition for biomass fuels. A more recent review on biomass combustion and ash behaviours by Hupa [70] again notes the lack of knowledge surrounding co-firing of biomass blends.
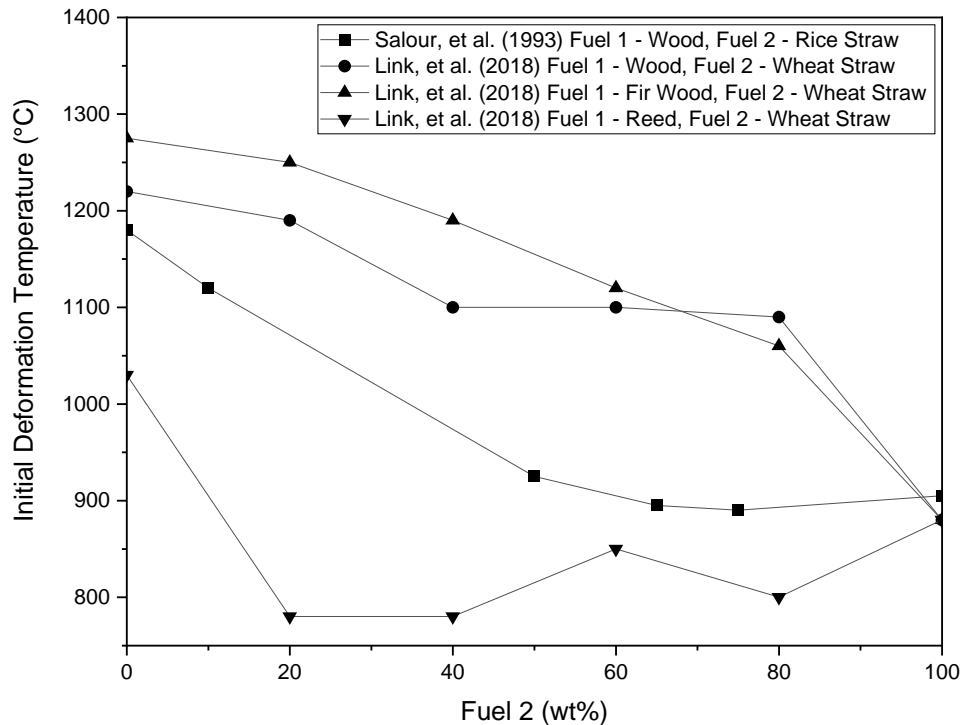
Figure 2.10: *Variations in initial deformation temperature (IDT) for several different biomass-biomass fuel blends. Data from the work of Salour, et al. [148] and Link, et al. [149].*

Salour, et al. [148] blended rice straw with wood, in order to control the severe agglomeration ordinarily caused by rice straw. When combusted at a bed temperature at or below 800°C, blends of up to 50% rice straw were acceptable. Beyond this, defluidization time decreased with increasing rice straw fraction. Salour, et al. [148] also measured key ash fusion temperatures such as the initial deformation temperature (IDT). These were found to be non-linear in behaviour. Figure 2.10 provides an example of this behaviour with the IDT, as well the recent work of Link, et al. [149] who saw similar complex non-linear behaviours with three different biomass blends. It can be seen in Figure 2.10 that between the four fuel blends tested in the works of Salour, et al. [148] and Link, et al. [149], there are significant differences in IDT trends with fuel blend ratio. For example, the wood-wheat straw blend tested by Link, et al. [149] almost plateaus between 40 and 80% wheat straw, whilst the fir wood-wheat straw blend gives a relatively constant decline in IDT with increasing wheat straw fraction. The wood-rice straw blend tested by Salour, et al. [148] shows a significant

decline in IDT, reaching a minimum at between 65% and 75% rice straw, before the IDT increases by around 20°C as rice straw is increased to 100% of the fuel blend. These substantial differences in ash behaviours when blending biomass fuels illustrates the need for further work in this area.

Davidsson, et al. [84] examined the effects of biomass co-firing in a 12MW$_{th}$ CFB with a mixture of 86% wood and 14% straw pellets on an energy basis. This produced a high level of alkali deposits compared to their coal-based tests, a result of alkali metal content in the straw. Concentrations of KCl in the flue gas rose from around 3-4ppm with wood pellets to 20ppm with the 14% straw blend.

Thy, et al. [150] investigated the agglomeration behaviour of a blend of wood with between 2.6-25.0wt.% rice straw. They found a strong positive correlation between increasing amount of straw and severity of agglomeration, with blends of 2.6wt.% rice straw producing mild agglomeration whilst those of 9.6% and above resulted in defluidization and large plugs of agglomerates being extracted. A visual estimation of the proportion of the bed that suffered from agglomeration produced an exponential relationship between percentage agglomerated and percentage rice straw content.

Elled, et al. [151] explored usage of a wood-straw fuel blend. A two-layer coating was formed on bed particles, the inner layer dominated by potassium silicates, whilst the outer layer comprised primarily of calcium silicates. Whilst these results broadly align with what is typically seen in a single fuel system, a closer comparison was not drawn.

Skoglund, et al. [152] co-fired a mixture of 90wt.% wheat straw with 10wt.% municipal sewage sludge, a fuel comprising of over 40wt.% ash, with large amounts of calcium, iron and aluminium. The addition of the sewage sludge increased initial defluidization temperatures by 200°C in comparison to use of wheat straw only. Agglomeration mechanisms also shifted more towards discontinuous ash deposits and necks on bed material, with less evidence of coating layers and reaction with the bed material than was seen when using wheat straw alone. It was suggested that this was due to the calcium, aluminium and sulphur in the municipal sludge having a beneficial effect on alkali capture similar to how an additive might behave (discussed in section 2.3.10).

Silvennoinen & Hedman [153] examined the effects of co-firing wood biomass with up to 30wt.% sunflower seed hull pellets or oat seeds in a 75MW$_{th}$ commercial BFB. During their experimentation, no agglomeration was detected, a result of an intentional

reduction of temperature to 750°C which would bring the system to just above the melting point of potassium-silicate eutectics (742°C).

Becidan, et al. [154] modelled the effects of a binary system consisting of straw with either peat or sewage sludge on alkali chloride formation; a key driver of corrosion [80, 81]. Non-linear relationships were exhibited with increasing weight percentages of peat or sewage sludge, and the mechanisms and elements affecting formation and decomposition of alkali chlorides changed with fuel blend ratios. This further highlights the complexities of using biomass fuel blends.

The study of biomass ash fusion temperatures performed in the work of Vassilev, et al. [46] resulted in a mapping of biomass ash categories by composition and their typical initial deformation and hemispherical ash fusion temperatures. This could be used to provide a qualitative indication of expected agglomeration issues for different dual-biomass fuel blends. However, ash fusion tests cannot provide a quantitative indication of at what temperature agglomeration becomes an issue, as seen in the work of Skrifvars, et al. [103]. Further, this data would not account for the potential interactions of the two ashes with each other, or interactions with the bed material.

2.3.6.3 Fuel Particle Size

Lin, et al. [124] performed an experimental run with smashed straw pellets of particle size <1mm, to compare against straw pellets of sizes 1-10mm but did not find a notable change in defluidization time. The work of Yu, et al. [130] looked at the effect of straw fuel size, with a comparison of small straw bales against milled straw powder, in a lab-scale BFB. Use of the powder allowed for a total fuel feeding of 281g, as opposed to 110g for the bales, prior to defluidization. However, the low density of straw powder may allow for it to be easily entrained within the flue gas. An analysis of the amount of unburnt carbon within the fly ash was not provided, nor an analysis of the potassium retained within the bed at the end of the run. Therefore, it cannot be stated if this elevated level of fuel feeding before defluidization is simply due to fuel becoming entrained within the flue gas.

Burton & Wei [155] looked at the effect of fuel particle size in the context of fluidized bed pyrolysis. A relation between biomass fuel particle size and 'sand loading' was drawn; this latter term being defined as the mass of bed sand adhered to fuel particles normalised against the total mass of fuel fed. Sand loading increased with fuel particle

size up to 430µm, and then decreased until reaching a plateau at around 1500µm. This was suggested as being due to transfer of the sticky alkali coating within the fuel particle being convection controlled to a particle size of 430µm, and diffusion controlled at larger sizes.

Also related are the combustion profiles of a fuel. Chirone, et al. [128] performed a comprehensive investigation into combustion profiles and characteristics of three pelletized fuels: wood, straw, and sludge. Fuels underwent several repetitions of a combustion-quenching process, to examine the condition and structure of fuel pellets at successive times. With sludge a "shrinking core" pattern was seen, where the initial size of the pellet was preserved with an ash skeleton that remained after burn-off of the carbon. Wood followed a "shrinking particle" pattern, whereby the pellet slowly shrank and fragmented over time. Straw took a pathway almost between these two. Shrinkage of the pellet was observed, but an ash skeleton did remain, and this ash skeleton had bed sand adhered to it. This ash skeleton supports the melt-induced agglomeration observations of Lin, et al. [124] and Chirone, et al. [125] whereby an agglomerate is formed in the shaped of a fuel particle (section 2.2.3).

2.3.6.4   Fuel Moisture

Fuel moisture has not been investigated in relation to agglomeration behaviour in the literature. This may be of interest due to the high relative moisture content of biomass fuels, e.g. wood has been reported as having a moisture content of 40-70% [82]. This moisture content affects parameters such as the fuel heating value, bed temperatures, and flue gas composition during combustion [42, 82]. Higher moisture content negatively affects the overall boiler efficiency, as additional heat energy is used on the fuel drying phase of combustion, and larger variations in moisture content will affect combustion control [156]. However, it is known that water will leach out soluble fractions alkali metals and alkaline earth metals responsible for agglomeration problems [44], thus there is some benefit in the fuel initially being exposed to a higher moisture content.

2.3.6.5   Fuel Feeding Rate

Fuel feeding rate has not been directly investigated as a factor, largely because a higher fuel feeding rate for a FBC unit would imply a higher thermal rating. Therefore, higher temperatures will naturally result if other operating conditions remain constant, the

effects of which are described in section 2.3.1. Moreover, it will of course provide more fuel ash to drive agglomeration and other ash issues.

2.3.7 Bed Material

As is evident throughout section 2.2, a common denominator for agglomeration is the presence of large quantities of silica within the bed material. Thus, research has been ongoing for alternative bed materials. A selection of these results are summarised in Table 2.3.

Substituting SiO_2-based sands for materials dominant in Mg, Al or Ca has a proven positive effect on reducing agglomeration, as doing so reduces or eliminates the availability of silicon for agglomeration. The exception is for fuels that contain sufficient amounts of Si to drive the formation of alkali-silicate melts themselves, such as straw, as seen in several works [84, 114, 130]. Use of different bed materials does still have some positive effect on lengthening defluidization time in these cases though.

More recently, Knutsson, et al. [157] investigated the potential of mixing bed materials to balance performance and economic aspects, an idea little explored in the literature. Varying mixtures of one to all of silica sand, bauxite (Al_2O_3), K_2CO_3, and $CaCO_3$, were thermodynamically modelled and tested experimentally. The presence of bauxite with silica sand or K_2CO_3 weakened agglomeration tendency over silica sand alone, as did blends with $CaCO_3$, which had a stronger effect on reducing agglomeration tendency. Knutsson, et al. [157] state that calcium forms a barrier preventing further diffusion of potassium into silicate melts. This appears to be an exploitation of the protective capabilities of calcium described by He, et al. [119], by forming a calcium-silicate protective layer faster than one would otherwise arise during the natural progression of coating-induced agglomeration.

Corcoran, et al. [158] trialled a blend of quartz sand with up to 40wt.% ilmenite ($FeTiO_3$) when combusting wood. It was found that a very thin layer of potassium from fuel ash would initially form on the ilmenite, and this would disappear as the potassium diffused into the bed particle, thus removing its availability for driving agglomeration. Iron was found to migrate outwards to the surface of the ilmenite bed particle, and calcium from fuel as was observed to form a layer on the surface of the ilmenite particle. This calcium layering may have prevented further diffusion of potassium inwards, similar to the calcium observations of Knutsson, et al. [157] and He, et al.

[119]. These agglomeration behaviours were again confirmed in a subsequent paper by the group, with further detailed agglomerate analysis of samples with longer exposure times [159]. Recently, energy supplier E.ON has begun using an ilmenite-based bed material named "Improbed" in several of their FBC units [160]. Similarly, researchers at the CANMET Energy laboratory are actively studying the use of ilmenite as a bed material option in pressurized fluidized bed combustion and chemical looping combustion [161].

Table 2.3: *Table summarising the effect of varying bed material on agglomeration. Results taken from the literature as noted.*

Reference	Bed Material	Composition	Fuel(s)	Effect on Agglomeration
Olofsson, et al. [90]	Bone ash	44.2wt.% CaO, 28.8wt.% P_2O_3	Straw	Reduced agglomeration tendency compared to quartz sand.
Olofsson, et al. [90]	Mullite	75.2wt.% Al_2O_3, 24.5wt.% SiO_2	Straw	Reduced agglomeration tendency compared to quartz sand and better than bone ash or magnesite. Noted as being due to high melting point of alumina silicates.
Olofsson, et al. [90]	Magnesite	84.4wt.% MgO, 7.55wt.% CaO, 3.93wt.% SiO_2	Straw	Reduced agglomeration tendency compared to quartz sand.
Nuutinen, et al. [107]	GR Granule (commercial/proprietary)	Proprietary (Mg-based, SiO_2-free)	Various: woody, wastes, industrial residues	Prevented agglomeration in cases where a quartz sand bed otherwise did experience agglomeration.
Fernández Llorente, et al. [158]	Limestone	$CaCO_3$	Brassica, Thistle, Almond shells	Prevented agglomeration in cases where a quartz sand bed otherwise did experience agglomeration.
De Geyter, et al. [159]	Potassium feldspar	66.2wt.% SiO_2, 19.3wt.% Al_2O_3, 8.2wt.% K_2O	Bark, olive residue, wheat straw	Increased agglomeration risk with bark and olive residues, no effect on wheat straw (agglomeration still occurred). Note that K-feldspar may be a constituent of natural sand.
De Geyter, et al. [159]	Plagioclase	54wt.% SiO_2, 27wt.% Al_2O_3, 11wt.% CaO	Bark, olive residue, wheat straw	Increased T_{aggl} for olive residue, no effect on bark, no effect on wheat straw (agglomeration still occurred). Note that Plagioclase may be a constituent of natural sand.
De Geyter, et al. [159]	Olivine	49.5wt.% MgO 45.0wt.% SiO_2	Bark, olive residue, wheat straw	Increased t_{def} for olive residue, no effect with bark, no effect on wheat straw (agglomeration still occurred).

Reference	Bed Material	Composition	Fuel(s)	Effect on Agglomeration
Liu, et al. [160]	Aluminous bed material	75.93wt.% Al_2O_3, 19.92wt.% SiO_2	Cotton stalk	Agglomeration issues after 38h of operation, as opposed to 8h for silica sand, when using 200kW$_{th}$ CFB.
Davidsson, et al. [83]	Olivine	$(Mg, Fe)_2SiO_4$	80% woody + 20% straw blend (energy basis)	Higher T_{aggl} compared to sand. No reaction between melt-layers and olivine. Agglomerates formed over time due to presence of straw & melt-induced agglomeration.
Davidsson, et al. [83]	Blast furnace slag	Ca/Mg/Al silicates	80% woody + 20% straw blend (energy basis)	Higher T_{aggl} compared to sand and olivine. No reaction between melt-layers and blast furnace slag. Agglomerates formed over time due to presence of straw leading to melt-induced agglomeration.
Yu, et al. [128]	Aluminous bed material	Al_2O_3	Rice straw	Increase in t_{def} though melt-induced agglomeration still occurred due to fuel.
Corcoran, et al. [155]	Quartz sand + Ilmenite (up to 40wt.%)	$FeTiO_3$	Wood chips	Reduction in agglomeration tendency – potassium diffused into the centre of the bed particle thus was less available to form alkali-silicate melts.
Grimm, et al. [112]	Olivine	49.0wt.% MgO, 41.0wt.% SiO_2, 8.4wt.% Fe_2O_3	Willow, wood residues, wheat straw, wheat distiller's dried grain with solubles (DDGS)	Fewer agglomerates with willow & wood residues compared to quartz sand bed, plus different coating layer composition (Mg/Si/Ca vs. Si/K/Ca). No reduction in agglomeration tendency with wheat straw or DDGS.

Reference	Bed Material	Composition	Fuel(s)	Effect on Agglomeration
Kirnbauer & Hofbauer [115]	Olivine	46.8wt.% MgO, 39.8wt.% SiO_2, 10.3wt.% Fe_2O_3	Wood	Used industrial-scale dual-fluidized bed gasifier – no agglomeration issues – though calcium additives such as dolomite also used which are known to mitigate agglomeration.
Chaivatamaset & Tia [161]	Alumina sand	>98wt.% Al_2O_3	Eucalyptus bark	No observation of agglomeration despite operational times 30+ times longer than those with silica sand, which underwent defluidization.
Enestam/Valmet Technologies [162]	AggloStop (Diabase)	50wt.% Feldspar $(NaAlSi_3O_8+CaAl_2Si_2O_8)$, 25wt.% Pyroxene (X-Y-$Si_2O_6$), 5wt.% Biotite $(K(Mg,Fe)_3(AlSiO_{10})(OH)_2)$, 15wt.% olivine $((Mg,Fe)_2SiO_4)$ 4wt.% Magnetite (Fe_3O_4)	-	Listed as an example of an alternative inert bed material solution offered by Valmet for agglomeration mitigation. Not quantitative or qualitative information given in presentation.
Wagner, et al. [96]	K-feldspar, quartz sand	K-feldspar: SiO_2 (65.7wt.%), Al_2O_3 (17.9wt.%), K_2O (14.74wt.%)	Bark, wheat straw, chicken manure, and mixtures chicken manure with bark and straw	K-feldspar had a lower tendency to form ash layers, which would minimise agglomerate formation. Suggested as being due to the high amounts of Al_2O_3 present, where Al^{3+} would act as a strong cation to prevent inclusion of K^+ in structure.

2.3.8   Bed Material Particle Size

Figure 2.11 provides graphs of the effect of changing average bed particle size (d_p) on defluidization time from four separate works. The trend exhibited is that with an increase in bed particle size, there is a reduction in defluidization time. Some notes on these graphs are as follows:

- Lin, et al. [124] maintained a constant temperature and superficial gas velocity, U, between the two d_p values. They suggested that poorer mixing due to the smaller U/U_{mf} ratio for the larger particles led to a lower defluidization time.

- Chaivatamaset, et al. [132] also maintained a constant fluidizing gas velocity across the bed particle sizes. Tests for all fuels at 900°C also showed decreases in defluidization time with increases in d_p.

- Yu, et al. [130] used a near constant U/U_{mf} value for all three particle sizes, as opposed to maintaining a constant U value as Lin, et al. [124] and Chaivatamaset, et al. [132] did. However, Yu, et al. [130] also hand fed bundles of straw every 20 seconds as fuel. This non-continuous fuel feeding method have affected results somewhat.

- Lin & Wey [127] combusted municipal solid waste (MSW) within a fluidized bed, a fuel with similar agglomeration characterisations to biomass due to its high Na content. They note that sand particles up to 770µm acted as a Geldart Group B powder, whilst the 920µm sand acted as a Group D powder. This change in Geldart classification is accompanied by a sharp decline in defluidization time.

The distinction between the Geldart particle classifications by Lin & Wey [127] is perhaps an important one: particles in Group B favour bubbling behaviour at U_{mf}, whilst Group D will spout as they more readily form large bubbles [9, 162]. This raises the question of the potential impact of different Geldart particle classifications on agglomeration during FBC of biomass, and if a wider study may reveal relationships between particle size, Geldart particle classification, and agglomeration. For example, perhaps the bubbling behaviour of Group B acts to minimize the formation of potential agglomerates by improved bed mixing, whereas Group D materials may allow for bed material to end up grouped together, promoting temperature non-uniformities and agglomerate formation.

Scala & Chirone [129] reported a different trend for increases in d_p (Table 2.4). Increases in d_p by a factor of 2-3 led to an approximate doubling of defluidization time for all fuels and scenarios. In the pine seed shells data, fuel feed rate was reduced to increase amounts of excess air which may explain increases in defluidization time. However, this was not the case for the virgin olive husk fuel, which exhibited the same trend. The reasoning for this put forth by Scala & Chirone [129] was that large particles will participate in more energetic collisions, making it harder for adhesive forces to mitigate these and cause adhesion between the particles.
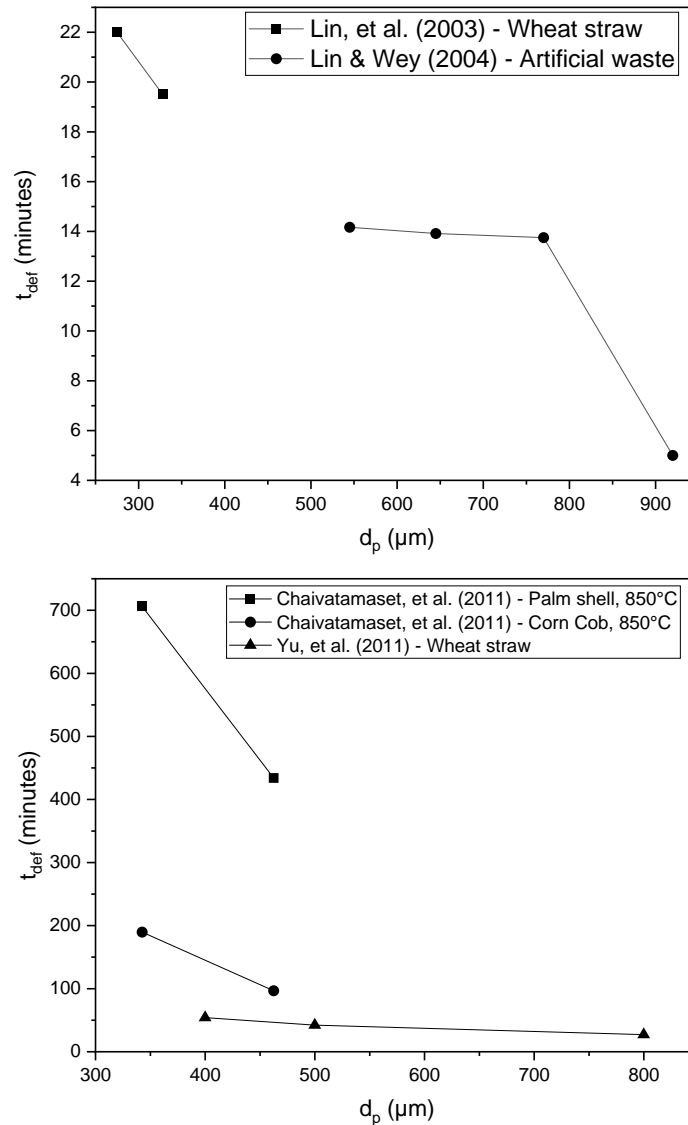
Figure 2.11: *Graphs showing the effect of changing average bed particle size on defluidization time, t_{def}. Based on the works of Lin, et al. [124], Lin & Wey [127], Chaivatamaset, et al. [132], and Yu, et al. [130].*

Table 2.4: *Summary of the effects of bed particle diameter variations on defluidization time from the work of Scala & Chirone [129], using a quartz sand bed.*

Fuel	Temperature (°C)	Fluidizing Gas Velocity (m/s)	Excess Air (%)	d_p (µm)	t_{def} (mins)
Virgin Olive Husk	850	0.61	77	212-400	197
Virgin Olive Husk	850	0.61	76	600-850	348
Pine Seed Shells	850	0.55	35	212-400	320
Pine Seed Shells	850	0.50	75	212-400	388
Pine Seed Shells	850	0.54	58	600-850	702

Lin, et al. [133] performed a comprehensive study on the effects of different d_p distributions of sand on defluidization time, albeit for MSW as opposed to biomass. Four d_p distributions were selected:

- A narrow distribution of d_p between 590-840µm

- A Gaussian distribution where d_p ranged between 350-1190µm

- A binary distribution where 59% of bed mass was 840-1000µm, whilst the remainder was 500-590µm

- A flat distribution, ranging between 350-1190µm
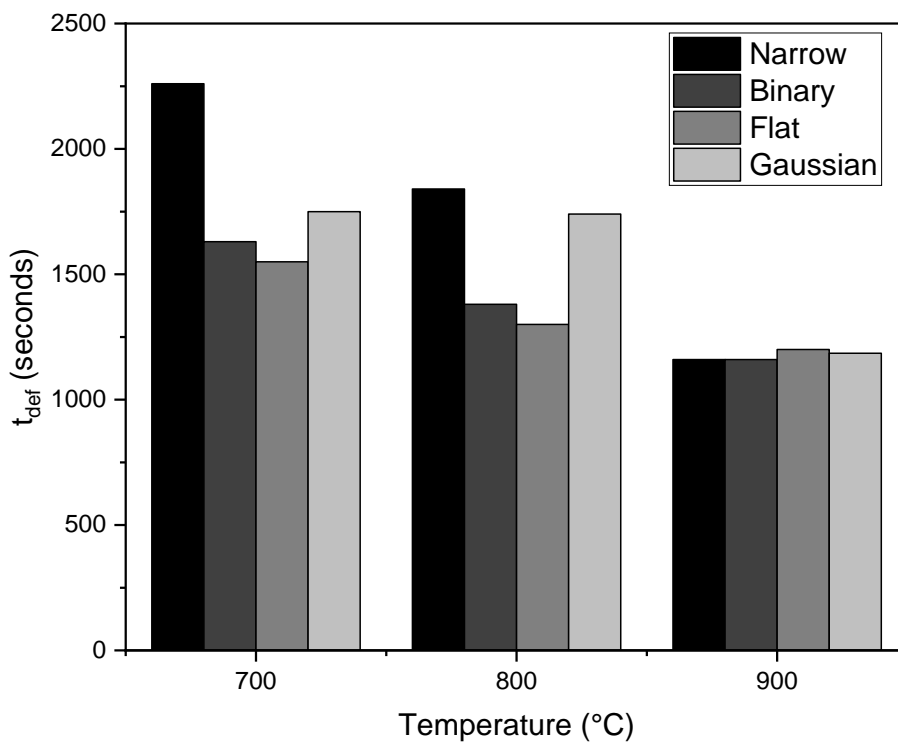
Figure 2.12: *Chart showing the effect of particle size distribution on defluidization time for operating temperatures of 700°C, 800°C, and 900°C, when combusting municipal solid waste on a fluidized bed. Data from the work of Lin, et al. [133].*

Perhaps the most interesting result arose by varying operating temperature from 700°C, to 800°C and then to 900°C, shown in Figure 2.12. The narrow and Gaussian distributions both showed noticeably larger values of defluidization time at 700°C and 800°C than the binary and flat distributions, upwards of 20% greater. At 900°C however, there was almost no difference in defluidization time between the distributions, perhaps indicating severe ash melting due to the temperature. Similar results were obtained when varying fluidizing gas velocity and the Na concentration within the bed.

The work of Lin, et al. [133] indicates the potential importance of particle size distribution. The narrow distribution displayed some sizable increases in defluidization time over the other distributions at moderate temperatures and sodium contents, a behaviour displayed to a lesser extent by the Gaussian distribution. This would imply that once an optimal particle size has been determined, the distribution used should be as tight as possible around this size, as presumably oversized fractions may act to drive agglomeration (as larger particle sizes were a negative in the work of others [124, 130, 132]). However, different distributions of smaller particles were not examined in this work, and these were seen to produce longer defluidization time times in the work of others [124, 130, 132]. Therefore, further work into finding the optimal particle size distribution, in parallel to determining the optimal particle size, may be worthy of investigation.

2.3.9 Bed Spatial Location

As noted in section 2.2.2 in the discussion of the work of Öhman, et al. [112], there may be the potential for different spatial zones of the bed to experiences different levels of agglomeration severity. This may be a factor of gas distribution uniformity and mixing patterns (section 2.3.4), or due to large bed areas with fuel only fed to one or few locations in/on the bed. This is particularly applicable to commercial boilers, where bed cross-sectional areas can be upwards of tens of metres squared [21, p. 236], allowing the potential for variations in bed mixing patterns. The only available work to the authors' knowledge that covers the topic of spatial variances in agglomeration is that of Duan, et al. [163], who sampled agglomerates from three distinct bed vertical height strata in a lab-scale FBC unit. The potassium concentration of bed material and agglomerates from each vertical stratum was analysed with inductively coupled plasma mass spectrometry (ICP-MS), and it was observed that sampled from the upper vertical strata (bed surface,

onto which fuel was fed) had upwards of 3x as much potassium as samples from the two lower vertical strata. This is strongly indicative that there is variation in quantities of components key to agglomeration throughout the bed, though other important elements (such as sodium, phosphorous, calcium, etc.) were not analysed, nor was there analysis of agglomerate structures or mechanisms at these different locations. This does once again indicate that bed scale variances in agglomeration behaviour would be on interest.

2.3.10 Additives

The use of additives to minimize or eliminate agglomeration has been a key area of research. Wang, et al. [164] provide a short review on additive usage during biomass combustion to mitigate ash challenges both within the bed and those further up the boiler, such as fouling and corrosion.

The work of Steenari & Lindqvist [165] identified kaolin and dolomite as increasing the ash melting temperature for straw ash, with the former having a greater effect. Öhman & Nordin [166] trialled kaolin, comprising primarily of kaolinite ($Al_2Si_2O_5(OH)_4$) with some Halloysite ($Al_2Si_2O_5(OH)_4(H_2O))_2$). An additive dosage equal to 10wt.% of the quartz sand bed was used, with bark and wheat straw as fuel. For wheat straw the agglomeration temperature, T_{aggl}, increased from 739°C to 886°C, whilst for bark it increased from 988°C to 1000°C. The kaolin used had transformed into meta-kaolinite and absorbed potassium, thus denying potassium for agglomeration.

Olofsson, et al. [91] experimented with the addition of mullite, calcite, clay, and a clay-calcite mixture, each 10wt.% of the bed, for different bed materials and fuels. Mullite was found to largely mitigate agglomeration, clay worsened agglomeration due to its potassium content of 1.28wt.%, whilst calcite was present in agglomerates but had a somewhat positive effect on reducing agglomeration severity.

Davidsson, et al. [84] trialled several additives in a 12MW$_{th}$ CFB for the combustion of a blend of wood pellets and straw pellets on a quartz sand bed. When using kaolin as an additive, T_{aggl} of cyclone ash samples were over 100°C above those of samples where kaolin was not used. A molar ratio of kaolin to alkali of 0.85 was sufficient to maintain a $T_{aggl} > 1100$°C. The effects of ammonium sulphate and sulphur were also monitored. These additives are typically used for corrosion control [80, 81]. In theory, these would convert gaseous KCl into K-sulphates, and favour the release of potassium into the

gaseous form. Ammonium sulphate gave a small increase in T_{aggl} of around 50°C, whilst sulphur had no such effect.

Vamvuka, et al. [167] tested kaolinite $(Al_2Si_2O_5(OH)_4)$, clinoclore $((Mg,Al,Fe)_6[(Si,Al)_4O_{10}](OH)_8)$ and ankerite $(Ca(Mg,Fe,Mn)(CO_3)_2)$ for the combustion of olive kernel and olive tree wood on a Na-feldspar bed. The authors state that this bed material was selected itself to reduce agglomeration, thus will affect the apparent effectiveness of these additives. All three additives prevented agglomeration during the tests, retaining alkali species within the bottom ash.

Zabetta, et al. [72] discuss the commercial experiences of Sumitomo SHI FW (formerly Foster Wheeler) with additives. They too note that kaolin has been found to be the most effective, but also list some alternatives used with their boilers such as bauxite, emalthite, sillimanite, and diatomaceous earth. These materials are noted to contain one or more of silicon-, aluminium- or iron-oxide which react with H_2O to form HCl, transferring the alkali to the mineral used and preventing the formation of KCl. Another paper from the same group [168] details the success of using pulverized coal ash as an additive to prevent agglomeration in a bench-scale and $1MW_{th}$ pilot-scale CFB with variety of biomass, including straws. This additive was seen to capture potassium in a similar manner to kaolin, reacting to form potassium aluminosilicates. The benefit of pulverized coal ash is that it is a cheaply available waste product, however it may vary substantially in composition depending on source and original combustion technology, and it was also noted that fine ash may lead to increased fouling issues.

Lin, et al. [169] investigated the addition of calcium and magnesium for incineration of waste. Both reduced agglomeration tendency and increased defluidization time, when the molar ratio of Na, which drove agglomeration in waste incineration, to Mg or Ca was below 2. Above this ratio there was no inhibiting effect.

A recent study by Clery, et al. [170] into different biomass pellets dosed with an aluminosilicate additive using flame emission spectroscopy has shown that the use of an additive causes a retention of upwards of 60% of the potassium content of the biomass in the bottom ash, as opposed to being released into the gas phase. Whilst this study was performed outside the context of FBC, this does highlight the value of a better fundamental understanding of chemistry changes when using additives, and how this may affect both agglomeration and the propensity of other ash issues.

The work of Chi, et al. [171] examines the use of 1.5wt.% lime addition to miscanthus and wheat straw fuel pellets in a pilot-scale BFB, this dosage being selected to achieve a K/Ca ratio of ~1. The addition of lime the pellets more than doubled defluidization times, and prevented it entirely for 14 hours of operation for wheat straw, despite average bed temperatures being higher than tests with regular pellets, at 900°C as opposed to 820-880°C. This shows a significant benefit when the additive is embedded within the fuel pellet, however this methodology would add cost to commercial units, as pelletized fuels with an additive would be required, as opposed to use of chipped fuels with an additive powder mixed into the bed material which are commonly used at present [72].

To summarise, additives that are rich in Mg, Ca, or Al have a positive effect in reducing agglomeration tendency, similar to use of alternative bed materials (section 2.3.7). Kaolin has been widely successful with wood fuels. From the works of Lin, et al. [169] and Chi, et al. [171], it would appear that additives may be particularly effective when the ratio of the most problematic alkali metal, Na or K, to Ca or Mg is well below 2, ideally ~1. Such a rule may also apply to aluminium-based additives such as kaolin though would require experimentation to confirm. Additives generally retain alkali species within the bottom ash, thus preventing it from contributing to fouling, slagging, or corrosion. Agglomeration may still proceed for fuels that produce melt-induced agglomeration, though additives still have a positive effect. It would be of interest to investigate the effects of varying additive dosage, relative to the molar amount needed for the fuel feed rate. This could help determine the relative technical benefits of under and overdosing additives on both bed agglomeration and other downstream issues such as slagging, fouling, and corrosion.

2.3.11 Coating Thickness & Bed Agglomerate Loading

The idea of a "critical coating thickness" and the effects of liquid layering on particles in a fluidized bed is one that been discussed in the literature for many years. For example, Seville & Clift [172] noted that the continuous addition of liquid layers to fluidized particles of Geldart group B would cause them to transition to Geldart groups A and C, as inter-particle forces are enhanced. A "critical coating thickness" would be the point at which neck formation between ash-melt coated particles occurs and bed agglomeration proceeds. Brus, et al. [173] performed an analysis of coating thickness over time, taking samples from industrial scale FBC plants, and stated that the critical

coating thickness is less than 10μm. The recent work of He, et al. [119] provides a systematic investigation into coating thickness over time for a lab-scale BFB, 30MW$_{th}$ BFB, and 122MW$_{th}$ CFB. An initial rapid growth of coating layers occurred over the first several days in the full-scale units. This growth rate declined as diffusion of calcium into the melt began and higher melting point calcium compounds formed. However, there was no further discussion of a critical coating thickness. Others in the literature have also mentioned the idea of a critical coating thickness with little other discussion [109, 113, 121, 174].

Sevonius et al. [175, 176] have investigated the direct addition of different potassium salts [175] and sodium salts [176] to an externally heated fluidized bed when using a quartz sand bed material, to determine the amount of each alkali salt needed to defluidize the bed and further explore agglomeration mechanisms. In the case of potassium salts [175], only potassium carbonate reacted with bed material to form potassium silicates, with potassium chlorides only melting to act as a glue, whereas potassium sulphates were unreactive. Around 0.16wt.% (of bed mass) KCl or 1wt.% K_2CO_3 were needed to cause bed caused defluidization. When using sodium salts [176], around 0.1wt.% (of bed mass) NaCl or 0.6-1.0wt.% Na_2CO_3 were needed to cause bed defluidization. A synthetic agglomeration test methodology has also been used by Anicic, et al. [177] to investigate the behaviours of quartz sand with K_2CO_3, who also observed significant reaction between K_2CO_3 and the quartz sand bed material. It should be noted that whilst these synthetic agglomeration tests are a useful idea for determining the behaviour of one specific component with regards to agglomeration, such tests would not give a complete picture of how the component under investigation behaves in a real FBC environment and contributes to agglomeration. For example, they do not account for factors such as fuel particle breakdown behaviour, bed hot-spots, interactions with other ash components or additives, etc.

Related to coating thickness and the necessary amount of alkali metals to trigger defluidization, is the idea of agglomerate loading within the bed, i.e. the quantity of agglomerates needed to begin defluidization. Michel, et al. [178] studied this topic for quartz sand, raw, ad calcined olivine when adding miscanthus ash to a heated bed. Fresh bed material was of size range 400-500μm, with the bed material sieved and measured afterward and the fraction above 500μm deemed to be an "agglomerate". An "agglomeration ratio" was defined as:

$$A\ (\%) = \frac{m_a}{m_i} \times 100$$

Where m_a is the mass of agglomerates in the bed ($d_p > 500\mu m$) and m_i is the initial mass of the bed. For the three bed materials, it was found that an agglomeration ratio of 3% was needed to cause defluidization. Whilst there does not appear to be other supporting or corroborating literature for this at present, specific to the effect of biomass ash of a fluidized bed, it may serve as a useful reference figure for operators and perhaps is a viable topic for investigation with other biomass ashes as opposed to just miscanthus ash.

2.3.12 Size & Scale of Fluidized Bed

For generating solutions to industrial problems at the lab- or pilot-scale, it is important to understand the applicability of results and findings to full-scale FBC plants. Many researchers have investigated agglomeration in full-scale plants and performed direct comparisons to samples produced by lab- or pilot-scale facilities. Visser [110] looked at agglomerates from both the lab-scale and the 80MW$_{th}$ Cuijk FBC unit in the Netherlands. The two operational differences between these setups were that the lab-scale unit had fuel fed directly into the bed, whilst for Cuijk it was above-bed, and that there was a constant bed renewal and replenishment cycle in effect at Cuijk. This bottom ash removal and bed replenishment ability is a common agglomeration control strategy within industry [72, 123]. However, it is also one not available to most lab- and pilot-scale facilities. It is of note that variations to replenishment rate to determine the effect on agglomeration is not something that appears to have been examined in the literature, but equally would require a suitable lab- or pilot-scale facility.

Visser [110] concluded that lab-scale agglomeration testing provided a representative view of the initial stages of plant-scale agglomeration. The constant replenishment of sand at the Cuijk bio-energy plant was believed to be the cause of some of the differences in the chemistry of outer coating layers, due to providing fresh material for chemical reactions. Furthermore, samples at Cuijk had thicker coatings due to a longer average residence time in the bed compared to the lab-scale agglomerate samples.

Others have also observed consistent results between lab- and full-scale facilities, be it for topics such as agglomeration mechanisms, additives, or fuels, albeit with the same

shortcomings such as those seen by Visser [110], e.g. thinner coatings due to shorter residence times [108, 109, 119, 153].

One difference suggested by Chirone, et al. [125] is that a pilot-scale fluidized bed provided a longer defluidization time compared to a lab-scale setup due to higher inertial forces in the bed. A comparison between a pilot- and lab-scale unit resulted in a defluidization time that was 3.6 times longer at pilot-scale and had a higher ash content within the bed at time of defluidization (4wt.% versus 2wt.%). Chirone, et al. [125] suggested an increase in inertial forces inside the bed when moving up in scale would counteract the formation of weaker agglomerates that might otherwise cause a quicker onset of defluidization. Therefore, at plant-scale higher inertial forces may also assist in lengthening defluidization time.

2.3.13   Summary of Effects of Operational Variables

Table 2.5 summarises the effect of operational variables on agglomeration.

Increases in combustion temperature have a sizable effect on agglomeration, by increasing the amount of alkali-silicate melt that is generated and making it less viscous. Therefore, a lower temperature is desirable, insofar as it does not have too great of an impact on the conditions of raised steam at full scale.

From the limited literature available on agglomeration in PFBC units, the final agglomerates formed in PFBC units seem of similar composition and type to those that would form in an AFBC.

Increases in the fluidizing gas velocity, U, have consistently produced longer values of defluidization time in the literature. This appears to be a result of two factors:

- Better in-bed mixing preventing the formation of localized temperature hot spots or bed dead-zones.
- Higher kinetic forces of bed particles that may overcome adhesive coating or melt forces.

There is little research on the effects of static bed height, and what is available is not conclusive. Work using a constant U value across several bed heights has produced an increase and decrease in defluidization time with increasing bed height, indicating perhaps the involvement of other factors. Additionally, increases in bed height allow for coalescence of bubbles to larger sizes. Therefore, will be increased turbulence at the bed

surface where the bubbles exit, which in turn may affect combustion behaviour of the fuel particles and agglomeration behaviour.

Table 2.5: *Table summarising the effect of various operational variables on reducing agglomeration severity.*

Effect on REDUCING Agglomeration Severity			
Conflicting or Unknown	**No Effect**	**Minor**	**Major**
Increase/decrease bed height	Increase/decrease pressure	Decrease mean d_p	Decrease temperature
		Different particle size distribution (Gaussian, narrow)	Increase U/U_{mf} ratio
		Decrease fuel particle size	Decrease fuel feed rate
			Decrease alkali metal/alkali metal + Si content of fuel
			Use of Al/Mg/Ca-based additives
			Decrease bed material SiO_2 content (use of Al/Mg/Ca-based bed material)

Investigations into bed material particle size have generally shown that increasing d_p, even whilst maintaining a constant U/U_{mf}, leads to a reduction in defluidization time thus worsened agglomeration. Variations of bed particle size distribution for larger bed particles have shown that Gaussian and narrow distributions provide longer defluidization time values, implying that once an optimal particle size has been found, the particle size distribution should be tightly focused on it to avoid potential negative effects of under- or over-sized particles.

Alternative bed materials that comprise primarily of aluminium-, calcium-, or magnesium-oxides, as opposed to the SiO_2, have been shown to reduce or eliminate agglomeration. A change of the bed material can increase the ash fusion temperature of complexes forming, and in doing so reduce melt phases. The exception is where a fuel is rich in both alkali metals and SiO_2, such as straw, which will form a melt-induced agglomerates with just its fuel ash contents. Related to the topic of bed material is that of spatial location in the bed. From the few works available, there is some indication of variation in key components for agglomeration through the bed, though it is not fully explored.

Similar to bed materials, aluminium-, calcium-, or magnesium-based additives have been shown to be effective. Kaolin in particular has shown itself to be successful in reducing or eliminating agglomeration several times within the literature. Both additives and bed materials have been noted to have a large effect on emissions, particularly chlorine, which can drive corrosion mechanisms.

Fuel has a large influence on agglomeration. Fuels with increasing amounts of alkali metals such as potassium exhibit more severe agglomeration, typically melt-induced agglomeration, and lower values of defluidization time. Co-firing of fuels is something primarily explored in the context of coal-biomass or wood-straw mixtures within the literature. A common trend for biomass blends is that relationships between blend ratios and agglomeration factors such as melt temperatures are non-linear. Fuel particle size has received some attention, with smaller particle sizes giving better combustion efficiencies and longer values of defluidization time. This is perhaps due to combustion taking place at higher regions of, or just above, the bed.

Coating thickness and critical values for triggering agglomeration are of general interest. Growth rates are typically quicker at the start and then trail off due to diffusion of Ca into the K-silicate melt, forming a Ca-silicate melt of higher melting point. Neck formation between coated particles can occur at coating thicknesses less than 10µm. Investigations into the total agglomerate loading in a bed needed to trigger defluidization suggest a value of 3% of the bed as agglomerates, though this was only performed for miscanthus ash.

The applicability of lab- and pilot-scale results to full-scale facilities has been explored within the literature. Mechanisms and behaviours generally map well to full-scale facilities for the initial triggering of agglomeration. Over time, there is a divergence due to replenishment of bed material in full-scale facilities, plus longer residence times, leading to thicker coatings on bed particles.

2.3.13.1   Recommendations for Further Work

- Large bed heights allow for further coalescence of bubbles, leading to greater turbulence at the surface of the bed, as well as enhanced combustion efficiencies [21, 138]. Gatternig & Karl [120] observed that less dense fuel particles "floated" on the surface of the bed, reaching higher temperatures, and

exacerbating agglomeration issues, thus there may be interest in the effects of bed height on agglomeration severity.

- Smaller particle sizes have generally been shown to lengthen defluidization time, and certain particle size distributions (Gaussian, narrow) have been shown to lengthen defluidization time albeit with larger average particle sizes. Therefore, it would be of interest to trial different size distributions of a smaller mean particle size, to see if similar findings are apparent, and if there may be an optimum size range and size distribution.

- Several alternative bed materials and additives have been shown to mitigate or prevent agglomeration in numerous studies, with some such as olivine (bed material) and kaolin (additive) being used in industrial installations. Investigatory work into new bed material and additives would always be welcomed, but also more comprehensive studies into the effects of alternative bed materials and additives on other phenomena driven by the alkali metal content of biomass fuels, such as slagging, fouling and corrosion. Some alternatives bed materials and additives have been observed to have large effects on alkali chlorides and HCl, which drive corrosion within the boiler.

- As noted in section 2.2.4.3, variation in agglomeration on a spatial basis through the bed may be of interest, with the limited work available providing some proof that variation of potassium through the bed is a phenomenon and may therefore affect localised agglomeration issues.

- There may be some interest in blending of bed materials, perhaps to balance performance with cost, and investigating impact on the whole boiler system.

- There may also be some interest in trialling different dosage rates of additives from under to overdosing relative to the molar amount needed for the given fuel and investigating the cost and performance impact on the whole boiler system.

- Co-firing of biomass-biomass blends and the effect on agglomeration is something that has received little work outside of wood-straw mixtures. From current works, biomass ashes have exhibited complex, non-linear relationships for properties such as initial ash deformation temperature. Work in this area could aid in assessing the viability of such blends for larger scale FBC units.

- Studies into optimising bed replenishment rates may be of interest, as no work on this area seems apparent in literature. However, this may be challenging from

the perspective of finding a suitable and available test facility or full-scale unit on which a study could be conducted.

2.4 Modelling of Biomass Chemistry

This section provides a brief overview of agglomeration modelling using the thermochemical software package FactSage. Other agglomeration modelling and prediction methods are discussed in the work of Morris, et al. [87], with an extensive and comprehensive review into agglomeration prediction approaches given by Bartels, et al. [75]. In addition, an introduction and brief review of the random forest machine learning algorithm, as applied to the study of biomass fuels, is also given. Machine learning techniques have received a significant amount of attention in recent years across many contexts and may be a viable approach to gain new insight from large fuel data sets from commercial biomass power stations.

2.4.1 FactSage

Use of the thermochemical modelling software package FactSage [179] has gained popularity in recent years as a tool to predict slag formation and ash behaviours of fuels. This is due to the advancement of computational power and the better breadth and accuracy of thermochemical data sets [151, 180]. FactSage, like other thermochemical modelling tools such as HSC Chemistry or MTDATA [181, 182], uses the CALPHAD approach (CALculation of PHAse Diagrams) to Gibbs free energy minimization. The work of Saunders and Miodownik [183] provides a comprehensive explanation of the underlying theory behind Gibbs free energy minimization, the CALPHAD approach, and the structure and development of software packages such as FactSage.

The Gibbs free energy (ΔG) is a measure of the ability of a reaction to spontaneously proceed, and is defined through the following equation (at constant pressure):

$$\Delta G = \Delta H - T\Delta S$$

Equation 2.3

Where ΔH is enthalpy, T is temperature and ΔS is entropy. This equation has its basis in the second law of thermodynamics: total system entropy can never decrease and can only increase towards a state of maximum entropy. For a chemical reaction to occur spontaneously in the forward direction (to make products), the value of ΔG must be negative, whereas for it to proceed spontaneously in the reverse direction (to make

reactants) the value of ΔG must be positive. Chemical equilibrium, the point at which ΔG = 0, is the point at which the system is at its maximum entropy and further spontaneous reaction will not occur. Gibbs free energy minimization is an iterative method to find the chemical equilibrium of a system (i.e. when ΔG = 0) for a given set of chemical inputs and constraints (e.g. temperature, pressure, mass, mole fractions). It is this mathematical approach that is fundamental to CALPHAD-type software packages such as FactSage.

To perform Gibbs free energy minimization, the underlying Gibbs free energy of compounds at different conditions must be determined [183, pp. 261-291]. This generally involves experimentation to produce unary, binary, ternary and in some cases quaternary system phase diagrams over variable temperature ranges (e.g. the K_2O-SiO_2 binary system). The better mapped each phase system is, and the more reliable the data, the better the accuracy of any resultant calculation. Given experimental data, software developers then optimize these chemical systems. This optimization process involves taking the data and ensuring there is mathematical self-consistency to the result when calculated through the software, in doing so often revealing systematic errors or conflicting results. These optimized systems are then added to chemical databases, which are groupings of similar sets of chemical data. For example, the FToxid database in FactSage covers a range of metal-oxide systems. With this data, FactSage can then be used to calculate key thermochemical data for an input system. For example, the solidus which is the temperature at which a mixture is fully solid, the liquidus, the temperature at which a mixture is fully liquid, or a eutectic point, at which the liquidus is equal to the solidus for a given mixture.

Many binary, ternary or higher chemical systems do not have full sets of reliable phase data, leading for the need for interpolation or extrapolation based on available data or lower order systems. This can be fraught with inaccuracy and errors, though clearly it is unfeasible to experimentally validate all binary, ternary, or higher systems. The present approach is for developers to ensure sufficient data for key binary, ternary, and occasionally quaternary systems. Key systems are those that have the biggest magnitude impact on the Gibbs free energy of a multicomponent system, or those that are otherwise are integral to understanding of the chemical behaviour of a system [183, pp. 312-313]. FactSage has seen more use for modelling of biomass ash melts over other

thermochemical modelling software packages due to having better databases for modelling ash melts and slags, notably FTSalt and FToxid [181].

When applying FactSage to biomass ash modelling, there are still important systems for which there is insufficient or conflicting experimental data, rendering part of the respective phase diagrams incomplete [181]. Consequently, this reduces the ability of the software developers to accurately optimize these systems within FactSage, thus affecting the accuracy of the end-users' modelling activities. For example, it is known that there is a lack of fundamental experimental data for K- and Ca-phosphate systems [184], which is notable due to the high amount of phosphorous present in some biomasses such as cereals [44], and the role of phosphorous of driving agglomeration in phosphorous rich biomass fuels [185] as discussed in section 2.2.1. A second shortfall is the lack of experimental validation of the K_2O-CaO-SiO_2 ternary system (see also Figure 2.1 for this phase diagram as introduced in section 2.2.1) in the FToxid database [181], an integral system of components for agglomeration behaviours as discussed in section 2.2, with the primary reference being that of Morey, et al. from 1930 [93]. Berjonneau, et al. [186] revisited this system and observed liquidus temperature discrepancies of up to 200°C, which highlights the need for more fundamental chemistry work in this area.

Despite these shortcomings, FactSage can still add value when used in addition to experimental techniques. The work of Fryda, et al. [187], whilst using older databases, is an example of FactSage being used to predict melt formation fractions across typical FBC operating temperatures. With FactSage, there was a prediction of 25-45% less melt formation when the silica in bed material was not included in the model. Fryda, et al. [187] note that this was more realistic for their fuels, as from their SEM/EDX observations there was not significant interactions between bed material and fuel ash. This highlights the fact that FactSage does not consider physical realities of the bed, notably that it considers all silica equally reactive, and does not have any allowance for bed material porosity or size for example. Therefore, care needs to be taken to configure any model to best reflect the real observed agglomeration behaviours.

Across a two-part paper, Zevenhoven-Onderwater, et al. [188, 189] modelled predicted ash behaviours and then experimentally tested this prediction, in the context of fluidized bed gasification. In three of thirteen cases, no agglomeration was predicted by the

model, but was found during experimentation. In the other ten cases, the model agreed with experimental findings, with the predicted agglomerates either found via visual inspection of the bed or confirmed through SEM/EDX analysis, indicating good accuracy of the model. The model also appeared to have good quantitative agreement with experimental results from an SEM/EDX analysis of agglomerates. For example, for miscanthus on a dolomite bed, a 20% potassium oxide solid phase was predicted, compared to an approximate 25% potassium oxide phase being observed in an agglomerate sample.

The more recent work of Rizvi, et al. [180] examined slag formation quantities and compositions using FactSage, for pine wood, peanut shells, sunflower stalks, and miscanthus. All fuels were predicted to have some liquid slag formation at 700°C, however each fuel had different responses to increases in temperature. For example, both peanut ash and pine wood maintained relatively constant liquid slag fractions through the typical FBC operating temperature range of 800-900°C. Miscanthus on the other hand exhibited a 10-15% increase. It should be noted though that this work does not consider the fuel in the presence of the bed material, only the fuel alone, and doing so would likely encounter many of the similar challenges highlighted by Fryda, et al. [187].

There is also room for simpler models for biomass ash behaviours during combustion that draw upon knowledge from FactSage models and experimentation to predict difficulties with new fuels. The work of Boström, et al. [190] is an example of such a conceptual model and draws out the key primary and secondary ash transformation reactions, and reaction orders, then applies them to different fuels to predict expected slagging potential. Such models may be of use in a plant operations environment, with the authors noting that future work would include building such an integrated tool for process modelling purposes.

2.4.2 Random Forest Machine Learning Approaches

Random forest is an ensemble machine learning algorithm. It is an approach that was developed in the late 1990's that offers improved robustness over singular decision trees as a predictive modelling approach for a given set of data [191]. With random forest, many separate decision trees are used, with each one making a prediction. The aggregate results of these trees are then used to make the "final" prediction. In the

context of a regression study, the prediction results of all decision trees are averaged to create the final prediction. Random forest has been widely applied across academia and industry. For example, a search for the term "random forest" in the citation database Scopus [192] returns over 37,000 results (as of November 2020), with over 31,000 of these items published since 2015.

The works of James, et al. [193] and Hastie, et al. [194] provided detailed reference texts covering, amongst other techniques, random forest theory and methodology. Like many machine learning modelling processes, the creation of a random forest model is divided into a training phase, where the forest is "grown" by inputting a proportion of the total data, and the testing phase, where the predictive capabilities of the trained model are evaluated against a testing set of data that the model has not previously "seen". Subsequent predictions, with new incoming data, would then be inputted into this trained and tested model.

Random forest uses the common machine learning approach of bootstrapping sample data [193, pp. 187-190]. In bootstrapping, multiple input data sets are created by random sampling of the input data with replacement. That is, a data sample may be sampled and be present several times within the same bootstrapped data set, with the total number of samples in the bootstrapped data set equalling the total number of samples in the original data set. Each bootstrapped data set is then given to a decision tree. A further unique aspect to the random forest approach is that at each decision node in each tree, a random subset of data features (i.e. input 'x' variables) is selected as the basis upon which to split the node [193, pp. 319-321]. The proportion of the data features selected can be defined by the user. This is done to decorrelate trees and reduce variance. If there was a very strong feature present at every splitting point, such a feature might otherwise always be used to split the data across all trees, thereby leading to overfitting of all the decision trees.

The splitting point at each tree node is decided on the basis of the greatest reduction of mean squared error (MSE) [194, pp. 307-308]. To better understand this, consider a 'x-y' scatter plot where the y-axis is the prediction target for the model, and the x-axis is the data feature used for splitting the data set. A point along the x axis can be selected to split the data set. The average 'y' value for each half of the data can then be calculated and evaluated versus the real 'y' value of the training data to evaluate the MSE. The x-

axis splitting point can then be varied to reduce the MSE of the split. This tree splitting and growth process continue to the point at which a split can no longer satisfy the user defined settings for the minimum samples per leaf or split, or the maximum tree depth setting. Once each tree has made a prediction, these predictions are averaged, with this average then presented as the predicted value of the model.

A downside to the random forest approach is that by relying on many trees, with each using a subset of data and splitting on the basis of a subset of features at each point, it can be more difficult to visualise the key decisions and variables in comparison to the use of a singular decision tree [193, pp. 315-316]. However, as noted, this approach has been widely proven to be less susceptible to bias and variance, and in general is more robust and capable of making better predictions than a singular decision tree [191]. Furthermore, there are ways to assess important variables to the random forest, such as evaluating the permutation importance of input data features.

In recent years, a handful of papers have applied random forest in the context of fuel, combustion and/or fluidized bed studies and have shown it to be a viable predictive modelling approach [195, 196, 197, 198]. In the work of Ge, et al. [195], random forest and other decision tree approaches were used to identify fuel types based upon flame spectra data. Four different biomass fuels were used in testing. A total of 4000 data points were collected, with seven data features used for prediction in the tree models. After tuning of the random forest model, the average identification success rate after ten trials with the model was 98.7%. This was the lowest of the prediction accuracies for the tree models tested, with the gradient boosted decision tree model achieving the highest accuracy of 99.5%. Gradient boosting is a commonly applied approach in literature [193, pp. 321-322], but at the cost of a longer model training time as trees are sequentially rather than concurrently grown. Despite this, an average prediction success rate of 98.7% for random forest clearly shows it to be a viable option for prediction.

Zhang, et al. [196], applied random forest for the prediction of the moisture content of biomass pellets in a fluidized bed dryer, using a total of 12 input data features. When the tuned model was applied to online prediction with a lab-scale unit, the relative error was +/- 13%, providing a prediction within 50ms of the online measurements being received. The authors state that this level of accuracy is acceptable for their application, and the model is thus viable for prediction. The rapid prediction time here of 50ms also

highlights another benefit of random forest, in that it can be used in conjunction with live input data to create real-time predictions of key parameters.

Elmaz, et al. [197] considered the use of random forest with proximate fuel analysis data to classify fuels into one of four types: coal, wood, agricultural residue, or manufactured biomass. Various models were used in addition to random forest, on close to 600 fuel data sets taken from the Phyllis2 [199] database. With random forest, a classification accuracy of about 90% was seen, which is a good level of accuracy. No model tuning was applied by the authors. Therefore, it is likely this could be further improved upon if the authors were to have used better model hyperparameters. This study by Elmaz, et al. [197] shows that random forest can be applied to reveal underlying compositional groupings in fuels, hence the ability of the model to classify fuels by type with good accuracy.

To the authors' knowledge, no published studies have applied the random forest algorithm to the study of large biomass fuel data sets from commercial biomass power stations. In thermal power generation a comprehensive understanding of the input fuel feedstock is essential to ensure optimal operation of the plant and to identify any potential challenges in advance [20, pp. 18-54]. Therefore, the ability to gain a deeper level of insight regarding biomass fuel feedstocks and their underlying relationships would be highly advantageous for commercial plant operators and lead to more efficient fuel use and operation and could lead to better mitigation of ash challenges such as agglomeration. The study of Elmaz, et al. [197] showed that random forest can be successfully applied to the "simple" problem of fuel identification. Therefore, it would be of interest to apply this technique to the challenge of a larger data set and the prediction of parameters within the fuel, e.g. quantities of a given contaminant. If successful, this would in turn reveal the underlying relationships within the fuel composition that feed into these predictions.

2.4.3 Modelling Summary

Thermochemical modelling software packages such as FactSage can be used to improve the understanding of the fundamental chemical behaviours at high temperatures, and for the prediction of potential melting and agglomeration issues. There are known shortcomings to the use of FactSage as a tool, particularly surrounding a lack of underlying experimental data for key biomass ash systems, but nonetheless FactSage

has shown value as a tool in several prior works for prediction of ash melting issues of relevance to agglomeration.

Machine learning approaches such as the random forest algorithm have shown promise in their predictive ability when applied to biomass fuel data sets and combustion scenarios, within the limited published works that exist at present. Therefore, it would be of interest to apply this technique to a large-scale industrial fuel data set, to determine what useful insight can be attained.

2.5 Chapter Summary

Sections 2.2.4, 2.3.13, and 2.4.3 provide more detailed summaries and suggestions for further work for each area examined within this review. The main findings from this review are as follows.

There is a wealth of mechanism research when combusting biomass on SiO_2-based bed materials, with agglomeration mechanisms being of the coating- or melt-induced variety. For coating agglomeration in the case of SiO_2-based bed materials, there is the common occurrence of two or three distinct particle layers, with a higher presence of potassium within the fuel causing the "inner-inner" third layer. Sufficient growth of the calcium-based "inner" layer appears to prevent further formation of K-silicate melts with the bed particle, and as the layer changes in composition further diffusion of calcium is limited. Melt-induced agglomeration is the result of sufficient silica and alkali metal content in the fuel forming an ash melt. In some cases, the ash skeleton shape of the particle appears to allow the formation of agglomerates similar in shape to that of the fuel particle. Further work is particularly needed into mechanisms when using alternate bed materials and additives, with consideration given to the effects on the whole boiler system.

Of the operating variables, fuel, bed material, additives, fluidizing gas velocity and temperature have the greatest effect on agglomeration severity. An overall ranking of parameters examined is given in Table 2.5. Most other variables have received some degree of attention, though may benefit from some deeper studies. Co-firing of dual-biomass blends, alternative bed materials, and use of additives stand out as areas where further work could add significant value and understanding to the field.

Thermochemical modelling of biomass ashes with software such as FactSage has been seen to be a useful tool to enhance knowledge and produce qualitative and quantitative predictions of biomass ash melting issues when used together with experimental methods. However, there is an implicit need for users to understand the shortcomings around use of FactSage, such as the chemical systems for which there is a known lack of accuracy, or the optimal ways to translate real observed phenomena into the theoretical chemical environment of FactSage. Machine learning approaches such as random forest have shown promise as a predictive approach when applied to biomass fuel studies across a limited number of published studies, however further work and application is required to determine their limits.

Chapter 3
Methodology

3.1 Introduction

This chapter begins by detailing the equipment and methods used to carry out the research activities performed in this thesis. This includes equipment specifications, methodologies, and a discussion of known shortcomings with the equipment and methods. Thermochemical modelling of biomass ash was performed with the software package FactSage. The generic approach taken to the use of this software is outlined in this chapter. Specific model parameters used for each FactSage simulation case are listed together with the discussion of results in Chapter 6. Data analytical and machine learning techniques used in the study of the Sembcorp Energy UK fuel data set in Chapter 7 are also described. These methods are principal component analysis and random forest regression. In the final section of this chapter, specification data is given for all the fuels, bed materials and additives that were used, along with a brief discussion of each.

3.2 Pilot-Scale Fluidized Bed Combustor

A pilot-scale bubbling fluidized bed combustor was used as the principal method of experimentation. This unit is located at the Low Carbon Combustion Centre (LCCC) in Beighton, Sheffield. A few years prior to this work, the unit underwent a significant number of modifications and a full re-commissioning, as described in the work of Chilton [137]. The unit is pictured in Figure 3.1, with Figure 3.2 and Figure 3.3 offering process flow diagrams of the combustor and gas analysis systems respectively.

Figure 3.1: Picture of the pilot-scale fluidized bed combustor used for experimental work.

3.2.1 Air Supply

Air for the fluidized bed is supplied via the forced draft "main fan" (see Figure 3.2). This fan provides air to five different streams:

- Process air – the main fluidizing air stream entering the bed.
- Under-bed air – used for under-bed gas burner combustion, with a continual air bleed to control the temperature of the under-bed gas burner when not in use.
- Over-bed air – used for over-bed gas burner combustion, with a continual air bleed to control the temperature of the over-bed gas burner when not in use.
- Sight-glass air – used to cool the sight glass.
- Blanketing air – used to prevent fuel combustion within the 5" continuous screw feeder housing.

A slight negative pressure was maintained in the combustion chamber during tests by the extraction fan located just after the cyclone. This was done to prevent the escape of pollutant gases such as carbon monoxide into the surrounding atmosphere. A secondary (uncontrolled) small extraction fan is positioned after this larger extraction fan and was left running when the fluidized bed combustor unit was not in use for continual gas extraction as a safety precaution.

3.2.2 Start-up Gas Burners

Two gas burners were used to heat the bed during start-up. The over-bed burner is located above the bed and is angled downwards to heat the top of the bed during start-up. The under-bed burner is below the unit, prior to the plenum, with the heated mixture of gas burner flue gas and process (fluidizing) air entering the bed via the bubble caps. In some tests, the over-bed burner was removed to minimise the air input above the bed. This also meant that the over-bed burner bleed air was no longer required.

3.2.3 Fuel Feeding

Three fuel hoppers were available, each with a variable feed-rate screw. These are connected to a continuous 5" screw that feeds fuel onto the bed surface. When a new fuel was used for the first time, the speed setting for the variable screw feeder connected to the hopper was calibrated to determine the mass flow rate of the fuel. To do this, a segment of the continuous 5" screw feeder housing was removed, and a collection vessel was placed under the opening. The fuel was fed at different screw speed settings for 20-30 minutes, and the collection vessel was weighed. This enabled the creation of a calibration curve of fuel mass flow rate against screw speed for the fuel, which was then used in experimentation.

One point of note regarding the continuous 5" screw is that it has a non-linear rate of fuel feeding. When calibrating the mass flow rates of fuels and observing fuel exiting the screw, it was apparent that there was a continual cycle of small quantities of fuel followed by an intermittent larger "slug" of fuel. This meant that over shorter time scales of 1-2 minutes, there was an observable variation in fuel feeding rate, which could be seen during tests in the form of a cycling/oscillating emissions graphs. For reporting purposes, emissions were averaged over time periods upwards of 15 minutes to negate this effect.
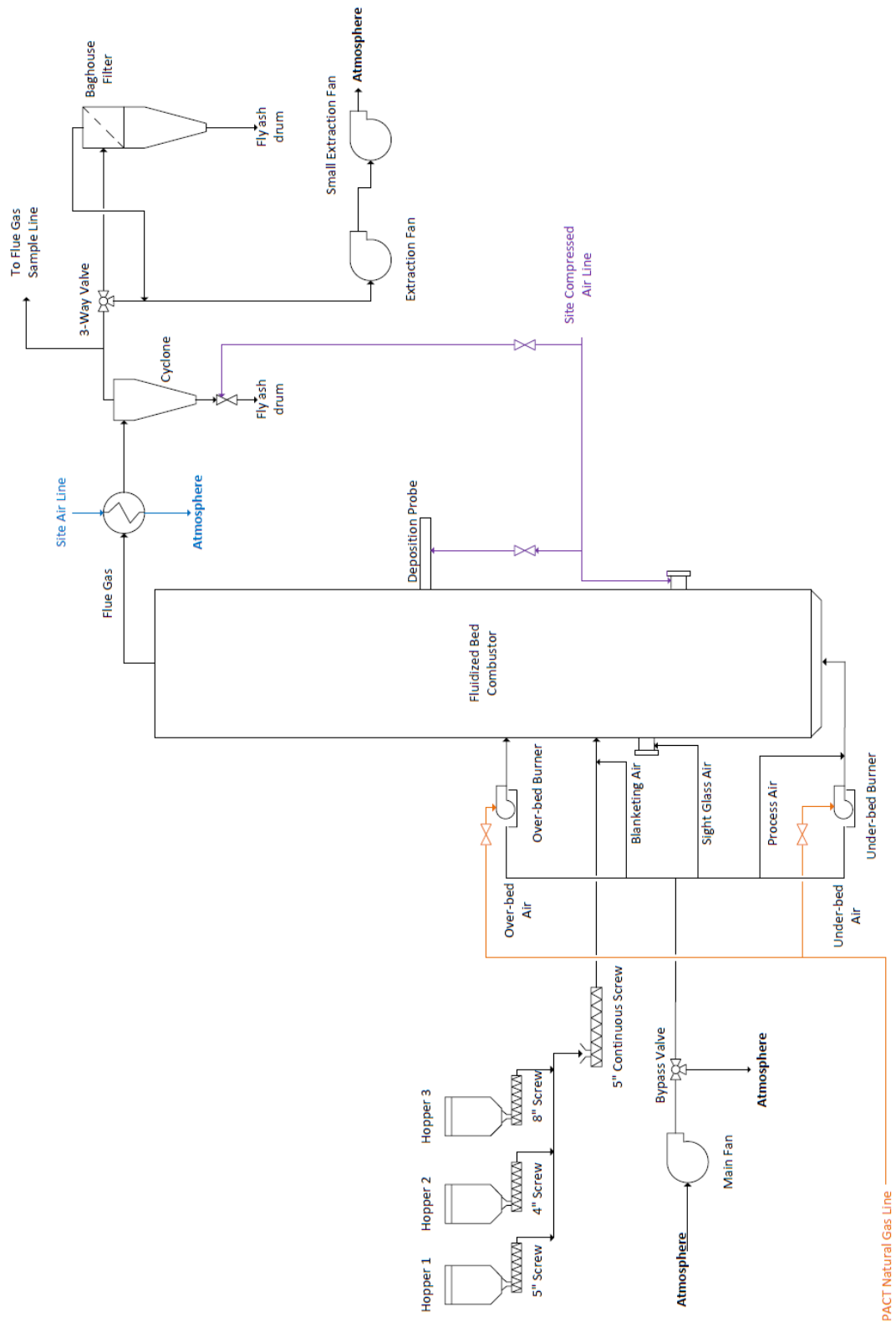
Figure 3.2: *Process flow diagram of the pilot-scale fluidized bed combustor.*
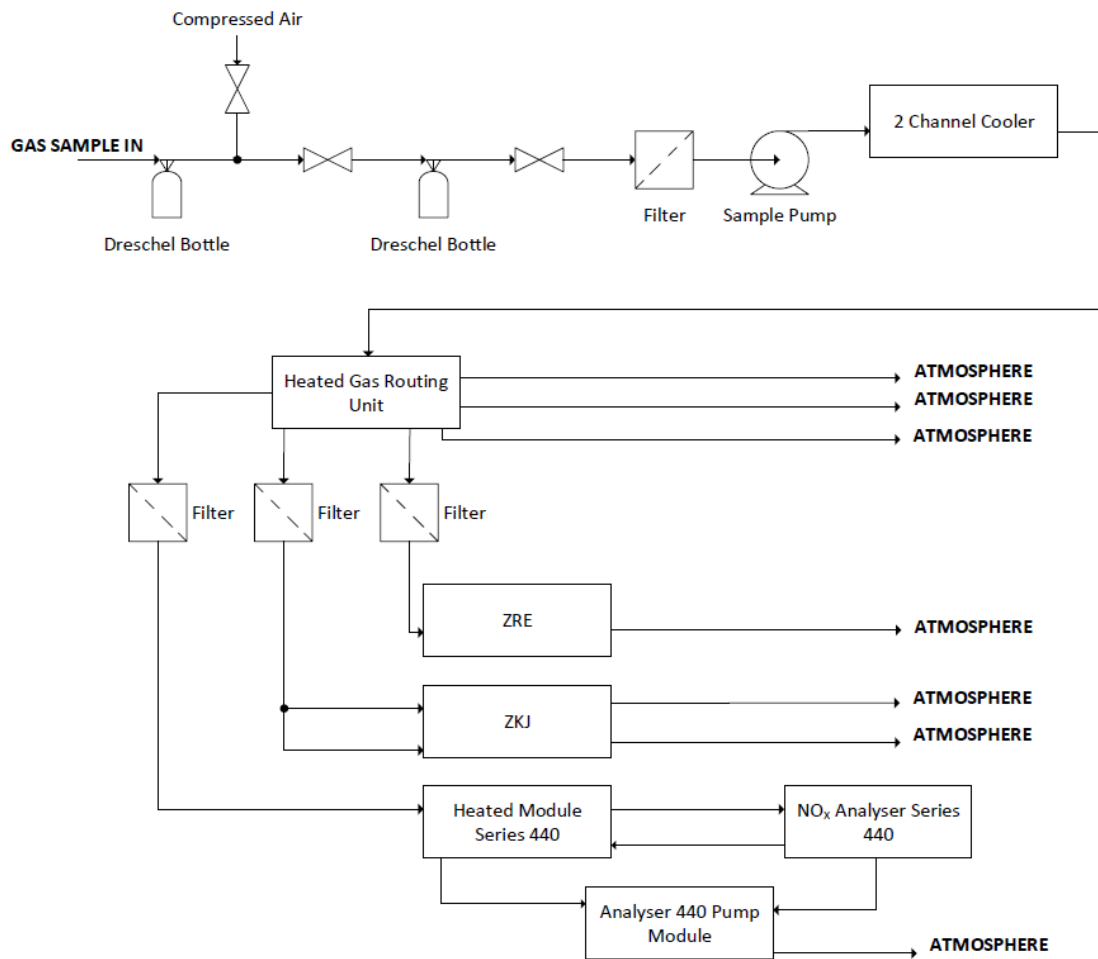
Figure 3.3: *Process flow diagram of the flue gas analysis system present on the pilot-scale fluidized bed combustor.*

3.2.4   Bubbling Fluidized Bed

The air distribution plate at the base of the bed has 30 evenly spaced bubble caps arranged in a square pitch. Air from the primary air and under-bed burner streams enters the bed through these bubble caps and fluidizes the bed. The combustion chamber is 0.39m wide by 0.35m long in the bed region. Bed heights of up to 0.4m were successfully fluidized, with a bed height of 0.24m found to be optimal from the perspective of minimizing start-up time and allowing for a well-mixed bed. A removable hatch door allowed for access to the bed for bed loading, sampling, and maintenance. A sight glass is present on the hatch door, with a second sight glass around 0.4m above it as part of the furnace structure. These sight glasses enabled observation of combustion and bed behaviour at the bed surface and in the region between the bed and screws feeder. Combustion occurred on the bed at a target temperature range of 800-900°C, with flue gases drawn upwards and out of the freeboard by the extraction fan (see section 3.2.1).

As mentioned, a bed height on 0.24m was found to be optimal for the rig, and this was used across most of the testing in Chapter 4-Chapter 5 unless specified otherwise. This bed height corresponded to a mass of 40kg of bed material for each test. In the additive test campaign of Chapter 5, the additive dosage used formed part of this total 40kg, with the balance to 40kg comprising of the sand bed material.

3.2.5 Flue Gas Cooling and Extraction

Flue gas exiting the freeboard first passes through an air-cooled heat exchanger, where it is cooled from around 400°C near the top of the freeboard to 150-200°C exiting the heat exchanger. Flue gas then enters a cyclone for fly ash removal, before being released to atmosphere. A bag-house filter is also present on the pilot-scale unit for optional use after the cyclone. However, it was not used during tests and was sealed off via a valve.

A sample line for flue gas analysis was inserted after the cyclone, to enable collection of flue gas with a minimum of particulate material. This sample line could be moved to other tapping points during tests when required, such as for verifying gas compositions upstream or in the freeboard. This sample line routed flue gas into the flue gas analysis system, discussed in the subsequent section 3.2.6. Fly ash was collected from the cyclone ash collection drum and stored.

3.2.6 Flue Gas Analysis

The flue gas analysis system is shown diagrammatically in Figure 3.3. Flue gas passes through two dreschel bottles packed with a glass wool fibre material for large particulate removal, before flowing through a micro-filter into the sample pump. The gas sample is driven through a cooler for moisture removal, and then enters a heater prior to analysis. At the heater, the sample is split into three streams, each of which passes through a micro-filter before entering one of:

- A Fuji Electric single beam non-dispersive infrared sensor (NDIR) gas analyser (ZRE), for measurement of NO (ppm), SO_2 (ppm), and CO_2 (vol.%) content [200].
- A Fuji Electric dual beam NDIR gas analyser (ZKJ), for measurement of SO_2 (vol.%), CO (ppm), and O_2 (vol.%) content [201].

- A Signal Group [202] Series 440 (Model 443) chemiluminescence NO_x analyser machine, for measurement of NO (ppm) or NO_x (ppm) content.

In the case of the NDIR analysers, infrared light is passed through the gas sample, and the absorption of different wavelengths of the infrared light is used to find the concentration of the different gaseous components [203]. For the NO_x analyser, NO reacts with ozone to produce NO_2, emitting visible and infrared light in amounts that correspond to NO concentration. For NO_2 detection, NO_2 is first converted to NO and then the same principle is applied [203]. All gas analysers were regularly calibrated by the operators with certified calibration gas cylinders supplied by BOC Ltd. As per the respective manufacturer documentation, the ZRE and ZKJ analysers have a repeatability value of ±0.5%, whilst the NO_x analyser has a repeatability value of ±1%.

A compressed air line connection was also present at the start of the flue gas analysis loop. This was used during tests to backflush any accumulated moisture or particulate material in the sample line to prevent blockages.

3.2.7 Pressure Measurements

Several static pressure measurement probes and transmitters are located on the fluidized bed combustor. These enabled measurement of

- Pressure above and below the bed, and differential pressure across the bed.
- Pressures in the plenum and freeboard sections of the unit.

3.2.8 Temperature Measurements

Numerous thermocouples are located throughout the unit to enable detailed temperature monitoring. These include:

- Seven thermocouples located along the vertical axis of the bed and above-bed region.
- Various other thermocouples located through the freeboard, heat exchanger, cyclone, fuel feeding, and air supply systems.

3.2.9 Deposition Probe

The pilot-scale unit has an air-cooled deposition/corrosion probe fitted in the freeboard, approximately 1.45m above the air distribution plate, and 0.6m above the fuel feeding screw. Four coated metal coupons were fitted to the probe by screws, as seen in Figure

3.4, to determine the effects of flue gases on different anti-corrosive metal coatings. The materials on these coupons are listed in section 3.8.4. The probe was inserted into the boiler such that the four metal coupons faced upwards and were on the leeward side of the probe in relation to flue gas flow in the freeboard. The probe was used for consecutive tests at identical operating conditions, to amass a total run-time with the probe inserted of around 50 hours.

Figure 3.4: *Air-cooled deposition probe fitted in the pilot-scale unit. Note the four coupon locations on the probe – these are on the leeward side of the probe when inserted into the FBC unit. Details on coupon composition is given in section 3.8.4.*

3.2.10   Data Logging

Temperature, pressure, and emissions data were recorded using a bespoke process monitoring program created in National Instruments LabVIEW (Figure 3.5). This presented live numerical and graphical readouts of process data, allowed for recording time-stamped comments, activated safety alarms as necessary, and saved data to a spreadsheet file for later analysis. It should be noted that no process control changes could be made using this program, with all operating changes made using manual valves and switches.
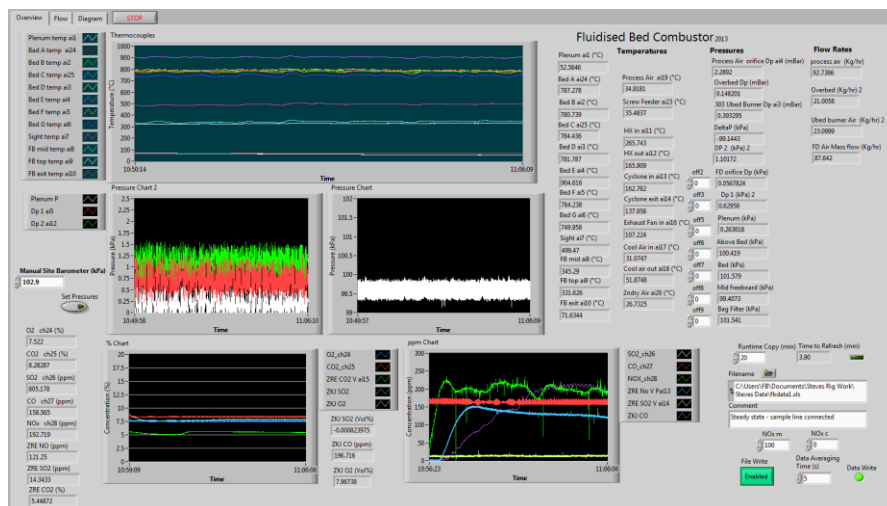
Figure 3.5: *LabVIEW monitoring program used during pilot-scale tests.*

3.2.11   Key Design Differences Versus Commercial BFB

The pilot-scale FBC unit has several key design differences versus a typical commercial BFB boiler design. These design differences must be understood to better contextualise results in comparison to a commercial BFB boiler.

The first of these is the lack of secondary and tertiary air inputs into the freeboard. Within a commercial boiler, air staging is employed to control air availability and temperatures in the boiler for emissions and combustion management, with air staging usually resulting in 40-60% of air being injected above the bed [11, 204]. Consequently, the combustion of volatiles, which can often comprise upwards of 70% of biomass fuels [42, 44], is driven into the freeboard region, allowing for more direct heat transfer with the water filled wall tubes of the boiler [205, 206]. Air staging also helps to mitigate NO_x formation via fuel and thermal mechanisms in commercial boilers. The freeboard in commercial BFB boilers typically has temperatures in the 1000-1200°C range, below the range at which thermal NO_x formation becomes a significant concern [207, 208]. Within the pilot-scale unit, whilst a low level of above-bed combustion may occur due to the sight-glass, blanketing, and over-bed burner bleed air inputs, it is not intended by design. As a result, most combustion within the unit will occur in the bed or directly above the bed surface. This fact was frequently observed during tests as a flame that extended from the bed surface (typically 0.2-0.3m above the base of the air distribution plate) to the height of the fuel feeder screw (0.85m above the base of air distribution plate), but little further. Lower temperatures of 250-500°C were seen in the freeboard. Limiting the flame height to that of the screw feeder by manipulating air and fuel flow rates is also due to safety concerns. This was done to reduce the risk of a fire in the screw feeder line, therefore is an unavoidable limitation of the rig that enforced hard limits to the operational envelope.

Closely related to the issue of secondary/tertiary air inputs is the topic of combustion excess air ratio. Overall boiler excess air figures within commercial boilers, whilst rarely quoted in literature, fall within the 20-40% range [11]. Within the pilot scale unit, values of 60-90% were more typical. These higher values were used for several reasons. The first is temperature control, as all combustion occurred within the bed, but it was still desired to match a typical commercial boiler bed temperature of 800-900°C. The pelletized fuels used (discussed later in section 3.6) had much lower moisture contents (15-25%) than what would be expected from a typical "fresh" chipped wood source for

example (35-50wt.%) [44]. This lower moisture content further increased temperatures. Furthermore, lower fuel flow rates were used to control bed temperatures, but this subsequently meant that when operating at 2-3U/U_{mf} to create a bubbling fluidization regime, the overall excess air ratio for combustion was in the 60-90% range. Increasing the fluidization ratio to a higher rate (e.g. 5-7) caused low temperature issues due to fuel input limitations. A wetter fuel feed may allow for better control of bed temperatures and a higher net input of combustible material thus driving down the over excess air ratio. However, there was difficulty in feeding wetter fuel sources without causing blockages in the fuel feeding system.

The net effects of the lack of air staging and higher excess air ratios on results, in comparison to a commercial boiler, would be the following:

- Volatiles combustion occurs in the above-bed region instead of the freeboard, so may have some effect on bed behaviours (agglomeration).
- Emissions are more dilute due to greater excess air, though they are normalized to 6vol.% O_2 during analysis.
- Pollutant profile up the freeboard would greatly differ to that of a commercial boiler due to different combustion and temperature profile. However, emissions are only analysed from a sample point downstream of the freeboard.
- Reduced temperature in the freeboard due to a lack of air staging and freeboard combustion may affect slagging and corrosion behaviours in the freeboard. This is of particular importance for use of the deposition/corrosion probe (section 3.2.9).
- In a commercial boiler, air availability is more limited in the bed due to air staging, whilst the freeboard zone provides areas of 1000-1200°C, allowing for different gaseous reactions to occur. In the pilot-scale BFB unit, combustion reactions in the gas phase would mostly occur in the bed and above-bed region at 800-900°C.

A further difference related to air input is the lack of air pre-heating. In commercial boilers, incoming fluidizing and over-fire air streams are pre-heated to 200-400°C through heat exchangers in the boiler back-pass, recovering heat from exiting flue gas [21, pp. 211-215]. In the pilot-scale BFB unit however, air is fed directly into the combustion chamber at temperatures slightly above atmospheric values (due to the main

fan leading to minor heating of the fluidizing air to ~25-40°C). During start-up, use of the under-bed gas burner increased the plenum temperature to around 900°C, which would pre-heat incoming fluidizing air, however this cooled down over time to around 50°C once the under-bed burner was switched off. Therefore, through the bulk of the test period on biomass fuels, fluidizing air was heated on entry to and contact with the bed, leading to a cooler lower bed zone than what might be expected in a commercial BFB boiler. As was observed through testing, this was never an issue that prevented effective combustion in the bed. However, it may have had a slight quenching effect on any molten ash or agglomerates in very close proximity bubble caps, preventing the development of larger agglomerates.

A final notable difference of the pilot-scale unit compared to a commercial BFB boiler is the lack of bottom ash screws for bed/ash removal and bed replenishment [209]. This means that during pilot-scale tests, the ash inventory in the bed will continually increase until it is sufficient to enable complete defluidization of the bed. Others have evaluated this difference in the literature (as discussed in Chapter 2 section 2.3.12), and found that initial agglomeration mechanisms are the same regardless of the presence/use of bed removal capabilities, though there are differences over longer time-spans (several days) [110].

3.3   Pilot-Scale FBC Unit Experimental Procedures

3.3.1   Start-up Procedure and Control Philosophy

A simplified start-up procedure for the pilot-scale fluidized bed combustor is as follows:

- Before operation, ensure analyser units, pressure sensors, and filters are clean and correctly calibrated. Also, ensure that fuel feeding screws are calibrated, hoppers sufficiently filled with fuel, and that bed material has been filled to the correct height and specification.
- Turn on gas analysers, compressed air supply, and the LabVIEW monitoring program.
- Turn on the heat exchanger fan, and the main and extraction fans.
- Open gas supply valves and turn on the over-bed burner (if fitted).
- Once a steady over-bed burner flame has been achieved, turn on the under-bed burner. Increase air flows to the over-bed and the under-bed burners to increase rate of heating as required.

- Increment process air until bed is fluidized.

- Once bed temperatures are sufficient (upwards of 700°C) and bed fluidized, turn off the over-bed burner and begin fuel feeding.

- Once steady fuel feeding is achieved, turn off the under-bed burner.

After switching to biomass fuel, the operator modulates air and fuel flow rates to match those that are required for the test. Generally, these conditions are chosen before the test as they will achieve a well-fluidized bed with steady pressure, temperature, and emissions behaviours. Tests were typically run until the bed defluidized or the end of the test day was reached.

3.3.2   Data Analysis and Reporting

Process data from pilot-scale experimentation underwent further analysis after each test to generate plots of temperature, pressure, and emissions behaviour, and to identify any trends or behaviours of interest. This data was then subsequently compared between different tests and operating conditions.

Temperature, pressure, and emissions data is reported in Chapter 4 and Chapter 5 on an average basis for various test cases. For test cases that achieved a steady state of combustion, a 15-30 minute window of data at this steady state was used to calculate the average value which was thus reported. Care was taken to ensure no operational changes were included within this averaging window (e.g. cleaning/replacing analyser filters). For tests which ran for shorter operational times (e.g. under ~30 minutes) where a steady state of combustion was not achieved, the final 5 minutes of data leading to bed defluidization was excluded, with the 10-15 minutes of data preceding this excluded data then used to generate an average value which was thus reported.

Defluidization time data is also reported in Chapter 4 and Chapter 5. Defluidization time in this thesis is defined as the time from the initial feeding of biomass fuel to the point at which bed defluidization was recorded. Experimental notes and observations were cross compared with temperature, pressure, and emissions data to ensure the accurate determination of the point at which the bed defluidized in each test. Defluidization time is reported to the nearest minute.

3.3.3   Sample Retrieval

After each experiment, the hatch door to the bed was removed and the bed was photographed in an undisturbed state. Bed material and agglomerate samples were taken in a methodical manner. The bed was divided into seven lateral zones (A-G) across the "mid" and "upper" regions, and one lateral zone in the "lower" region, for a total of 15 discrete bed zones as shown in Figure 3.6.

Samples were taken from each bed zone, so that during analysis spatial variations in composition or structure could be identified. Samples were retrieved using a metal spatula and stored in a clean collection jar, to prevent contamination. A mixture of types of samples were taken after each experiment, e.g. loose bed particles, agglomerates of varying sizes, and partially combusted fuel particles. This allowed for a broader analysis of different agglomerate types. Qualitative notes of any differences in bed conditions by zone were made during bed collection as appropriate.

Fly ash samples were also collected from the cyclone fly ash collection drum after each test.
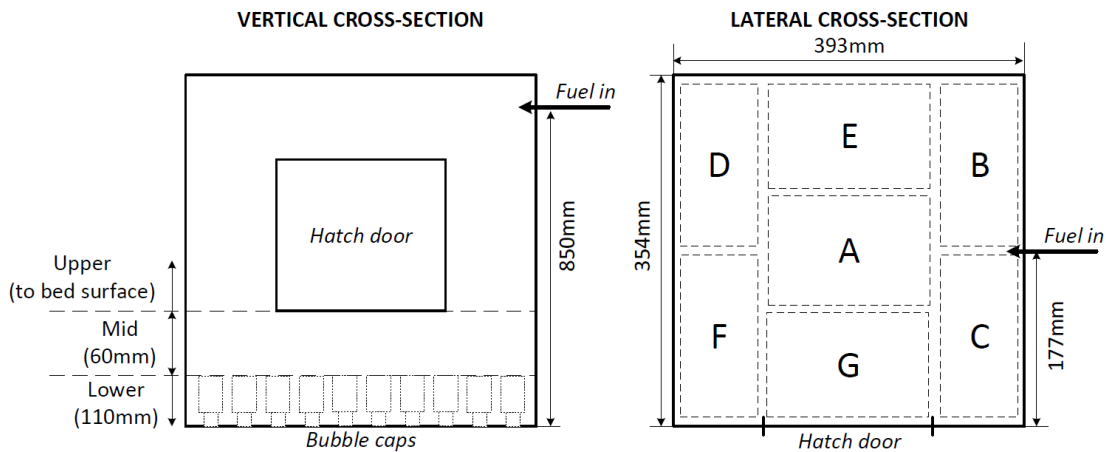
Figure 3.6: *Diagram showing how the bed was divided into different lateral and vertical zones for sampling.*

3.4 SEM/EDX Analysis

3.4.1 Sample Preparation

Prior to analysis via scanning electron microscopy with energy dispersive X-ray spectroscopy (SEM/EDX), agglomerate samples underwent an extensive preparation process. Samples were selected for analysis based upon the need to create a broad set of sample data across all conditions tested, or if a sample was noted to be of special interest during bed retrieval.

The first stage of sample preparation was mounting in a 1.25" cup using a Buehler EpoThin resin and hardener mixture [210], which was mixed according to the manufacturer specification. In the case of larger samples that did not fit the sample cup, some were carefully broken apart so that only the feature of interest remained. In other cases, a larger sample cup was used for this initial mounting stage, with the subsequent cross-sectioning step then used to isolate and extract the feature of interest. After allowing 24 hours for the resin to harden, the solid samples were removed.

The mounted agglomerate samples were then cross sectioned along their broadest section or through a feature of interest to expose a face for SEM/EDX analysis. Cross-sectioning was performed on a Struers Secotom 50 cutting and sectioning machine [211], using a diamond edged cutting wheel suitable for sand-type materials. Figure 3.7a shows an example of a sample after this stage.
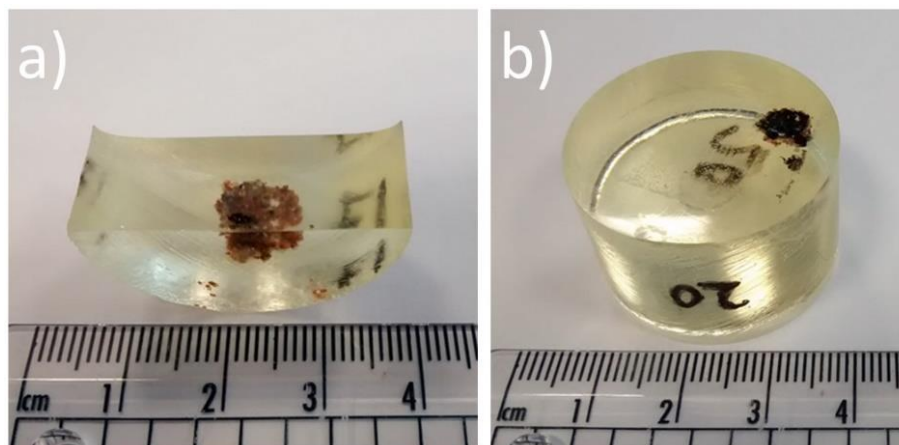
Figure 3.7: Agglomerate samples undergoing preparation for SEM/EDX. a) Resin-mounted sample after cross-sectioning. b) Sample after cross-sectioning, re-mounting and polishing.

After cross sectioning, the samples were washed with water and isopropyl alcohol, dried, then mounted once more in a 1.25" sample cup using the Buehler EpoThin resin mixture. This was to ensure that they were the correct size for later use in a Buehler

Automet 250 Pro grinding and polishing machine [212]. Samples underwent three grinding stages from a coarse to a fine grinding paper, followed by two polishing stages (3µm followed by 1µm polishing pads) to attain a mirror finish on the sample face. An example of a polished sample is shown in Figure 3.7b.

Finally, the polished samples had a strip of silver paint applied across the resin mount, or a coating of carbon paint across the mounted sample, to ensure conductivity in the SEM machine. The sample face was then carbon coated using an Edwards High Vacuum "Speedivac" [213] carbon coating machine, or a Quorum Q150 carbon coater [214]. This coating process was performed on four samples at a time to ensure that each sample received a suitably thick carbon layering for good quality SEM/EDX imaging. Carbon coating was used to prevent sample charging, as the samples are non-conductive. It was selected over other forms of coating (e.g. gold) as it is a light element with no peak overlap against other elements [215, pp. 647-673], which aids in the accurate identification of elements during EDX analysis.

At this point, the samples were ready to undergo SEM/EDX analysis. Samples were stored in sealed containers throughout the preparation process, to prevent contamination or damage to the sample surface.

3.4.2 SEM/EDX Analysis

SEM/EDX was performed on samples for structural imaging, and qualitative and standardless ("semi-quantitative") quantitative composition analysis. The work of Goldstein, et al. [215] provides a detailed explanation of the fundamentals of SEM/EDX theory, operation, and analysis. In SEM, a high energy electron gun is fired at a sample under a vacuum. The electrons from the beam can meaningfully interact in one of two ways. The first of these is that the beam electrons undergo elastic scattering and lose energy, escaping the sample, in what is termed backscattering. The size of the atoms that are struck by the beam electrons that give rise to backscattering determines the energy loss of the electrons. Therefore, by detecting only backscatter electrons it is possible to visualise both composition changes (e.g. between two metals) and changes to the specimen topography. The second possible meaningful interaction with beam electrons is that the specimen electrons are knocked out of the sample in an inelastic collision, and gain energy. These exiting specimen electrons are termed secondary electrons. As these secondary electrons do not gain much energy relative to their

original state, secondary electron detectors are only used for imaging of sample topography. EDX analysis relies upon the interaction of the beam electrons with specimen atoms [215, pp. 271-295]. When specimen electrons are knocked off their shell by a beam electron, there is a change in energy states of the atom. As electrons in the specimen move down to the next respective shell following the loss of an electron, there is the release of energy in the form of a characteristic X-ray. This characteristic X-ray is unique to the element; hence the element can be identified. The resultant peak intensities are then used together with the manufacturer fitted standard results by the analysis software to quantify the amount of an element present [215, pp. 427-436].

To obtain good quality imaging and composition data, it is integral, particularly for EDX, that the sample is both a polished flat surface and is coated. This is therefore the reasoning for the extensive sample preparation method outlined in section 3.4.1. Whilst the electron beam only has a penetration depth of a few microns into the sample [215, pp. 65-67], the presence of a rough or uneven sample surface would lead to far more complicated electron interactions with the sample. In early trials with small "whole" agglomerates mounted directly onto a sticky carbon tape, it was difficult to attain even a good carbon coating on the sample to prevent charging during imaging. In such a situation, any effective chemical analysis via EDX was found to be extremely challenging, hence all samples undergoing the extensive preparation process (section 3.4.1).

As agglomerate samples were cross sectioned through the broadest part of their structure or through a feature of interest, SEM/EDX analysis involved examining all areas of this cross-sectional face to find any important indicators of mechanisms or behaviours. These locations were then imaged at several levels of magnification, and an EDX analysis of their composition was performed. For quantitative EDX analysis, upwards of four locations of interest were chosen per mounted sample (e.g. ash coating layers, ash deposit on a particle, ash join between particles). Quantitative EDX point or area analysis was then performed at upwards of three areas of each of these locations of interest, meaning that a minimum of 12 data points were taken from each sample. These numbers were minimums, with the vast majority of samples undergoing far more EDX analysis than this. Data was then averaged where appropriate, for the determination and discussion of mechanisms and trends. At some EDX sites, line or mapping analyses were also performed if thought to add further value. This comprehensive approach of

taking numerous measurements per sample, then using average values in analysis, was done to mitigate the otherwise inherent inaccuracy of standardless EDX analysis. On a single element or single measurement basis, this can be up to 15wt.% [215, pp. 427-436] depending on the instrument and software used, hence approach of collecting large amounts of data the utilising the average value for analysis and discussion. This comprehensive approach of using averaged standardless EDX data from numerous locations has been commonly used in prior agglomeration studies in the literature such as by He, et al. [119, 216] and Grimm, et al. [114]. In addition, due to the nature of the project, EDX analysis was conducted in many sessions across four years, over which period machines underwent regular calibration and maintenance regimes by university technicians and manufacturer technicians as per their service intervals. Therefore, any sudden significant changes in data outputs over time would have been identified and handled when collating data for analysis.

The SEM/EDX work was performed using either an FEI Inspect 50 SEM fitted with an Oxford Instruments X-Max EDX, or a ZEISS Evo MA-15 SEM with an Oxford Instruments X-Max EDX probe. Across both microscopes, beam energy was set to 20kV except in very rare cases (e.g. a localised region of a sample was charging, and the beam energy needed to be reduced). This 20kV beam energy was needed to ensure sufficient characteristic X-ray emissions for EDX. The working distance of the microscope was generally 9-11mm depending on the sample.

3.5 XRD Analysis

3.5.1 Sample Preparation

Prior to XRD analysis, samples were ground to a fine powder. This was done to ensure that there were sufficient crystallites in the sample to enable a high degree of sample diffraction, and that the powdered sample would form a flat surface in the sample holder, preventing any specimen height displacement or roughness errors [217, pp. 287-300]. The samples were hand ground using a mortar and pestle until the powder felt smooth in a sample bag. This approach was applied to a representative set of agglomerates for a given test, e.g. several pellet shaped agglomerates and ball shaped agglomerates of mixed sizes, producing around 5-10g of powder which was sufficient for analysis. The powder was then placed into a clean, back-loaded sample holder. A back-loaded sample holder was standard for the machine used, and minimises the risk

of contamination of the sample face, ensures a level sample face to prevent specimen height displacement error, and reduces the likelihood of preferred orientation error that might otherwise arise if compacting or levelling the analysis face of the sample [217, pp. 290-295].

3.5.2 XRD Analysis

Qualitative X-ray diffraction (XRD) analysis was performed to determine crystalline phases in agglomerate samples. XRD theory is discussed extensively by Pecharsky & Zavalij [217]. Electrons are fired at a metal target to generate characteristic X-rays. When these X-rays strike a sample, they interact with the sample electrons. This interaction is not enough for the electron to be knocked off the atom, with either coherent (elastic) or incoherent (inelastic) scattering of X-rays instead occurring. In incoherent scattering, the X-rays exiting the sample have a different wavelength to those entering the sample and no phase relationship, leading to destructive interference occurring. In coherent scattering, these scattered X-rays are of the same wavelength as those entering the sample and are detected by the X-ray detector and registered as a peak or spike in X-ray intensity. Different compounds diffract at different angles and to different intensities, with each compound having a characteristic diffraction pattern. The diffractometer moves through a given range of angles when analysing a sample to record the occurrence of different peaks in X-ray intensity. The result, a sample diffraction pattern, is then compared against diffraction pattern databases to identify the crystalline compounds present within the sample.

Samples were analysed in a PANalytical X'Pert[3] Powder [218]. This machine used copper K-α radiation for X-ray generation (X-ray wavelength of 1.5406Å), with a 45kV voltage and 40mA amperes, both of which are standard for diffractometers using copper K-α radiation. For analysis, the machine was operated in powder reflection mode, with a 10-80° 2θ start-end angle, a 1° programmable divergence slit, a 2° anti-scatter slit, a 0.0131° step size, and a 0.0445°/s scan speed. Scanning was performed in continuous mode, with sample rotation of 8/s. These settings were found to give the optimal combination of scanning time and signal-to-noise ratio, with peaks easily identifiable for phase identification purposes. The machine underwent regular calibration and maintenance by university technicians and manufacturer technicians as per its' service intervals.

Phases in the resultant diffraction patterns were identified with the International Centre for Diffraction Data (ICDD) PDF-4+ database and the ICDD SIeve+ software tool [219]. In this identification process, all possible peaks were first marked, with the software then evaluating possible matches. Phases were identified until all peaks were identified, or until the remaining peaks were only suggested to be the result of compounds that are unlikely to not be of importance for agglomeration or ash melting behaviours. It was seen in both in the literature review (Chapter 2 section 2.2) and in SEM/EDX studies in this thesis that ash-agglomerate formations were typically comprised of K, Na, Si, O, Ca, Al, Mg, and P, and these elements would be expected to form compounds such as silicates, sulphates or phosphates.

3.6   FactSage

An introduction to the underlying theory behind FactSage and its strengths and weaknesses in relation to biomass ash modelling was given in Chapter 2 section 2.4. The FactSage "Equilib" module was used for the modelling work in this thesis. This module calculates the most likely system to form at equilibrium for a given set of input conditions (component composition/mass, temperature, pressure). The module can simulate the change in system stepwise over a user defined range of temperatures or pressures. The generic modelling approach to use of Equilib, applicable to all cases, was as follows:

- Database selection.
- Input of reactant data (e.g. fuel, air/flue gas, bed material, etc.).
- Methodical selection & testing of solutions from each database.
- Simulation of the final case, and retrieval of data set.

The above four stages are discussed in the following subsections. Specific case details (e.g. solutions enabled, issues encountered) are discussed in Chapter 6.

3.6.1   Database Selection

For all cases, the FactPS, FToxid, FTsalt and FTpulp databases were enabled. FactPS is the pure substance database. FToxid is the oxide database, for metal oxides and slags. FTsalt covers pure salts and salt solutions. FTpulp is targeted for the pulp and paper industry, as well as combustion and corrosion applications. These databases are the only ones of direct importance for biomass ash modelling in FactSage. Each database

contains a range of user-selectable solutions, with each solution containing numerous compounds which can be disabled if deemed irrelevant. Solution selection is discussed in section 3.6.3.

3.6.2 Input of Reactant Data

All available composition data for a given fuel ash was entered into FactSage as a starting point, along with a quantity of chlorine typical for the fuel. This chlorine value was taken from an average of fuel data in the ECN Phyllis2 biomass database [199]. An analysis of the chlorine content of the fuels used in experimental testing was not available for the modelling work, but chlorine is known to play a key role in alkali metal reactions in the gas phase [220], hence it was important that a quantity was included within the model.
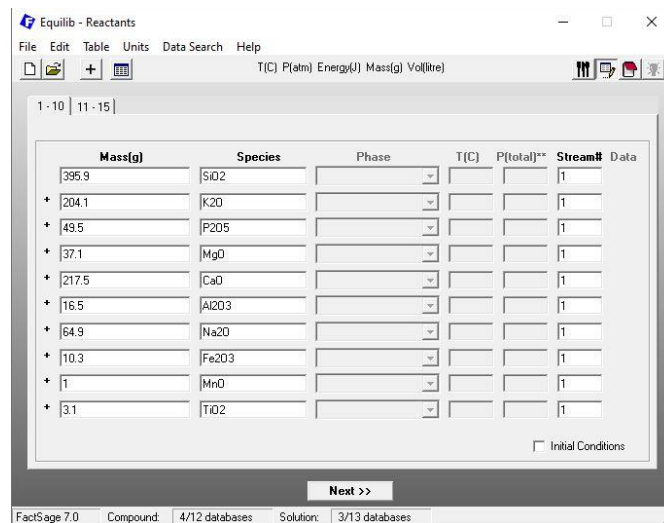
Figure 3.8: Reactant data entry screen in the Equilib module of FactSage.

The lack of chlorine data specific to the fuels modelled here will impact the model results for each fuel, as it is known that chlorine contents can vary by fuel source, season, and rainfall, with some research consequently suggesting that water washing biomass is beneficial to reduce chlorine contents [139]. Whilst it would be ideal to use chlorine data for these specific fuels, upwards of 30 data sets from Phyllis2 were used to create the average chlorine value for each fuel. This large number of data sets would act to somewhat mitigate the general variability of chlorine data. This data is listed in Appendix C, and is discussed where relevant in Chapter 6. It is also worth noting that the focus of the study was on ash melting and the influence of this on agglomeration severity, whereas chlorine content is more important for corrosion behaviours [81]

which were not the focus here. Dependent on the case to be modelled, masses of air, flue gas, or additives were also included. An example of the reactant data entry screen is shown in Figure 3.8.

3.6.3 Solution Selection

A methodical approach was taken to determine which database solutions to enable for a given model case. Documentation for each database and their respective solutions was first consulted to determine which solutions contained compounds of interest for ash melting or agglomeration behaviour. All solution phases of interest were enabled, and a simple simulation case performed with a 100°C temperature stepping over a 500-1500°C range. An example of the solution selection and case setup window is shown in Figure 3.9. Any solutions that produced a "0g" maximum mass over this temperature range were deselected, as they did not result in the formation of a compound at any temperature. For some models, this process had to be repeated several times due to limits on the maximum number of concurrently enabled FactSage database solutions, and the fact that some solutions conflicted with others, therefore an assessment had to be made as to which was the more useful. The entirety of this process was repeated for each simulation case (i.e. each fuel plus air combination, each additive dosage). This ensured that all solutions of importance were enabled for each case. This was important because, for example, a higher additive dosage would change the expected stable solid phases and slag quantities. This can be visualised by plotting an example liquidus projection ternary phase diagram (e.g. K_2O-CaO-SiO_2) and observing how increases to one component shifts the relative location of the input chemical system and the stable solid phases that would form.

The FToxid-SLAGA solution was the only solution that was always enabled, with other FToxid slag solutions (e.g. SLAGB, SLAG?), and the FTsalt-SALT and FTpulp-MELT solutions disabled. These slag, salt, and melt solutions rely on similar components and caused convergence issues when enabled together. More importantly, FToxid-SLAGA is the only solution to include all critical ash components from the perspective of agglomeration (i.e. K, Na, Ca, P, Si) whereas the other solutions lacked one or more of these, therefore they would not consider these components as part of melt formation. Whilst it is possible to selectively disable conflicting elements of the SLAG, SALT, and MELT solutions to allow them to work in unison, it was deemed an unnecessary additional level of complexity. Some simple trials were performed with both SLAG and

SALT enabled together successful, but there was not an appreciable, verifiable, improvement in output data.
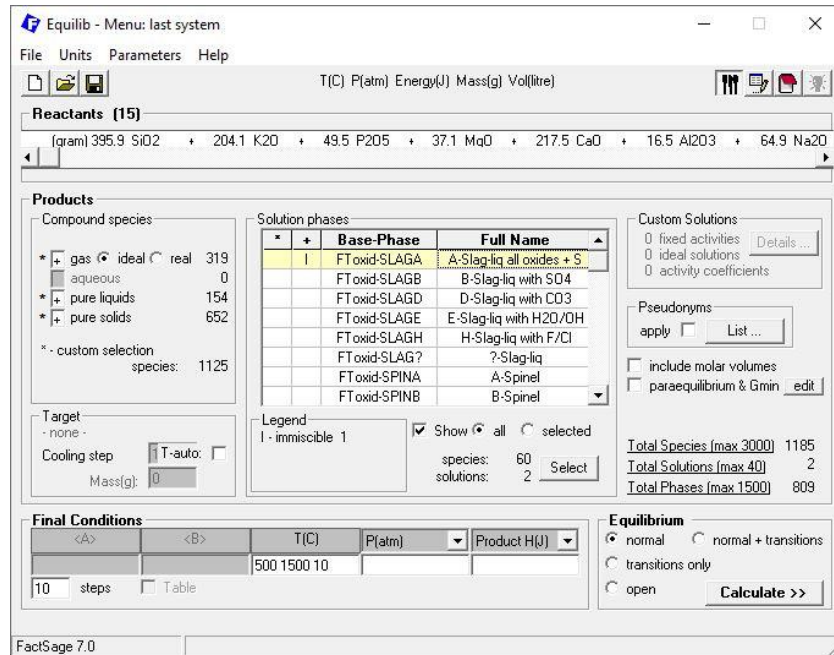
Figure 3.9: *Example of the solution selection and setup screen in the Equilib module of FactSage.*

3.6.4   Simulation

With the solutions selected and tested, the final stage was to run the case with a smaller temperature stepping to collect the data set for use in analysis. After testing multiple different temperature step sizes, a 10°C step was used for producing the final data for each case, as this provided the best balance between quality and continuity of data, and simulation run time. Final case run times varied between 30 minutes to upwards of 6 hours on a standard desktop computer (Intel Core i5-6600, 8gb RAM). The temperature range for each case was maintained at 500-1500°C. BFB boilers typically operate with bed temperatures between 800-900°C, with some potential to go out of this envelope to the mid-high 700°C or low-mid 900°C range, e.g. in the event of localised bed issues. Covering this larger temperature range in simulations gave a view of the full picture of ash behaviours and allowed for identification of any simulation abnormalities that may call into question the accuracy of the model. Final analysis and discussion of the data in Chapter 6 then generally focused on a narrower temperature range similar to that of the bed (e.g. 750-950°C).

Once the case simulation finished, data was first viewed using the built-in FactSage graphing tools to check for any immediate issues. If deemed acceptable, it was exported

to Excel for analysis. In the event of issues when running the final case simulation, a troubleshooting process began. The low-high bounds of the temperature range were narrowed by 100°C at a time, and the temperature step size was increased (e.g. to 25°C or 50°C). Step size and temperature range were then methodically adjusted to find the temperature point at which the simulation was failing. Once found, the final case was again run with a 10°C step, but with the simulation temperature range set to avoid this problematic temperature point. In some cases, it was necessary to revisit the solution selection process if a specific solution was causing conflicts at a lower temperature step size.

3.7 Fuel Study Data Analysis Approaches

In Chapter 7 a large fuel data set provided by Sembcorp Energy UK from their Wilton 10 biomass fluidized bed power station is analysed, with the objective of analysing key contaminants and evaluating the ability to expand the fuel envelope. Two advanced analytical approaches, principal component analysis (PCA) and random forest regression, were applied to this data set.

3.7.1 Principal Component Analysis

PCA is a widely used dimensional reduction technique that reduces a data set comprising of many variables to a handful of principal components (PCs) [221]. These PCs can then be used as a new set of variables for further analysis, or if meaningful, may be interpreted to describe a phenomenon or grouping in the data [221, pp. 63-64]. For example, rainfall readings at meteorological stations A, B, and C in city X can instead be reduced to "PC1" which describes rainfall in city X. A script was written in MATLAB R2019b [222] to manipulate the fuel data set into a useable form, apply the MATLAB pca() function [223], and plot the results. The MATLAB code is presented in Appendix I.

The seven variables of greatest importance from the fuel data were analysed: Ash content (wt.%), weighted average particle size (mm), and Cl, Pb, Zn, Na, and K content (mg/kg). Outliers were removed from this seven-variable group, leaving 2786 data sets from a starting amount of 3823. The reduction bounds used for outlier removal are shown in Table 3.1. Where a data point was removed for being an outlier, the entire data set for that time stamp was removed. Weighted average particle size was calculated by taking the mid-point of the particle size grades to calculate a weighted average. As part

of the MATLAB script, data was normalized on a 0-1 scale due to the use of different units between the variables. This is necessary to prevent any unintentional component bias in PCA when working across units and scales.

Table 3.1: *Maximum and minimum values for the fuel data set subject to PCA analysis, before and after the removal of outliers.*

Variable	Original data set		Refined data set	
	Minimum	**Maximum**	**Minimum**	**Maximum**
Ash (wt.%)	0.15	26.42	0.5	10
Cl (mg/kg)	0.1	20839	100	2500
Pb (mg/kg)	0.111	2473	10	300
Zn (mg/kg)	1.434	8652	15	500
Na (mg/kg)	0	3112.5	10	1300
K (mg/kg)	7.754	14866	200	2500
Particle size: >80mm (%)	0	82.83	*0**	*40.05**
Particle size: 50-80mm (%)	0	38.37	*0**	*38.37**
Particle size: 5-50mm (%)	7.55	98.60	*7.55**	*97.97**
Particle size: <5mm (%)	1.34	73.34	*2.5**	*73.45**

* A maximum/minimum cut-off was not used for particle size. These were the respective maximum and minimum values remaining after refining data for the other six variables.

3.7.2 Random Forest Fuel Data Modelling

3.7.2.1 Model Configuration, Creation, and Validation

The random forest regression machine learning algorithm was used with the large fuel set in Chapter 7. The underlying theory behind random forest is discussed in Chapter 2 section 2.4.2, with this section providing an overview of how the model was implemented in this work and the key model settings used across all cases.

The script implementing random forest was written in Python 3.8.5, using the Anaconda Python distribution and the Spyder integrated development environment. The source code is available in Appendix F. The following Python packages were utilised within the script:

- 'pandas' for data handling.
- 'Scikit-Learn' for random forest regression & various error metric functions.
- 'numpy' for additional mathematical functions.
- 'Matplotlib' for graphing.

To ensure the correct function and applicability of the model, a synthetic fuel data set was created containing random and correlated data ('y = mx' correlation). The model

accurately identified this correlation. A trial was also performed with an entirely random data set to examine the ability of the model to fit to random data during training. It was seen that the model could reasonably "fit" during training but lost all accuracy when used with the unseen and random testing data set. These exercises are described in Appendix G.

The Sembcorp fuel data set had a total of 30 data features (i.e. measurement variables) with 2786 data sets, after removal of empty rows and large outliers. This "cleaned" data set had the same data cleaning/outlier removal criteria applied as for the principal component analysis (described in section 3.7.1), with the difference being for the random forest data set all 30 data features remained in the data set as opposed to only the seven "key" contaminants in the PCA analysis. The full list of fuel data features is given in Appendix E. Six different fuel parameters were selected as prediction targets ("y-values"): Ash content (%), Cl (mg/kg), K (mg/kg), Na (mg/kg), Pb (mg/kg), Zn (mg/kg). In each modelling case, the remaining 29 data features were the input x-variables. These prediction targets were selected as they were identified as key contaminants contributing to slagging and corrosion issues in the boiler, as is also discussed in Chapter 7.

Table 3.2: Random forest hyperparameters used in modelling exercise, as well as the test/train split for the input data.

Parameter	Definition	Setting
n_estimators	Number of trees in the forest.	100*
max_features	Number of features selected at each splitting node as basis on which to split data.	10[a]
max_depth	Maximum levels of growth of each tree.	None*
min_samples_split	Minimum number of samples required to split a node.	2*
min_samples_leaf	Minimum number of samples required at each leaf after a split.	1*
bootstrap	Whether to bootstrap input data for each tree, i.e. sample with replacement.	True*
Test / Train Split	Proportion of data assigned to model training and testing.	70% training 30% testing[b]

* Denotes the value is the default value for the random forest regressor function.
[a] *Was selected as this is near-equal to p/3, where p is the number of input data features (29 in this case) used for the prediction of the target feature. A ratio of p/3 is a common 'rule of thumb' for random forest regression models [194, p. 592].*
[b] *Initial exploratory tests with lower and higher allocations to model training did not give an appreciable improvement to predictions.*

The random forest regressor model used near-standard model hyperparameters, as tabulated in Table 3.2. Model hyperparameter tuning was attempted and is discussed in

greater length in Appendix H. However, this tuning process was not found to result in a tangible improvement to prediction accuracy, in addition to being computationally intensive. Therefore, the near default hyperparameters in Table 3.2 were used in all modelling cases in Chapter 7.

3.7.2.2   Evaluation of Model Predictions

For each prediction case, two different results plots were created. In the first, the predicted y-value versus the real y-value for the testing data set was plotted to visualise the overall prediction quality. Permutation importance was also plotted. Permutation importance is a common measure of the importance of a data feature (i.e. an input x-variable) to the predictive capability of a model. The basic concept is as follows: a baseline accuracy score for the model, using either training or testing data, is first acquired. Then, using the testing data set, each feature (column) of input data is randomly shuffled, and the accuracy score then calculated when using this shuffled column. The difference between the baseline and randomly shuffled accuracy scores is the evaluated, to determine the permutation importance of each variable to the prediction. Shuffling a data feature that correlates to the predicted output should naturally incur a substantial penalty to prediction accuracy, and hence have a high permutation importance.

The formula for the implementation of permutation importance in Scikit-Learn is shown in Equation 3.1 [224]. In this, 'i' is resultant value for the feature under evaluation (e.g. data for chlorine, when predicting ash content), 's' is the score, and 'k' is the number of times the feature is to be randomly shuffled. This would then be applied for all input data features used in the prediction model. The scoring metric, 's', can be defined using built in error metrics or user created functions. In this work, the coefficient of determination, R^2, was used as the scoring metric 's'.

$$i_j = s - \frac{1}{K}\sum_{k=1}^{K} s_{k,j}$$

Equation 3.1

Several error measures were used to evaluate prediction performance of the model. These are the mean absolute percentage error (MAPE), mean absolute error (MAE), mean square error (MSE), root mean squared error (RMSE), coefficient of

determination (R^2), and the out-of-bag (OOB) error. The mathematical formulae for these are subsequently defined. These error measures are commonly applied in machine learning approaches to evaluate model performance.

MAPE is defined in Equation 3.2, where 'n' is the number of points predicted by the model, 'y' is the actual value and 'ŷ' is the predicted value. A lower value of MAPE is better.

$$MAPE = \frac{100\%}{n} \sum_{i=1}^{n} \left| \frac{y_i - \hat{y}_i}{y_i} \right|$$

<div align="right">*Equation 3.2*</div>

MAE is defined in Equation 3.3, where 'n' is the number of predicted points, 'ŷ' is the predicted value and 'y' is the actual value. A lower value of MAE is better.

$$MAE = \frac{1}{n} \sum_{i=1}^{n} |\hat{y}_i - y_i|$$

<div align="right">*Equation 3.3*</div>

MSE as implemented in Scikit-Learn is defined in Equation 3.4 [225]. Once again, 'n' is the number of predicted points, 'y' is the actual value, and 'ŷ' is the predicted value. The RMSE is the square root of the result of the MSE therefore is not explicitly shown here. Lower values of MSE and RMSE are better.

$$MSE = \frac{1}{n} \sum_{i=0}^{n-1} (y_i - \hat{y}_i)^2$$

<div align="right">*Equation 3.4*</div>

The coefficient of determination, R^2, as implemented in Scikit-Learn is shown in Equation 3.5 [225]. In this equation, 'y' is the real value, 'ŷ' is the predicted value, and 'ȳ' is the mean of the actual data. Values of R^2 closer to 1 indicate a better fit of the predicted versus actual values.

$$R^2(y, \hat{y}) = 1 - \frac{\sum_{i=1}^{n}(y_i - \hat{y}_i)^2}{\sum_{i=1}^{n}(y_i - \bar{y})^2}$$

<div align="right">*Equation 3.5*</div>

The out-of-bag (OOB) error is further measure of accuracy. As mentioned in Chapter 2 section 2.4.2, random forest uses bootstrapping of sample data for each decision tree. This means that not all training data is used for training each tree. The OOB score is an evaluation of the prediction error when using data samples that did not form part of the bootstrapped data sample as the inputs to the model. The OOB error is simply (Equation 3.6):

$$OOB_{error} = 1 - OOB_{score}$$

Equation 3.6

The OOB score can be evaluated on many different metrics, as defined by the user (e.g. MSE, RMSE, R^2, etc.).

3.8   Materials

3.8.1   Fuels

Composition data for the four pelletized biomass fuels used in testing is listed in Table 3.3, with pictures of each shown in Figure 3.10. These fuels were supplied by a major UK biomass power generation company, who had pelletized them. White wood pellets had a diameter of approximately 6mm, with the other three fuels having a diameter of approximately 8mm. All fuel pellets were up to approximately 20mm in length. There is significant variance in ash content, from a low of 0.5wt.% in white wood, through to 6.67wt.% in the wheat straw. Fixed carbon and volatile contents also vary by around 2wt.% and 8wt.% respectively. Moisture content is similar across the fuels, in part due to all fuels being pelletized and stored indoors. As per the ultimate analyses, carbon content varied by up to 7wt.% from white wood to wheat straw for example. There is also a sizable variation in fuel bound nitrogen content, a key contributor to NO_x emissions in BFB units via the fuel NO_x formation mechanism [207, 208].

The fuels used in this work were previously analysed alongside the works of Chilton [137] and Xing, et al. [45], where multiple different analysis methods were applied to find the most suitable approach for biomass fuel analysis. The following methods were used for the fuels data presented in Table 3.3:

- Ultimate analysis: ASTM D 5373.
- Proximate analysis: BS ISO 18122 (ash content), BS ISO 18134-1 (moisture content), BS ISO 18123 (volatile matter content).

- Calorific value: BS EN 15104:2011.

- Ash analysis: fuels were ashed at 900°C for 14 hours, prepared in the form of a fused disc, and then subject to X-ray fluorescence analysis.

Table 3.3: *Composition and specification data for the four biomass fuels used in the experimental campaign. Equations for the ash indices are listed across Equation 3.7–Equation 3.9. The fuels used in this study were analysed alongside the works of Chilton [137] and Xing, et al. [45].*

Property	White Wood Pellets	Oat Hull Waste Pellets	Miscanthus Pellets	Wheat Straw Pellets
Proximate Analysis (as received basis) (wt.%)				
Fixed carbon	16.95	15.96	16.67	17.82
Volatiles	76.70	72.56	70.56	68.38
Moisture	5.82	8.83	6.76	7.12
Ash	0.53	2.66	6.01	6.67
Ultimate Analysis (as received basis)				
Carbon (wt.%)	47.1	42.7	42.8	40.5
Hydrogen (wt.%)	5.4	5.3	4.9	4.8
Oxygen (by difference) (wt.%)	40.9	39.4	38.9	40.0
Nitrogen (wt.%)	0.2	1.1	0.6	0.9
Sulphur (wt.%)	<0.1	<0.1	<0.1	<0.1
Moisture (wt.%)	5.8	8.8	6.7	7.1
Ash (wt.%)	0.53	2.66	6.01	6.67
Gross calorific value (GCV) (MJ/kg)	18.04	17.24	17.70	16.05
Ash Composition (wt.%)				
SiO_2	39.8	56.0	56.5	38.4
K_2O	9.6	20.6	11.7	19.8
P_2O_5	2.2	7.9	3.9	4.8
MgO	6.3	4.8	3.2	3.6
CaO	22.7	3.9	13.5	21.1
Al_2O_3	7.5	0.8	1.4	1.6
Na_2O	6.6	1.7	3.0	6.3
Fe_2O_3	4.3	0.9	2.6	1.0
MnO	1.7	0.2	0.1	0.1
TiO_2	0.5	0.1	0.1	0.3
Ash ratios/indices (calculated)				
K/Ca ratio	0.84	10.56	1.74	1.88
K_2O/CaO ratio	0.42	5.28	0.87	0.94
Bed agglomeration index	0.27	0.04	0.18	0.04
Base-to-acid ratio	1.04	0.56	0.59	1.29
Alkaline earth oxides to alkali oxides	1.79	0.39	1.14	0.95

The fuel ash compositions exhibit large variances in key compounds for driving agglomeration, such as SiO_2, K_2O, and Na_2O. One of the more interesting variances is the higher quantities of CaO in white wood and wheat straw of around 20wt.%, as CaO

is known to participate in the formation of ash melt coating layers that are stable at high temperature and prevent further attack by alkali metals [122, 216]. Al_2O_3 is highest in the white wood at 7.5wt.%, which is of interest given the successful use of aluminosilicate materials such as kaolin as an additive to react with the alkali metal compounds of the fuel ash.

Figure 3.10: *Images of the four pelletized biomass fuels used across testing (scale is in mm). a) White wood. b) Oat hull waste. c) Miscanthus. d) Wheat straw.*

Several ash ratios & indices are listed in Table 3.3, with the reliability of these indices discussed further in the work of Morris, et al. [87]. Broadly speaking, these indices have not been found to provide a reliable indicator of agglomeration severity but have been applied in the works of others in various contexts. They have therefore been calculated and shown here as a point of reference and are included in some of the discussion in later chapters. The equations for the bed agglomeration index, base-to-acid ratio, and alkaline earth oxides to alkali oxides ratio are shown below across Equation 3.7– Equation 3.9.

$$Bed\ agglomeration\ index\ =\ \frac{Fe_2O_3}{K_2O + Na_2O}$$

Equation 3.7

$$Base\ to\ acid\ ratio\ =\ \frac{(Fe_2O_3 + CaO + MgO + K_2O + Na_2O)}{(SiO_2 + TiO_2 + Al_2O_3)}$$

Equation 3.8

$$Alkaline\ earth\ oxides\ to\ alkali\ oxides\ ratio\ =\ \frac{(CaO\ +\ MgO)}{(K_2O + Na_2O)}$$

Equation 3.9

3.8.2 Bed Materials

Table 3.4 lists the five physical and chemical details for each of the five bed materials used across testing, with pictures shown in Figure 3.11. Two particle size grades of silica sand and three particle size grades of olivine were selected. The silica sand materials were supplied by Universal Mineral Supplies (UMS) Ltd., whilst the olivine materials were supplied by LKAB Minerals Ltd. Particle sizes of the materials were confirmed against the supplier datasheets by hand sieving a 1-2kg batch of each. A secondary physical difference between the materials is that the olivine has a higher particle density than the silica sand, however, chemical composition is the main differentiator between the silica sand and olivine. Both size grades of silica sand are very similar in composition and almost entirely silica, whereas the three olivine grades contain only around 42wt.% silica, with the most abundant component being magnesium oxide at 46-50wt.%. There are also larger amounts of iron oxide present in the olivine, at around 7wt.%. Chemical differences amongst the three grades of olivine are near negligible, as are the differences between the two silica sand grades.

Table 3.4: *Specification data for the five bed materials used across the experimental campaign. Values are those quoted on supplier data sheet.*

Property	Sand 'A'	Sand 'B'	Olivine 'A'	Olivine 'B'	Olivine 'C'
Physical Properties					
Average particle diameter (μm)	639	853	536	664	1148
Bulk density (kg/m^3)	1639	1600	1700-1900	1600-1900	1600-1900
Particle density (kg/m^3)	2650[a]	2650	3300	3300	3300
Hardness (Mohs)	N/A	6.0-7.0	6.5-7.0	6.5-7.0	6.5-7.0
Composition (wt.%)					
SiO_2	97.15	97.00-99.80	41.58	42.06	42.06
Fe_2O_3	1.96	1.00-1.50	7.21	7.13	7.13
Al_2O_3	0.28	0.50-1.50	0.41	1.13	1.13
CaO		<0.20	0.06	0.45	0.45
MgO		<0.20	50.03	46.83	46.83
TiO_2	0.01	<0.20			
K_2O	0.05			0.07	0.07
Na_2O	<0.05				
Cr_2O_3			0.19	0.44	0.44
Mn_3O_4			0.10	0.10	0.10
ZrO_2				0.06	
Loss on ignition	0.44	Max. 3.0	Max. 2.0	Max. 2.0	Max. 2.0

[a] *Assumed to be same particle density as sand 'B'.*
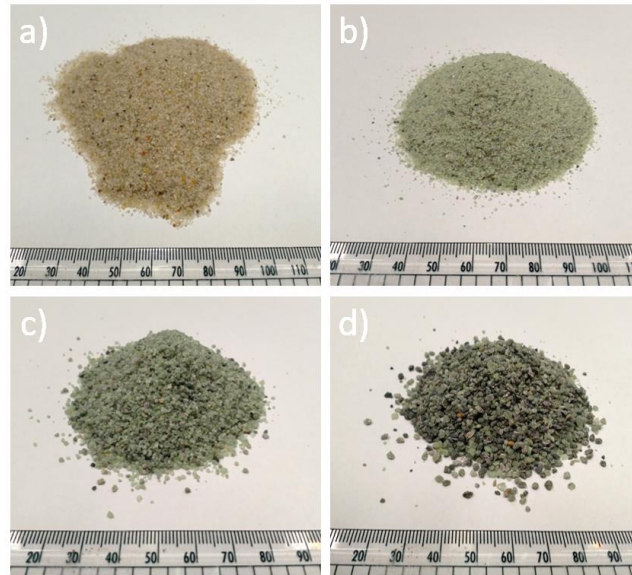
Figure 3.11: *Images of four of the five bed materials fuels used in testing (scale is in mm). a) Sand 'B'. b) Olivine 'A'. c) Olivine 'B'. d) Olivine 'C'. Sand 'A' (not pictured) had a similar visual appearance to that of sand 'B'.*

3.8.3   Additives

Two additives were used for the work in Chapter 5 and Chapter 6: kaolin and dolomite. Composition and physical data for each additive is given in Table 3.5, along with a picture of each in Figure 3.12. Both additives were supplied by Long Rake Spar Co. Ltd. Particle sizes for the additives were confirmed against the supplier data sheet by hand sieving a 1-2kg batch of each. These additives were selected as both showed potential in mitigating biomass ash issues in other works [164], with kaolin used in commercial fluidized bed boilers such as Wilton 10 operated by Sembcorp Energy UK. Chemically, the two additives are significantly different, with dolomite a calcium magnesium carbonate dominated by $CaCO_3$ and $MgCO_3$ in the form of $CaMg(CO_3)_2$, whereas kaolin is an aluminium silicate comprising of Al_2O_3 and Fe_2O_3 in the form of kaolinite. Both are in particle form, and have a fine particle size, smaller than that of either of the sand materials used in testing (section 3.8.2).

On heating dolomite, $CaCO_3$ and $MgCO_3$ decompose to release CO_2, becoming CaO and MgO respectively, hence the large mass loss on ignition. This thermal decomposition occurs at temperatures greater than around 800°C, though complete decomposition occurs over time scales of around 4 hours at isothermal conditions of around 780°C [226]. Calcined dolomite, which has been pre-heated to fully decompose into CaO and MgO, would have been a preferable option, but was not available due to resourcing issues during the test campaign.

Table 3.5: *Compositions and materials data for the two additives: dolomite and kaolin.*

Property	Dolomite	Kaolin
Physical properties		
Average particle diameter (μm)	343	559
Particle density (kg/m^3)	2850	2700
Composition (wt.%)		
Al_2O_3	0.41	42.00
CaO		0.07
Fe_2O_3	0.06	1.30
MgO		0.30
$CaCO_3$	52.70	
$MgCO_3$	45.50	
K_2O		2.00
SiO_2		54.00
TiO_2		
H_2O	0.22	
Other	1.11	0.33
Loss on ignition	47.70	

The kaolinite mineral ($Al_2Si_2O_5(OH)_4$) is the primary component of kaolin. Kaolinite undergoes dehydroxylation between 500-800°C, transforming to metakaolin ($Al_2Si_2O_7$) which is within the temperature range of the fluidized bed (800-900°C) [227, 228]. At higher temperatures upwards of 900°C, metakaolin has been shown to transform again to $Si_3Al_4O_{12}$ [227, 228], though these higher temperatures should be a rare/temporary occurrence within typical bed operation, if they arise at all.
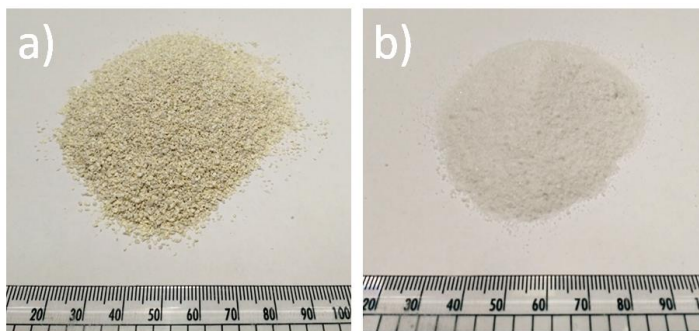
Figure 3.12: *Images of the two additives used in Chapter 5 (scale is in mm). a) Kaolin. b) Dolomite.*

3.8.4 Deposition Probe Coupons

Table 3.6 gives the compositions of the two different corrosion resistant coatings, and the SS304 base metal to which the coatings were applied. These were affixed to the deposition probe (section 3.2.9) for an extended operating period when using an olivine bed material with wheat straw fuel, where corrosion and deposition behaviours were

monitored. There was interest in the use of these coatings for superheater corrosion mitigation, hence their selection and use here [229]. Researchers at The University of Nottingham prepared and supplied the coated coupons, with this deposition/corrosion work constituting part of a larger project led by The University of Nottingham.

Table 3.6: *Composition of the coatings (NiAl, Stellite 6) used of the SS 304 coupons that were fitted to the deposition probe.*

Component	SS 304 base metal (wt.%) [230]	NiAl coating (wt.%) [229]	Stellite 6 coating [231]
Carbon	0.07		0.90-1.40
Nitrogen	0.10		
Aluminium		31.00	
Silicon	1.00		
Phosphorous	0.045		
Sulphur	0.015		
Chromium	17.50-19.50		27.00-32.00
Manganese	2.00		
Iron	Balance		
Cobalt			Balance
Nickel	8.00-10.50	69.00	
Tungsten			4.00-6.00
Others			Ni, Fe, Si, Mn, Mo

Chapter 4

The Effect of Operational Variables on Agglomeration

A version of this chapter has been published by the author in the form of a journal article [232]:

> *Agglomeration and the effect of process conditions on fluidized bed combustion of biomasses with olivine and silica sand as bed materials: Pilot-scale investigation.* **Morris, J.D.***, Daood, S.S., Nimmo, W. 2020. Biomass and Bioenergy, Vol. 142, Article No. 105806.*

Within this chapter, content has been expanded or abridged in different areas as required to be commensurate with normal thesis formatting.

4.1   Introduction

This chapter presents the results of a pilot-scale test campaign using a range of biomass fuels and bed materials at different operational conditions. As discussed in Chapter 2, several operational conditions and fuels/bed materials have received prior little attention, have conflicting results in the literature, or would benefit from additional knowledge. This chapter is an attempt to address some of these gaps, and to do so with a single pilot-scale BFB combustor, as opposed to the smaller lab-scale scale units more frequently used in academic literature.

Four biomass fuels are first compared across consistent operating conditions. A broad range of biomass fuels are used (white wood, oat hull waste, miscanthus, wheat straw). Woody fuels are well explored in the literature [106, 173], and were used here as a "good fuel" benchmark, whereas the others have received less attention in literature, particularly at the pilot-scale.

Operational characteristics were investigated; principally the effects of bed height [127, 132] and bed material particle size [127, 129, 130, 132]. These have received limited prior attention, or have produced conflicting results in prior literature, hence there was an opportunity to clarify previous work. Wheat straw was selected for a study with

olivine, a combination that has received no prior attention in combustion literature. Olivine has been the focus of some studies of agglomeration phenomena with biomass fuels, but these are overwhelmingly focused on its use with woody fuels, and in gasifiers where olivine also offers catalytic benefits [114, 116, 117, 118, 233, 234].

The larger size of the pilot-scale fluidized bed combustor opened additional angles for study. For agglomerate sampling, the bed was divided into distinct lateral and vertical zones. Agglomerate composition was compared across these zones, to determine if there was any spatial variance to agglomerate composition. This is also of interest due to bed mass transfer behaviours. Furthermore, a deposition probe was fitted during an extended study with olivine and wheat straw to investigate ash behaviours in the freeboard, a combination also not previously investigated in the literature.

4.2   **Experimental Matrix**

Table 4.1 shows the test matrix. The matrix was structured to maximise the degree of comparison possible. Variables in italicized parentheses are those which were varied 2-3 times for a given fuel and bed material combination. Where no variables are listed in parentheses, a given fuel and bed material was only tested at one set of operational conditions. The exact conditions used for each test are discussed in the respective results sections. Material specification data for the fuels and bed materials is given in Chapter 3 section 3.8.

Table 4.1: *Table showing the conditions covered across the test campaign. Text in parentheses denotes additional operational conditions that were varied across several tests for a given fuel & bed material combination.*

Fuel	Sand 'A'	Sand 'B'	Olivine 'C'	Olivine 'B'	Olivine 'C'
White Wood	✓ *(Bed height)*	✓			
Oat Hull Waste	✓ *(Bed height, U/U$_{mf}$)*	✓			
Miscanthus		✓			
Wheat Straw	✓ *(Bed Height, U/U$_{mf}$)*	✓	✓	✓ *(U/U$_{mf,}$ deposition probe)*	✓

For the "deposition probe" variable (with wheat straw and olivine 'B'), the probe was inserted into the FBC unit for an extended period of tests at consistent operational conditions of static bed height (h$_{bed}$) 24cm, fluidization number (U/U$_{mf}$) of 3-3.4 and 50-

60kW$_{th}$ thermal input. The probe was inserted for approximately 50 hours of operational time, achieved over numerous sequential tests. Metal coupons coated with anti-corrosive coatings were fitted to this probe, as described in Chapter 3 sections 3.2.9 and 3.8.4.

4.3   Results

4.3.1   Combustion Observations

Visual monitoring of bed behaviour and above-bed combustion was performed during each test through the sight glasses. During testing of each fuel with a 24cm bed of sand 'B' at 2-3U/U$_{mf}$ and 65kW$_{th}$, all four fuels were observed to produce a wide flame in the upper sight glass region, with an example image from a white wood test shown in Figure 4.1. The presence of burning embers in the upper sight glass region was also evident, with the fuels noted to produce large amounts of fly ash during retrieval of fly ash from the cyclone drum.

Figure 4.1: Example of the wide flames observed through the upper sight glass (approximately 1.1m above air distribution plate/0.3m above screw feeder). Image taken during a test with white wood and sand 'B' at 65kW$_{th}$.

As all the biomass fuels tested are high in volatiles content, from 68.38wt.% in wheat straw to 76.70wt.% in white wood, the presence of a high and wide flame above the bed is not unexpected [23, 44]. All four types of fuel pellets were observed to experience some degree of breakdown into finer fragments in the fuel screw feeder. This meant that a fraction of the fuel input was in the form of finer fuel fragments, as opposed to whole pellets only. These fine fuel fragments may not reach the bed surface during feeding, and instead be suspended in the fluidizing gas flow or be elutriated from the bed region

into the cooler freeboard region, undergoing less complete combustion as a result. This is in line with the observation of wide flames, high quantities of burning embers in the above-bed region, and the resultant high CO emissions seen for all four fuels (discussed in section 4.3.2.3).

In the context of a commercial BFB or CFB boiler, this breakdown of fuel pellets would be unlikely to negatively influence combustion efficiency. This is due to commercial boilers typically using air staging, enabling significant amounts of above-bed combustion in the wall tube regions to improve heat transfer and control NO_x pollutant emissions. Freeboard temperatures in commercial BFB boilers are around 900-1100°C [235], notably higher than typical bed temperatures of 800-900°C. In the pilot-scale BFB used here however, the very highest temperatures of 900-950°C were seen in localized areas of the bed, with lower temperatures seen in the freeboard. However, the breakdown and entrainment of fuel pellet fragments in a commercial fluidized bed boiler would also mean that more biomass ash is carried above the bed into this high temperature freeboard zone and thus be able to contribute to increased slagging, fouling, and corrosion issues, as opposed to remaining in the bed causing agglomeration [79]. Therefore, a commercial boiler operator may wish to consider these other ash issues and their countermeasures if using the pelletized fuels tested here.

4.3.2 Fuel Variation

Values for defluidization time, and average temperature, pressure and emissions data are listed across the subsequent sections. The definition of defluidization time and the process for determining operational data averages is detailed in Chapter 3 section 3.3.2.

4.3.2.1 Defluidization Time

Figure 4.2 shows the defluidization time, t_{def}, for the four biomass fuels at identical operational conditions. As is evident, white wood performed best out of the four fuels as bed defluidization did not occur. This agrees with industry experience, as woody fuels are preferred due to fewer agglomeration issues [72]. Oat hull waste and miscanthus both produced moderate t_{def} values, with miscanthus performing better than oat hull waste. These fuels have significantly more ash content than white wood, and higher relative contents of alkali metals within the ash thus have worse agglomeration issues. Oat hull waste has the second lowest ash content at 2.66wt.% in comparison to white wood with 0.53wt.%, whereas miscanthus and wheat straw both have upwards of 6wt.%

ash. Whilst oat hull waste does have a lower ash content, its ash also has elevated K_2O, a far lower quantity of CaO (3.9wt.% vs. 13.5wt.% in miscanthus ash), and slightly lower Al_2O_3. Calcium is known to create higher melting point coatings that prevent further potassium attack on silica bed materials and melt formation, mitigating agglomeration [119]. Calcium-based additive such as dolomite are known to show some effectiveness on this basis, as are aluminium oxide materials [164]. The recent work of Chi, et al. [171] has highlighted that the K/Ca ratio of a fuel may be of importance, and that as this trends towards a value of 1, agglomeration issues should be reduced. In the case of oat hull waste, the K/Ca ratio is 8.3 whereas for miscanthus it is 1.73, which is a substantial difference (see Chapter 3 section 3.8.1). This reduced CaO content is likely to be the reason for the poorer performance of oat hull waste in comparison to miscanthus, despite its lower ash and alkali metal contents. Wheat straw, the worst performing fuel, has the highest total ash content, K_2O, and Na_2O contents of the four fuels. This would drive severe agglomeration, hence its poor t_{def} value.
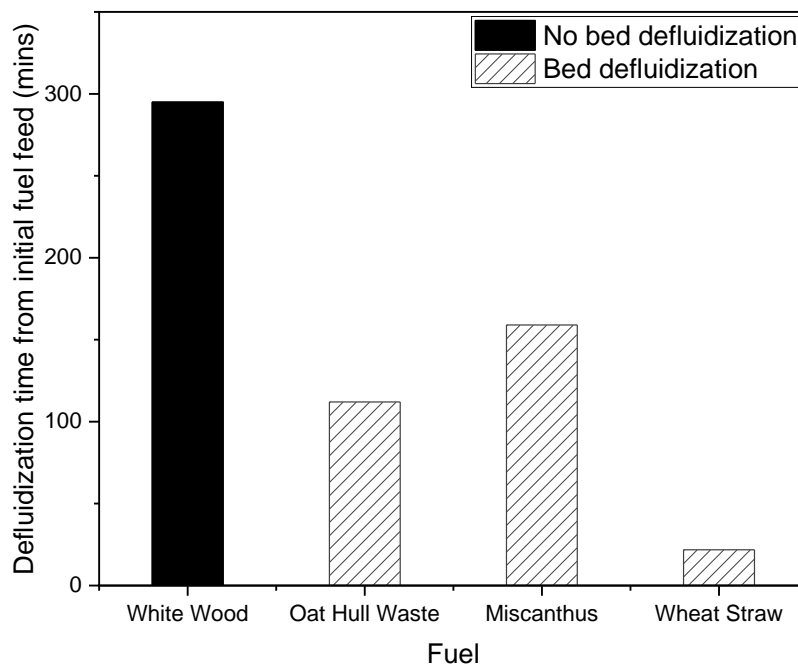
Figure 4.2: *Defluidization time (t_{def}) for the four different biomass fuels. Test conditions identical for all fuels: sand 'B', 24cm height, $2U/U_{mf}$, $65kW_{th}$.*

The results obtained here with wheat straw are comparable to the results of others with wheat straws. For example, Yu, et al. [130] and Lin, et al. [124] saw defluidization times between 40-80 minutes and 17-45 minutes respectively, with higher times only achieved by maintaining bed temperatures at or below 800°C. These authors defined defluidization time in the same way as is defined in this work: from initial fuel feeding

to the point of bed defluidization. This would naturally restrict the formation of molten alkali silicates, with initial melting of alkali metals occurring at around 750°C [106]. Both groups did however use smaller lab-scale units, with each using differing operational conditions (fluidizing gas velocities, bed particle sizes), which limits the ability to draw direct quantitative comparisons with the data obtained in this work.

4.3.2.2   Temperature Profile

Figure 4.3 shows the temperature profiles for the four biomass fuels tested at identical operating conditions. The same profile is seen for all four fuels: an increase in temperature through the dense bed region leading to a temperature peak above the bed surface at around 35cm from the base of the air distribution plate, with the temperature then declining when moving further upward. Temperatures are mostly in the 800-950°C range, with temperatures in the dense bed region on the lower end of this scale as is seen in commercial BFBs [235].
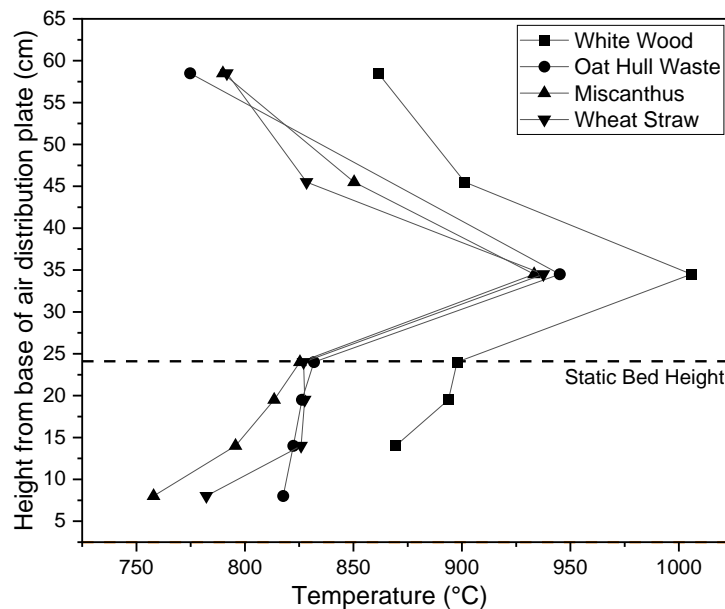
Figure 4.3: *Temperature profile for the four different biomass fuels. Test conditions identical for all fuels: sand 'B', 24cm height, $2U/U_{mf}$, $65kW_{th}$.*

For the three non-woody fuels – oat hull waste, miscanthus, and wheat straw – the temperatures are very similar across the profile. However, higher temperatures are recorded for white wood. There are a few possible reasons for this. There may have been testing irregularities or issues regarding fuel thermal input or air input. In the experimental notes for the white wood test, it was recorded that for the first two hours of testing the fuel feed was set to a slightly higher thermal rating ($67kW_{th}$) before being

returned to $65kW_{th}$, though aside from this no other irregularities regarding fuel or air input were recorded. It should also be considered that emissions for the white wood test, particularly carbon monoxide, which is an indicator of incomplete combustion, were lower than for other fuels as will be discussed in section 4.3.2.3. Therefore, air or fuel irregularities were likely minor contributory factors rather than significant ones. A further possible reason is mixing behaviour in the lower bed region (below ~7.5cm), where for white wood no temperature data was reported in Figure 4.3 due to a problem with the thermocouple. However, temperatures were higher than for the other fuels in the other dense bed regions indicating that the bed was well-mixed and therefore it would be unlikely that there was an issue specifically in this lower bed region. Further supporting this is the fact that there were no observable agglomeration issues during the white wood test as discussed in section 4.3.2.1. A final possible reason for this behaviour is the higher volatiles content of the white wood of 76.70wt.%, compared to oat hull waste which has the second highest volatiles content of 72.56wt.%. An elevated volatiles content would allow for more combustion in the upper regions of the bed and the above-bed area. This may not have caused the entirety of the temperature difference seen in Figure 4.3, e.g. there may also have been the fuel input irregularity as previously mentioned, but it may have been a contributory factor to the higher overall temperature profile. In literature, Ribeiro, et al. [236] observed a higher temperature profile with wood fuels. Temperatures in the high 800°C-low 900°C range were seen in the bed region, and up to 1100°C above the bed when using secondary air injection, which is comparable with the temperatures seen with white wood in Figure 4.3. Ribeiro, et al. [236] cited the high volatiles content of woody fuels as a cause of this high temperature profile.

4.3.2.3   Emissions

Figure 4.4a shows the NO_x emissions at 6% O_2 for the four biomass fuels at identical test conditions. NO_x emissions increased from fuel to fuel in the same order by which their fuel bound nitrogen contents increase, from lowest to highest: white wood (0.2wt.% nitrogen), miscanthus (0.6 wt.% nitrogen), wheat straw (0.9wt.% nitrogen), oat hull waste (1.1wt.% nitrogen). This would indicate that fuel NO_x mechanisms are the key NO_x formation routes, especially when considering that temperatures within the combustor (discussed in section 4.3.2.2) were far below the temperature at which thermal NO_x mechanisms become significant (around 1300°C) [208].

NO_2 levels are also notably high relative to NO levels, particularly in the case of white wood where NO_2 content is higher than NO content. NO content would typically be expected to be several times higher than NO_2 content, as shown in the study of Stubenberger, et al. [237]. This behaviour may be the result of the relatively cool freeboard region of the rig, a limitation of the rig in comparison to a commercial boiler as discussed in Chapter 3 section 3.2.11. Flue gas exits the relatively cool freeboard, is further cooled in a heat exchanger, and finally passes through a cyclone prior to sampling of the flue gas. This extended cool pathway for the flue gas, combined with the high excess air ratios of 40-60% (a limitation of the unit also noted in Chapter 3 section 3.2.11), may therefore have allowed for greater reaction of NO with O_2 to form NO_2. This is a process that ordinarily would occur in the immediate region around the stack where NO rich flue gas exits in high quantities and can react with atmospheric O_2 to form NO_2 [238].
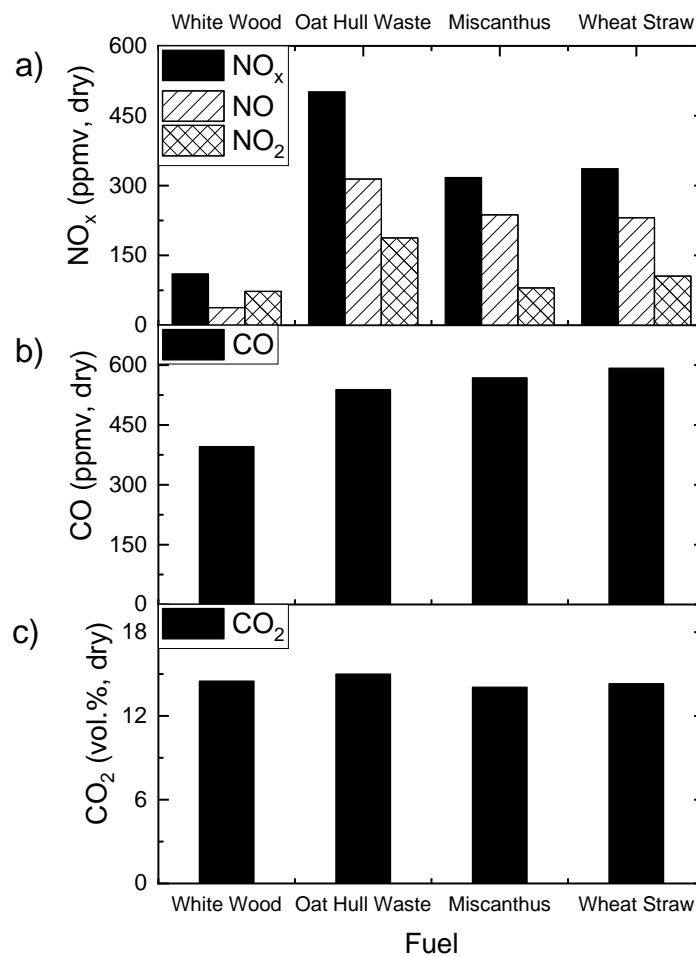
Figure 4.4: *Emissions at 6vol.% O_2 for the four biomass fuels tested. a) NO, NO_2, and combined NO_x emissions. b) CO emissions. c) CO_2 emissions. Test conditions for all data: sand 'B', 24cm bed height, $2U/U_{mf}$, 65kW$_{th}$.*

The EU industrial emissions directive (IED) quotes NO_x emission limits for large biomass combustion plants of capacity $50MW_{th}$ to $300MW_{th}$ as $300mg/m^3$ to $200mg/m^3$ (limits decreasing with increasing thermal input) [239]. NO_x emission in mg/Nm^3 at 6% O_2 are shown for each of the four fuels in Table 4.2. Of the four fuels tested, only white wood would meet achieve these limits if used in a larger combustion plant, having produced $199.58mg/m^3$ NO_x, though at this close proximity to the $200mg/m^3$ limit for larger plants some abatement would be desired (e.g. air staging). The other fuels all exceed the uppermost limit of $300mg/m^3$ to varying degrees. Very high emissions of NO_x with cereal fuels such as the oat hull waste tested here has been noted by others [240], thus it is likely that with oat hull waste several NO_x mitigation strategies would be needed in unison. As discussed in Chapter 3 section 3.2.11, the pilot-scale unit lacks air staging, which is a common feature of many commercial fluidized bed boilers and an effective NO_x control strategy, providing NO_x reductions of 30-50% [204, 207]. The application of air staging would likely bring wheat straw and miscanthus to within the emission limits of $300mg/m^3$ for a $50-100MW_{th}$ combustion plant, and this could be improved further at the both the feedstock end (lower nitrogen feedstock source, alterations to farming methods, etc.) or with further combustion control/flue gas treatment technologies (e.g. selective non-catalytic reduction) [241].

Table 4.2: *NO_x emissions in mg/Nm^3 for the four fuels tested, at $6vol.\%$ O_2. Test conditions for all data: sand 'B', 24cm bed height, $2U/U_{mf}$, $65kW_{th}$.*

Fuel	NO (mg/Nm^3) (dry)	NO_2 (mg/Nm^3) (dry)	NO_x (mg/Nm^3) (dry)
White Wood	50.45	149.13	199.58
Oat Hull Waste	419.71	385.11	804.81
Miscanthus	317.44	164.59	482.03
Wheat Straw	309.19	216.36	525.55

Figure 4.4b and Figure 4.4c show the CO and CO_2 emissions respectively for the four biomass fuels. CO_2 emission for all the fuels were near identical at $14-15vol.\%$. There is more variation in CO emissions, with white wood producing the lowest value at just under 400ppmv, whereas the other three fuels produced consistent values in the 550-600ppmv range. This may again be due to the difference in the volatiles content of the fuels, with the white wood having notably more ($5wt.\%+$) volatiles than the other fuels as discussed in section 4.3.2.2. The higher volatiles content likely led to the increased above-bed temperatures versus other fuels seen in Figure 4.3, allowing for more complete combustion of any entrained carbon fines, thereby reducing CO emissions as

is seen here. Excess air was at 65-70% for these tests, hence the high CO quantities observed are much more likely to be due to incomplete combustion because of reduced above-bed temperatures, as opposed to a lack of O_2 [20, pp. 49-50].

4.3.3   Bed Material & Size Variation

Table 4.3 shows the effect of changes to bed material on t_{def} when using the worst performing fuel, wheat straw, at consistent operational conditions. Fluidization number (U/U_{mf}) was 50% higher and thermal rating $15kW_{th}$ lower than the wheat straw tests conducted in section 4.3.2 hence the elevated defluidization time observed when using sand 'A' in comparison to sand 'B'. From the data shown in Table 4.3, the use of olivine provided a benefit in comparison to the use of sand, with t_{def} extended by upwards of 25%. This is due to the significantly different composition of the olivine in comparison to silica sand. The olivine has around 45wt.% less SiO_2 than silica sand and is a magnesium iron silicate material, therefore is far less reactive with alkali metals in biomass ash. This behaviour has previously been identified in the works of others such as Grimm, et al. [114], however no quantification was given as to the performance improvement of switching to olivine in these works. There are factors other than material chemistry, such as material wettability, that may also have contributed to this difference. These will be further discussed in comparison to the effect of using bed additives in Chapter 5. Whilst this is a significant proportionate improvement in defluidization time when using olivine with wheat straw, this change alone is unlikely to make wheat straw a viable choice as a single fuel option for commercial FBC units.

Table 4.3: *Table listing the effect of bed material and particle size on defluidization time when using wheat straw pellets. Conditions: 24cm bed height, $3U/U_{mf}$, $50kW_{th}$.*

Bed Material	t_{def} from initial fuel feed (mins)
Sand 'A'	131
Olivine 'A'	177
Olivine 'B'	164
Olivine 'C'	*N/A (no fluidization achieved)*

Use of olivine 'A', with a finer particle size of 536µm, in comparison to olivine 'B' of average particle size 664µm provided the longest overall t_{def} at almost 10% longer than that obtained with olivine 'B'. This would indicate that a smaller particle size is also beneficial for lengthening defluidization time. This finding with olivine is in agreement with the observations of others who have reported, with silica sand, a trend of longer defluidization times with a smaller particle size [124, 130], and runs contrary to those

that have reported the opposite trend [127, 132]. The likely reason for this behaviour relates to the difference in void size between larger and smaller bed particles, with the larger particles having larger voids between the particles, thus forming larger bubbles in the bed [242]. Instead of smaller dispersed bubbles through the bed, these larger bubbles coalesce together as they rise through the bed, further increasing in size. The net effect of this larger particle size would be the formation of less consistent and poorer quality mixing patterns in the bed. This would allow agglomeration to propagate more easily through the bed in zones of poorer mixing, thus causing reduced t_{def}.

An additional point to consider for the application of this finding is the degree of change to bed particle size distributions over time in commercial fluidized bed units, due to their continual bed material removal and replenishment operations [20, p. 147 & 226]. Moving to a finer bed particle size may be beneficial for mitigating agglomeration, however fine fractions of bed material are more susceptible to entrainment in flue gas flows, leading to increased bed material losses and costs for operators. Reductions to the fluidizing air flow rates to attempt to counteract this would alter the combustion profile through the boiler and this reduction in the fluidizing gas velocity would itself worsen agglomeration, as discussed in Chapter 2 section 2.3.3. Therefore, a balance point would need to be found for larger scale units to determine the smallest particle size grade that still aids in mitigating agglomeration issues whilst avoiding these other shortfalls.

A final test was attempted with olivine 'C' of average particle diameter 1148µm, as listed in Table 4.3. However, a steady fluidization regime could not be achieved during bed heating with natural gas, indicating that the limits of the pilot-scale unit had been surpassed. This was due to a significantly higher quantity of air being required to achieve the minimum fluidization velocity, increasing the heating time of the bed, and leading to excessively long start-up times. Furthermore, there was some in-bed accumulation and combustion of natural gas from the burners, possibly due to the larger void sizes of this bed material, which was compromising the safety of the test. Olivine 'C' may be suitable for a larger test facility, or with modifications made to the existing combustor, e.g. additional gas burners to shorten start-up and ensure complete natural gas burnout.

4.3.4　　　Static Bed Height Variation

Table 4.4 shows the effect of successive increases to bed height on t_{def} for oat hull waste and wheat straw. For both fuels, there is an apparent optimum h_{bed} of 24cm, which provides the longest t_{def}, regardless of the use of smaller or larger static bed heights. Oat hull waste exhibits a strong decline in t_{def} with bed heights other than 24cm, such that at a h_{bed} of 29cm it has a near identical t_{def} to the wheat straw, a far worse fuel for agglomeration severity (as discussed in section 4.3.2). It should be noted that the test conditions and sand bed material used here were different to those in the baseline fuel comparison tests of section 4.3.2 hence direct quantitative comparison is not applicable. As a result of the use of this finer sand material, considerably lower thermal ratings and higher fluidizing gas velocities were employed to achieve stable combustion conditions, both variables which are known to be beneficial in mitigating against agglomeration to an extent, hence t_{def} values here cannot be compared directly to those in section 4.3.2. In the case of the oat hull waste test at 19cm in Table 4.4 however, the defluidization time was very similar to that presented in Figure 4.2 under the less favourable operating conditions. Dense bed temperatures during the 19cm bed height test with oat hull waste (Table 4.4) were recorded as an average of 905°C, versus an average of 826°C in the dense bed (12-24cm) region as shown in Figure 4.3. Elevated temperatures are known to exacerbate ash melting and agglomeration issues from numerous prior studies [124, 130], therefore are likely part of the reason for this poorer performance even with more favourable operational conditions.

Table 4.4: Table listing the effect of static bed height (h_{bed}) on defluidization time from initial fuel feed. Conditions for all tests: sand 'A', 3U/U$_{mf}$, 50kW$_{th}$.

Bed height (cm)	Defluidization time from initial fuel feed (mins)	
	Oat Hull Waste	**Wheat Straw**
19cm	109	-
24cm	161	131
29cm	122	118
41cm	-	87

Differences in bed mixing phenomena may be the reason for the "optimum bed height" trend observed in Table 4.4. When using a deeper bed, there will be poorer vertical mixing of fuel and bed material due to greater coalescence of bubbles and larger bubbles erupting near the surface of the bed, instead of a dispersion of smaller bubbles across the entire depth of the bed in the case of a shallower bed [9, p. 127]. This would

make it easier for larger agglomerates to develop without being disrupted by bed mixing actions. With a shallower bed, whilst there is a more dispersed bubble flow and a more vigorous bed mixing pattern, there is also a smaller mass of bed material on which the same fixed thermal input of fuel is combusted. This increases the ash to bed ratio, making it easier for enough agglomerates to accumulate and cause bed defluidization.

The trend observed here perhaps clarifies the contradictory behaviours seen by Lin & Wey [127] and Chaivatamaset, et al. [132]. Both groups used very similar sized lab-scale FBC units with inner diameters of 10cm and 9cm respectively. Lin & Wey [127] used large static bed height to bed diameter (h_{bed}/d_{bed}) ratios upwards of 1.65 and observed decreasing t_{def} with increasing h_{bed}/d_{bed}, whereas Chaivatamaset, et al. [132] used lower h_{bed}/d_{bed} ratios of 0.5 and 1.0 and observed increasing t_{def} with increasing h_{bed}/d_{bed}. It may be that the two groups were only observing part of the trend observed in Table 4.4, i.e. had not reached the optimum bed height for their respective unit. Unfortunately, the two groups used fuels of a significantly different composition, therefore a conclusive quantitative comparison between their data and the findings made here cannot be made. More broadly, whilst the results obtained here cannot be used to conclusively reveal the relationship between bed height and defluidization time, they do suggest that more complex behaviour is occurring and may be worthy of a dedicated study, particularly as this is a parameter that would be relatively simple for commercial operators to make small adjustments to.

4.3.5 Bed Retrieval Observations

At the conclusion of a test (e.g. due to defluidization) the bed was allowed to initially cool for 1-2 hours with a reduced input of fluidizing air. The air flow was then switched off and the bed cooled to atmospheric temperatures over a period of 24+ hours. Visual observations regarding the bed condition and severity of agglomeration were recorded after each test during bed retrieval. A representative selection of agglomerates retrieved from the bed following tests with each fuel and sand 'B' plus wheat straw and olivine 'B', are pictured in Figure 4.5.

For tests with white wood or oat hull waste with sand, agglomerates were mostly small, frequently consisting of 2-5 weakly joined bed particles, similar to phenomena seen by others in cases of coating-induced agglomeration [110]. Oat hull waste agglomerates were occasionally in the form of larger pellet char cores with some weakly attached

sand particles. An example of this is seen to the right side of Figure 4.5b, which appears to be the early stage of a melt-induced agglomeration mechanism. These were very weakly bound however, with the char core fragmenting almost immediately upon light contact. Moreover, these agglomerates may have arose, in part, due to the char core not combusting at the end of the test as the rig cools down.
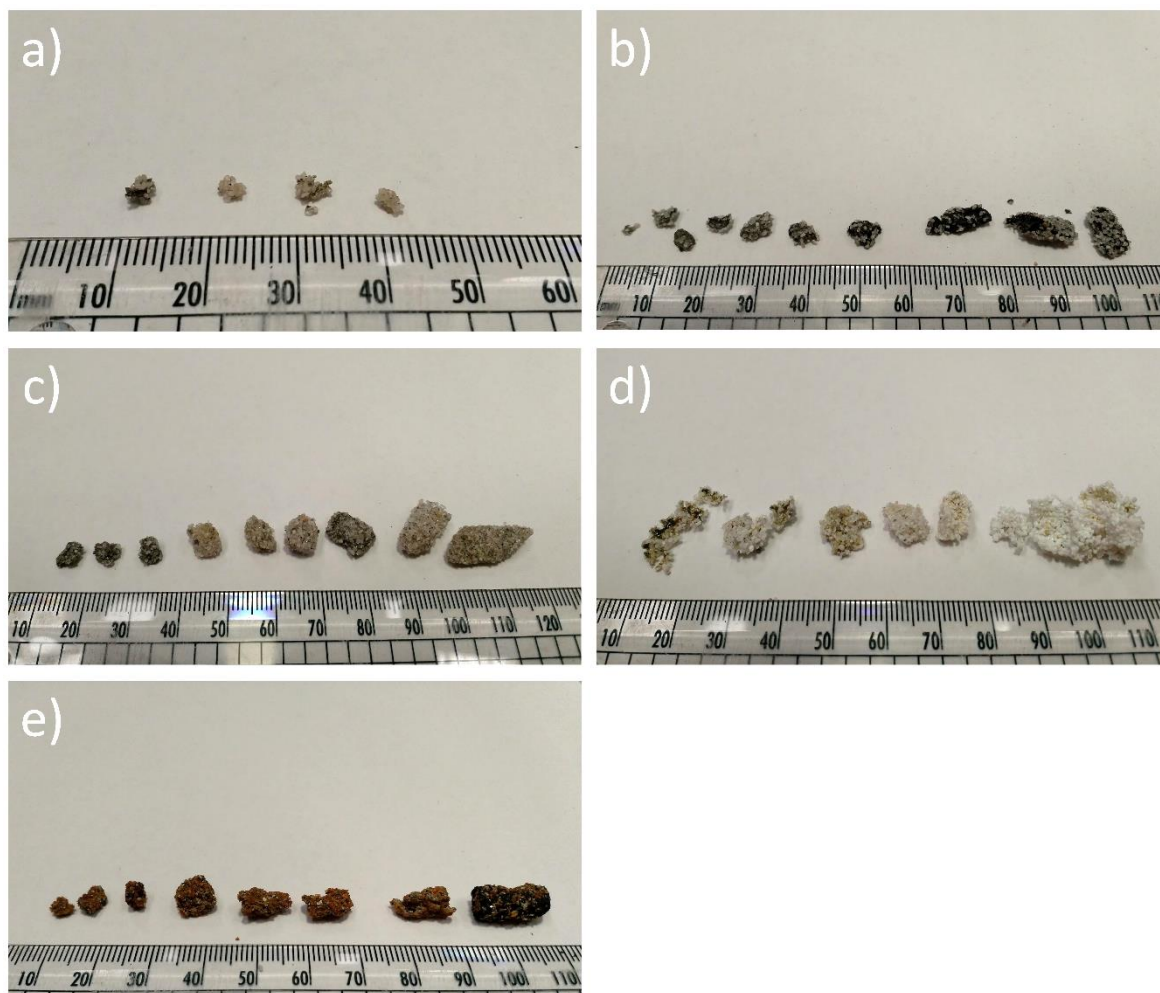
Figure 4.5: Representative examples of the types of agglomerates found after tests with each fuel and sand, and with wheat straw and olivine. Note that this is representative of the size and types of agglomerates that were formed but is not representative of the frequency with which each size of agglomerate was retrieved from the bed. Scale in mm. a) White wood & sand 'B'. b) Oat hull waste & sand 'B'. c) Miscanthus & sand 'B'. d) Wheat straw & sand 'B'. e) Wheat straw & olivine 'B'.

For wheat straw or miscanthus with sand, generally far larger agglomerate structures were found, some of which were upwards of 2cm in length/width, with the largest seen with wheat straw. There was the frequent occurrence of "pellet shaped" agglomerates, particularly with wheat straw. Some of these pellet-shaped agglomerates were a solid sand structure in the shape of a fuel pellet, whilst others were hollow or contained a partially non-combusted char core. The combination of these observations indicates that

melt-induced agglomeration mechanisms were dominant for wheat straw and miscanthus [124]. Of all the fuels and bed materials tested with sand, the highest frequency of agglomerates in the bed was observed after using wheat straw and sand, which is as would be expected given it had the lowest defluidization times of all the fuel and bed material combinations tested (section 4.3.2.1).

When using wheat straw with olivine as opposed to sand, there was a reduction in the frequency of agglomerates through the bed when compared to tests with sand, as observed qualitatively during bed retrieval. However, agglomerates were still of similar sizes to those found after tests with sand, as can be seen between Figure 4.5d-e. The right-most agglomerate in Figure 4.5e is another example of a char core with weakly attached bed material, showing a melt-induced agglomeration mechanism was occurring with molten ash in the pellet binding to bed material. Larger agglomerates were still visually observed to be more numerous in the bed after tests with wheat straw and olivine than for tests with any of the other fuels with sand. This highlighted how problematic wheat straw was as a fuel, even after changing bed materials. The specifics of wheat straw agglomeration and the phenomena of these pellet shaped agglomerates are investigated in greater detail in Chapter 5.

When retrieving bed material after some tests, there was the observation of more agglomerates in one zonal region of the bed than in others, however a consistent trend across fuels and operating conditions could not be determined purely via visual observations. A better qualitative or quantitative analysis method for recording overall bed condition may determine if there is such a trend. This could be achieved for example by sieving the bed in a zonal manner similar to how agglomerates were sampled (see Chapter 3 section 3.3.3). This would allow for the creation of a particle size distribution map of the entire bed, highlighting regions with more agglomerates or significantly different particle size distributions. The only consistent visual observation noted across all tests was a far lower frequency of agglomerates present in the lower vertical stratum of the bed, amongst the bubble caps (see Chapter 3 section 3.3.3 for bed zonal map). This was partly due to the difficulty of finding and retrieving agglomerates from the closely pitched bubble caps. However, even slower, more methodical sampling methods in this region (sampling with a spatula) revealed few sizable agglomerates for retrieval for any of the conditions tested. As a result, samples retrieved from the lower

vertical stratum of the bed were predominantly loose bed particles with the occasional agglomerate retrieved where found.

4.3.6   Deposition Probe Retrieval Observations

A picture of the deposit that formed on the deposition probe after approximately 50 hours of sequential tests using olivine 'B' and wheat straw is shown in Figure 4.6. The deposit was formed on the surface of a NiAl-coated metal coupon, on the leeward side of the probe. From the particle trail present on the side of the probe, it appears that the deposit formed in this location due to the gas flow moving away from the combustion chamber wall and losing velocity, possibly due to the formation of a vortex or similar around the probe, causing entrained particles to lose velocity and land on the probe. On retrieval, the deposit was noted to be loosely held together, with the "base layer" of the deposit that rested directly on the probe surface being the strongest deposit section. This was the only deposit formed on the probe, with the other metal coupons appearing unchanged. The deposit was removed from the NiAl coupon, which itself was inspected visually for any signs of corrosion or damage, though none could be seen. Both the ash deposit and the NiAl coupon underwent SEM/EDX analysis, which is discussed in section 4.3.7.6.

Figure 4.6: Image of ash deposit formed on deposition probe after approximately 50 hours of testing with wheat straw pellets and olivine 'B'. Four metal coupons were present on the probe, with the deposit formed on the third coupon (NiAl), approximately 20cm away from the combustion chamber wall. The coupons and deposit were on the leeward side of the probe.

4.3.7   SEM/EDX

The generic approach to SEM/EDX work was described in Chapter 3 section 3.4. In the case of quantitative EDX analysis, upwards of four sites of interest were chosen per sample, with quantitative point or area analysis performed at upwards of three locations per site of interest. For most samples, far more sites and locations were analysed than

this minimum. Table 4.5 summarises data on the mounted agglomerate samples analysed via SEM/EDX, broken down into the proportion of mounted samples analysed by fuel, and the types of mounted agglomerates samples analysed for each fuel. These samples were selected as they were representative of the vast majority of the agglomerates retrieved from the bed, therefore would be the main contributors to bed defluidization. Whilst some examples of larger agglomerates were retrieved in some test cases (as pictured in Figure 4.5), these were rarer occurrences and thus were not reflective of the agglomerates retrieved from the bed. Samples were analysed from most of the conditions tested experimentally. To see example images of each shape of agglomerate listed in Table 4.5, refer to images and discussion in section 4.3.5. A key aspect of the SEM/EDX analysis in this chapter was the dividing of the bed into discrete spatial zones, and sample comparison across these zones. The zonal map for this is given in Chapter 3 section 3.3.3.

Table 4.5: Summary of the types of mounted agglomerate samples analysed by SEM/EDX on both a overall by-fuel basis, and type of agglomerate by-fuel basis.

Fuel	Type of Agglomerate	Proportion of Samples
White Wood	*(All types)*	**21%**
	Bed material & smaller agglomerates (1-5 conjoined bed particles)	*100%*
Oat Hull Waste	*(All types)*	**37%**
	Bed material & small agglomerates (approx. 1-5 bed particles)	*43%*
	Mixed larger agglomerates (approx. 1-5mm diameter each)	*57%*
Miscanthus	*(All types)*	**16%**
	Bed material & small agglomerates (approx. 1-5 bed particles)	*33%*
	Mixed larger agglomerates (approx. 1-8mm diameter each)	*67%*
Wheat Straw	*(All types)*	**26%**
	Mixed larger agglomerates (approx. 1-8mm diameter each)	*40%*
	Pellet shaped agglomerates (approx. 1-8mm diameter, up to approx. 20mm in length each)	*60%*

4.3.7.1   Structural Variation with Fuel

Figure 4.7a-b shows typical bed particles after tests with white wood pellets and sand 'A'. Most sand particles did not have any ash coating layers, though where present they were typically of thickness <10µm, covering the entirety of the cross-sectional perimeter of the particle. These coatings appeared to have arisen due to the coating-

induced agglomeration mechanism seen in literature [106, 112, 173], of a uniform attack on the entire surface of the silica sand bed particle by alkali metals in ash. In some zones, there were segments of thicker ash coatings (>50µm), though these likely arose due to ash deposition hence their localized thicker nature. Ash-filled veins in sand particles were present in numerous areas (Figure 4.7a). In some cases, these veins widened to upward of 30µm. Due to their structural weakness, most agglomerates broke during retrieval or sample mounting. Those that remained intact typically displayed homogeneous ash joins, likely the result of two particles with coating layers colliding, perhaps with some involvement of an additional molten ash deposit [120], as shown in Figure 4.7b.
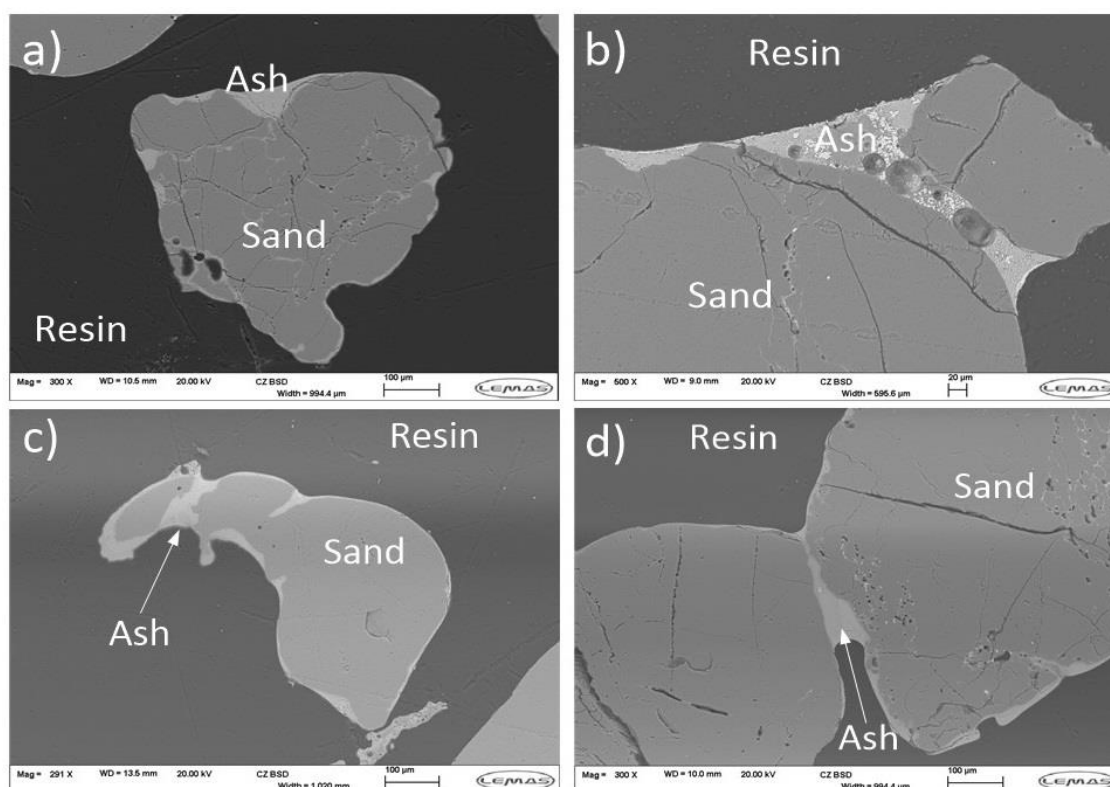
Figure 4.7: *SEM images of typical agglomerate structures observed for white wood and oat hull waste. a) White wood & sand 'A'. Homogeneous coating layers present around particle cross-sectional perimeter. b) White wood & sand 'A'. Bed particle fragments adhered together due to an ash melt. c) Oat hull waste & sand 'A'. Homogeneous coating layer across the entire cross-sectional perimeter of the bed particle. A deep ash intrusion in upper left section of particle has crossed its width. d) Oat hull waste & sand 'A'. Conjoined bed particles, both with ash coating layers, that have likely led to the formation of the central join.*

Oat hull waste pellets displayed very similar agglomerate structures to white wood pellets, with ash coating layers covering the entire cross-sectional perimeter of the particle, as well as the frequent occurrence of ash veins and ash intrusions into particles (Figure 4.7c). Once again, most agglomerates were very weak structurally and easily

broke apart, though particle joins that were left intact again appeared to be due to a collision of two particles with coating layers, as shown in Figure 4.7d. These behaviours indicate that coating-induced agglomeration was likely the predominant method by which agglomeration proceeded for oat hull waste.
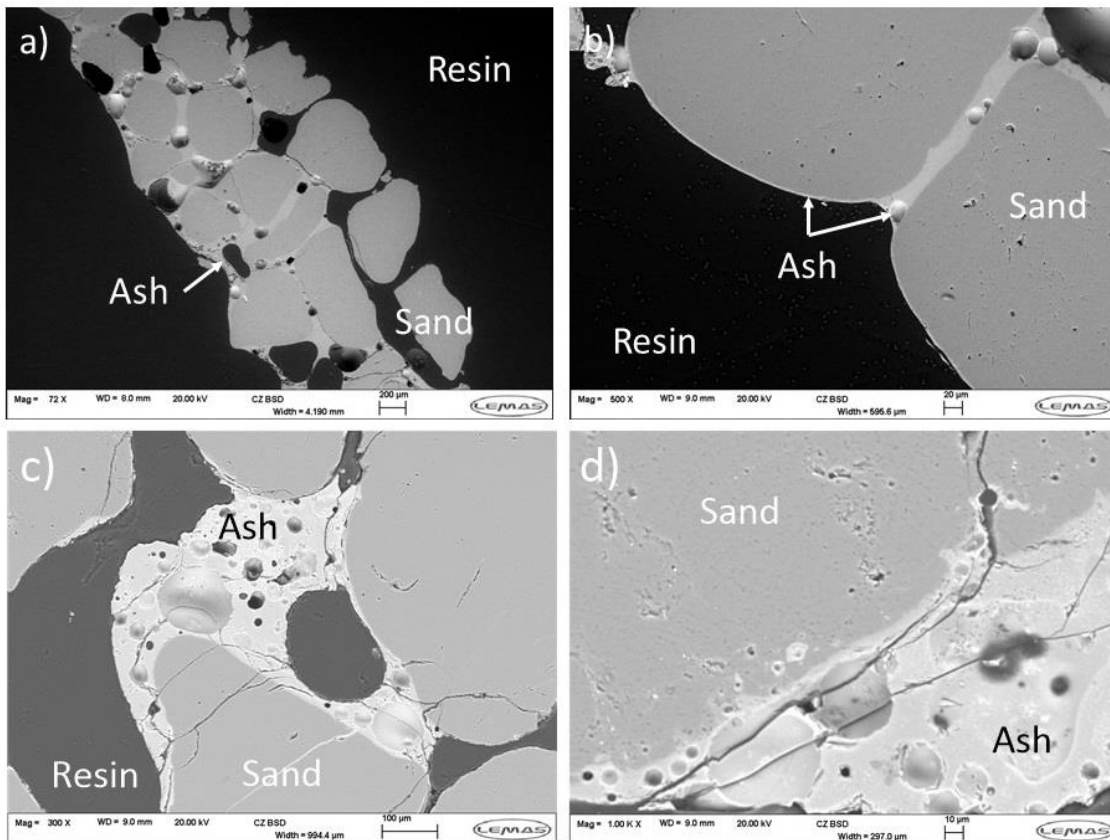
Figure 4.8: *SEM images of agglomerates with miscanthus and wheat straw. a) Miscanthus & sand 'B'. Large melt-induced agglomerate structure with sand embedded in ash phase. b) Miscanthus & sand 'B'. Two sand particles joined by a ~20μm ash deposit. Thin ash layer on outer particle surface due to early-stage coating layer formation. c) Wheat straw & sand 'A'. Bed particles were embedded in large ash deposits. d) Wheat straw & sand 'A'. Boundary between ash deposit and bed particle. Little evidence of direct reaction was found between the ash melt and bed particle, due to short operational times.*

Miscanthus and sand agglomerates were characterised by larger ash melt structures than those of white wood and oat hull waste. These are typical of a melt-induced agglomeration mechanism [110, 124], with examples shown in Figure 4.8a-b. Larger structures formed through the embedding of sand particles in ash, as pictured in Figure 4.8a, as well as the joining of sand material by discontinuous ash melts. There was still evidence of some coating-induced agglomeration occurring, with an example of an early-stage coating layer pictured in Figure 4.8b. The combination of both mechanisms with miscanthus is likely a result of it having a high ash content (6wt.%), yet still operating for long enough before defluidization for coating layer formation to begin.

Wheat straw presented large, melt-induced agglomerate structures, with an example shown in Figure 4.8c. These structures generally had a larger ash phase than was seen with the miscanthus. The large ash deposits allowed for the agglomeration of multiple particles, with deposits and joins frequently upwards of 50µm in width, similar to the observations of others when using straws [124, 126, 130]. Figure 4.8d shows a close-up image of a region with an ash melt boundary against a bed particle. At the surface of the bed particle, there was some movement of the ash melt into the surface level indentations of the bed particle, though there was less evidence of reaction between the ash and bed particle than was observed with white wood and oat hull waste (e.g. in the form of coating layer formation). This is likely due to the shorter t_{def} of wheat straw tests in comparison to the other fuels, limiting time for reactions between the bed material and ash to proceed to a significant degree.

4.3.7.2 Structural Variation with Olivine Use

Several key agglomerate structural phenomena were observed in samples from wheat straw and olivine tests. The first of these is deposition of ash onto olivine, as seen in Figure 4.9a, with an enhanced image of an ash layer shown in Figure 4.9b. These ash layer deposits were up to widths of around 30µm and were often suitably large enough to act as a binding material to form an agglomerate (as can be seen in Figure 4.9a). These were not of similar thicknesses around the entire particle perimeter and were discontinuous in nature. Therefore, it is unlikely they are the product of reaction between fuel ash and the olivine that is typical of coating-induced agglomeration, and instead were ash deposits from a melt-induced agglomeration mechanism that acted as a discontinuous ash phase to glue bed material together.
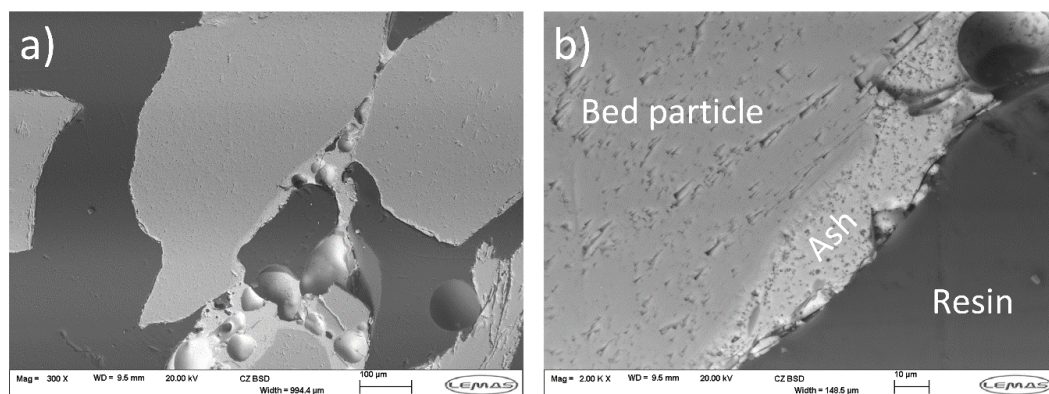
Figure 4.9: *SEM images of typical ash layering behaviour from wheat straw and olivine tests. Conditions: wheat straw, olivine 'B', 24cm bed height, 50kW$_{th}$. a) Image showing an ash melt layer deposit on an olivine bed particle. b) An enhanced image of the ash layer section.*

Cracked or fractured olivine bed particles were observed across numerous samples. An example of such a region is given in Figure 4.10a. As is evident from the EDX mapping analysis, the potassium component, in the form of a potassium silicate melt, has fully penetrated the fracture region, and within this fracture region remains present in similar abundance to what is seen in the outer ash layer. Calcium however is present mostly in the outer ash layer, with little to none present in the fracture regions. Others have observed inward migration of potassium into bed material fractures and cracks in the context of silica sand with woody fuels, where it is speculated that capillary action draws the ash melt inwards [120], or that the ash melt reacts with the bed particle in fracture regions to work its way inwards [119]. As the olivine is not as reactive with biomass ash as sand is, it is more likely that the potassium silicate melt fraction has moved into the fracture via physical means such as capillary action. This is supported by fundamental studies at elevated temperatures (1000°C+) that, when compared, show K_2O-SiO_2 melt systems [243] to have surface tension values over 50% less than those of CaO-SiO_2 melt systems [244] at equivalent conditions. This reduced surface tension would therefore allow for increased capillary action on the potassium silicate ash melt fraction. This behaviour would prevent olivine particles from fracturing if included as part of an agglomerate structure, therefore keeping the average particle size higher and making it easier for bed defluidization to occur.

In regions where there was a bulk ash melt phase with embedded olivine bed particles, there was frequently the occurrence of a calcium-rich layer at the olivine particle surface. An example of this is shown in Figure 4.10b together an EDX mapping analysis. It is apparent from Figure 4.10b that this calcium-rich layer appears to be in the form of calcium crystals, however, these crystals may have formed during ash cooling. Elled, et al. [151] similarly observed the formation of calcium crystals in some agglomerates from tests using a wood-straw fuel blend with a silica sand bed, though did not suggest a reasoning. Regardless, calcium is clearly driven to the olivine particle surface to form this calcium-rich layer. Others have observed the formation of a calcium-rich layer when using olivine in different contexts, such as fluidized bed gasification of wood [117, 118], miscanthus [116], or fluidized bed combustion of wood [114]. These other groups generally observed calcium layers to arise as a standalone feature on olivine particles, whereas here they were only observed on bed particles embedded in a large ash melt phase and was observed uniquely with the combustion of

wheat straw. This could be due to the wheat straw fuel used here which is predisposed to large ash melt formations, whereas the woody fuels and miscanthus used in the other studies have been seen to form coating layers both in other works and in this one.
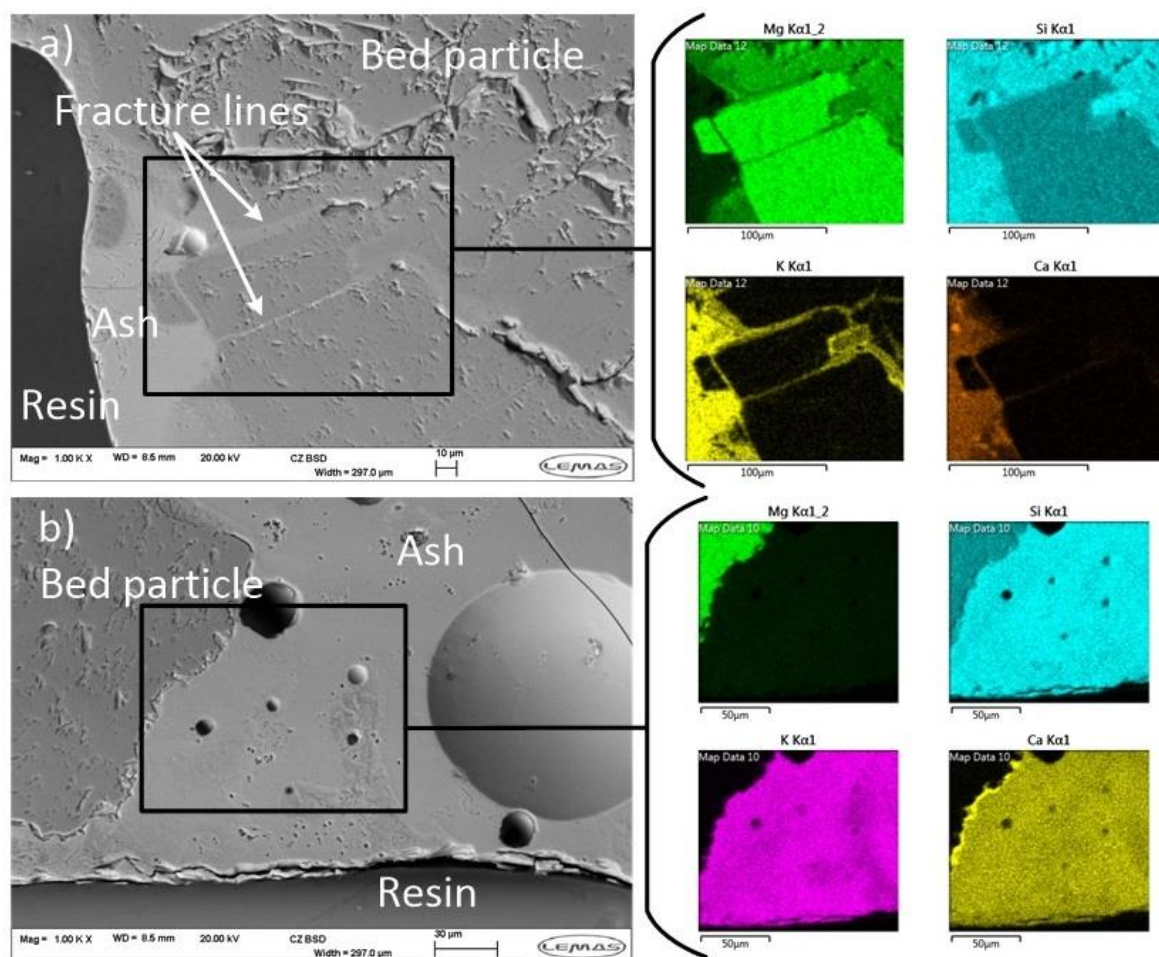
Figure 4.10: *SEM images & EDX maps of unique agglomeration mechanisms observed with olivine. a) SEM image of a region of an olivine bed particle with several cracks/fractures. There is a far higher abundance of potassium in the fracture region, versus calcium, when compared with relative levels in the outer ash layer. Conditions: wheat straw, olivine 'A', 24cm bed height, $50kW_{th}$. b) Example of the calcium-rich layers found on the surface of olivine bed particles that were embedded in a large ash melt phase. Conditions: wheat straw, olivine 'A', 24cm bed height, $50kW_{th}$.*

The differences in the fluidized bed size & scale could also be a dictating factor in the differences observed between this and other studies. Other works investigating olivine agglomeration mechanisms and observing layer formations have used industrial units with operational times upwards of dozens of hours [118]. The work of Kuba, et al. [118] presents a complete mechanism by which these calcium rich layers form with olivine. Kuba, et al. [118] proposed that calcium layering with olivine arises due to the ion substitution of Ca^{2+} into the outer olivine structure in place of either Mg^{2+} and $Fe^{2+/3+}$, with preference given to substitution of iron. The substituted magnesium or iron

components are expelled from the olivine as oxides, hence the creation of a calcium rich outer layer. An elemental analysis of the ash melt surrounding olivine particles (discussed subsequently in section 4.3.7.3) highlights elevated magnesium and iron levels, and reduced calcium levels. This suggests that the mechanism proposed for wood fuels and olivine proposed by Kuba, et al. [118] has occurred here with wheat straw, with a movement of calcium out of the ash and into the outer olivine particle surface accompanied by expulsion of iron and magnesium into the ash melt surrounding olivine.

4.3.7.3 Compositional Variation with Fuel & Bed Material

Figure 4.11 shows EDX data for ash layers when using white wood, oat hull waste and wheat straw with sand 'A', miscanthus with sand 'B', and wheat straw with olivine 'A'. Across all the data, some components presented large spreads in their composition data, represented with the 95% confidence interval bars, indicating that ash layers could frequently be quite heterogeneous with regards to chemical components despite their homogeneous appearance. This would indicate that the exposure times of bed material here (up to around 5 hours with white wood) were not long enough to produce the chemically homogeneous coating layers often seen in works that used samples from industrial boilers [110, 119] after exposure times upwards of 1-2 days.

When comparing ash layers in tests using the fuels with sand, the principal differences between the fuels are the Al, Si, P, K, and Ca content of ash layers. Al content of the white wood ash layers is high at 14wt.%, though this is what might be expected given that white wood ash itself has 5x the Al content of the next highest fuel, wheat straw (7.5wt.% versus 1.5wt.% for wheat straw, see Chapter 3 section 3.8.1). This high aluminium content in wood ash is also to be expected. Vassilev, et al. [44] analysed the composition of 86 different types of biomass and identified an average Al_2O_3 content of wood ash to be 5.09wt.%, versus 1.39wt.% for agricultural biomass and 2.71wt.% for straws. Whilst the white wood used here has higher Al_2O_3 content than the average reported by Vassilev, et al. [44] it is far below the maximum value reported of 15.12wt.%. This elevated Al content of the white wood may be beneficial in mitigating agglomeration, given that aluminosilicate additives such as kaolin are known to be effective in reducing agglomeration [72, 167] by forming stable alkali aluminosilicates. This higher Al content may therefore be a contributing factor to the excellent

performance of white wood in section 4.3.2, which was the only fuel that did not undergo bed defluidization.
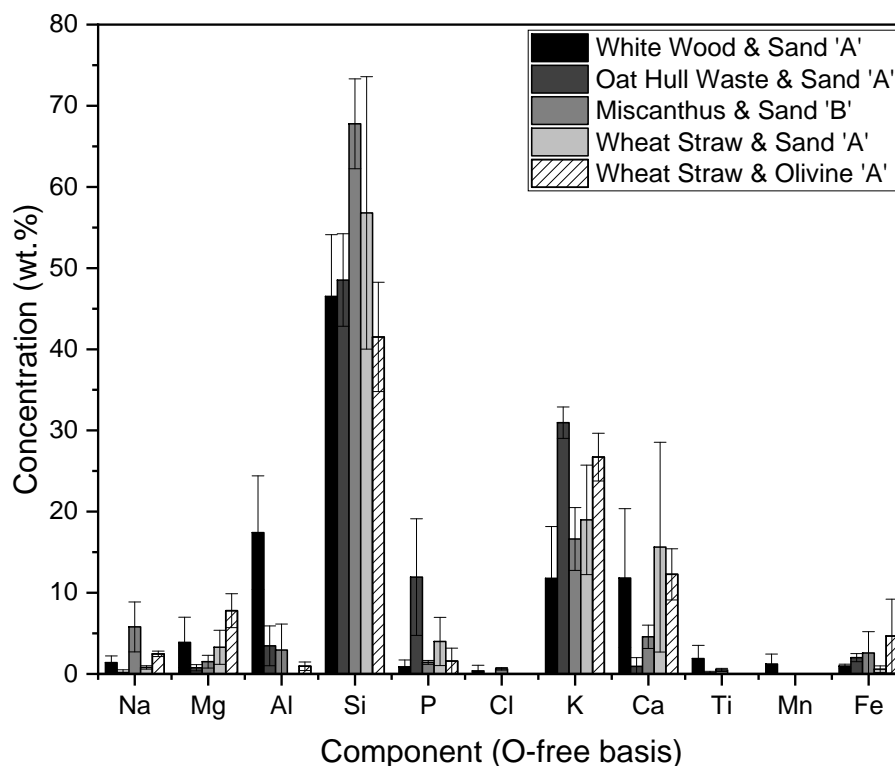
Figure 4.11: *EDX analysis showing the effect of fuel and bed material on ash layer composition. For white wood, oat hull waste and wheat straw: all samples for averaging taken from the 'mid' vertical strata, lateral zone A, from tests at consistent operational conditions (h_{bed} 24cm, 50kW$_{th}$). For miscanthus: samples averaged across all vertical strata at operational conditions of h_{bed} 24cm and 65kW$_{th}$.*

Both white wood and oat hull waste show similar Si contents in their ash coatings in Figure 4.11, whereas wheat straw presented notably more Si, albeit with more variance. Miscanthus showed the highest silica content within its ash melts and also had the highest Si content of any of the fuels ashes at 56.5wt.% (see Chapter 3 section 3.8.1). This behaviour is likely due to silica being a more integral factor in the larger ash phases found when using wheat straw and miscanthus and is a result of the melt-induced agglomeration mechanism whereby fuel ash itself drives ash melting and agglomeration. The higher phosphorous content of the oat hull waste ash likely assisted in the propagation of agglomeration, with others having noted phosphorous to react to form low melting point potassium phosphates in prior works [94, 95, 185]. Given the low quantity of calcium in the oat hull waste ash, it is likely that there was some formation of potassium phosphates, as opposed to direct reaction of potassium with silica in the sand, thereby worsening agglomeration. An example EDX mapping image

showing this phosphorous behaviour with oat hull waste is presented in Figure 4.12 showing the abundance of potassium and phosphorous in the central join region, and relative deficit of silicon in the same zone.
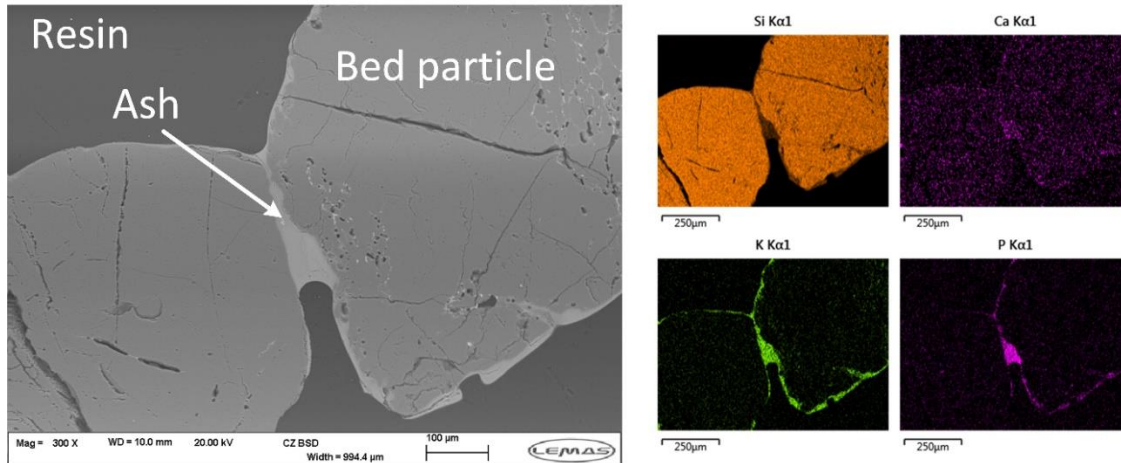
Figure 4.12: *EDX map of agglomerate sample from oat hull waste and sand 'A' test showing a join with high levels of potassium and phosphorous, likely evident of low melting point potassium phosphates forming to propagate agglomeration.*

As shown in Figure 4.11, when using olivine 'A' with wheat straw, there is around 8% MgO in the ash melt surrounding olivine, which is more than double the 3.6% MgO present in wheat straw fuel ash itself (see Chapter 3 section 3.8.1). Iron content is also elevated in the ash around olivine at around 5%, versus 1% Fe_2O_3 in the wheat straw ash itself. When considering contents of magnesium and iron in ash melts when using sand 'A' and wheat straw in Figure 4.11, there is around 4% magnesium and <1% iron, both of which are in line with what would be expected as per the fuel ash analysis (see Chapter 3 section 3.8.1). Furthermore, calcium contents in ash melts around olivine are on average around 4% lower than those in ash melts with wheat straw and sand 'A' (Figure 4.11). This adds further qualitative support to the theory that a mechanism similar to that proposed by Kuba, et al. [118] for wood fuels and olivine has occurred here, instead with wheat straw and olivine, as was discussed in detail in section 4.3.7.2. This mechanism is where calcium has migrated from ash into the outer crystal structure of the olivine, expelling magnesium and iron oxides from olivine into the ash, hence the elevated levels of these in the ash surrounding olivine.

4.3.7.4   Compositional Variation with Bed Location

Figure 4.13a shows the effect of static bed height on ash coating layer composition for white wood and oat hull waste pellets. The zone from which all samples were taken (mid vertical strata, zone A; refer to Chapter 3 section 3.3.3 for bed sampling zonal map) is a fixed location relative to the geometry of the combustion chamber. This location will therefore be lower relative to the bed surface with each increase to h_{bed}. There are a few consistent trends seen with increases to bed height for both white wood and oat hull waste, namely a decrease in Si and K content (albeit a minor decrease in K for oat hull waste), and an increase in Ca content. A likely explanation for this is the effect of increases to bed height on vertical mixing within the bed. As was discussed in section 4.3.4, bubbles will coalesce to larger sizes as they rise through a larger bed height, thereby changing the vertical mixing patterns in the bed. As fuel is fed onto the bed surface, the changes to the bed height and the resultant change to mixing regimes may reduce the amount of fresh fuel mixed into deeper regions of the bed, with the sampling location (mid vertical strata, lateral zone A) becoming deeper relative to the bed surface with each increase to h_{bed}. This lack of fresh fuel would limit the amount of potassium available to attack the sand bed particle, and instead allow calcium silicate compounds (e.g. $CaSiO_3$) to form in the ash layers. Calcium inclusion in melt layers may lead to both the displacement and release of potassium to the gaseous phase [245], and to the protection bed particles from further ash attack [119]. The combined effects of these behaviours would therefore lead to the composition variance in K and Ca seen here.

Figure 4.13b shows the differences in composition for agglomerate ash layers taken from the 'upper' and 'mid' vertical strata of the bed, for tests using oat hull waste and sand 'A'. In comparison to samples from the upper vertical strata, samples from the mid vertical strata presented less K and Al, and more Ca, albeit in very small amounts given the small amount of CaO in oat hull waste ash (3.9wt.%, of a total fuel ash content of 2.66wt.%). This is the same trend as seen with variation to bed height: moving down the bed, away from the surface onto which fresh fuel is fed, bed particle ash layers have less K and here very slightly more Ca. Once again, the reasoning for this composition difference across vertical strata is likely similar: a reduced availability of fresh potassium in lower regions of the bed allowing for formation of more calcium silicate in the ash layers and preventing further potassium reaction with the bed particle [119]. It

should be noted that the upper and mid vertical strata samples were retrieved from two distinct lateral bed zones, however differences across lateral bed regions showed alignment with these trends as will be discussed in the following paragraph.
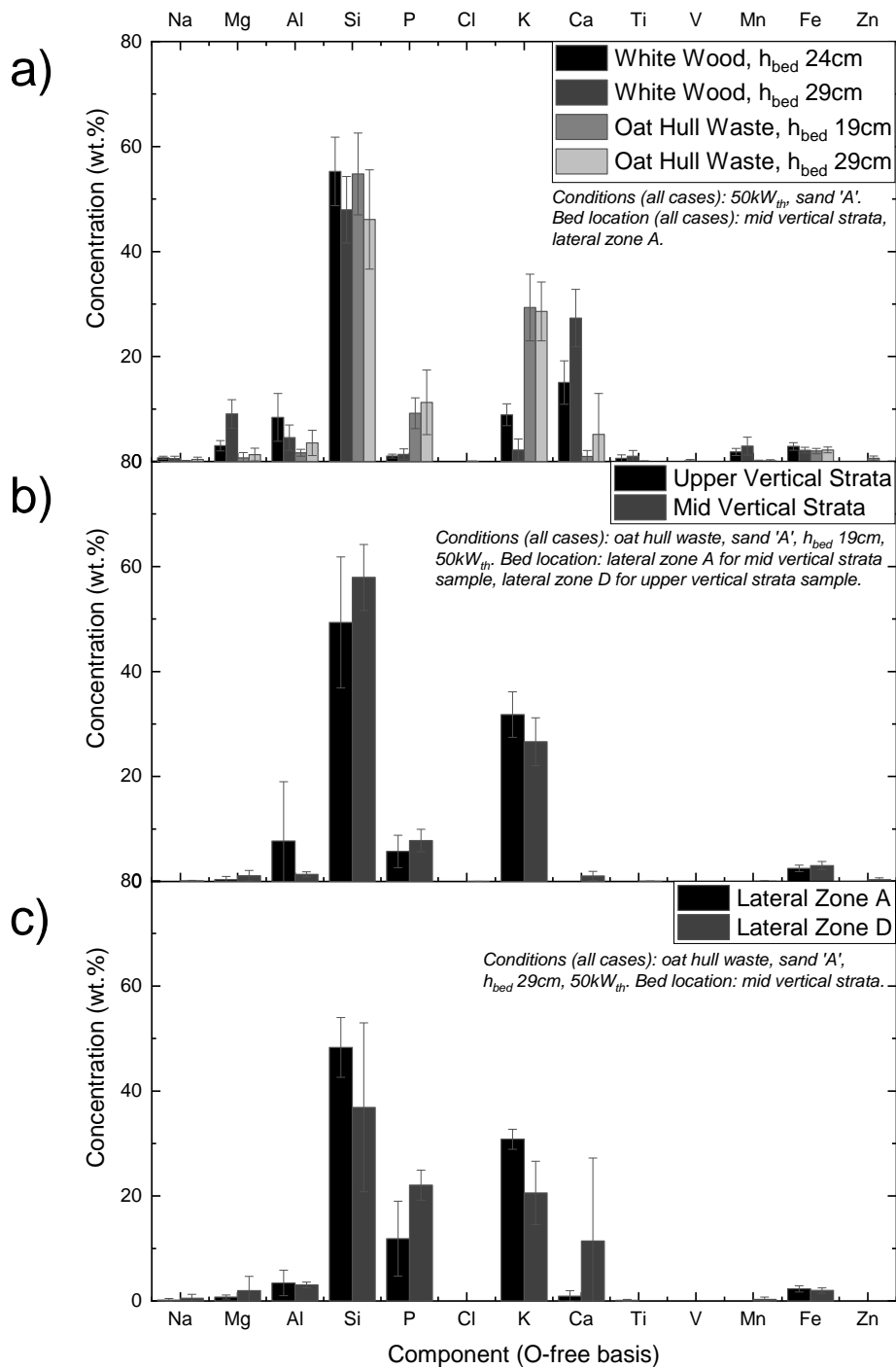
Figure 4.13: *EDX analysis showing the effect of spatial variation within the bed on ash layer composition. a) Effect of bed height on ash layer composition. Samples taken from same test conditions (sand 'A' at 50kW$_{th}$) and location (mid vertical strata, lateral zone A). b) Effect of moving from the upper to the mid vertical strata within the bed. Samples taken from lateral zone A for mid strata sample and lateral zone D for upper strata sample. Test conditions: oat hull waste, sand 'A', h$_{bed}$ 19cm, 50kW$_{th}$. c) Effect of moving from lateral zone A to zone D across the mid vertical strata. Test conditions: oat hull waste, sand 'A', h$_{bed}$ 29cm, 50kW$_{th}$.*

Differences in agglomerate ash layer composition across lateral sampling zones A and D at the 'mid' vertical strata of the bed were compared for an oat hull waste and sand 'A' test, and are shown in Figure 4.13c. As can be seen, there are clear compositional differences between agglomerate samples from zone D, a corner away from the fuel landing location onto the bed, versus zone A where fuel approximately lands in the centre of the bed. In zone D, ash layers presented elevated amounts of phosphorous and calcium, and lower amounts of silicon and potassium. Other elements were present in negligible amounts or had little to no variation between the two zones. As with bed height variation and vertical strata variation, agglomerates in regions further from the landing location of fuel onto the bed (zone D in this case) had reduced K and elevated Ca in their ash coatings. It is likely that this would be due to the same reasoning suggested previously for bed height and vertical strata agglomerate sampling variation: zones further from the fresh fuel feed landing location onto the bed receiving less fresh potassium, thus allowing for more development of calcium silicate in ash layers and less attack on the bed particle surface from potassium.

The only work in that literature to the authors knowledge that analyses agglomerate composition differences between different bed spatial locations is that of Duan, et al. [163], who analysed potassium contents of agglomerates retrieved from different vertical regions of the bed when using rice straw, as well as blends with coal. Duan, et al. [163] recorded that samples retrieved from higher regions of the bed had elevated potassium contents, which would agree with the observations and theory here. A potassium delta of around 2.75wt.% was seen by Duan, et al. [163] between their grid zone region and upper bed region for tests with rice straw only, albeit with a very large relative potassium difference (0.25wt.% in the grid zone, 3wt.% in the upper bed region). In comparison, the largest potassium delta here was 6.7% between the two white wood cases when comparing samples between bed heights in Figure 4.13a, but this had a far smaller relative potassium difference than the 12x delta observed by Duan, et al. [163]. When comparing across the mid and upper vertical strata in Figure 4.13b, samples from the mid vertical strata presented ~5% less K and ~6% less Al, and ~4% more Ca. This potassium delta is similar to the 6.7wt.% delta seen with white wood samples when comparing between bed heights in Figure 4.13a, and is larger than the absolute difference seen by Duan, et al. [163] (2.75wt.%), however again shows a far smaller relative difference than the 12x delta seen by Duan, et al. [163]. Lateral

composition variances were not analysed by Duan, et al. [163], and have not received prior attention in the literature to the authors knowledge, so cannot be compared in a similar manner.

These findings of spatial variance in agglomerate ash layer composition laterally and vertically would suggest that if a targeted agglomeration mitigation method were to be designed, it would be best to target location(s) in which fresh fuel initially lands on and mixes into the bed. The cross-sectional bed area of the pilot-scale fluidized bed used here is only 39x35cm with a single screw feeder, whereas industrial BFB boilers often have cross-sectional lengths/widths upwards of several metres, with multiple screw feeders [22]. Therefore, there may be value in exploring a bed zonal analysis of agglomerates in a commercial BFB boiler to determine the amount of variance when moving to a larger scale with a more complex fuel feeding arrangement.

4.3.7.5 Impact of Material and Locational Variation on Agglomerate Composition

Across sections 4.3.7.3-4.3.7.4, it can be seen that changes to fuel, bed material, bed height, and bed location have varying degrees of impact on agglomerate composition. Table 4.6 summarises the relative impact that changes to each of these conditions had on agglomerate ash layer composition. This is summarised in terms of the typical variation and the maximum variation seen in ash content when comparing the impact of different fuels, bed materials, bed heights, or spatial location of a sample. This table thus quantifies the impact of changes to each of these factors and allows determination of the most important factors for mitigating agglomeration.

Fuel and bed material both had the largest relative influence on ash layer compositions in agglomerates, with fuel the greatest of the two. This is as would be expected, given that changes to fuel will alter the input chemistry of the ash system that leads to the formation of agglomerates, whilst changing from a silica sand to olivine bed material will alter the reactivity of the ash with the bed material.

In comparison, more subtle changes to ash layer composition arose when altering bed height or sampling from different areas of the bed. Variation to lateral bed location of the sample appeared to have the biggest effect of the spatial changes. This showed a maximum of a 10wt.% difference in calcium composition. There was little significant difference between the impact of changes to bed height versus changes to the vertical

sampling location. This is understandable as changes to bed height, when sampling from the same fixed bed location, is in effect the same as sampling from a different vertical stratum as discussed in section 4.3.7.4. Furthermore, the relatively shallow bed height (24cm) may have limited the degree of change compared to what might be seen in a commercial boiler for example. Overall, only changes to the input chemistry of the bed will have a considerable impact on agglomerate chemistry, with spatial variances apparent but not nearly as severe. This raises the question as to the impact of additive use for agglomeration mitigation, which is the focus of Chapter 5.

Table 4.6: *Table summarising the impact of different fuel, operational, and locational variables on agglomerate composition as investigated in this work. This summarises the typical impact and the largest observed impact of each variable, e.g. switching from white wood to wheat straw fuel, or sand to olivine bed material, or upper to mid vertical strata, etc.*

Variable	Figure	Typical Impact on Average Ash Layer Composition (wt.%)	Largest Observed Impact on Average Ash Layer Composition (wt.%)	Overall Impact on Ash Layer Composition
Vertical Bed Position	Figure 4.13b	2-5	8	**LEAST**
Bed Height	Figure 4.13a	0-3	9	
Lateral Bed Location	Figure 4.13c	5-8	10	
Bed Material	Figure 4.11	3-8	15	
Fuel	Figure 4.11	5-10	20	**GREATEST**

4.3.7.6 Deposition Probe Samples

4.3.7.6.1 Ash Deposit

Figure 4.14a shows a SEM image of a portion of the full height cross-section of the ash deposit which formed on the deposition probe (pictured in Figure 4.6). The height of the deposit is approximately 2200µm, with a particle size gradient visible of smaller particles towards the bottom on the deposit (adjacent to the probe) and slightly larger particles in the upper deposit. This size gradient indicates that there was likely the initial formation of a rough layer of smaller particles and ash on the probe, which then allowed for larger particles to remain in place when falling onto the probe. The entire lateral length of the deposit was analysed, however there did not appear to be any significant lateral variation in structure or composition of the deposit, in terms of either the presence of ash particles or loose bed particles. This may be due to the relatively low age of the deposit (approximately 50 hours), with a longer exposure times required the development of different strata or layers as is typical of slagging behaviours in

commercial boilers [79]. Bed particles in the deposit were likely derived from the fines fraction of the olivine bed material, or fragmented pieces of larger olivine particles, as they generally varied in length/width from 20-200µm, despite the test campaign being performed with olivine 'B' of a 664µm average particle size.
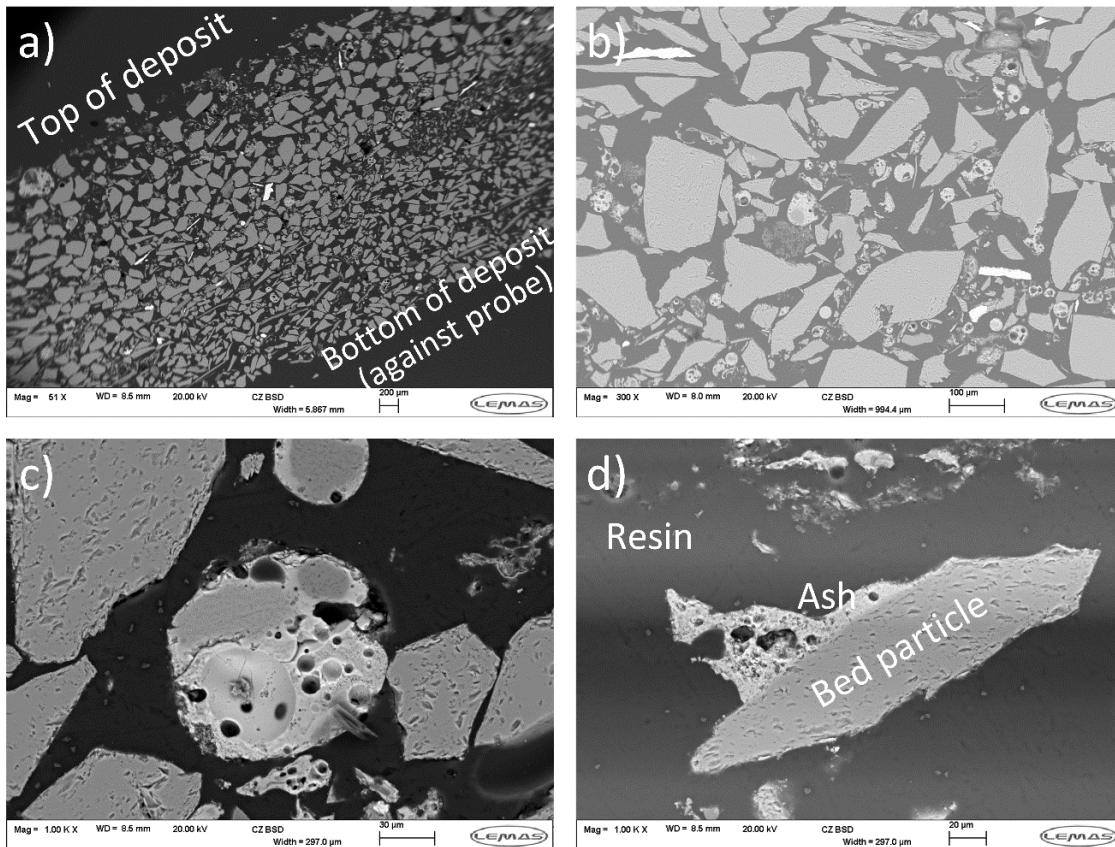
Figure 4.14: *SEM images of the probe deposit formed during wheat straw and olivine 'B' tests. a) Cross-section of the deposit. A size gradient of smaller particles towards the bottom of the deposit (against the probe surface) and larger particles at the top of the deposit is clearly visible. b) Typical section of the probe deposit, showing the mixture of bed particles and ash deposits. c) Closer image of an "ash ball" frequently seen throughout the deposit structure. d) Ash deposit on a bed particle, similar in structure to what would be found within the bed after a test.*

Figure 4.14b shows a SEM image of a smaller section of the deposit. As can be seen, it is formed of mixed fragments of bed material and small fly ash "balls" (shown in greater detail in Figure 4.14c). In some cases, there was direct deposition of ash onto bed particles in the deposit, as shown in Figure 4.14d. This suggests that the formation of the deposit was due to ash adhering to the bed particles on the probe.

Figure 4.15 compares the average composition of ash deposit sites analysed from the probe deposit versus bed agglomerates from olivine and wheat straw tests. The ash deposit composition on the probe differed from that of bed agglomerates, in that it had less silicon, magnesium, and potassium content, but more calcium and phosphorous

content. This left the ash deposits on the probe closer in composition to that of the wheat straw fuel ash itself, with similar potassium and calcium contents, and a silica content slightly under 40wt.% (see Chapter 3 section 3.8.1 for full fuel ash composition). This indicates that ash in the deposit underwent little direct reaction with the bed particle fragments on the probe. It should be noted that as discussed in sections 4.3.7.1 and 4.3.7.3, there was generally little reaction in between ash and olivine in the bed, therefore even less would be expected on the probe given that it was at a lower temperature of around 500-600°C in comparison to the bed at 800-900°C. Therefore, the formation mechanism of the deposit appears to be due to the deposition of molten fly ash and bed particles onto the probe after having lost velocity in the vicinity of the probe, with the molten ash acting as a glue to hold the deposit together where possible. It may also be possible that some bed particles were coated with ash prior to landing on the probe, either when entrained in the gas, or prior to entrainment in the bed.
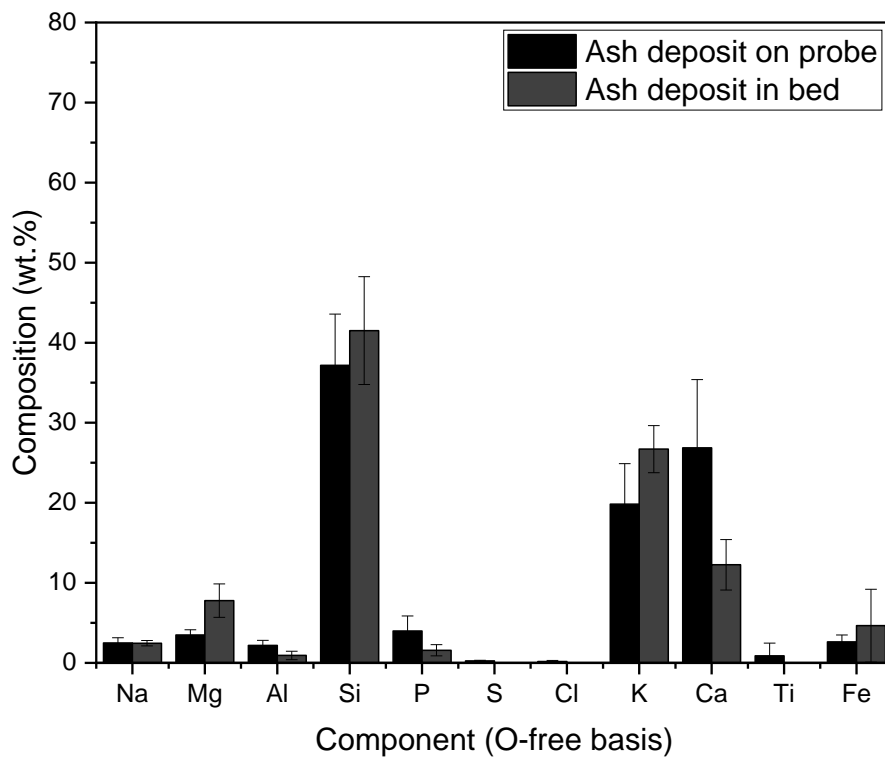
Figure 4.15: *EDX data for ash deposits on the probe (after having using wheat straw and olivine 'B') versus averaged EDX data from a bed sample following a wheat straw and olivine 'A' test. Multiple sites of a similar nature were averaged to produce the above graph. Note that chemical compositions of olivine 'B' and olivine 'A' are near identical.*

4.3.7.6.2 Spent NiAl Coupon

The NiAl-coated coupon upon which the deposit was found (pictured in Figure 4.6) was cross-sectioned along its longest axis, and the entire length examined with SEM/EDX to determine if any initial signs of corrosion or damage could be observed. Example sections of the coated coupon, together with the location of six EDX analyses sites, are shown across Figure 4.16. As can be seen, the outer surface of the coating is uneven, likely from application. Overall, the coating area generally appears uniform and homogeneous, with no evidence of damage or attack (e.g. pitting [246]).
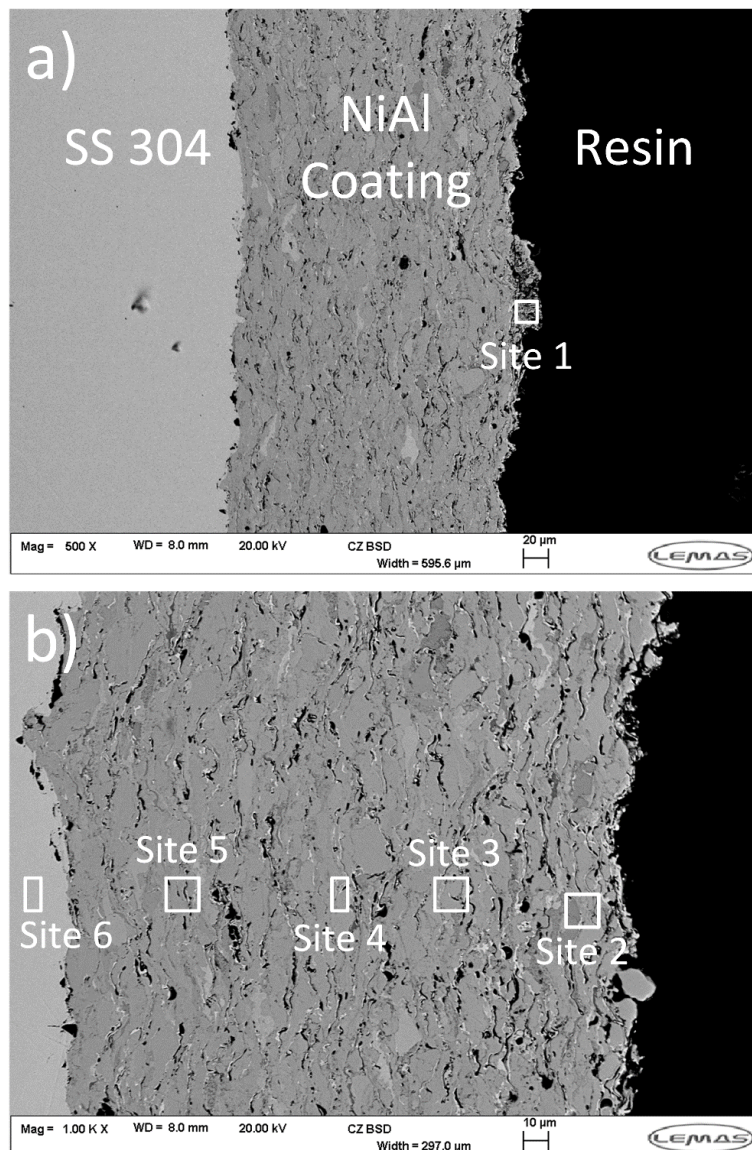
Figure 4.16: *SEM images of a cross-section of the coated NiAl coupon upon which the ash deposit was formed, with EDX locations marked and numbered. EDX results for all six sites given in Table 4.7. a) Image of the only section of the coupon where an anomaly could be found with the "lifting off" of some of the coating in the "site 1" region. b) Further magnified SEM image of the coating, which underwent EDX analysis across its' entire cross-section.*

EDX data for the six sites marked in Figure 4.16 is given in Table 4.7, together with the original specification for both the NiAl coating layer and the stainless steel (SS) 304 base metal. Site 1 was taken from a different location on the coupon than sites 2-6 and was the only location along the length of the coupon at which it appeared a small fragment (~60x20µm) of the coating may have "lifted off" from the bulk of the coating (as seen in Figure 4.16a). Site 1 shows a 10-12wt.% decrease in nickel content versus sites 2-5 and the NiAl coating specification, and a corresponding increase in oxygen content to 15wt.%. This implies there was some oxidation of nickel in the coating at this location. Sites 2-5, taken from the second location on the coupon, generally have very similar compositions, with only very low levels of oxygen shown in sites 3-5 (closer to the base metal than site 2). The base metal (site 6) shows a composition near identical to the SS 304 material specification.

Overall, this would indicate that the NiAl coupon did not suffer any corrosion or attack from the gaseous environment or deposit over the test period, aside from the single ~60x20µm location noted (site 1) in which a portion of the coating appeared to have "lifted off" from the bulk coating. This may itself have been the result of a fabrication imperfection. Others have tested this NiAl coating recently in highly corrosive gaseous environments (high HCl, KCl) for periods of 250 hours and observed corrosion of the coating [229], therefore a longer study would be more beneficial to observe corrosion mechanisms within a FBC environment. However, due to the realities of operating the pilot scale FBC unit (no bed ash removal leading to eventual defluidization, availability of operators, time within the working day to safely operate the unit) it was unrealistic to attain such an operational time for this work campaign.

Table 4.7: *EDX data for the six sites shown in Figure 4.16, plus the specification data for the SS 304 base metal and NiAl coatings.*

EDX Site	Description	Composition (wt.%)							
		O	Al	Si	Ca	Cr	Mn	Fe	Ni
1	NiAl Coating	15.26	25.84		0.14				58.76
2	NiAl Coating		27.44						72.56
3	NiAl Coating	2.48	23.35						74.17
4	NiAl Coating	1.54	24.84						73.62
5	NiAl Coating	2.75	25.44						71.8
6	SS 304 Base Metal			0.41		18.90	1.61	71.39	7.7
-	NiAl Coating Specification		31.0						69.0
-	SS 304 Specification *(major components only)*			1.00		18.50	2.00	69.02	9.25

4.4   Chapter Summary

White wood was found to be the best fuel as it did not undergo bed defluidization during testing. This was due to its very low ash content (~1wt.%). Miscanthus was marginally better than oat hull waste, but both experienced defluidization. Wheat straw was by far the worst fuel tested, with defluidization times around or below 30 minutes at identical operating conditions to the other fuels, driven by a combination of high ash content and high alkali metal content.

NO_x emissions increased in the order of increasing fuel bound nitrogen content, indicating that fuel NO_x mechanisms are the primary driver of NO_x formation. Only white wood would meet the EU IED NO_x limits without the use of additional NO_x mitigation methods (e.g. air staging, selective non-catalytic reduction).

In changing operational conditions, it was seen that a 24cm bed height was the optimum for the unit and gave longer defluidization times than larger or smaller bed heights. It is suggested that this is because of reduced ash to bed volume at lower bed heights, and poorer bed mixing at larger bed heights. Olivine was seen to lengthen defluidization times by upwards of 25% when using wheat straw. This is due to its lower silica content causing reduced reactivity with biomass ash, though other physical factors may also have contributed to this difference as will be discussed in Chapter 5. Smaller size grades of olivine further extended defluidization times with wheat straw by 10%.

White wood and oat hull waste agglomerated mostly via a coating-induced agglomeration mechanism, whereas miscanthus and wheat straw did so through a melt-induced agglomeration mechanism. Melting was more severe with the wheat straw versus miscanthus, hence its far worse performance in comparison to the miscanthus.

New agglomeration behaviours were seen with wheat straw and olivine, a combination not tested previously in the literature. The potassium silicate fraction of ash melts penetrated deeply into fractures and cracks in olivine particles. This behaviour would prevent particles that are part of an agglomerate from disintegrating along these fracture lines, due to the ash melt holding the structure together. This would keep the average particle size higher and shorten the time to defluidization. Previously, others have only seen inward reaction of ash with sand to generate this behaviour, whereas here there was no reaction with the olivine, and it was more likely due to capillary action drawing in the potassium silicate melt fraction. Calcium rich layers were seen to form around

olivine particles embedded in wheat straw ash. It is suggested that this is due to the inclusion of calcium into the olivine matrix and the expulsion of magnesium and iron.

Investigations into spatial variances in different zones of the bed showed that ash layers on agglomerates retrieved from zones further from the landing location of fresh fuel onto the bed had less potassium and more calcium. This is likely due to a lower availability of potassium further from the fuel feed location, allowing calcium silicate to form in ash layers and prevent the continual attack on the bed particle by potassium.

From extended use of a deposition probe with wheat straw and olivine, a small deposit consisting of fine bed material (50-200µm) and fly ash was formed on the leeward side of the probe. There was limited reaction between the ash and bed material on the probe, likely due to the reduced temperature of the probe location in the freeboard versus the bed, though little reaction in general was seen between the olivine and wheat straw ash. This deposit likely formed due to carryover of fines that then lost velocity around the probe and hence formed a deposit. No evidence of significant corrosion could be found on the NiAl coated coupon that the deposit was situated on, likely due to the combination of short exposure time (approximately 50 hours) and the relatively low temperature at the probe location of 500-600°C. A small ~60x20µm region showed some minor oxidation of nickel and had physically lifted off from the coupon.

Chapter 5

The Effect of Bed Additives on Agglomeration

A version of this chapter has been submitted by the author to a peer reviewed journal:

> *The effect of using kaolin and dolomite additives to mitigate agglomeration with challenging agricultural biomass fuels. **Morris, J.D.**, Daood, S.S., Nimmo, W. Unpublished manuscript under submission.*

Within this chapter, content has been expanded or abridged in different areas as required to be commensurate with normal thesis formatting.

5.1   Introduction

The use of additives to mitigate ash issues with biomass fuels has been trialled for around 20 years [87, 165]. As discussed in Chapter 2 section 2.3.10, aluminium, calcium, and magnesium rich additives have all been shown to have some positive effect on raising ash melting points, which would in turn reduce agglomeration issues [164]. There have also been many works in recent years performing fundamental studies into ash and additive blends [165, 170, 247, 248, 249]. However, as was also discussed in the literature review, there are no available works on the optimization of additive dosage rate and usage [84] for agglomeration mitigation. Moreover, most work using additives, both commercially and within academic literature, has focused on their use with woody fuels [72, 166, 167] as opposed to non-woody fuels, such as straws and wastes [116, 178]. Non-woody are increasingly likely to be considered as a partial feedstock within FBC units in the UK, due to the high demand placed on wood fuel stock within the UK, a point noted in Chapter 1 section 1.5. As seen in Chapter 4, all the non-woody fuels that were tested displayed severe agglomeration tendencies and would need additional measures such as additive use to be viable fuels.

In this chapter, the impact of varying additive dosage is explored for two additives, kaolin and dolomite, used with two agricultural biomass fuels, wheat straw and miscanthus. The objective was to evaluate the effect of varying additive dosage (on a

wt.% additive to wt.% fuel ash basis), determine the performance benefit of each additive, and determine the fundamental agglomeration mitigation behaviours of each additive with each fuel. As in Chapter 4, the impact of these changes on operational performance (temperatures, emissions, defluidization times) and agglomeration mechanisms has been considered.

5.2 Experimental Matrix

Specification data for all fuels, bed materials and additives used in this chapter is given in Chapter 3 section 3.8. The same batches of pelletized wheat straw and miscanthus fuels that were used in Chapter 4 were also used here. As seen in Chapter 4, wheat straw was by far the worst of the four fuels for agglomeration severity, whereas miscanthus was notably better. The selection of these two fuels therefore presented a case of a "very bad" fuel and an "ok" fuel. Moreover, these fuels have received little to no attention with regards to their agglomeration behaviours when using additives [116, 171]. Sand 'B' from the work in Chapter 4, the composition for which is given in Chapter 3 section 3.8.2, was selected as the bed material for testing. This will henceforth be referred to as only "sand" in this chapter. This material was selected because in the context of a commercial FBC boiler, an operator may weigh up the cost-benefit of a total bed material change (e.g. to olivine) versus use of sand with a smaller amount of additive.

The kaolin and dolomite additives trialled are substantially different to each other. Dolomite is a very fine powder consisting of $MgCO_3$ and $CaCO_3$. Kaolin is closer in particle size to the sand, and is an aluminosilicate, comprising 42wt.% Al_2O_3, 54wt.% SiO_2. Both additives have seen some amount of testing and success in literature for biomass ash issues [164], with kaolin receiving notably more attention for agglomeration mitigation, and is used in commercial boilers with woody fuels [72]. Therefore, both were ideal candidates for testing with challenging agricultural fuels.

The experimental matrix for this chapter is given in Table 5.1. Tests of each fuel with no additive were performed as part of work in Chapter 4, and this data is used in this chapter as a point of comparison. Operational conditions were kept identical across all tests, of a 65kW$_{th}$ thermal rating, 24cm bed height, and 2U/U$_{mf}$ fluidization number. A target operational time of 2 hours with additive was chosen as a set point. Additive dosages were calculated based on the equivalent fuel ash mass fed over this 2 hour period, i.e.:

$$M_A = M_{FA} \times D_A$$

Equation 5.1

Where M_A is mass of additive (kg), M_{FA} is the calculated mass of fuel ash fed into the unit over 2 hours at a $65kW_{th}$ fuel input, and D_A is the additive dosage (%). If this 2 hour operational target was reached, the test would continue until the point of defluidization, or until no time remained in the day for the test to continue.

Table 5.1: *Experimental matrix for the additive dosage trials discussed in this chapter.*

Additive	Wheat Straw	Miscanthus
No additive	Yes	Yes
Kaolin	50% (0.927kg)	150% (2.627kg)
(wt.% additive/wt.% fuel ash)	150% (2.915kg)	
	300% (5.831kg)	
Dolomite	50% (0.927kg)	50% (0.876kg)
(wt.% additive/wt.% fuel ash)	150% (2.915kg)	150% (2.627kg)

The additive dosage was added to the bed in one batch during rig preparation, together with the sand. The additive dosage formed part of the 40kg of bed material used in each test to create a 24cm bed height, with the balance to 40kg comprising of sand (as was also described in Chapter 3 section 3.2.4). The additive was added to the middle layer of the bed, with further sand added on top to create the 24cm bed height. It was not placed onto the bed surface during loading. This was done to minimize the risk of any entrainment during start-up with the gas burners, which uses a higher total air flow rate through the bed than is used during operation on biomass. Fluidization of the bed during the start-up period was assumed to mix the additive in the bed. Mixing of the additive in the bed was visually qualitatively confirmed when retrieving bed samples, as the bed and agglomerates were methodically retrieved and sampled with a hand shovel from each zone of the bed. It must be stated that a shortcoming here is the lack of quantitative evaluation of additive mixing throughout the bed. Sieving each zone of the bed after a biomass test would not have been viable, as ash would accumulate on bed material and additive particles thereby distorting their original size distributions. However, it would have been possible to perform a zonal sieving of the bed following a cold fluidization test to confirm even mixing of the additive throughout the bed, but unfortunately this was not performed here.

5.3   Results

Values for defluidization time, and average temperature, pressure and emissions data are listed across the subsequent sections. The definition of defluidization time and the process for determining operational data averages is detailed in Chapter 3 section 3.3.2.

5.3.1   Operational Data

5.3.1.1   Defluidization Time

Figure 5.1 displays defluidization time data for all tests. Baseline data for wheat straw and miscanthus without additives is taken from Chapter 4 and is used for comparison as it was performed at the same operational conditions. Looking firstly at the defluidization time data for wheat straw with additives, neither additive, at any dosage, caused an appreciable increase to defluidization time. Defluidization time remained around the 22 minute value that was seen with no additive use. When operating with wheat straw and additives, it was consistently seen that, as when using no additives, the bed condition would rapidly decline with near immediate visible agglomeration issues seen through the sight glass. A steady state was not achieved in any of these wheat straw tests. It was observed that as wheat straw pellets on the bed were visibly red hot, undergoing char oxidation, they would begin accumulating bed material on their surface. Pellet shaped agglomerates were commonly found following tests with wheat straw. Prior work using wheat straw without additives [124, 130] has shown it to have severe agglomeration issues due to high ash content as was seen in Chapter 4 section 4.3.2.1. However, fundamental studies on the melting behaviours of straw ash with kaolin or dolomite have shown clear increases to ash melting temperatures and reductions in sintering issues [165, 247], a behaviour that here has not translated to the wheat straw pellets in the context of a fluidized bed.

The defluidization time data for miscanthus shown in Figure 5.1 presents an entirely different trend to that of the wheat straw. All three miscanthus and additive test cases prevented bed defluidization, with the time shown on Figure 5.1 reflecting the time from the start of fuel feeding until the end of the test day, versus the baseline result without additive usage of a 159 minute defluidization time. Others have seen benefits to additive use with miscanthus. The work of Kaknics, et al. [116] tested miscanthus with dolomite on an olivine bed and showed that there was evidence of chemical interaction between the dolomite and ash. Similarly, Chi, et al. [171] trialled miscanthus pellets that

were impregnated with a lime additive, as opposed to a bed additive, and observed a substantial increase to defluidization times.
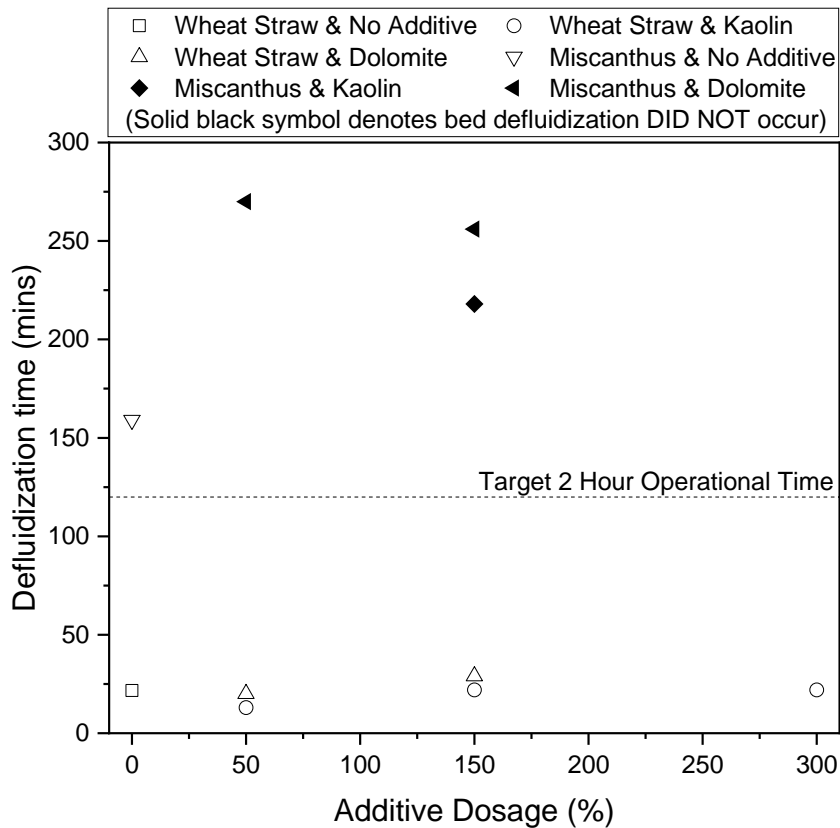
Figure 5.1: *Defluidization time for wheat straw and miscanthus at all additive and additive dosages tested. Note that bed defluidization did not occur for any miscanthus test with kaolin or dolomite. This was due to a lack of time in the day for the respective tests to continue.*

There does not appear to be an apparent chemical reasoning for the significant performance difference between the two fuels with additives. Both wheat straw and miscanthus have similar ash contents (6.67wt.% for the former, 6.01wt.% for the latter). Wheat straw has lower SiO_2 (38.4wt.% vs. 56.5% in miscanthus), but higher K_2O (19.8wt.% vs. 11.7wt.% in miscanthus) and CaO (21.1wt.% vs. 13.5wt.% in miscanthus). The K/Ca ratio is relatively similar (1.87 for wheat straw, 1.73 for miscanthus), with others suggesting a lower value of this ratio to reduce agglomeration severity [171]. Given the similarity is K/Ca ratios between the fuel, it would appear that other factors, such as physical behaviours and the formation of wheat straw agglomerates around fuel pellets as mentioned previously, are more important here. These will be discussed in greater detail in section 5.4.

5.3.1.2   Temperature Profile

Figure 5.2a-b gives the temperature profile for each fuel with and without additives. Both fuels present a very similar profile, of a peak in temperature at around 10cm above the static bed height surface level, indicating that most combustion is still occurring at the bed surface region. This differs from a commercial bubbling fluidized bed boiler, where most combustion occurs in the freeboard region, a shortfall discussed in Chapter 3 section 3.2.11. Temperatures in the bed region here are mostly all within the 800-900°C range, with some localised areas at the top/bottom of the analysed area diverging slightly out of these bounds. This is similar to typical operational temperatures for the bed region in commercial BFB boilers which are 800-900°C [21].
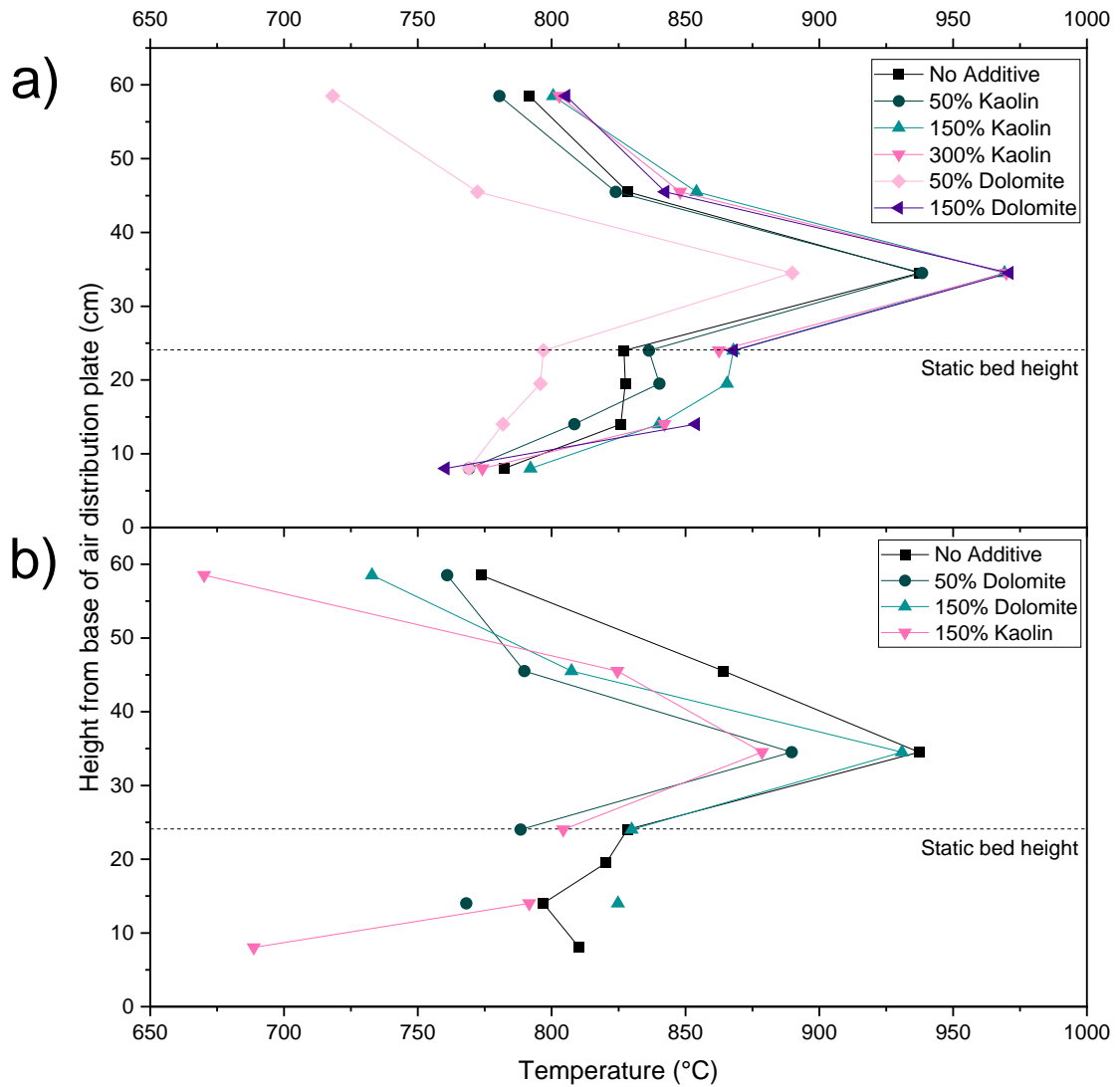
Figure 5.2: Temperature profiles across the bed and above-bed regions when varying kaolin and dolomite dosage. a) Profile for wheat straw with additives. b) Profile for miscanthus with additives.

There is little difference between the profiles with and without additive use. With wheat straw, the greatest divergence is evident in the 50% dolomite test, where some temperatures (e.g. just below 60cm) diverge by around 60-80°C versus those seen during other tests. However, it bears repeating that a steady state of combustion was not achieved for wheat straw due to the short defluidization time, with these temperature profiles reflecting averages of those attained during the short operational time (<30 minutes in all cases). With miscanthus, the temperatures seen are again similar between the fuels. The exception would be the top and bottom ends of the 150% kaolin test profile (8cm & 59.5cm) which are up to 100°C lower than those seen in the other tests. Unlike with wheat straw, miscanthus did not experience bed defluidization with additives so these profiles are averages of steady state data. It is expected that at the pilot-scale there is a larger opportunity for unexpected variation during tests, due to the scale of the unit. Therefore, ideally a repeat of the miscanthus and 150% kaolin case at minimum would have been performed. The low temperature in the 8cm region would itself mitigate agglomeration issues as reduced temperature is known to minimise ash melting [72]. However, it was noted in visual observations of bed retrieval both in this campaign (in subsequent section 5.3.2) and in Chapter 4 section 4.3.5 that at this lower bed region amongst the bubble caps, little to no agglomerates were retrieved across any test therefore there was unlikely to be a notable difference due to this temperature deviation.

5.3.1.3   Differential Pressure Across the Bed

Figure 5.3 presents the evolution in bed differential pressure (DP) across the total run time from initial fuel feeding for the tests with wheat straw and additives. Run time has been re-based to a percentage of total operational time from initial biomass fuel feeding (0%) to bed defluidization (100%). Data is not available for the 300% kaolin test due to issues with the differential pressure probe during this test, with bed defluidization instead visually recorded by the operator.

In all cases in Figure 5.3, from 0-~75% of the run time, there is substantial variation in DP around an average of 10-12mbar, with oscillations from <5mbar to 20mbar. This variation is a result of the motion of the bed under fluidization. The 150% dolomite test shows a slightly higher average DP, with values generally lying in the 12-15mbar range as opposed to 10-12mbar, though still spiking between 5-20mbar. There is also less variation to the DP value for the 150% dolomite test, particularly in the latter half of the

test run. This may be due to a slight error from some minor overfilling bed material to above the 24cm bed height, as air flow rates did remain steady at a fluidization number of $2U/U_{mf}$. Over the last quarter of the run time for the no additives and kaolin cases, DP across the bed decreases towards 0mbar as the bed undergoes defluidization and the fluidizing air flow channels through the static bed body. In the case of the two dolomite tests, the trend towards defluidization occurred more rapidly than for the other tests, in the last ~10% of the run time. This is not necessarily a finding of significance for the dolomite, as the run times in general were very short with wheat straw (<30mins, Figure 5.1) therefore the real difference between these two declining DP phenomena is only a matter of minutes in real time.
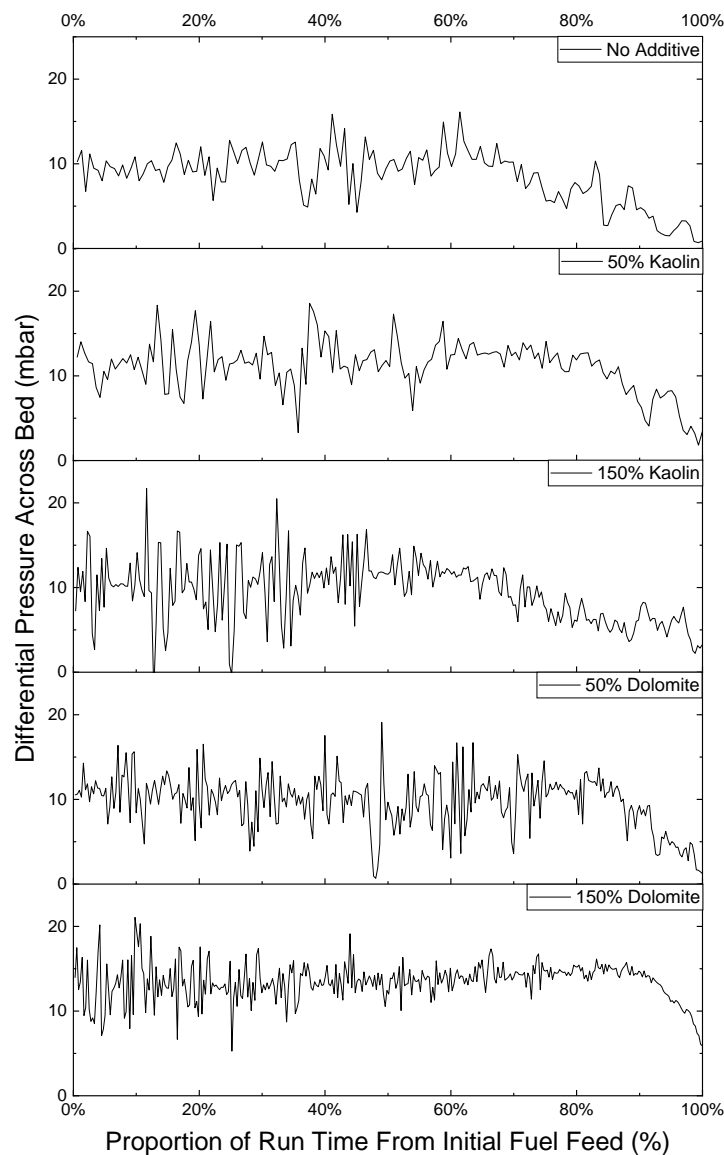
Figure 5.3: *Evolution of differential pressure across the bed for wheat straw and additive tests, from initial biomass fuel feeding to defluidization. Data for 300% kaolin test not pictured due to issues with the differential pressure probes.*

151

Figure 5.4 presents DP across the bed for the miscanthus tests. Again 0% of the run time represents initial fuel feeding, with 100% being the end of fuel feeding or bed defluidization. DP across the bed generally oscillates around 10mbar. In the first ~10-20% of each run, there is generally more variation to DP values, with some oscillations seen again between 5-20mbar. Over time, there is a very slight increasing trend seen to average bed DP. This is due to the accumulation of agglomerates in the bed raising the average bed particle size [9, pp. 71-74]. For the case with no additives, over the last ~2.5% of operational time there is a rapid decline in bed DP trending towards 0mbar, similar to the behaviour seen with wheat straw defluidization. This corresponds to just under 4 minutes of real time.
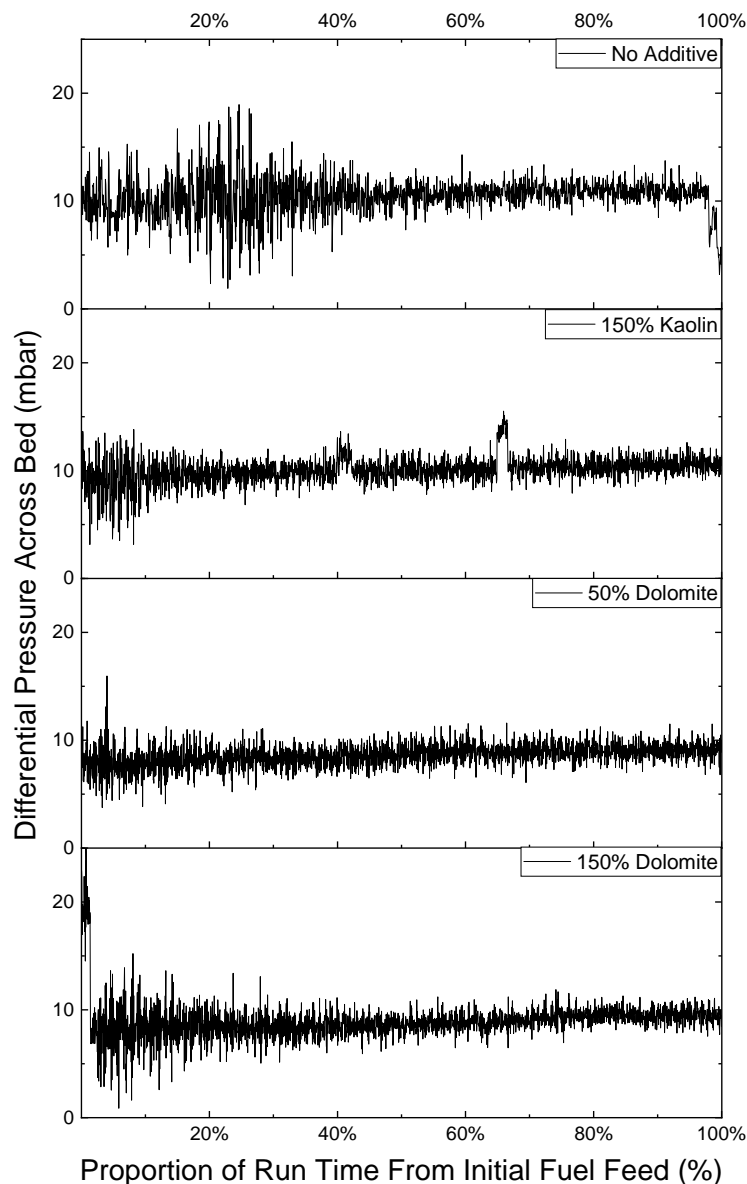
Figure 5.4: *Evolution of differential pressure across the bed for all miscanthus and additive tests, from initial biomass fuel feeding to defluidization or the end of fuel feeding.*

The observed behaviour of a sudden drop in DP at the point of defluidization is well known in literature [9, pp. 71-74, 75], with others such as Chirone, et al. [125] and Scala & Chirone [121] attempting to predict the onset of defluidization on the basis of DP variance. Such an analysis was attempted here but did not reveal any new insight. For wheat straw, this was due to the very short operational times and large amount of variation over this run time, evident in Figure 5.3. For miscanthus the lack of defluidization, and rapid onset of defluidization seen in the case of the no additive test, meant that again no new insight could be made for defluidization prediction purely based on DP across the bed. The pressure data for both fuels does show the similarity in bed hydrodynamic behaviour regardless of the additive used. This is a positive observation considering that the additives were both of a notably lower average particle size than the sand bed material (853μm for the sand, versus 559μm for kaolin and 353μm for dolomite) therefore could otherwise have negatively impacted bed mixing patterns. One potential improvement for the FBC unit, particularly for defluidization prediction, would be to have multiple pressure probe ports around the bed, to measure bed DP in different areas. This may allow for quicker identification of agglomeration issues and is a common equipment configuration in commercial BFBs [75].

5.3.1.4   Emissions

Emissions data for the miscanthus and wheat straw with additives tests are presented on a 6% O_2 basis in Table 5.2. For wheat straw, these values show some degree of difference versus the no additive case, particularly in terms of CO content. However, as noted previously, a steady state was not achieved for any wheat straw tests due to the very short operational times, thus limiting the accuracy of the average taken here. Emissions for miscanthus and additives show more substantial variations, with the 150% dosage cases of each additive resulting in higher CO emissions and lower NO emissions than the no additive and 50% dolomite cases. Above-bed temperatures were observed to be 50-80°C cooler in these 150% dosage tests, which may be the cause of the differing emissions (Figure 5.2). The high levels of CO across the board are likely due to the lower temperatures (700-800°C) seen at 59.5cm in Figure 5.2, which would be even lower at higher areas of the freeboard thus preventing complete combustion of any entrained fines or char particles. Again, this is a design limitation of the current equipment, and would not be an issue in a commercial BFB due to better fuel delivery and air staging leading to a far hotter freeboard and more complete combustion [21].

Table 5.2: *Summary of emissions for all fuels and additive dosages tested. Emissions are presented on a 6% O_2 basis.*

Fuel	Additive	Dosage	CO_2 (vol.%)	CO (ppmv)	NO (ppmv)	NO (mg/m^3)	NO as NO_2 equiv. (mg/m^3)
Wheat Straw	None		14.27	594.94	226.97	238.34	365.46
	Kaolin	50%	13.79	485.11	270.87	284.44	436.15
		150%	14.51	458.00	272.84	286.52	439.33
		300%	14.90	578.86	254.86	267.63	410.36
	Dolomite	50%	14.06	550.91	237.88	249.80	383.03
		150%	15.70	707.67	211.62	222.22	340.74
Miscanthus	None		14.06	568.16	237.02	248.90	381.65
	Kaolin	150%	14.66	911.30	130.59	152.88	234.41
	Dolomite	50%	13.52	525.87	253.35	137.13	210.27
		150%	13.69	779.40	145.58	266.05	407.94

Based on the NO emissions alone, all the test cases would exceed the EU Industrial Emissions Directive (IED) limits for NO_x if used in a larger combustion plant, which are set at 200mg/m^3 for a 300MW$_{th}$ combustion plant [239]. NO emissions have also been presented on the basis on NO_2 equivalent in Table 5.2, as NO rapidly oxidises to NO_2 in atmosphere [250]. These NO levels alone would exceed the total NO_x levels for large combustion plants under directive 2010/75/EU [239]. This would further worsen if assuming the formation of additional NO_2 in the boiler, which could not be measured in this test campaign. Therefore, both fuels would require additional NO_x mitigation strategies (e.g. air staging) if used in a commercial plant as was also concluded in Chapter 4 section 4.3.2.3.

5.3.2   Bed Retrieval Observations

Bed retrieval observations for wheat straw and miscanthus with no additive were discussed in Chapter 4 section 4.3.5. A selection of example agglomerates retrieved following testing with additives is presented in Figure 5.5. With additives, both miscanthus and wheat straw continued to produce agglomerates that were typical of a melt-induced agglomeration mechanism [124]. This was apparent as agglomerates were generally in larger structures (>0.5cm) which are typical of melt-induced agglomeration processes, as opposed to being comprised of a small (i.e. a few bed particles), weakly joined structure, which is more typical of a coating-induced agglomeration mechanism [106]. One clear distinction between the fuels was that wheat straw produced notably more of the fuel pellet shape type of agglomerates than miscanthus did. This was a

universal observation across the additive dosages tested. Whilst miscanthus did produce some of these pellet shaped agglomerates as pictures in Figure 5.5, there was generally a broader mixture of agglomerate sizes.
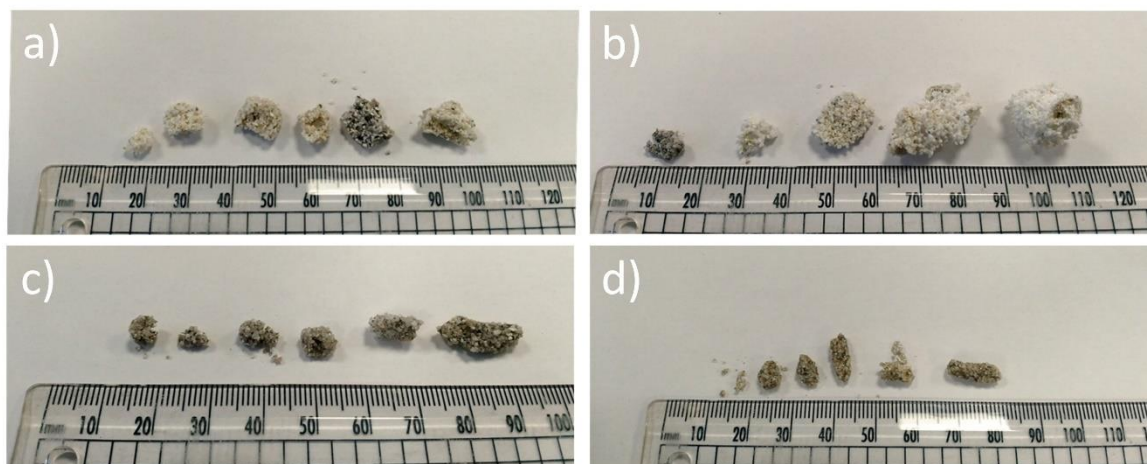
Figure 5.5: *Example of the agglomerates retrieved from the bed across a selection of the different additive case conditions. Scale is in mm. a) Wheat straw & 300% kaolin. b) Wheat straw & 150% dolomite. c) Miscanthus & 150% kaolin. d) Miscanthus & 150% dolomite.*

Agglomerates were sampled from the bed across the three vertical spatial zones as defined in Chapter 3 section 3.3.3. Once again, there were generally little to no agglomerates retrieved from the lower vertical zone amongst the bubble caps, in part due to the difficulty of sampling from this region with the limited space available. No significant trends were recorded from the sampling activity in terms of agglomerate variation across the vertical or lateral axes of the bed. With regards to the impact of different additive dosages, again no qualitative visual differences in agglomeration were apparent between the two additives or the varying dosage rates. There was the clear observation of increased amounts of additive particles within the bed when using higher dosages, which was to be expected and added confidence to the idea that there was not entrainment and loss of large quantities of additive material from the bed despite their smaller particle sizes. It would be difficult to determine the exact quantity of additive material that is unused or lost from the bed, due to the potential for it to contribute to deposition or fouling in the freeboard or heat exchanger, plus inclusion in bed agglomerates, making it highly difficult to create a mass balance. One way to attempt this, in the case of kaolin which impacts alkali chloride content of the gas [84], would be to use an in-situ alkali chloride monitor (IACM). The time for a known quantity of additive to stop having an impact on the alkali chloride content of flue gas could be equated versus the theoretical length of time which it would take for the additive to fully

react with ash, to determine the real proportional consumption of additive. This does assume that the additive in the bed would cease to have an effect at the same point at which it also ceases to affect the alkali chloride balance of the flue gas. IACMs are commercially available [251], but such a device was unavailable here due to cost.

5.3.3 SEM/EDX Approach

The baseline SEM/EDX approach discussed in Chapter 3 section 3.4 was continued here: for each sample upwards of four sites of interest were selected, followed by the collection of quantitative EDX data at upwards of three locations from each site. This minimum was far exceeded for most samples. Quantitative EDX spot/area data was classified based on the type of feature under analysis. A list of these classifications, and a description of each, is given in Table 5.3. This enabled a much broader "meta-analysis" of the chemistry of typical features in agglomerates when using additives, to determine the movements and behaviours of chemical components. A systematic approach of this type to analysis of agglomerates with additives has not been performed in previous works [84, 95, 164, 166, 167, 252], and it has enabled a much clearer picture as to the mechanisms involved, as opposed to just collecting EDX data from a handful of locations and making a judgement as is common in other works.

***Table 5.3:** EDX measurement location classifications. These definitions are used throughout discussions and graphs in sections 5.3.4-5.3.5.*

EDX Measurement Location Classification	Description
Bulk ash melt	Any large ash melt or deposit phase, away from any of the other EDX locations listed below.
Coating layer	Ash coating layer arising from a coating-induced agglomeration mechanism [111].
Ash layer	Discontinuous ash deposit/layer. Thickness ~<50µm. Larger deposits classified as bulk ash melts.
Ash join	Ash join between sand-sand, sand-additive, or additive-additive. Thickness ~<50µm. Larger deposits classified as bulk ash melts.
Additive particle core	Central ~1/3 of an additive particle.
Additive mid/outer particle region	Region between the additive particle core and the ~20µm outer rim of the additive (the rim being the *additive adjacent to its surroundings*, see below).
<x> adjacent to <y>	Region of <x> adjacent to <y> (within ~<20µm). For example, ash melt adjacent to kaolin is the ash melt composition within ~<20µm of the adjoining kaolin particle.

5.3.4   SEM/EDX – Wheat Straw & Additives

5.3.4.1   Agglomerate Structure

Figure 5.6a-f shows SEM images of wheat straw from tests with and without additives. Figure 5.6a-d presents example SEM images of wheat straw with additives, Figure 5.6e-f display the same SEM images of wheat straw and sand without additives discussed in Chapter 4 section 4.3.7.1 (Figure 4.8). These are shown again here as a point of comparison.

Figure 5.6a-b shows two example SEM images of agglomerate structures when using wheat straw with kaolin as an additive. Figure 5.6a is a typical example of a large ash melt structure, a segment of a "pellet shaped" agglomerate, which is typical of a melt induced type agglomeration mechanism [124]. Numerous sand and kaolin particles have become embedded within the large ash melt phase. This type of structure was frequently observed with wheat straw, and in such a situation the additive would have had little effect due to the sheer size of the ash melt phase.

Figure 5.6b is a close-up image of a smaller ash structure with adjoined sand and kaolin. On the lower right sand bed particle, a thin ash coating layer has been annotated. These coating layers, arising from a coating induced agglomeration mechanism [111], were observed here when using additives with wheat straw. Due to the very short operational time, these coating layers remained very thin ($<3\mu$m) and were not seen to be the cause of any joins between bed particles.

Figure 5.6c shows a large ash melt structure with multiple embedded dolomite and sand particles, similar to Figure 5.6a with kaolin, again highlighting why the dolomite had very little impact on the defluidization time of the wheat straw. Figure 5.6d shows a small segment of an ash melt with embedded kaolin and dolomite. The dolomite was very heterogeneous, and sizable ash intrusions into the dolomite structure such as those in Figure 5.6d were frequently observed.

Across samples for both additives, no visual differences could be observed based on dosage or sampling location in the bed. The only difference between dosages was the higher quantity of additive particles when using a higher additive dosage.
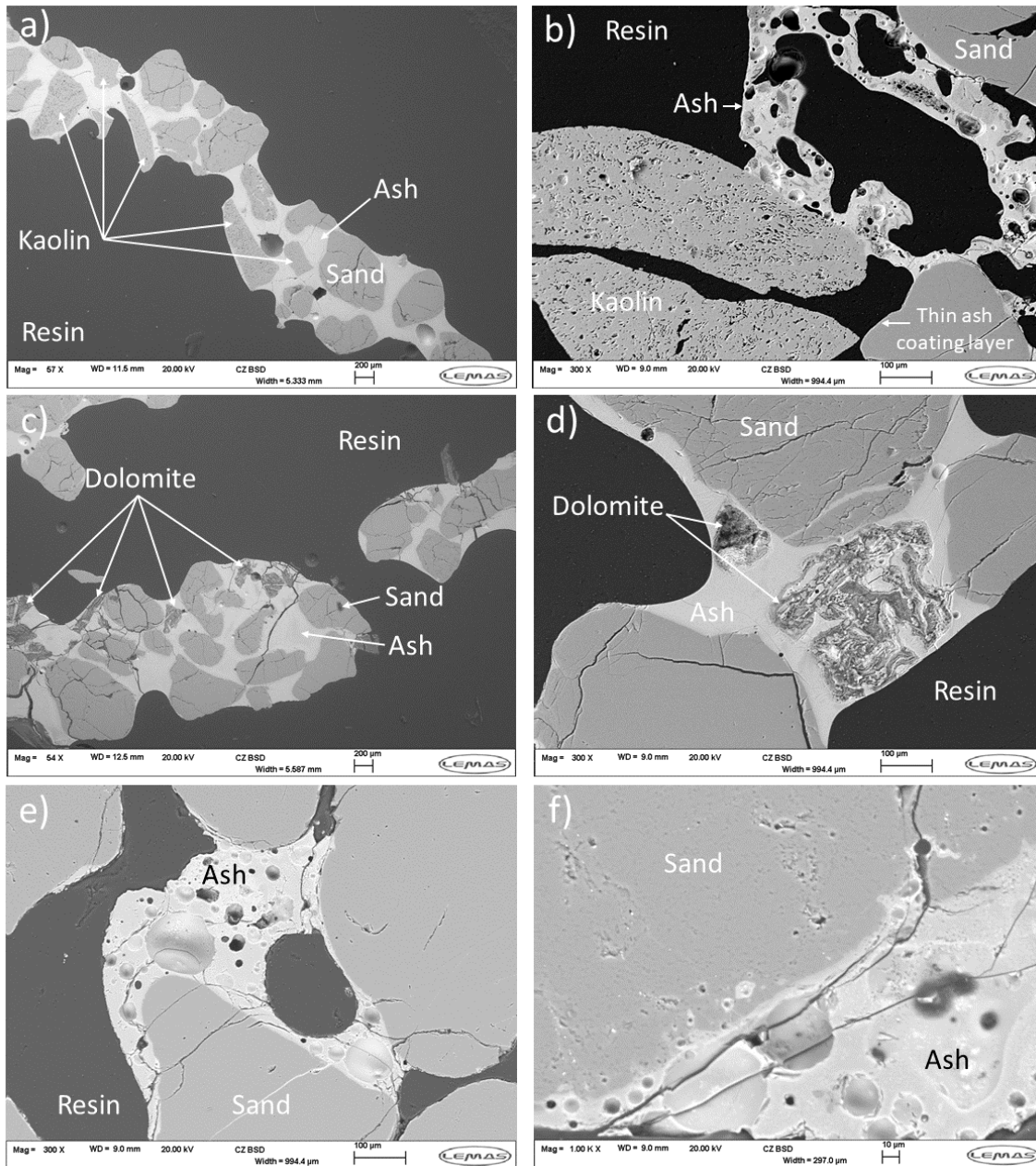
Figure 5.6: *SEM images showing typical agglomerate structures when using wheat straw and additives, with the no additive cases from Chapter 4 also shown for comparison. a) Large ash melt structure with multiple embedded kaolin and sand bed particles. b) Smaller ash melt structure with adjoining kaolin particle. Note the presence of a very early stage, thin ash coating layer in the light shade of grey on the sand bed particle marked. Coating layers were a very rare occurrence with wheat straw. c) Large melt structure with multiple embedded dolomite and sand bed particles. d) Two dolomite particles embedded in an ash melt structure. The right-most dolomite particle has several zones of significant ash intrusion. e-f) Examples of melt formations with wheat straw & no additives, previously shown in Figure 4.8c-d. Figure 5.6e highlights the large ash phases without additives, also present with the used of additives, whilst Figure 5.6f shows the beginnings of ash intrusions into the extremities of sand particles.*

5.3.4.2   Use of Kaolin

Figure 5.7 shows the composition of ash melts on or around sand bed particles and kaolin particles when using wheat straw as a fuel. In ash melt regions adjacent to bed particles, potassium was 4-5wt.% higher than in the bulk ash melt, and calcium content was around 4-5wt.% lower than in the bulk ash melt. This indicates that there was the formation of a potassium rich layer, or "leading edge of attack" directly adjacent to bed particles within the larger ash melt. This shows that within these ash melts typical of melt-induced agglomeration [124], there are reactions between ash and bed particles that are similar to those that would be seen in coating-induced agglomeration [112]. Ash composition around kaolin particles is likewise presented in Figure 5.7. Ash melt regions adjacent to kaolin particles show elevated potassium content and reduced calcium versus the bulk ash melt, suggesting a similar movement of potassium towards the kaolin particle surface as was seen adjacent to bed particles.
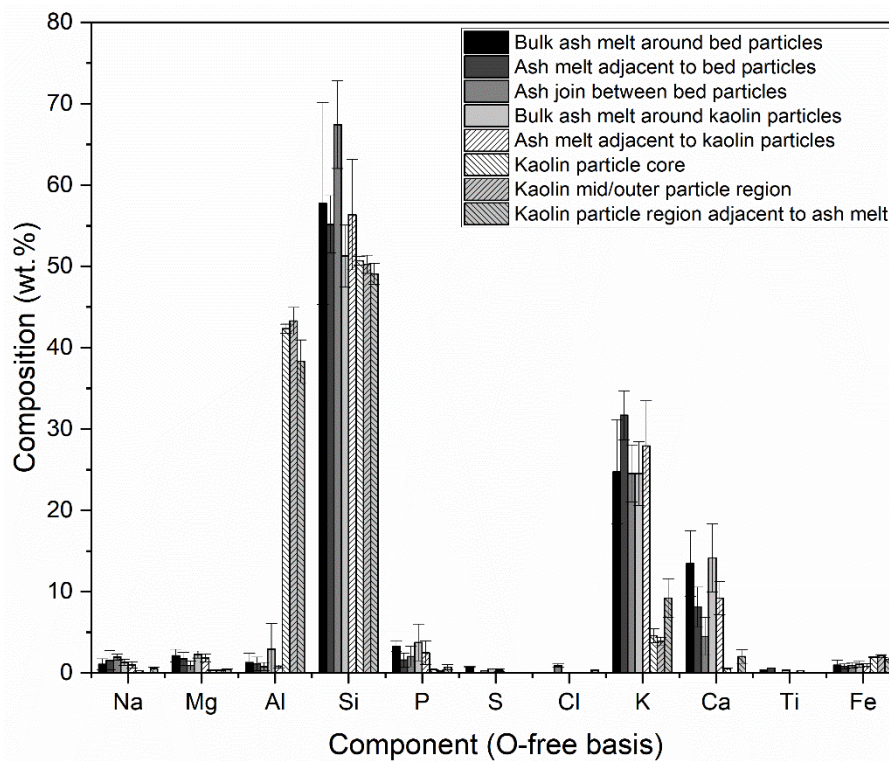
Figure 5.7: *EDX average ash composition on and around sand bed particles and kaolin particles when using wheat straw fuel, together with an analysis of kaolin particle composition under the same conditions. This data is also tabulated in Table 5.4.*

Table 5.4: *Tabulation of the data shown in Figure 5.7. EDX average ash composition and 95% confidence intervals on and around sand bed particles and kaolin particles when using wheat straw fuel, together with an analysis of kaolin particle composition under the same conditions. Data on an O-free basis.*

Component	Bulk ash melt around bed particles	Ash melt adjacent to bed particles	Ash join between bed particles	Bulk ash melt around kaolin particles	Ash melt adjacent to kaolin particles	Kaolin particle core	Kaolin mid-outer particle region	Kaolin particle region adjacent to ash melt
Na (wt.%)	1.07±0.68	1.56±1.17	1.96±0.40	1.33±0.39	1.00±0.37	0.30		0.55±0.20
Mg (wt.%)	2.14±0.79	1.75±0.80	0.92±0.57	2.28±0.43	1.85±0.45	0.36±0.02	0.34±0.02	0.44±0.09
Al (wt.%)	1.28±1.16	1.14±0.82	0.79±0.52	2.93±3.18	0.81±0.17	42.33±0.57	43.29±1.68	38.34±2.63
Si (wt.%)	57.73±12.40	55.18±3.54	67.43±5.40	51.28±3.82	56.38±6.79	50.69±0.55	50.26±1.12	49.07±1.26
P (wt.%)	3.30±0.67	1.62±0.86	2.04±1.27	3.76±2.26	2.51±1.44	0.43±0.03	0.28	0.74±0.31
S (wt.%)	0.75±0.04			0.50	0.35±0.12			
Cl (wt.%)			0.91±0.22					0.35
K (wt.%)	24.74±6.37	31.68±2.98	24.54±3.51	24.50±3.92	27.93±5.56	4.58±0.86	3.93±0.49	9.23±2.34
Ca (wt.%)	13.47±4.03	8.13±2.44	4.50±2.32	14.16±4.18	9.22±2.08	0.49±0.15		2.02±0.82
Ti (wt.%)	0.37	0.61		0.36		0.30		
Fe (wt.%)	0.98±0.62	0.83±0.30	0.93±0.30	1.09±0.35	0.82±0.36	1.97±0.07	2.11±0.16	1.69±0.17

Composition data for kaolin particles adjoining wheat straw ash is also given in Figure 5.7. Kaolin particle averages show very small 95% confidence intervals, indicating a homogeneous chemical structure to the kaolin. There is almost no difference between the kaolin particle core and mid-outer regions, indicating little deep interaction between the kaolin and ash. In kaolin particle regions adjacent to ash there is a clear compositional difference, with decreased aluminium content and near doubled potassium content. This aligns with the prior observation of elevated potassium in ash adjacent to kaolin particles and suggests the mechanism of interaction is the movement of potassium in ash towards the kaolin particle surface, followed be the reaction of the potassium with the kaolin region adjacent to the ash. Others have observed kaolin to directly react with alkali metals from biomass fuel ash [247, 252]. Fundamental studies of ash mixtures with kaolin have shown the reaction of potassium with kaolin to reduce quantities of gas phase KCl, whilst also reducing potassium silicate melt formation by forming high melting point kalsilite ($KAlSiO_4$) [253]. An example of the reaction pathway to form an alkali aluminosilicate between potassium chloride and kaolin is shown below [254]:

$$Al_2O_3.nSiO_2 + 2KCl + H_2O \rightarrow K_2O.Al_2O_3.nSiO_2 + 2HCl_{(g)}$$
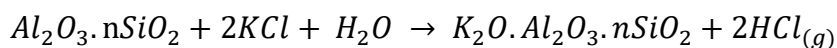
Equation 5.2

5.3.4.3   Use of Dolomite

Figure 5.8 shows composition data for wheat straw ash on and around sand and dolomite particles when using a dolomite additive. This same data is also tabulated in Table 5.5. Ash melt regions adjacent to bed particles show higher potassium and lower calcium content than the bulk ash melt region surrounding bed particles. This is again an indication of potassium forming a leading edge of attack against sand bed particles as discussed in section 5.3.4.2.

The bulk ash melt around bed particles and around dolomite particles, and ash adjacent to dolomite particles, all show higher levels of magnesium and calcium than the other regions analysed. This is particularly notable when considering the ash composition of the wheat straw ash (3.6wt.% MgO, 21.1wt.% CaO). This would suggest movement of calcium and some magnesium out of the dolomite and into the surrounding ash. Higher calcium content in ash melts when using dolomite has been observed by others, where it was suggested that this is due to release of calcium from the dolomite, diluting the ash

melt and reacting to form calcium silicates (e.g. $CaSiO_3$) [165, 247]. Those that have tested dolomite in the context of fluidized bed combustion with biomass either did not investigate or did not note the presence of elevated magnesium in ash [115, 178, 247]. This inclusion of additional magnesium and calcium into the ash melt would allow for the formation of stable high melting point calcium and magnesium silicates, e.g. $CaSiO_3$ with melting point of 1510°C [247] or $MgSiO_3$ with melting point of 1910°C [169], thereby reducing the quantity of molten slag and increasing operational times. Recent fundamental studies of dolomite and straw ash blends have shown the formation of high melting point calcium silicates and calcium magnesium silicates [253]. This supports the stance that these compounds are likely to have formed here also. This would suggest that dolomite has interacted with biomass ash through movement of calcium and magnesium content into the ash, raising eutectic melt temperatures. As with kaolin, it is again clear that there was positive chemical interactive between the wheat straw ash and additive despite the lack of impact on defluidization time (section 5.3.1.1).
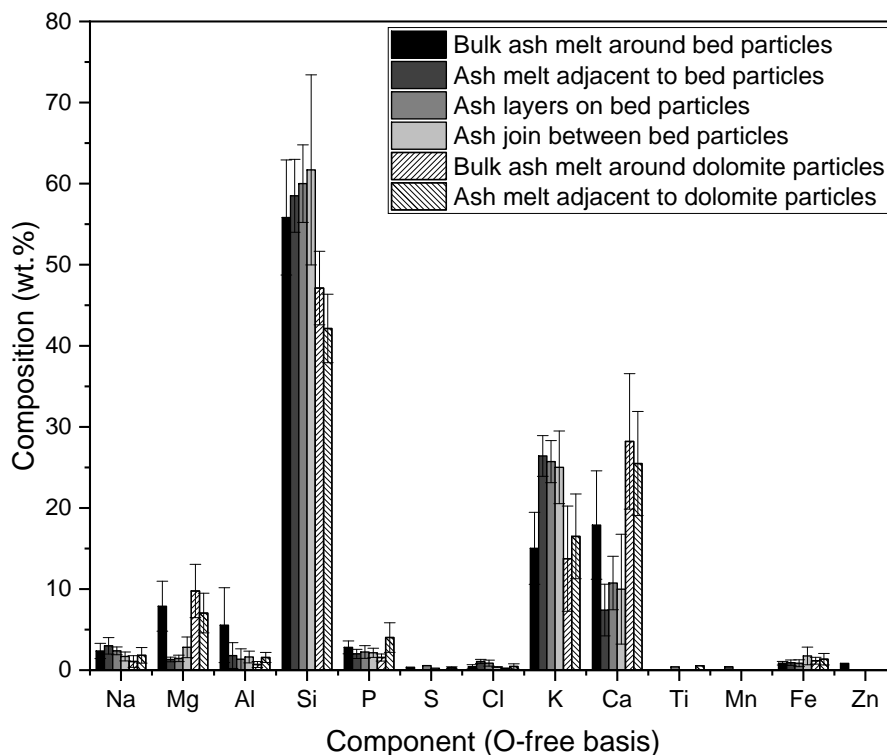
Figure 5.8: *Average ash composition on and around sand bed particles and dolomite particles when using wheat straw with dolomite, together with an analysis of dolomite particle composition under the same conditions. This data is also tabulated in Table 5.5.*

Table 5.5: *Tabulation of the data shown in Figure 5.8. Average ash composition and 95% confidence interval on and around sand bed particles and dolomite particles when using wheat straw with dolomite, together with an analysis of dolomite particle composition under the same conditions. Data on an O-free basis.*

Component	Bulk ash melt around bed particles	Ash melt adjacent to bed particles	Ash layers on bed particles	Ash join between bed particles	Bulk ash melt around dolomite particles	Ash melt adjacent to dolomite particles
Na (wt.%)	2.36±0.94	2.99±1.02	2.37±0.48	1.68±0.55	1.06±0.71	1.81±0.96
Mg (wt.%)	7.88±3.08	1.31±0.29	1.44±0.40	2.80±1.27	9.76±3.29	7.03±2.45
Al (wt.%)	5.54±4.62	1.79±1.59	1.34±1.28	1.61±0.73	0.69±0.37	1.56±0.62
Si (wt.%)	55.82±7.09	58.50±4.50	59.99±4.78	61.69±11.72	47.12±4.53	42.13±4.22
P (wt.%)	2.80±0.79	1.99±0.57	2.23±0.78	2.13±0.56	1.55±0.44	4.01±1.83
S (wt.%)	0.35		0.55	0.23		0.30±0.09
Cl (wt.%)	0.40±0.26	1.06±0.26	0.85±0.37	0.38±0.02	0.21	0.44±0.33
K (wt.%)	15.02±4.44	26.41±2.51	25.71±2.60	25.01±4.48	13.74±6.49	16.49±5.23
Ca (wt.%)	17.89±6.68	7.40±3.19	10.74±3.30	9.98±6.78	28.20±8.35	25.48±6.42
Ti (wt.%)			0.39			0.54
Mn (wt.%)		0.40				
Fe (wt.%)	0.85±0.23	0.91±0.33	0.85±0.42	1.75±1.09	1.16±0.42	1.34±0.71
Zn (wt.%)	0.82					

5.3.5 SEM/EDX – Miscanthus & Additives

5.3.5.1 Agglomerate Structure

Figure 5.9 shows representative SEM images of agglomerates when using dolomite or kaolin with miscanthus across Figure 5.9a-d. Figure 5.9e-f shows the examples of miscanthus with no additives first discussed in Chapter 4 section 4.3.7.1 (Figure 4.8), which are shown again here as a point of comparison. Figure 5.9a-b shows structures when using kaolin. Often, agglomerate structures were smaller than those seen with wheat straw and additives (section 5.3.4.1). Additive particles were frequently joined to sand via discontinuous ash deposits rather than the very large ash phases seen with wheat straw. Occasionally, there was the occurrence of coating layers typical of a coating induced agglomeration mechanism [111]. Whilst these coating layers arose more frequently than with wheat straw due to the far longer operational time, they were not observed to be the sole cause of any joins between particles. The overall agglomeration mechanism remained that of melt-induced agglomeration [124].

Figure 5.9c-d shows agglomerates structures with dolomite and miscanthus. Figure 5.9c is an example of a larger agglomerate structure, where sand is joined by an ash melt and dolomite has stuck to the outer extremities of this melt. Figure 5.9d is a magnified SEM

image of a join between dolomite and as an ash deposit on sand. As noted, larger ash melts, with embedded additives particles, were far rarer with the miscanthus than they were with wheat straw. The examples shown in Figure 5.9 were more typical for miscanthus and additives, of a smaller ash melt phase with conjoined sand particles and additive particles stuck to the outer edges of ash melt deposits.
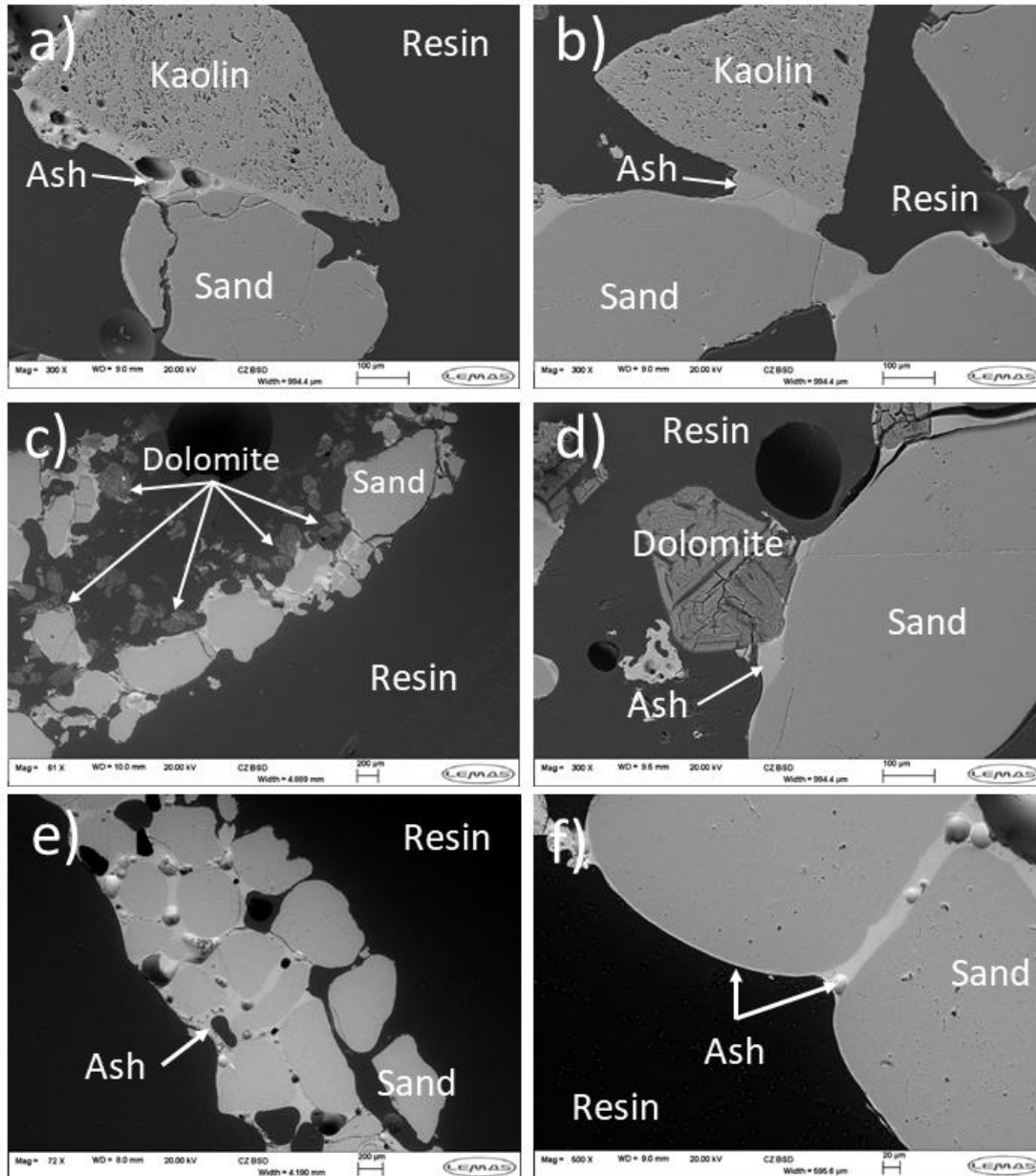
Figure 5.9: *SEM images of typical agglomerate structures when using kaolin or dolomite with miscanthus, with no additive cases from Chapter 4 also shown for comparison. a) Typical ash join between kaolin and sand. Ash deposition evident around both the kaolin and sand particle. b) Thick ash deposit conjoining sand and kaolin. c) Larger ash melt structure with multiple sand particles and dolomite particles loosely attached to exterior. d) Close-up example of dolomite particle stuck loosely to an ash deposit on a sand particle. e-f) Examples of melt formations with miscanthus & no additives, previously shown in Figure 4.8a-b. Figure 5.9e shows a large agglomerate structure formed when using miscanthus & no additives, whilst Figure 5.9f shows a close-up image of a join between two sand particles and the beginnings of a coating layer typical of coating agglomeration.*

5.3.5.2 Use of Kaolin

Figure 5.10 shows average ash composition on and around kaolin and sand bed particles when using miscanthus as a fuel, together with an analysis of kaolin particle composition under the same conditions. This data is also tabulated in Table 5.6. As can be seen, ash composition around bed particles is largely homogeneous. There is slightly elevated potassium and aluminium contents in the ash melt adjacent to kaolin particles versus the bulk ash melt. This is a smaller relative change than seen with wheat straw (section 5.3.4.2), but still indicative of movement of potassium towards kaolin as was also identified in section 5.3.4.2.
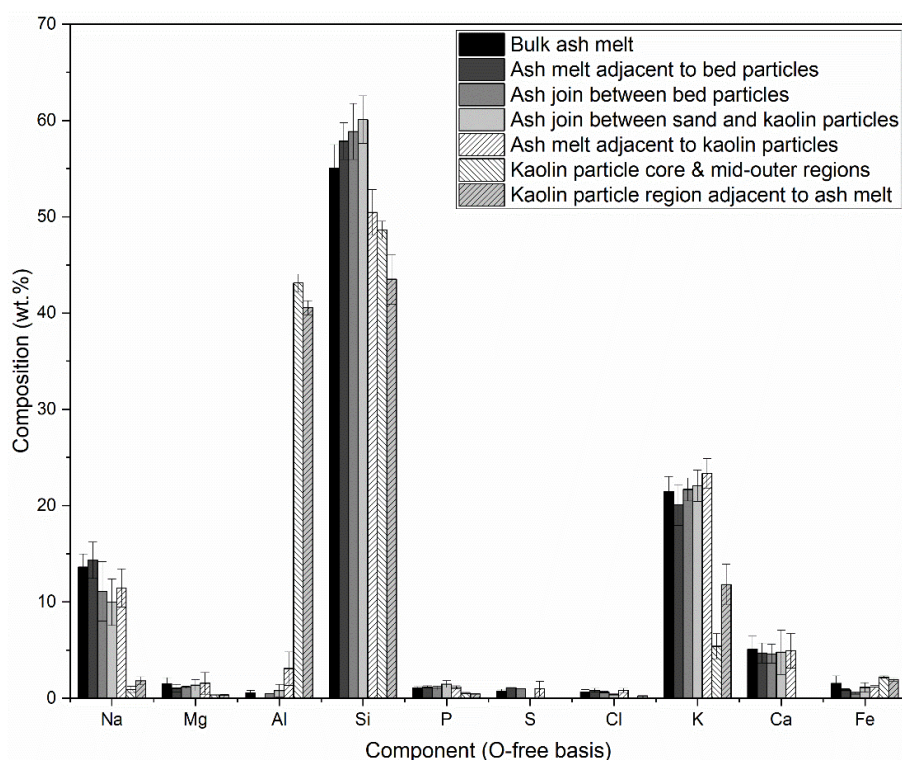
Figure 5.10: *Average ash composition on and around sand bed particles and kaolin particles when using miscanthus fuel, together with an analysis of kaolin particle composition under the same conditions. Data also shown in Table 5.6.*

This movement of potassium in ash towards kaolin is perhaps more evident when also examining the data for kaolin particle regions adjacent to ash in Figure 5.10. Here, there is a near doubling of potassium content in regions of kaolin particles adjacent to ash, versus the combined average of the kaolin particle core and mid/outer regions. Likewise, there is also a slightly lower Al content in the kaolin particle adjacent to ash region. This again suggests some degree of movement of Al out of the extremities of kaolin and into the adjacent ash, as well as the aforementioned movement of potassium

towards and into the extremities of the kaolin. As discussed with wheat straw, this potassium interaction with kaolin would result in the formation of high melting point alkali aluminosilicates, as would any movement of aluminium into the ash [247, 248]. The smaller relative movement of potassium towards kaolin particle surfaces seen with miscanthus may be due to the longer operational time with miscanthus allowing for more of the potassium to react with kaolin, as opposed to merely moving towards it as was seen with the wheat straw.

Table 5.6: Tabulation of the data shown in Figure 5.10. Average ash composition and 95% confidence intervals on and around sand bed particles and kaolin particles when using miscanthus fuel, together with an analysis of kaolin particle composition under the same conditions. Data on an O-free basis.

Component	Bulk ash melt	Ash melt adjacent to bed particles	Ash join between bed particles	Ash join between sand and kaolin particles	Ash melt adjacent to kaolin particles	Kaolin particle core & mid-outer regions	Kaolin particle region adjacent to ash melt
Na (wt.%)	13.61±1.35	14.33±1.88	11.10±3.09	9.96±2.42	11.43±1.98	0.92±0.33	1.80±0.43
Mg (wt.%)	1.50±0.64	1.03±0.41	1.13±0.10	1.34±0.57	1.54±1.14	0.33±0.01	0.33±0.06
Al (wt.%)	0.57±0.25		0.45	0.79±0.64	3.06±1.73	43.11±0.94	40.55±0.73
Si (wt.%)	55.05±2.43	57.85±1.91	58.85±2.92	60.07±2.47	50.43±2.37	48.61±0.91	43.51±2.57
P (wt.%)	1.07±0.12	1.17±0.12	1.05±0.19	1.45±0.36	1.13±0.16	0.50±0.16	0.43
S (wt.%)	0.70±0.22	1.09	0.98		0.97±0.78		
Cl (wt.%)	0.66±0.24	0.82±0.21	0.62±0.07	0.41±0.10	0.81±0.22		0.23
K (wt.%)	21.46±1.55	20.05±2.11	21.67±1.19	22.05±1.64	23.35±1.51	5.39±1.29	11.80±2.12
Ca (wt.%)	5.08±1.40	4.69±1.03	4.61±0.98	4.77±2.30	4.92±1.78		
Fe (wt.%)	1.53±0.77	0.85±0.10	0.51±0.10	1.10±0.50	1.14±0.20	2.20±0.10	1.93±0.20

Figure 5.11 shows an EDX line analysis across the cross-section of a kaolin particle with no large adjoining ash deposits, whilst Figure 5.12 shows a similar line analysis for a kaolin particle fully embedded in ash. From Figure 5.11, it is apparent that there is generally little overall variation in aluminium or potassium content across the cross-section of the kaolin particle. There is a spike in potassium content to twice its average at around 20µm and 920µm, suggesting there was some limited reaction between potassium in ash and the surface of this kaolin particle. This was perhaps due to reaction with vapour phase KCl in a manner similar to that discussed by Wang, et al. [248] where KCl is absorbed and potassium reacts with kaolin to form a stable alkali aluminosilicate (Equation 5.2). Aside from this, there was little other evidence of this particle undergoing reaction with miscanthus ash.
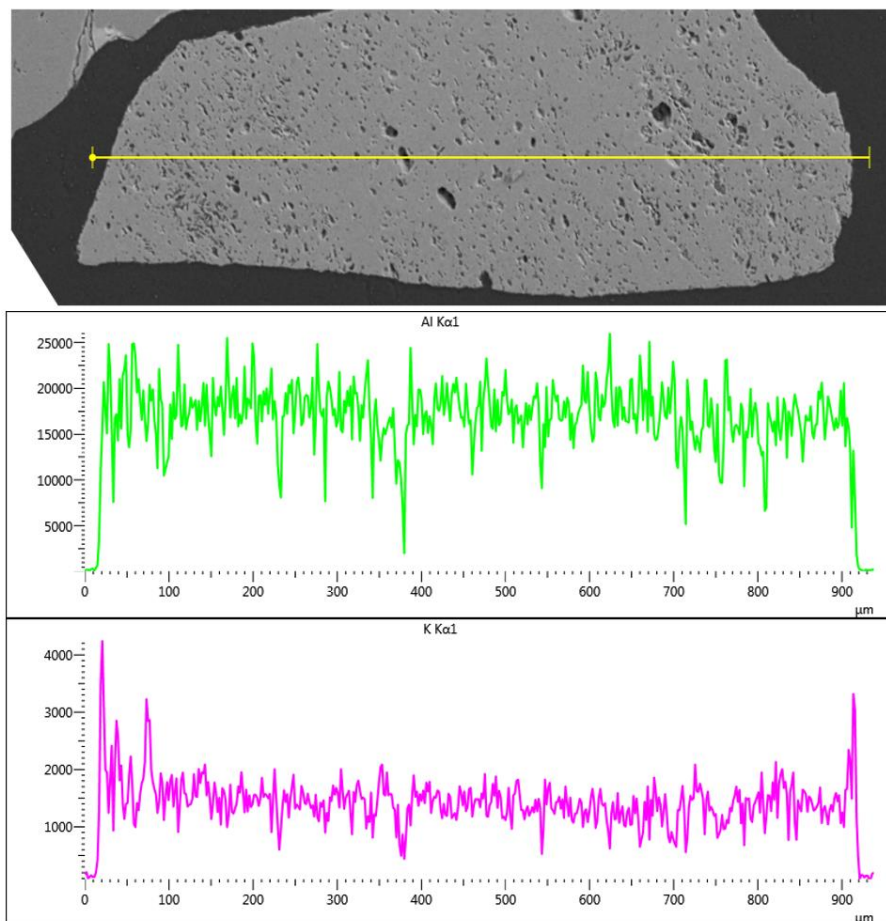
Figure 5.11: *EDX line analysis of a kaolin particle with no adjoining large miscanthus ash deposits. Note the sudden spike in potassium content at each side of the kaolin particle, suggesting some minor reaction with potassium on the particle extremities.*

The line analysis in Figure 5.12 of a kaolin particle fully embedded in ash presents a different profile. Al content remains mostly consistent across most of the particle, with an average count rate of 20,000cps similar to the kaolin particle without adjoining ash in Figure 5.11. There is a slight decrease in Al content on each side of the kaolin particle, particularly on the right side between 240-270µm, suggesting some movement of Al out of the kaolin; a trend seen in the overall EDX data analysis (Figure 5.10). With potassium, there is a clear uptake from the ash into the right side of the particle between 210-270µm with the total count rate approximately doubling over this range. This again supports the previous observation of potassium reaction with the kaolin in regions adjacent to ash (discussed in section 5.3.4.2) and shows that it has reacted to a significant depth within the kaolin (around 60µm from the perimeter surface). There is also a smaller elevation in potassium content between 30-75µm. Whilst no substantial changes to average potassium content were seen in the kaolin particle core region (Figure 5.10), some particles such as that shown in Figure 5.12 display significant

inward reaction of potassium into the kaolin. This is perhaps due to the length of exposure time to ash for this specific kaolin particle. Over exposure time scales longer than the 4-5 hours achieved with miscanthus (such as in a commercial boiler), deeper levels of reaction may be possible, and this would be of importance when maximising the value of kaolin use commercially. This investigation into the depth of reaction of potassium into kaolin is not something that has otherwise been considered in papers investigating biomass ash agglomeration with kaolin [84, 247, 248, 252].
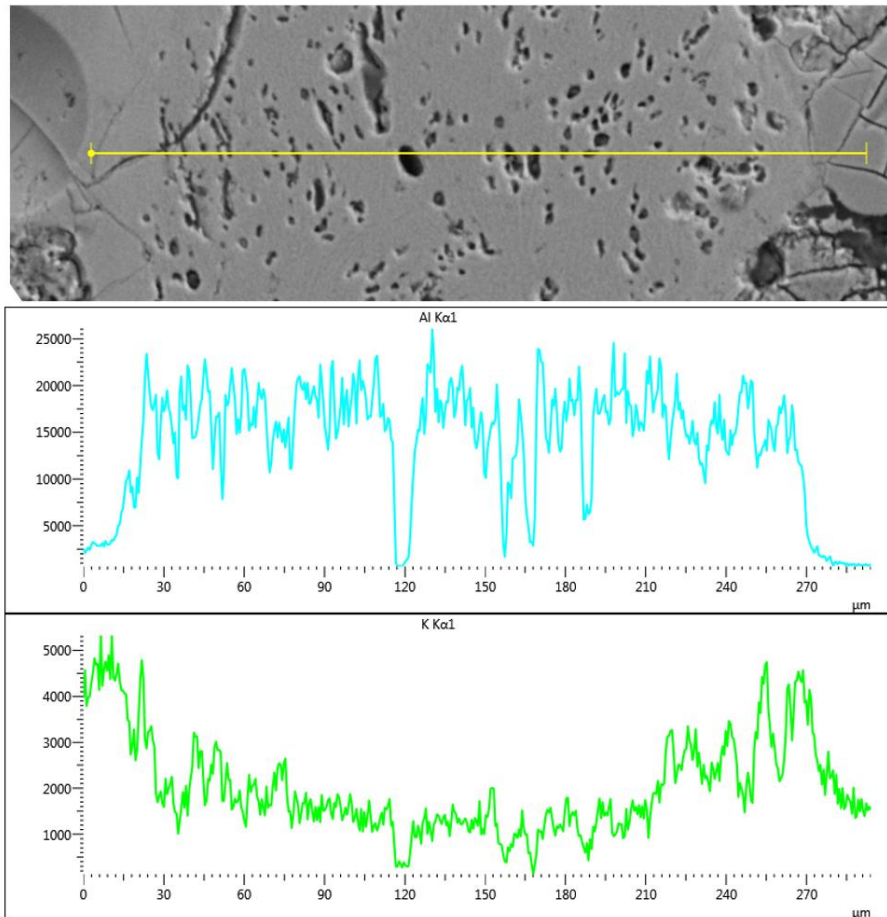
Figure 5.12: EDX line analysis of a kaolin particle fully embedded in a miscanthus ash melt.

5.3.5.3 Use of Dolomite

Figure 5.13 shows average agglomerate ash compositions when using dolomite with miscanthus, as well as variation in dolomite particle composition. Regions of ash melts adjacent to dolomite particles have elevated calcium and magnesium content, again suggesting movement of calcium and magnesium into the ash melt from the dolomite. This is similar behaviour to that seen when using dolomite with wheat straw (section 5.3.4.3) and provides supporting evidence for previous theories that postulated that

calcium and magnesium would move into the ash from dolomite [165, 247]. This release of calcium and magnesium to the melt would raise the eutectic melt temperature and minimise the melt fraction. Ash joins between sand particles and ash layers are rich in potassium and silicon, with reduced calcium content versus the bulk ash melt composition. This is another example of the behaviour seen with wheat straw, whereby a potassium silicate melt forms a leading edge of attack to further react with silica in the sand bed particle (sections 5.3.4.2 and 5.3.4.3).

The dolomite particle composition data in Figure 5.13 has reasonably large 95% confidence intervals, due to its high degree of chemical heterogeneity. Despite this heterogeneity, there is evidently lower magnesium and calcium content in regions of dolomite particles adjacent to ash, versus the average of the particle core and mid-outer regions. This again supports the theory that dolomite releases calcium and magnesium content to surrounding ash, thereby increasing the eutectic melting point and mitigating agglomeration [165, 247].
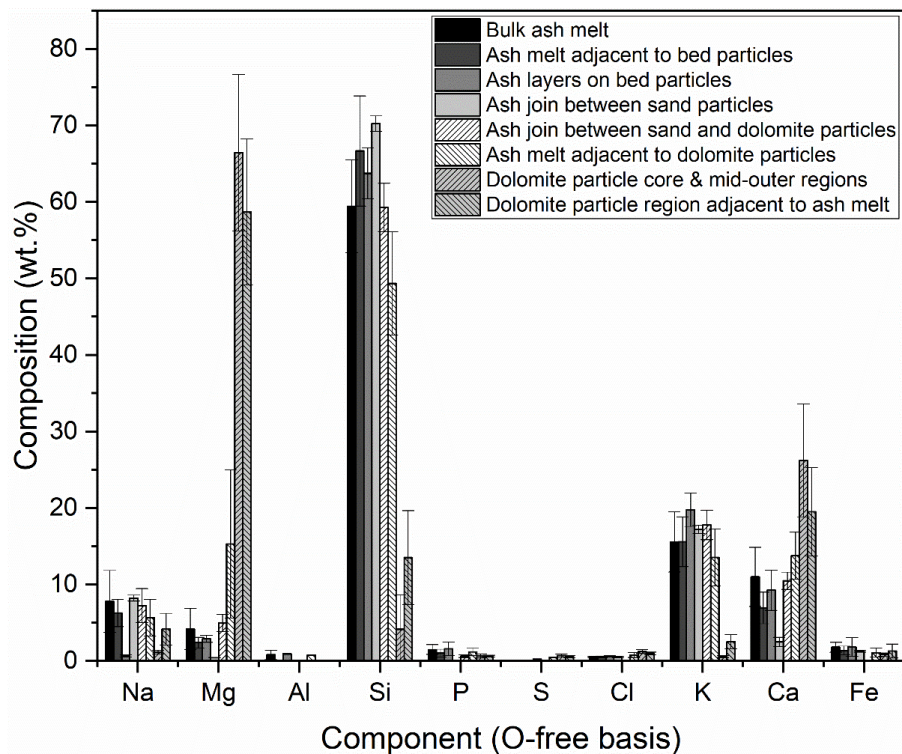
Figure 5.13: Average ash composition on and around sand bed particles and dolomite particles when using miscanthus fuel, together with an analysis of dolomite particle composition under the same conditions. Data also tabulated in Table 5.7.

Table 5.7: *Tabulation of the data shown in Figure 5.13. Average ash composition and 95% confidence intervals on and around sand bed particles and dolomite particles when using miscanthus fuel, together with an analysis of dolomite particle composition under the same conditions. Data on an O-free basis.*

Component	Bulk ash melt	Ash melt adjacent to bed particles	Ash layers on bed particles	Ash join between sand particles	Ash join between sand and dolomite particles	Ash melt adjacent to dolomite particles	Dolomite particle core & mid-outer regions	Dolomite particle region adjacent to ash melt
Na (wt.%)	7.78±4.05	6.28±1.80	0.65±0.15	8.22±0.39	7.24±2.22	5.66±2.39	1.17±0.23	4.16±2.07
Mg (wt.%)	4.19±2.68	2.39±0.69	2.88±0.45	0.43±0.02	4.98±1.12	15.30±9.70	66.43±10.24	58.72±9.53
Al (wt.%)	0.81±0.56		0.92		0.10	0.75		
Si (wt.%)	59.44±6.01	66.66±7.20	63.73±3.32	70.25±0.99	59.28±3.16	49.34±6.77	4.14±4.49	13.52±6.13
P (wt.%)	1.50±0.64	1.04±0.50	1.60±0.89		0.63±0.17	1.20±0.53	0.65±0.29	0.64±0.11
S (wt.%)				0.23		0.49	0.71±0.21	0.59±0.15
Cl (wt.%)	0.54±0.08	0.52±0.12	0.62±0.09	0.51±0.10		0.78±0.32	1.23±0.26	0.99±0.16
K (wt.%)	15.56±3.93	15.59±3.26	19.76±2.19	17.21±0.52	17.79±1.93	13.54±3.71	0.60±0.14	2.53±0.94
Ca (wt.%)	10.99±3.87	6.94±2.05	9.24±2.63	2.49±0.59	10.48±1.13	13.76±3.07	26.19±7.40	19.51±5.79
Fe (wt.%)	1.79±0.65	1.37±0.57	1.83±1.22	1.26±0.10		1.08±0.58	0.85±0.19	1.29±0.92
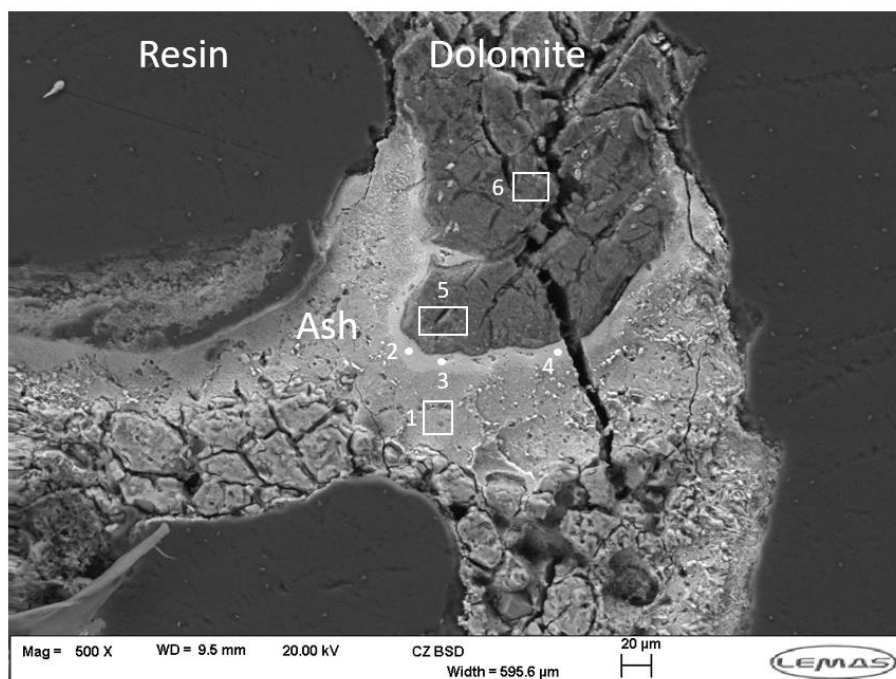
Figure 5.14: *Image of a dolomite particle embedded in ash, with a clear layer structure visible on the border of the dolomite-ash. Locations marked 1-6 underwent EDX analysis, with data given in Table 5.8.*

Figure 5.14 shows the unique example of a distinct calcium rich layer surrounding a dolomite particle. This behaviour was not observed in previous works investigating dolomite use with biomass fuels in fluidized beds [116, 131]. EDX data for the locations marked on Figure 5.14 is given in Table 5.8. The lighter shaded region surrounding the dolomite particle contains 60wt.% calcium content (points 2-4). Also notable about this ash is its very high sodium content (region 1), and comparatively low potassium content. As can be seen from analysis of points 5-6, the dolomite itself is magnesium rich and nearly entirely calcium depleted, despite the material specification for dolomite quoting a value of 30.60wt.% CaO (see Chapter 3 section 3.8.3). This would suggest that calcium from the dolomite has almost entirely migrated into this calcium rich layer. It has then moved into the broader ash melt (region 1) which has a calcium content of 32.26wt.%, versus an average calcium content in the miscanthus bulk ash melt region, when using dolomite, of around 15wt.% (Figure 5.13). A review of the literature did not reveal any previous observations of this behaviour, in studies with biomass or other fuels, making it difficult to draw further comparisons.

Table 5.8: *Table listing EDX compositional data for the points labelled 1-6 on Figure 5.14.*

EDX Location	Component (wt.%)							
	Na	Mg	Si	P	S	Cl	K	Ca
1	26.61	0.33	38.15	2.39			0.27	32.26
2	5.75	0.73	22.39	4.45	0.26		0.65	65.78
3	5.68	0.96	22.36	4.22	0.34		0.70	65.73
4	4.55	1.07	21.69	3.39	0.81		0.70	67.78
5	2.75	90.10	1.28	0.88	0.56	1.03	0.59	2.79
6		89.45		0.82	0.70	1.64	0.41	7.00

Figure 5.15 shows a line analysis across the cross section of a dolomite particle with no adjoining ash or evidence of reaction with ash. Magnesium content is largely consistent across the cross-section of the dolomite particle, except in fractures or cracks. Calcium content is much more variable. There is a peak towards the centre-left side of the line analysis, with calcium content then steadily dropping when moving to either side of the dolomite particle. There are, however, a few peaks in calcium content amongst this steadily declining trend. This provides a clear example of the heterogeneity and variance that was observed in the dolomite, both structurally and in terms of EDX quantitative analysis.
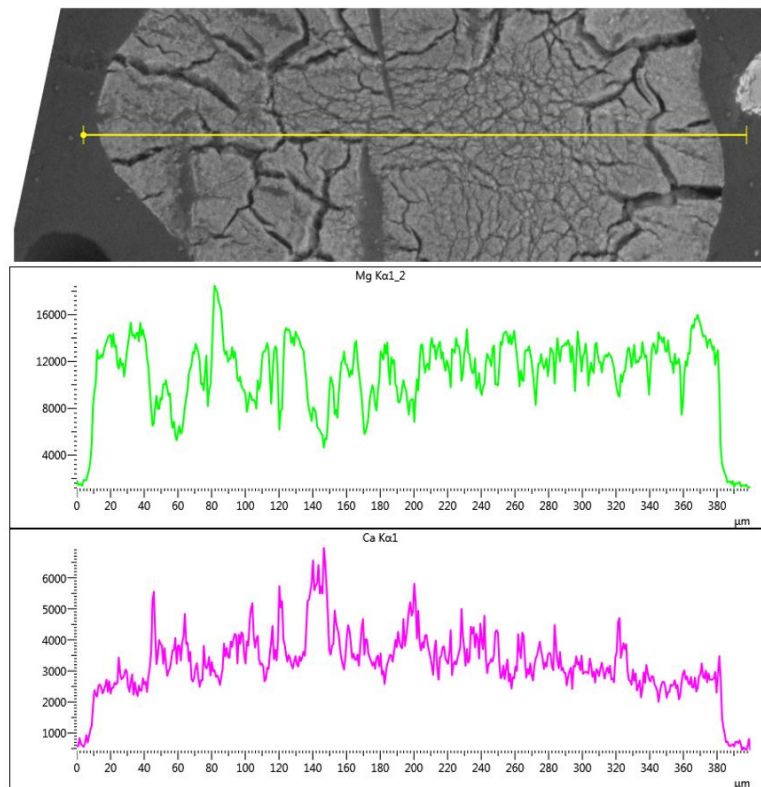
Figure 5.15: *EDX line analysis over the cross-section of a dolomite particle with no adjoining ash material or other evidence of interaction with ash. Analysis shows variation in magnesium and calcium content across the particle. Of note is the high variation in calcium.*
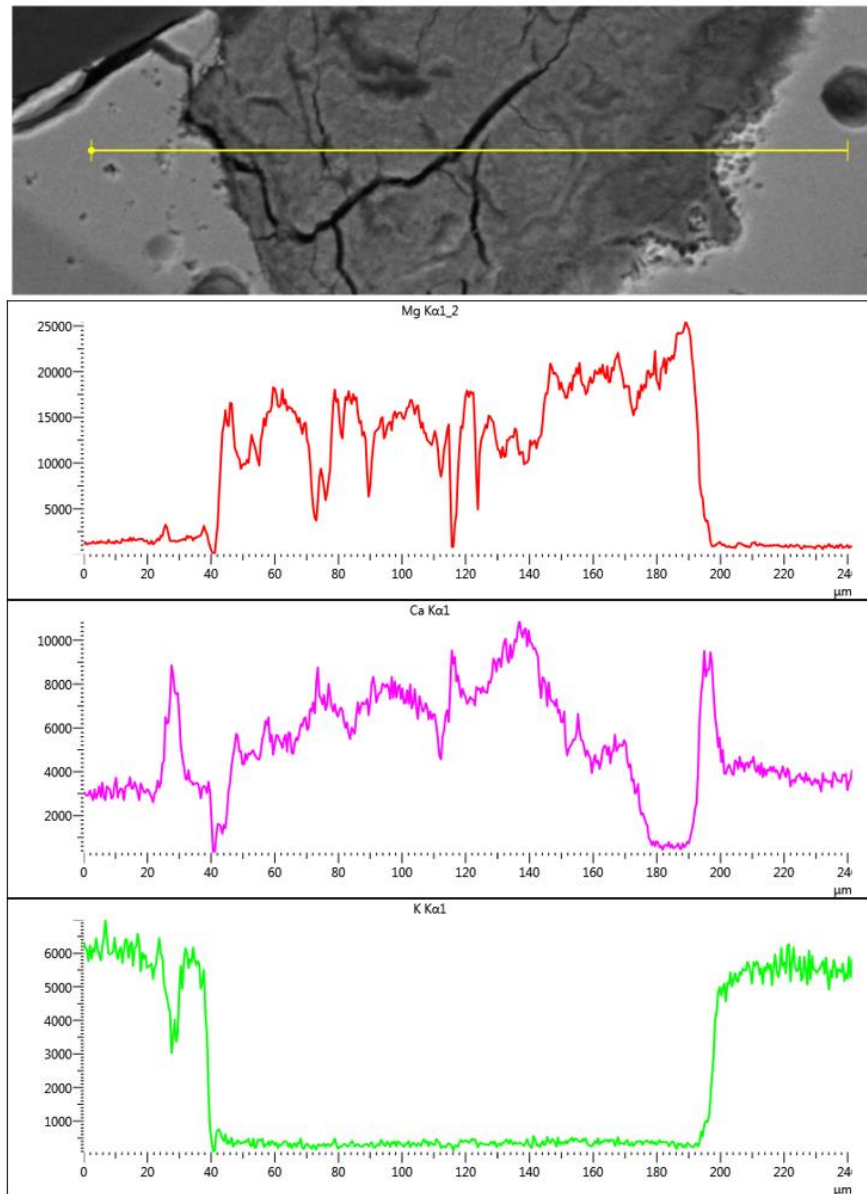
Figure 5.16: *EDX line analysis across the cross-section of a dolomite particle embedded in ash. Variation in magnesium, calcium, and potassium is shown. High variation in magnesium and calcium is apparent, along with little uptake of potassium at the perimeters of the dolomite particle. It is apparent that there has been some depletion of calcium in the dolomite at each border with the ash.*

Figure 5.16 shows the line analysis of a dolomite particle near fully embedded in ash and presents a different profile to that of Figure 5.15. Magnesium content rises to a peak on the right side of the dolomite particle, showing the heterogeneity of the dolomite particle. Calcium content shows a peak roughly in the middle of the particle, and then steadily drops off to near-zero content on each side of the dolomite particle adjacent to the ash (at 40-43µm and 179-190µm). When moving to the ash side of the ash-dolomite interface, there is then an immediate, very large spike in calcium content at 23-40µm and 190-200µm, rising to levels almost as high as the peak calcium content in the

dolomite and far higher than those of the surrounding bulk ash melt. This is a clear indication of movement of calcium content out of the dolomite particle and into the ash at dolomite regions adjacent to ash. This may be an early stage to the formation of a calcium layer as seen in Figure 5.14. Potassium contents were very low across the dolomite particle, showing that the dolomite does not mitigate agglomeration by potassium uptake, as was the case for the kaolin.

5.3.6 XRD Analysis of Agglomerates

A total of eight samples across varying additive and fuel combinations were analysed with XRD to determine the crystalline phases present, as per the approach detailed in Chapter 3 section 3.5. The diffraction patterns for wheat straw samples are shown in Figure 5.17, with those for miscanthus samples shown in Figure 5.18. Each diffraction pattern represents a distinct bed sample taken from different test conditions or different vertical strata in the bed, with these bed vertical strata defined in Chapter 3 section 3.3.3.

As can be seen across Figure 5.17-Figure 5.18, the dominant phase in all the diffraction patterns is silica (SiO_2), which in some cases is the only phase present. This dominance of silica content is as would be expected given that a 97%+ silica sand bed material was used in testing (Chapter 3 section 3.8.2), and so naturally would comprise most of the powdered agglomerates. It should be noted that not all silica peaks identified are identical as some are different polymorphs of silica, though this is not of importance to agglomeration behaviours therefore this was not delineated on the diffraction patterns. Some other phases were identified, such as a calcium-aluminium-silicate phase (Figure 5.17b, d & e) and a magnesium oxide phase (Figure 5.18c). The formation of a calcium-aluminium-silicate in Figure 5.17b would be expected, given the potential for reaction between aluminium content in kaolin and calcium in ash. It would be less expected in the case of Figure 5.17d & e where wheat straw and dolomite were used, as dolomite is a calcium magnesium carbonate, though is still reasonable given the 1.6wt.% Al_2O_3 content of wheat straw ash.
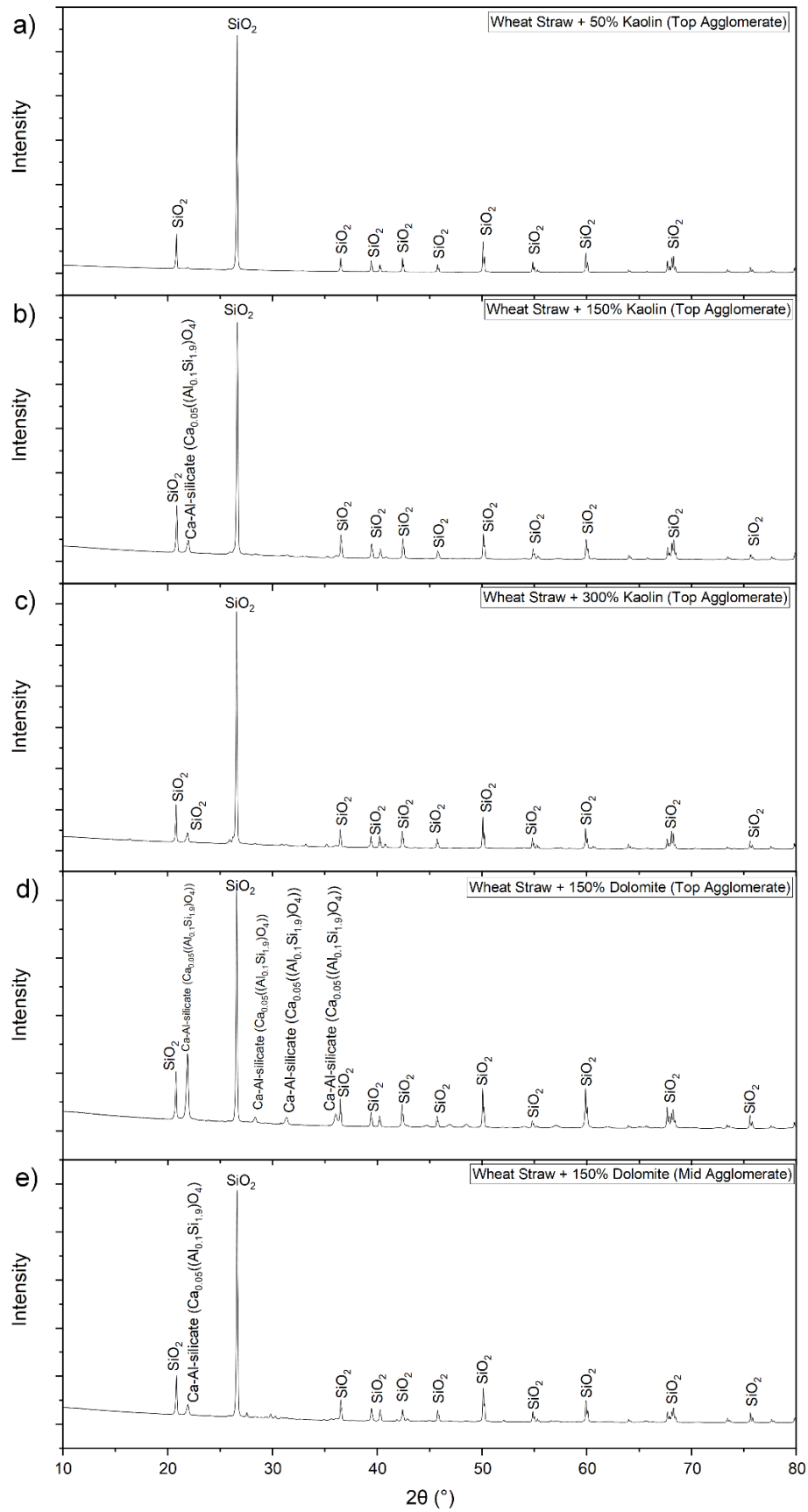
Figure 5.17: *Diffraction patterns for various wheat straw and additive agglomerate samples with conditions indicated. Samples from top or middle vertical bed strata, as defined in Chapter 3 section 3.3.3.*
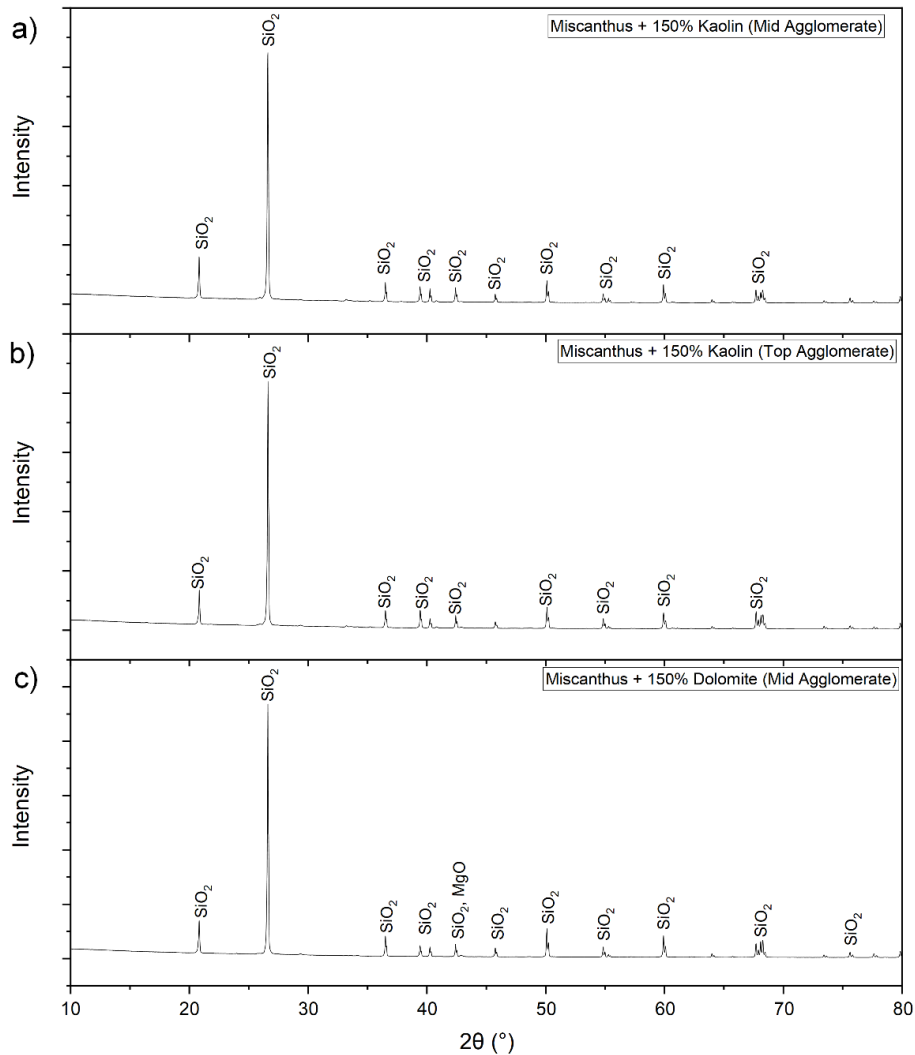
Figure 5.18: *Diffraction patterns for various miscanthus and additive agglomerate samples with conditions indicated. Samples from top or middle vertical bed strata, as defined in Chapter 3 section 3.3.3.*

The general lack of components from ash and additives in the XRD analysis is an unexpected outcome, as both ash and additives were clearly part of agglomerate structures as seen in sections 5.3.4.1 and 5.3.5.1. Samples were subjected to several repetitions of exploratory XRD analyses prior to the final analysis that produced the diffraction patterns shown in Figure 5.17-Figure 5.18. Phase identification analysis was then performed multiple times on the data, including the final data set, to ensure that every possible phase of relevance to agglomeration behaviours had been identified. Moreover, some samples analysed were from the same test, albeit sampled from different vertical strata of the bed, e.g. Figure 5.17d & e, and Figure 5.18a & b. Some very minor peaks are unlabelled across the diffraction patterns, but these are either additional minor silica peaks or they are peaks that correlate to phases of no importance/relevance to agglomeration mechanisms (e.g. Zn, Cu, or Ti compounds). As

noted in Chapter 3 section 3.5 the approach to phase identification was to continue matching peaks in the SIeve+ program until none of the remaining potential matching compounds were of relevance to agglomeration. Therefore, every effort was made to identify every phase of relevance in the samples.

Others in the literature have successfully identified ash or additive components when performing XRD on agglomerates with similar fuels or additives to those used here, such as Kaknics, et al. [115], Chi, et al. [171], and Grimm, et al. [185]. These authors have identified silicate and phosphate components that would be expected based on ash composition and SEM/EDX analysis, such as KAl-, Ca-, Mg- and CaMg-silicates, and Ca-phosphates. However, whilst these authors do state the settings used for their XRD analysis, they do not state how many samples were analysed in total, or how many times each sample was analysed prior to production of their final data set. In theory, the powder used in XRD should be homogeneous and therefore should produce similar diffraction patterns, and thus similar phase peaks, each time. However, ash content accounts for a very small proportion of the total agglomerate mass, which creates difficulty in preparing a truly homogeneous powder. The critical ash mass to form an agglomerate has not been definitively quantified in the literature but is thought to be <2% of the bed mass (see Chapter 2 section 2.3.11), highlighting how little of the mass of an agglomerate the ash phase may account for.

There is perhaps some evidence of a minor amorphous phase in the samples, visible in the form of a small "hump" in intensity from 10-35° [217, p. 342], particularly in the case of Figure 5.17b-d. Tiainen, et al. [255] have similarly observed biomass ash to form a partially amorphous phase, and this amorphous phase may contain the some of the ash derived elements. However, this would not explain the lack of components from the additive particles appearing the in the diffraction patterns. Both additive particles were seen to form part of agglomerate structures in sections 5.3.4.1 and 5.3.5.1, with neither kaolin nor dolomite likely to undergo any melting prior to 1000°C [165, 249], far in excess of bed temperatures seen during tests (section 5.3.1.2), which would be the only means by which these could form part of an amorphous phase.

Sample availability was also highly limited for this study, due to circumstances outside of the authors' control (a severe natural flooding of a laboratory causing sample loss). Whilst the eight samples analysed here were considered viable – i.e. had sufficient

agglomerates to produce enough powder for XRD analysis – a broader availability of samples would have enabled a more insightful analysis. The XRD study performed here is inconclusive as to the true agglomerate phase compositions when using additives. Further study of additional samples, if they were available, would be highly beneficial.

5.4 Efficacy of Additives for Agglomeration Mitigation

From the analysis of agglomerate chemistry when using additives across sections 5.3.4 and 5.3.5, there are distinct mechanisms by which the additives interact with the fuel ash. When using kaolin, there is the movement of potassium in the ash melt phase towards the kaolin particle surface, at which point it reacts with the kaolin to form a potassium aluminosilicate, a reaction which has been seen previously [166, 247, 253]. This reaction primarily occurred within areas of the kaolin particle adjacent to the ash melt (within $<20\mu m$ of an ash melt). One example of deeper reaction of potassium with kaolin to a depth of $60\mu m$ was seen with miscanthus (see Figure 5.12).

When using dolomite, there is the release of calcium and magnesium content from the dolomite into the surrounding ash melt phase. This would lead to the formation of high melting point magnesium silicates, calcium silicates, and calcium magnesium silicates, which have been observed in fundamental studies of wheat straw ash blends with dolomite [253]. In two cases when using dolomite with miscanthus (see Figure 5.14 and Figure 5.16), there was the near total depletion of calcium content from regions of dolomite adjacent to ash, and deeper into the particle core in the case of Figure 5.14. Previous works have speculated that dolomite may release calcium content to dilute the alkali metal content of ash melts and increase the melting temperature [165]. Here, this behaviour is confirmed in the context of agglomeration mitigation, with calcium and smaller quantities of magnesium released to the ash.

It is clear that there was chemical interaction between both fuel ashes and additives from SEM/EDX, but the wheat straw pellets did not realise any performance improvement from this in the form of averting bed defluidization or lengthening defluidization time. As noted in section 5.3.2, a significant proportion of the agglomerates retrieved following wheat straw tests were of the shape of a fuel pellet, a phenomenon observed by others with straw pellets when not using additives [124]. During combustion tests with wheat straw pellets, it was observed that as the pellets devolatilized and began char combustion, they stuck to bed material and additives

(Figure 5.19a). Recent single fuel pellet combustion studies on wheat straw by Strandberg, et al. [256, 257] have shown that at 700°C, the pellet maintains its shape through char oxidation with ash forming small molten beads on the surface of the pellet, with ash melt bubbles forming on the surface under combustion at 1000°C. Straw pellets were also seen to maintain their shape through char oxidation in an earlier single pellet fuel study by Chirone, et al. [128]. It is proposed that it is these physical mechanisms – the release of ash to the wheat straw pellet surface and the lack of breakdown of the char pellet structure – that prevent additives from being an effective mitigation measure with wheat straw. These behaviours allow the pellet itself to act as a "ready-made" agglomerate platform, hence bed material and additive adhering to pellets to wheat straw pellet char cores to form pellet shaped agglomerates. This would explain the lack of change to wheat straw defluidization time with increased additive dosage, as there was a consistent thermal input (fuel pellets) across the different dosages tested, hence a consistent input of these "ready-made" agglomerate platforms.
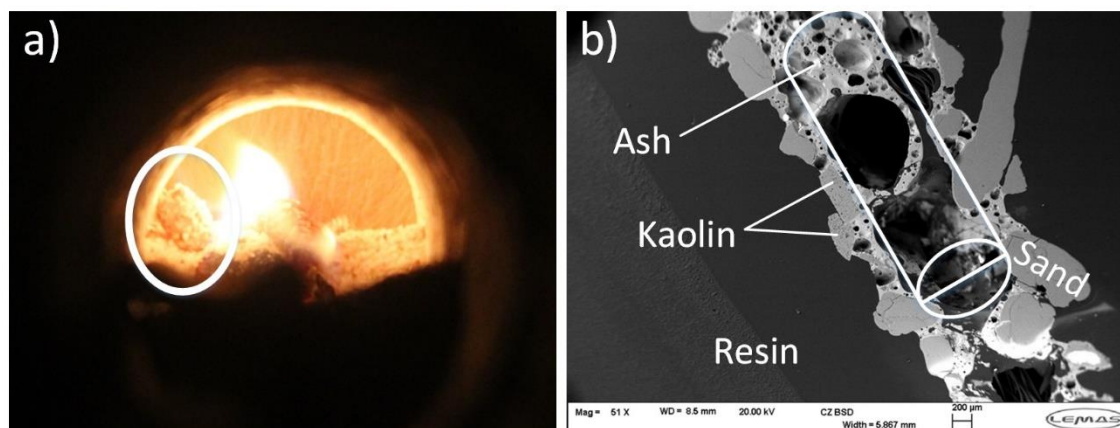
Figure 5.19: a) Picture taken during a combustion test with wheat straw and dolomite, showing bed particles adhered to the fuel pellet surface. b) Backscatter SEM image of a cross-section of a pellet shaped agglomerate collected following a test with wheat straw and 150% kaolin. The overlaid cylinder in white is the hypothetical position of the core (i.e. not the whole pellet) of the original wheat straw pellet, which fully combusted to leave the hollow core and pellet shaped agglomerate that is seen. It should be noted that the width of this region is approximately 1200µm (1.2mm), versus the original pellet diameter of 8mm. This difference is because of the shrinking of the pellet as the combustible material is lost, and the action of bed forces on compacting the remaining pellet shaped agglomerate.

This theory does leave areas for future investigation. Ash content alone does not offer an indicator as to the likelihood of a fuel to exhibit this behaviour, given that both fuels have ash contents between 6-7wt.%. Therefore, a better understanding of these fundamental ash release and fuel particle breakdown mechanisms, and their root cause, would aid operators in determining if additives could be a suitable agglomeration mitigation method for a fuel. A recent work by He, et al. [258] tested the effect of

doping a wood fuel with different salts (KCl, K_2SO_4, K_2CO_3, all with KH_2PO_4) up to a consistent 3wt.% potassium content. Interestingly, agglomerates when using K_2SO_4 and K_2CO_3 retained a far larger size and shape than those with KCl. Therefore, the relative quantities of different alkali salts within the wheat straw may be of critical importance to the breakdown effects of the fuel pellet structure, though this would need further investigation. It may also be of interest to test other wheat straw fuel particle shapes or form factors with additives, e.g. powders or bales. These have been previously tested without additives [124, 130] and performed poorly, though they may respond differently than pellets to additive use. If a positive response with additives is seen, this would indicate that the pellet form factor or pelletization process may be negatively impacting the ash release or ash structure breakdown behaviour.

Of the two additives tested here with miscanthus, kaolin at the 50% dosage would be preferred. All the dosages used with miscanthus were seen to prevent defluidization. Kaolin was seen to instead absorb potassium content to mitigate agglomeration. In doing so, it would prevent volatilization of potassium to form KCl, which would otherwise contribute to corrosion [84]. Dolomite however was only seen to release calcium and magnesium content which did mitigate agglomeration through formation of higher melting point silicates but would still allow for the free movement of potassium into the vapour phase to cause slagging and corrosion issues downstream.

5.5 Efficacy of Alternative Bed Materials in Comparison to Additives Utilisation with Wheat Straw

In Chapter 4 section 4.3.3, it was seen that the use of olivine with wheat straw resulted in around 25% longer defluidization times. Agglomerates with olivine and wheat straw still frequently formed in the shape of fuel pellets, though also frequently formed in smaller structures as shown in Chapter 4 section 4.3.5. Within this chapter, it has been shown quite clearly that use of additives had no impact on agglomeration severity with wheat straw, despite chemical interaction between additives and ash. This would suggest that several contributory factors, aside from just the beneficial chemistry of olivine and its low silica content, may have benefitted the use of olivine with wheat straw.

One potential contributing factor is the wettability of silica sand in comparison to olivine. There are two types of wetting: spontaneous, in which the wetting of a droplet

on a flat surface is evaluated, and forced, in which the wetting of a liquid on a moving surface is evaluated [259, pp. 54-56]. Contact angles below 90° denote a material with good wetting, whereas materials with a contact angle above 90° are classed as non-wetting [259, p. 44]. Most wetting experimentation investigates spontaneous wetting. Regardless of the type of wetting analysis, experimentation demands an isothermal system, a known liquid composition, clean surfaces, and negligible or controlled external forces [259, pp. 54-56]. As can be imagined, wettability conditions in a real fluidized bed system would be in contradiction of almost all these conditions. Kaknics, et al. [116] and Michel, et al. [178] performed studies into the spontaneous wettability of olivine with miscanthus ash and found contact angles of 90°, which implies that olivine is on the borderline between wetting and non-wetting, and that at best olivine is very weakly wetting. This contradicts the statement of Kaknics, et al. [116] that olivine has good wetting potential. Unfortunately, a similar study was not performed into silicas sand wettability, but they did state that silica sand appeared to have a better wettability than olivine when examining agglomerate structures as part of fluidized bed tests with miscanthus. Whilst this study was on spontaneous wetting (flat, non-moving surface) under ideal conditions, it does suggest that olivine is poorly wetting.

Another contributory factor to the improved performance of wheat straw with olivine is that test conditions were more favourable than those with additives. Tests with olivine had a larger U/U_{mf} ratio (3.0 vs. 2.0), a lower thermal rating (50kW_{th} vs 65kW_{th}), and the particle size of olivine was also finer than that of the silica sand (536-664µm, versus 853µm for the silica sand). These factors are all beneficial for lengthening defluidization times in the case of the olivine tests, as was discussed in Chapter 4 section 4.3.3 and Chapter 2 section 2.3. Changes to the bed hydrodynamic regime because of the finer particle size and higher U/U_{mf} ratio, in combination with the poorer wettability of the olivine may have been particularly beneficial. For example, this may have meant that the poorly wetting olivine particles that did glue to the extremities of partially molten wheat straw fuel pellets may more easily detached, or that these poorly wetted structures were more easily broken apart. To validate this theory and elucidate the underlying phenomena, additional fundamental testing would be required. This should include measurement of the spontaneous and forced wetting contact angles with both the silica sand and olivine bed materials with wheat straw ash, as well as fluidized bed testing of both bed materials and wheat straw, albeit with identical particle size

distributions and U/U$_{mf}$ ratios. This would define underlying behaviours and minimise uncontrolled variables, allowing for the determination of the key underlying variable that enables the defluidization time benefit when using olivine with wheat straw.

5.6 Chapter Summary

A comprehensive study was performed on the use of kaolin and dolomite bed additives at varying dosage rates with miscanthus and wheat straw fuels. With miscanthus, all additives and dosages that were trialled prevented defluidization from occurring (215+ minute operational time), versus a 159 minute defluidization time without additive use. With wheat straw however, no additive or dosage, including a 300% kaolin dosage, had any noticeable effect on defluidization time. The use of additives did not appear to have an appreciable effect on temperature profile or emissions during combustion, though known shortcomings with the design of the fluidized bed rig and its combustion profile (discussed in section 3.2.11) may have masked these.

Agglomerates retrieved from the bed following tests with wheat straw and additives were frequently fuel pellet shaped, whereas those from miscanthus tests with additives were generally smaller with less of these pellet shaped agglomerates. It was seen visually during tests that bed material would bind to the wheat straw pellets during char oxidation, hence the formation of large amounts of these pellet shaped agglomerates.

Clear, distinct, agglomeration mechanisms and interactions with additives were observed through SEM/EDX analysis. Both fuels formed agglomerates via a melt-induced agglomeration mechanism. Wheat straw agglomerates were characterised by large ash melt phases with embedded sand and additive particles, whereas miscanthus agglomerates typically formed through discontinuous ash melt lumps that glued together bed and additive material. With both fuels, there was clear evidence of interaction with both additives, despite only miscanthus seeing an improvement to defluidization time with additive use. When kaolin was used, there was the clear movement of potassium towards the kaolin particle surface and reaction with kaolin, likely forming potassium aluminosilicates e.g. $KAlSiO_4$. This inward movement was quite significant, with elevated potassium levels to depths of up to 60µm in the kaolin. To the authors' knowledge, no other previous agglomeration studies have considered the extent to which kaolin reacts with potassium in agglomeration studies, nor have they taken the systematic approach of classifying and comparing across distinct regions on

agglomerate structures when using additives. With dolomite, there was the release of calcium content and some magnesium into the ash, likely forming high melting point calcium and magnesium silicates (e.g. $CaSiO_3$). Previous studies in the literature have only speculated that the dolomite would release calcium content into ash, with little if any study of this behaviour in the context of bed agglomeration. Here however, this release of calcium and magnesium from dolomite and into the surrounding ash has been proven.

XRD analysis of eight agglomerate samples from a range of test conditions to determine key phases was inconclusive. Whilst a silica phase dominated the diffraction patterns, as would be expected due to use of a silica sand bed material, there were few other phases present derived from ash content or additives, despite clear evidence of their presence during SEM/EDX analysis. There are several possible reasons for this, such as a general under-representation of these component in samples, limitations on the number of available samples due to external factors, and ash content forming an amorphous phase as opposed to crystalline phases. Further work in this area would be recommended if samples were available.

The proposed reason for wheat straw seeing no increases to defluidization time with additive use is that there was a lack of physical breakdown of the fuel pellet structure, with ash released to its surface, allowing the pellet to act as a "ready-made" agglomerate platform. This behaviour of the pellet adhering to bed material was visually observed during tests and in the agglomerates retrieved afterward. It would explain why regardless of additive dose, defluidization time remained the same as there was a constant (thermal) input across all tests of these "ready-made" agglomerates. Previous studies into straws producing these pellet shaped agglomerates have not considered the phenomena and its potential implications beyond mere observance of its occurrence. To explore this theory further, the next chapter will cover theoretical thermochemical modelling of additive performance to compare with findings here.

Chapter 6

Thermochemical Modelling of Agglomeration

Parts of this chapter have been submitted by the author to a peer reviewed journal:

> *The effect of using kaolin and dolomite additives to mitigate agglomeration with challenging agricultural biomass fuels.* **Morris, J.D.**, *Daood, S.S., Nimmo, W. Unpublished manuscript under submission.*

Within this chapter, content has been expanded or abridged in different areas as required to be commensurate with normal thesis formatting.

6.1 Introduction

Thermochemical modelling tools such as FactSage have been applied in biomass ash studies over the past 10-15 years to better understand chemical behaviours that are otherwise difficult to observe or analyse experimentally. Some of these works were discussed in Chapter 2 section 2.4. Generally, thermochemical modelling studies have been in support of experimental biomass ash melting tests (e.g. ash fusion testing) or binary mixtures of a biomass ash with an additive. Of these works, a smaller subset has applied FactSage to agglomeration studies.

In this chapter, the agglomeration behaviours of miscanthus and wheat straw when used with additives, as tested experimentally in Chapter 5, are further investigated. Two distinct thermochemical modelling approaches have been applied to better understand the agglomeration mechanisms involved. In the first approach, fuel ash composition, additive dosage, and flue gas environment are used for modelling the extent of agglomeration across the whole bed. In the second approach, rarely applied in literature, EDX composition data from Chapter 5 is modelled. Different spatial locations on agglomerate structures are modelled, as was analysed in Chapter 5, sections 5.3.4 and 5.3.5 (e.g. bulk ash melt region versus ash region adjacent to additive particles). This approach was chosen to gain an insight into localised agglomerate melting behaviours. In the final section of this chapter, the accuracy and uncertainty of the two FactSage

modelling approaches is considered. This includes an evaluation of the overall efficacy of FactSage as a predictive tool for agglomeration severity.

6.2 Effect of Additive Use and Dosage

6.2.1 Objectives & Modelling Matrix

Work in Chapter 5 comprised a substantial experimental campaign where miscanthus and wheat straw were tested with varying dosages of kaolin and dolomite. The broad conclusion was that miscanthus responded very well to both additives, preventing bed defluidization, whereas wheat straw received no positive benefit with additives. It was proposed that physical behaviours surrounding pellet breakdown and ash release were the cause of this poor performance. As FactSage modelling is on a purely chemical basis, this provided an opportunity to examine the additive dosage scenarios tested in Chapter 5 on a chemical basis, to determine if the performance seen in Chapter 5 is better explained due to chemical or physical reasons.

Several works in the literature model dolomite or kaolin with biomass ashes [249, 260, 261, 262], but few consider varying dosage rates of additives (also referred to as "additive ratio") [253, 263, 264], nor model the fuel ashes used here (miscanthus and wheat straw). Moreover, these works focus on a comparison of ash modelling to experimental ash melting studies, as opposed to agglomeration studies. Works that have used FactSage in agglomeration studies [94, 122, 151, 184, 265] do not model additive use. Therefore, the approach taken here of modelling agricultural fuels with varying additive dosages and comparing findings to real fluidized bed performance extends the boundaries of FactSage application.

Table 6.1 summarises the basic fuel ash and gas inputs for the modelling cases. Table 6.2 shows the eleven different additive dosage cases modelled for each of the two fuels, as well as the FactSage solutions enabled in each case. These cases represent the experimental conditions in Chapter 5. When selecting the FactSage solutions used in each model (Table 6.2), the systematic approach to solution selection as described in Chapter 3 section 3.6 was applied for each additive dosage. This was because increases to the additive dosage would shift the relative position of the cases in the key ash ternary systems. For example, with successive doses of kaolin, the K_2O-Al_2O_3-SiO_2 system would be shifted towards the Al_2O_3-rich region due to additional quantities of the aluminosilicate kaolin available in the system.

Table 6.1: *Basic fuel and gas environment inputs used for all fuel ash/additive modelling cases. Refer to Table 6.2 for details on additive inputs and FactSage solutions used for each modelling case.*

Model Inputs	Wheat Straw		Miscanthus	
Ash Mass (g)	1000		1000	
Equivalent Mass of Fuel Combusted (kg, to form 1000g ash)	*14.9*		*16.7*	
Fuel Chlorine Content (wt.% daf)[1]	0.434		0.215	
Chlorine Mass (g)	63.3		55.4	
Gas Mass (kg)	Stoichiometric Flue Gas + 25% Air		Stoichiometric Flue Gas + 25% Air	
	CO_2	22.15	CO_2	26.18
	O_2	4.01	O_2	4.81
	N_2	66.05	N_2	79.13
	SO_2	0.02	SO_2	0.03
	H_2O	6.44	H_2O	7.35

[1] *Chlorine content taken as an average of chlorine content for each fuel in the Phyllis2 database [199]. Refer to Appendix C for information on the data sets used.*

Table 6.2: *Table summarising additive mass inputs and the FactSage solutions used for each fuel ash/additive dosage case.*

Model Inputs	No Additive	50% Kaolin	150% Kaolin	300% Kaolin	50% Dolomite	150% Dolomite
			Wheat Straw			
Additive Mass (g)	0	500	1500	3000	500	1500
FactSage Solutions[1]	FToxid: SLAGA (I), cPyrA (I), WOLLA (+), MeL_A (+), NCSO (+), Brau (+) FTsalt: ACL_B (J), CSOB (J), KSO_ (I)	FToxid: SLAGA (I, cPyrA (I), WOLLA (+), MeL_A (+), Neph (+), NCSO (+), Feld (+), Brau (+) FTsalt: ACL_B (J), CSOB (J), SCMO (+)	FToxid: SLAGA (I), SPINA (I), cPyrA (I), OlivA (I), CORU (I), Neph (+), Feld (+), Brau (+) FTsalt: SCMO (+)	FToxid: SLAGA (I), SPINA (I), Cord (+), Mull (I), Feld (+), Brau (+) FTsalt: SCMO (+)	FToxid: SLAGA (I), SPINA (I), Mel_A, OlivA (I), Neph (+), NCSO (+), Brau (+), KASH (+) FTsalt: ACL_B (J), CSOB (J)	FToxid: SLAGA (I), SPINA (I), MeO_A (I), aC2SA (+), OlivA (I), NCA2 (+), FTsalt: ACL_B (J), CSOB (J)
			Miscanthus			
Additive Mass (g)	0	500	1500		500	1500
FactSage Solutions[1]	FToxid: SLAGA (I), cPyrA (I), WOLLA (+), MeL_A (+), Feld (+), Brau (+) FTsalt: CSOB (J)	FToxid: SLAGA (I), cPyrA (I), oPyr (+), Feld, (+), Brau (+), Rhod (+) FTsalt: SCMO (+)	FToxid: SLAGA (I), Cord (+), Mull (I), CORU (I), Feld (+), Brau (+) FTsalt: SCMO (+)		FToxid: SLAGA (I), cPyrA (I), WOLLA (+), Feld (+), Brau (+) FTsalt: CSOB (J), KCOH (I)	FToxid: SLAGA (I), Mel_A (+), Neph (+), KASH (+) FTsalt: CSOB (J), KCOH (I)

[1] *Refer to Appendix D for further detail on each solution used.*

6.2.2   **Phase Formations: Wheat Straw with Additives**

Figure 6.1 shows the predicted slag plus liquid mass that would form for each additive case on a gram per kW_{th} fuel input basis with wheat straw. This is shown over a 750-950°C temperature range which bounds the upper and lower temperature extremities of the bed in a typical biomass fired fluidized bed boiler [23], and as were seen experimentally in Chapter 4 and Chapter 5. As can be seen, all kaolin dosages and the 150% dolomite dosage result in a substantially lower total melt quantity than the no additive case. There is a notable rise in melt quantity in the 150% dolomite case from around 880°C onwards. The 50% dolomite case however, is predicted as having a greater slag plus liquid quantity than the no additive case from 750-860°C. Taken at face value, this would suggest that the poor experimental performance of the wheat straw with 50% dolomite seen in Chapter 5 section 5.3.1.1 may be due to unfavourable chemistry at a low dosage of dolomite. However, it would not explain why the 150% dolomite dosage, and all kaolin dosages, are predicted to have a far smaller total melt fraction here yet performed so poorly with the wheat straw experimentally.
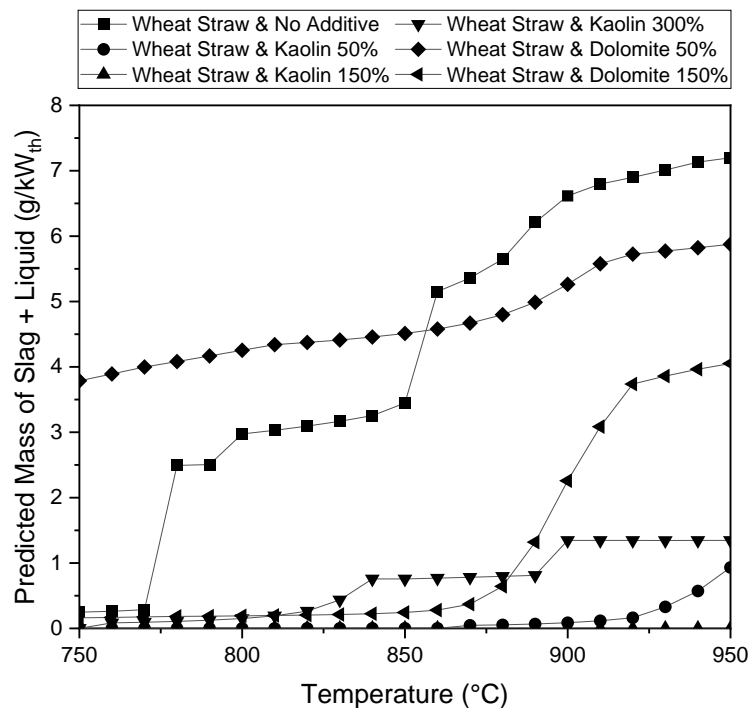
Figure 6.1: *Total slag plus liquid quantity formed on a gram per kW_{th} fuel input basis for all wheat straw cases modelled.*

Outside of the 50% dolomite case, the results presented in Figure 6.1 suggest that the physical behaviours surrounding pellet breakdown and ash release to the pellet surface, as discussed in Chapter 5 section 5.4, were the primary reason for the poor performance

of additives with wheat straw. This is because FactSage only considers the chemical equilibrium state of a system, therefore if chemical reasons were behind the poor performance of additives a greater slag formation quantity would be predicted with additives. Dolomite is seen to be a poorer additive than kaolin, producing a larger melt fraction in both dosage cases. This agrees with the experimental findings of Llorente, et al. [247], who for several fuels observed continued sintering of ash when heated to 1000°C with dosages of dolomite up to 200%. Similarly, in several ash melting studies, others have seen kaolin to have a significant positive effect toward reducing ash melting issues [164, 247, 249], which agrees with the FactSage prediction made here.

Figure 6.2-Figure 6.7 show the phase chemistry for wheat straw and each of the additive cases, again over a 750-950°C temperature range. The parentheses after each component in the legend denotes: the phase of the component (solid, liquid, gas) or in the case of a solid solution, the FactSage solution from which the component is derived (e.g. cPyrA, see Table 6.2 for solutions). Where a solid is denoted "s1", "s2", etc., this denotes a different polymorph of the solid, i.e. a different crystal structure.

As can be seen in Figure 6.2-Figure 6.7, there are significant variations in the amount of slag and liquid phases formed in each case, with the kaolin cases generally producing little to none across the board. The higher kaolin dosage cases, 150% and 300% (Figure 6.6 and Figure 6.7), have a lower quantity of KCl in gas. This is a result of the reaction of potassium with kaolin to form potassium aluminosilicates, such as $KAlSi_3O_8$, which is formed in both cases. This removal of KCl from the gas phase would be beneficial for corrosion mitigation. This has been seen experimentally by others such as Davidsson, et al. [84] who observed up to an 85% reduction in the KCl content of flue gas when using a high kaolin dosage (molar ratio 10:1 kaolin:alkali metal). Here, moving from a 50% to 150% kaolin dosage results in the removal of the entirety of the KCl content from the gas phase. This prediction is therefore likely to be an overestimation of the effectiveness of kaolin, due to some of the assumptions and shortcomings of FactSage (e.g. assuming chemical equilibrium is reached, components are all well mixed, etc.). A decrease in gas phase KCl mass due to potassium capture was not seen in models with the dolomite.

In the no additive case, solid phases in the 750-850°C range are mostly comprised of calcium magnesium silicates and sodium calcium silicates ($CaMgSi_2O_6$ and $Na_2Na_2Ca_3CaSi_6O_{18}$) and a mixture of other minor phases such as potassium silicates,

chlorides and sulphates. Moving beyond 850°C with the formation of additional slag, the remaining solid phases are predominantly calcium silicates and calcium magnesium silicates such as $CaSiO_3$ (wollastonite) and $Ca_2Mg_1Si_2O_7$. These are stable high melting point compounds (e.g. wollastonite has a melting point of 1548°C [266]). XRD analysis of wheat straw ashes after 2 hours of heating at 800°C by Dodson, et al. [267] showed $CaSiO_3$ to be the primary crystalline compound, which does differ from what the model here shows (no $CaSiO_3$ formation until around 850°C). However, the composition of Dodson, et al.'s [267] wheat straw did differ substantially to that used here, with higher K_2O and lower Na_2O and CaO, all of which would shift the relative position of the ash in key ternary systems such as K_2O-CaO-SiO_2 thereby affecting the formation temperature of solid compounds. Therefore, the prediction made here would still appear to be reasonable.

In the 50% and 150% dolomite cases shown in Figure 6.3 and Figure 6.4 respectively, it is apparent that there is less variation with temperature in the number and quantities of components than in the no additive case (Figure 6.2). This is due to the lower slag formation and higher stability of solid phases that form with use of the dolomite. Solid phases in the 50% dolomite case comprise overwhelmingly of calcium magnesium silicates ($CaMgSiO_4$ and $Ca_3MgSi_2O_8$), and smaller quantities of KCl and $KAlSiO_4$. In the 150% dolomite case, around 50% of the total phase mass is predicted to be $Ca_3MgSi_2O_8$ until around 890°C at which point some of this is lost with the formation of Ca_2SiO_4 and additional slag. MgO is a further major component, at around 10% of the total system mass over the entirety of the temperature range. There is a greater variety of minor components than in the 50% dolomite case though, such as the formation of potassium and sodium carbonates, though all these components combined only account for around 20% of the total system mass. These predicted components are in good general alignment with the XRD analysis of wheat straw ashes and 15% dolomite blends at 900°C by Li, et al. [253]. Li, et al. [253] saw the formation of $CaMgSiO_4$, $KAlSiO_4$, K_2CO_3, and KCl. No $Ca_3MgSi_2O_8$ was seen, though this may be due to the lower overall quantity of dolomite in relation to ash (15%, versus 50% and 150% modelled here).

Examining the kaolin phase data across Figure 6.5-Figure 6.7, it is clear that as with the dolomite, there is far less variation with temperature in the components and quantities of the solid phases than for the no additive case. In the 50% kaolin dosage case, there

are several major solid phases: $KAlSi_2O_6$, $NaAlSiO_4$, $CaSiO_3$, $CaMgSi_2O_6$, and $Ca_5(PO_4)_3(OH)$ (hydroxyapatite). The former of these accounts for around 40% of the total system mass, with the others around 7-12% each. As noted previously, slag is near negligible, as is the gas phase. Moving to the 150% kaolin case, $KAlSi_2O_6$, $CaAl_2Si_2O_8$, $KAlSi_3O_8$, and $NaAlSiO_4$ each represent between 10-25% of the total system mass. At the highest dosage case, 300% kaolin, there is further homogenization of the phases. Around 90% of the total system mass is comprised of four components: $CaAl_2Si_2O_8$, $KAlSi_3O_8$, $NaAlSi_3O_8$, and Al_2SiO_5. There is a lot of similarity between these cases, namely due to them all forming substantial quantities of potassium aluminosilicates and, to a lesser extent, sodium- and calcium-aluminosilicates. This aligns with the experimental observations via SEM/EDX in Chapter 5 sections 5.3.4-5.3.5, of the kaolin absorbing and reacting with potassium content of the ash, which would form potassium aluminosilicates as has been seen here. Li, et al. [253] observed the formation of the potassium aluminosilicate $KAlSiO_4$ after XRD analysis of wheat straw ashes with 15% kaolin. Other compounds with greater silica contents, such as $KAlSi_3O_8$ that were predicted by FactSage here were not seen by Li, et al. [253], though this may be due to the lower dosage of kaolin that they used (15%, as opposed to 50-300% modelled here).
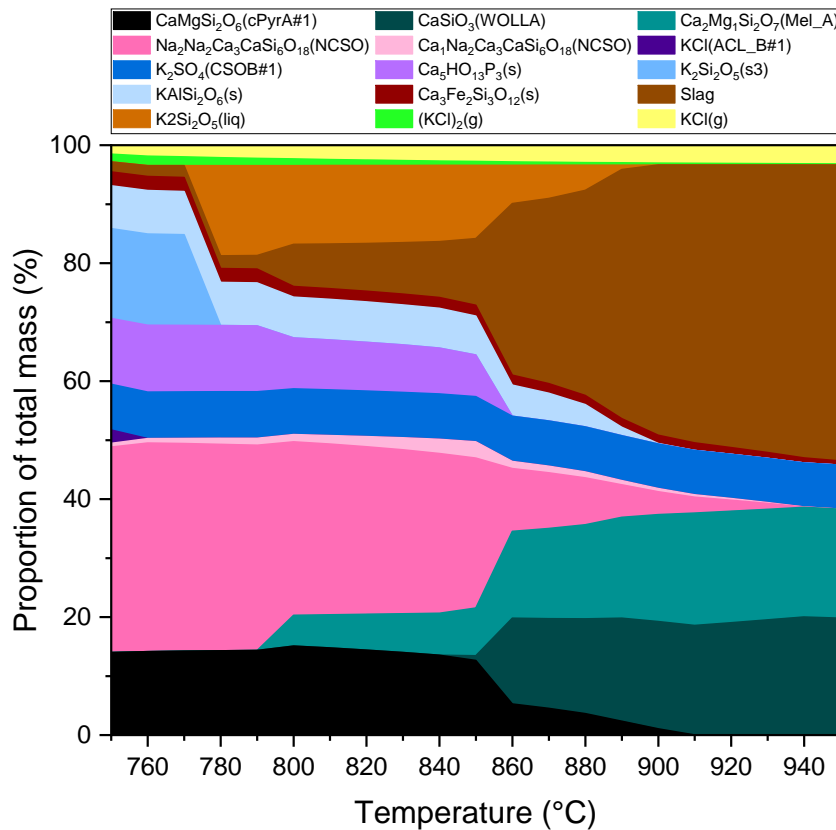
Figure 6.2: Phase chemistry for wheat straw & no additive case.
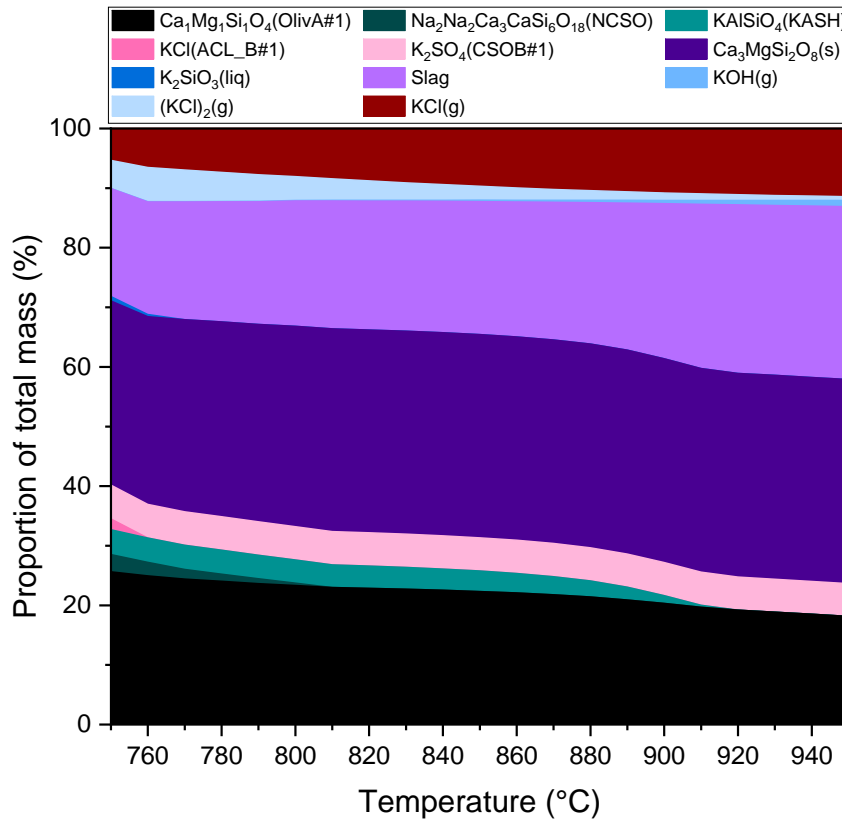
Figure 6.3: *Phase chemistry for wheat straw & 50% dolomite case.*
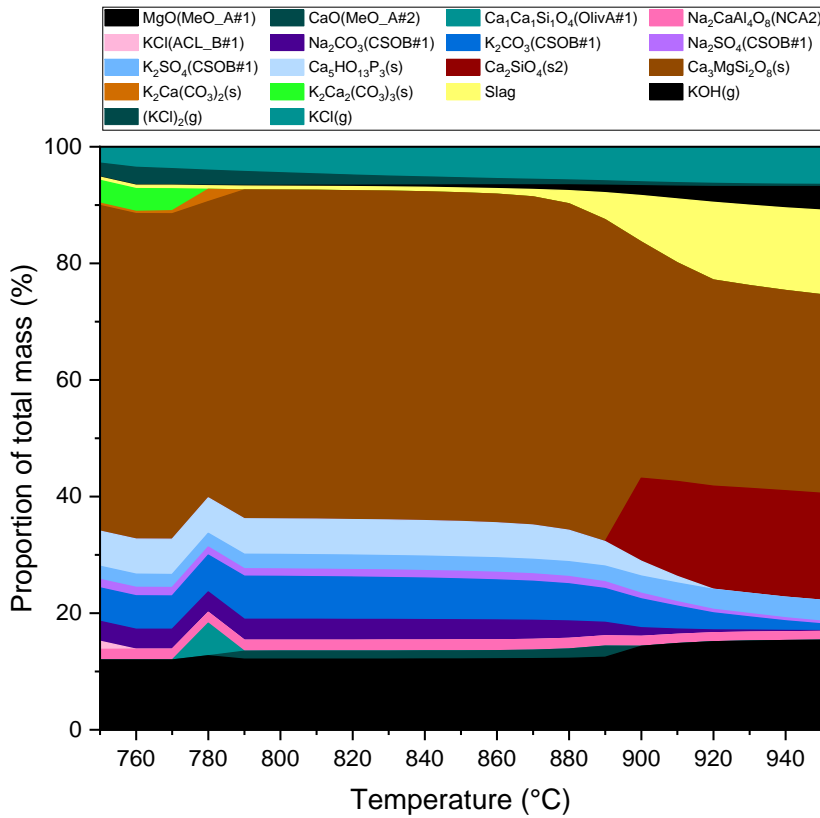
Figure 6.4: *Phase chemistry for wheat straw & 150% dolomite case.*
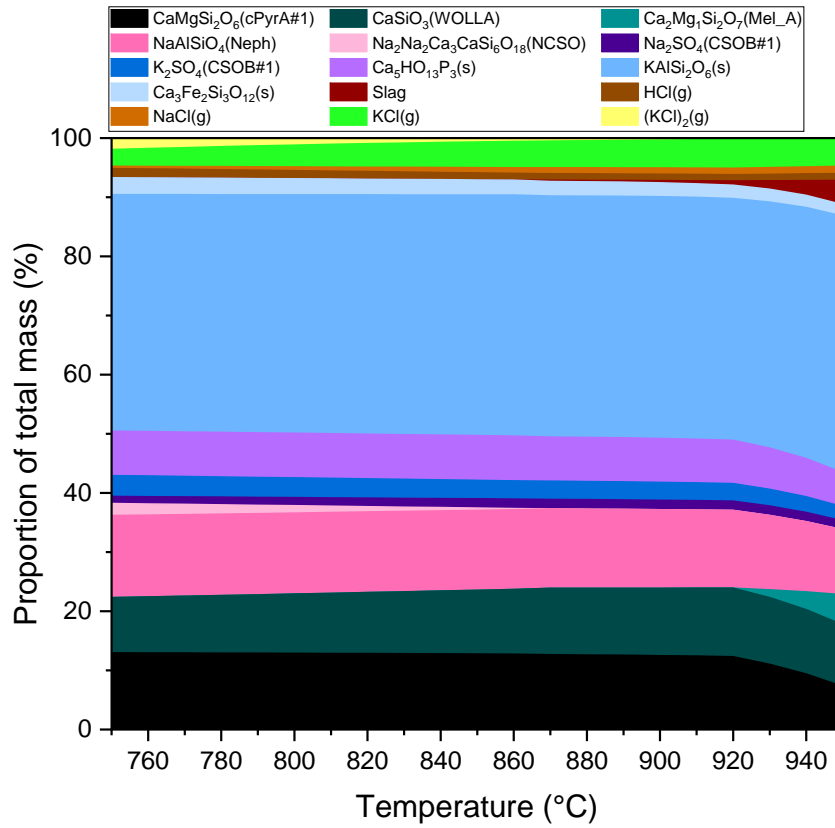
Figure 6.5: Phase chemistry for wheat straw & 50% kaolin case.
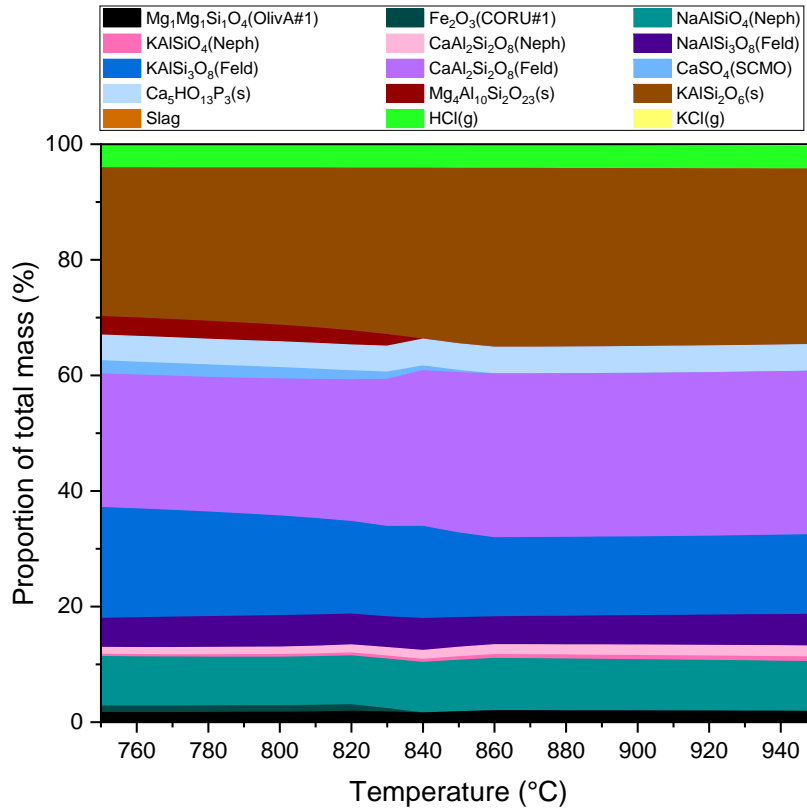
Figure 6.6: Phase chemistry for wheat straw & 150% kaolin case.
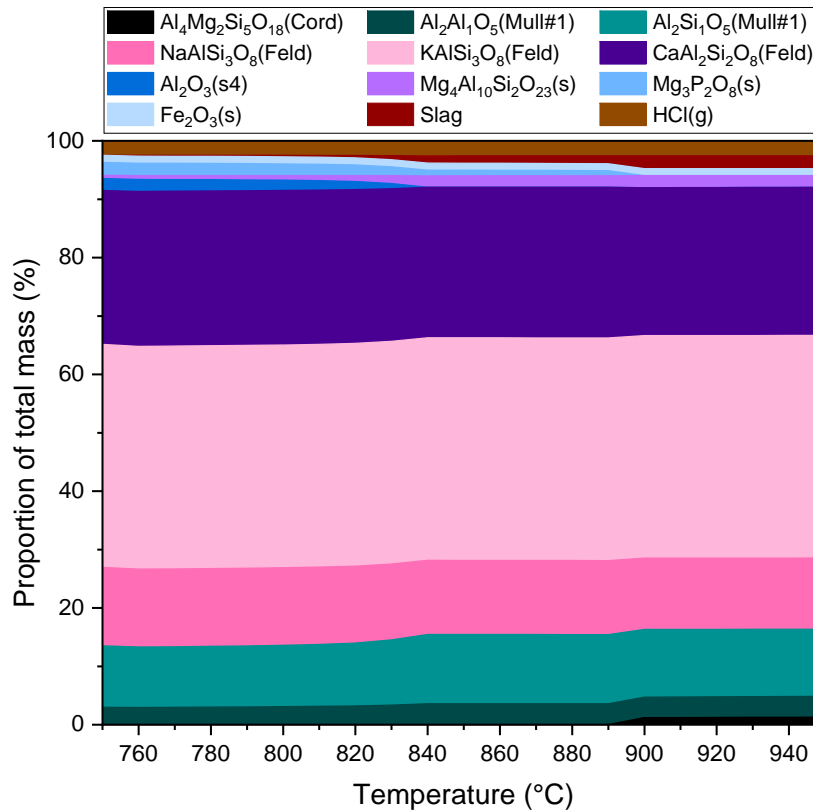
Figure 6.7: Phase chemistry for wheat straw & 300% kaolin case.

6.2.3   Phase Formations: Miscanthus with Additives

Figure 6.8 shows the total mass of slag plus liquid formed for miscanthus in each modelling case on a gram per kW$_{th}$ of fuel input basis. All the additives were predicted to provide a substantial reduction in total slag plus liquid content, particularly at temperatures greater than 850°C. It can also be seen that the use of kaolin results in the least total melt content across the board. There is some minor additional slag/liquid production in the 150% kaolin case versus the 50% kaolin case, perhaps suggesting some degree of melting of the silica in the kaolin. However, this may be due to the way FactSage considers all inputs to be well mixed and reach equilibrium [179], ignoring the physical realities of the kaolin structure (e.g. available surface area for interaction with ash). The 50% dolomite case sees a near doubling in slag plus liquid quantity from 830-850°C, due to some melting of the KAlSi$_3$O$_8$ solid phase and the inclusion of SiO$_2$ and K$_2$O into the slag phase.
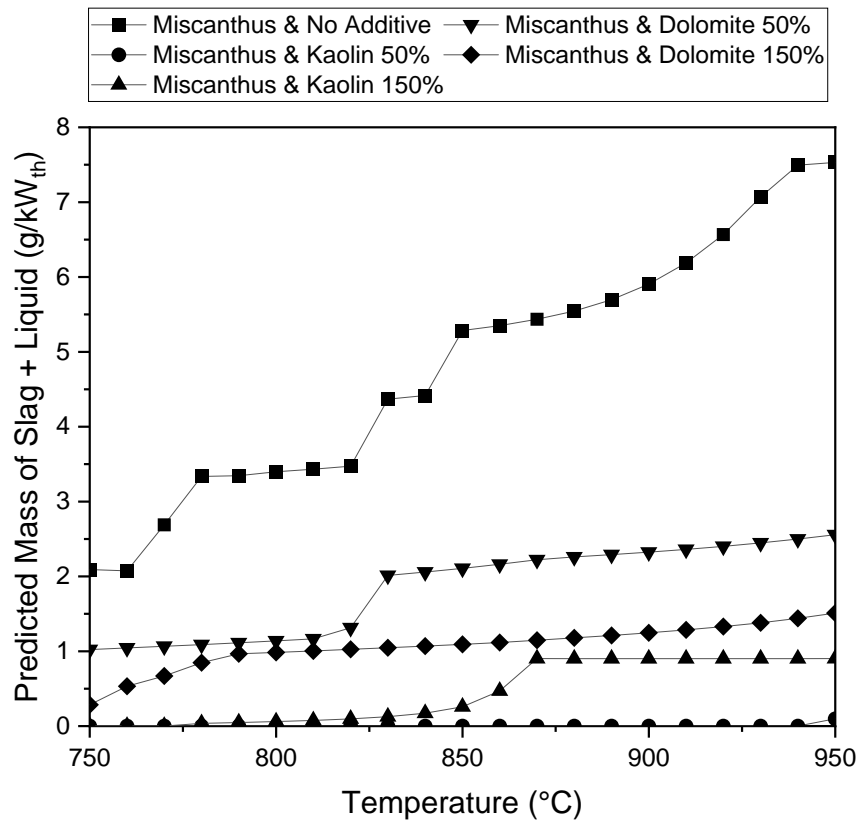
Figure 6.8: *Total slag plus liquid quantity formed on a gram per kW$_{th}$ fuel input basis for all miscanthus cases modelled.*

These results would again suggest that the kaolin is the superior additive for reducing ash melting issues, further enhanced by its ability to capture gaseous KCl which would otherwise contribute to corrosion issues [84]. Considering that even the 50% kaolin dosage is predicted to nearly eliminate ash melting issues over the 750-950°C temperature range, a lower dosage would likely be viable. This is also supported by the lack of defluidization issues when using either additive at a 50% dosage during testing with miscanthus. Therefore, it would be suggested that a slag plus liquid content of the order of 2g/kW$_{th}$ input, as predicted as the upper levels of slag produced in the 50% dolomite case, is a manageable quantity of slag plus liquids in the bed whilst still maintaining good fluidization. This figure could be used in future additive optimisation modelling work as a target maximum slag plus liquid value.

Figure 6.9-Figure 6.13 shows the phase chemistry over the 750-950°C range for miscanthus ash in each of the additive dosage cases. No fundamental studies of miscanthus ash and dolomite and/or kaolin could be found in the literature, which limits the ability for a similar comparison as was made for wheat straw in section 6.2.2. In the no additive case, there is a significant number of solid phases disappearing as the

quantity of slag rapidly increases with temperature. Below around 850°C, prominent solid phases include $CaMgSi_2O_6$, $Ca_5(PO_4)_3(OH)$, SiO_2, $Na_2Ca_3Si_6O_{16}$, plus several other minor phases. Beyond 850°C, there is homogenization of the solid phases to just $CaMgSi_2O_6$, $CaSiO_3$, SiO_2, and $Ca_3Fe_2Si_3O_{12}$ by 950°C. Kaknics, et al. [115] heat treated miscanthus ashes to 1000°C and then performed XRD, observing the occurrence of $CaMgSi_2O_6$, $CaSiO_3$, Ca_2SiO_4, $MgSiO_3$ and SiO_2, which is in broad alignment with the predictions made here, supporting their general reliability.

As was seen with the wheat straw in section 6.2.2, moving to dolomite results in less variation to phases, with a system dominated by a handful of solid phases. In the 50% dolomite case (Figure 6.10), $CaMgSi_2O_6$ accounts for around 55% of the total system mass, with all other solid phases amounting to at most 30% of the system mass. These other phases are a variety of different calcium silicates, sodium silicates, potassium aluminosilicates, and others. Moving to a 150% dolomite dosage (Figure 6.11), there is further homogenization of the solid phases, to a system that is around 50% $Ca_3MgSi_2O_8$, 20% Mg_2SiO_4, and 10-20% other solids. This is broadly as would be expected, given that the higher availability of calcium and magnesium in the system would allow for the formation of calcium magnesium silicates with greater calcium quantities, and for the formation of magnesium silicates. However, it should be noted that in the analysis in Chapter 5 sections 5.3.4.3 and 5.3.5.3, calcium was the primary component seen to migrate out of the dolomite and react with the ash, whilst the magnesium mostly stayed within the dolomite structure with less outward migration. FactSage, however, assumes all components are well mixed and reach equilibrium, so cannot fully capture the underlying physical behaviours.

Looking at the miscanthus and kaolin data, in the 50% kaolin case (Figure 6.12), the main solid phases are $CaMgSi_2O_6$, $NaAlSi_3O_8$ and $KAlSi_3O_8$, which are around 10%, 15% and 50% of the total system mass respectively. In the 150% kaolin case (Figure 6.13), the main solid phases are SiO_2, $CaAl_2Si_2O_8$, $KAlSi_3O_8$, and $NaAlSi_3O_8$, which between them account for around 70% of the total system mass. Again, there is similarity between these cases, notably in formation of alkali aluminosilicates. Greater variation in quantities of each can be seen across the temperature spectrum in the 150% kaolin case, which is a different behaviour than was seen in the 50% kaolin case (Figure 6.12).
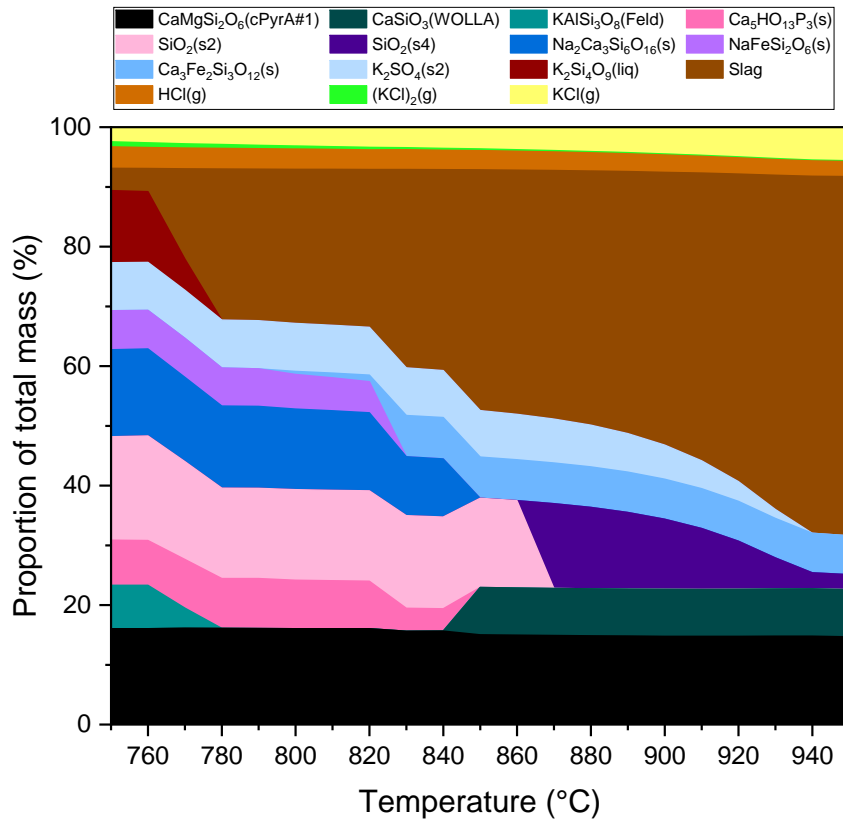
Figure 6.9: *Phase chemistry for miscanthus & no additive case.*
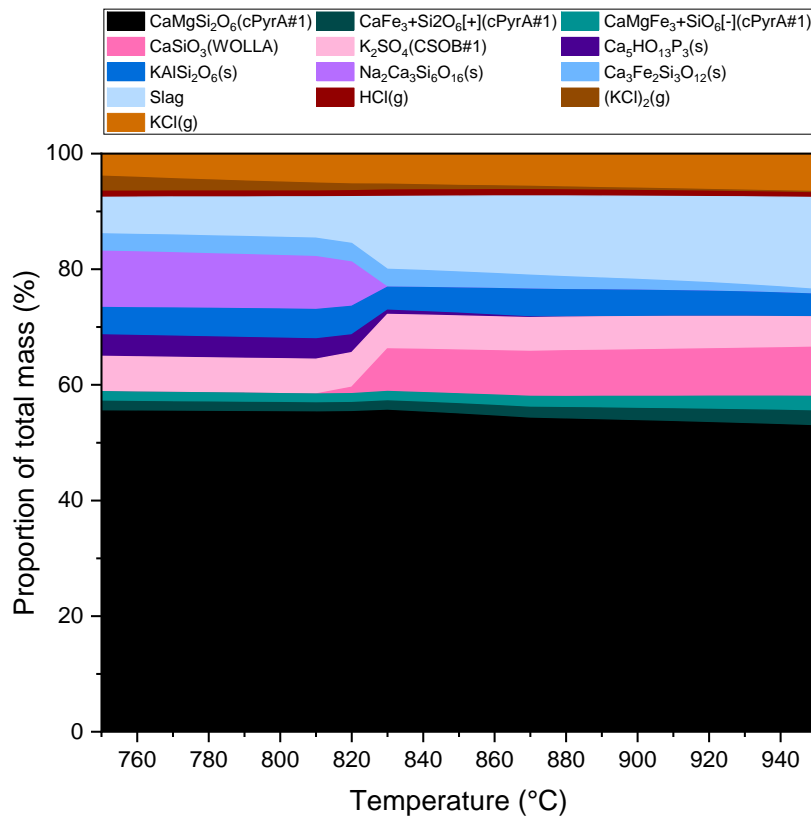
Figure 6.10: *Phase chemistry for miscanthus & 50% dolomite case.*
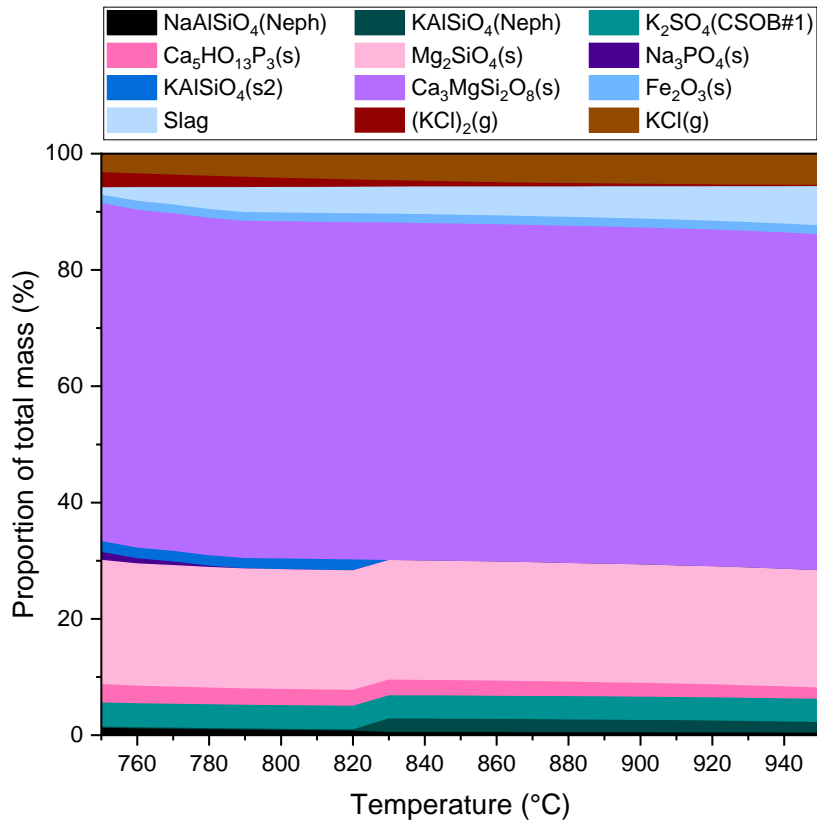
Figure 6.11: *Phase chemistry for miscanthus & 150% dolomite case.*
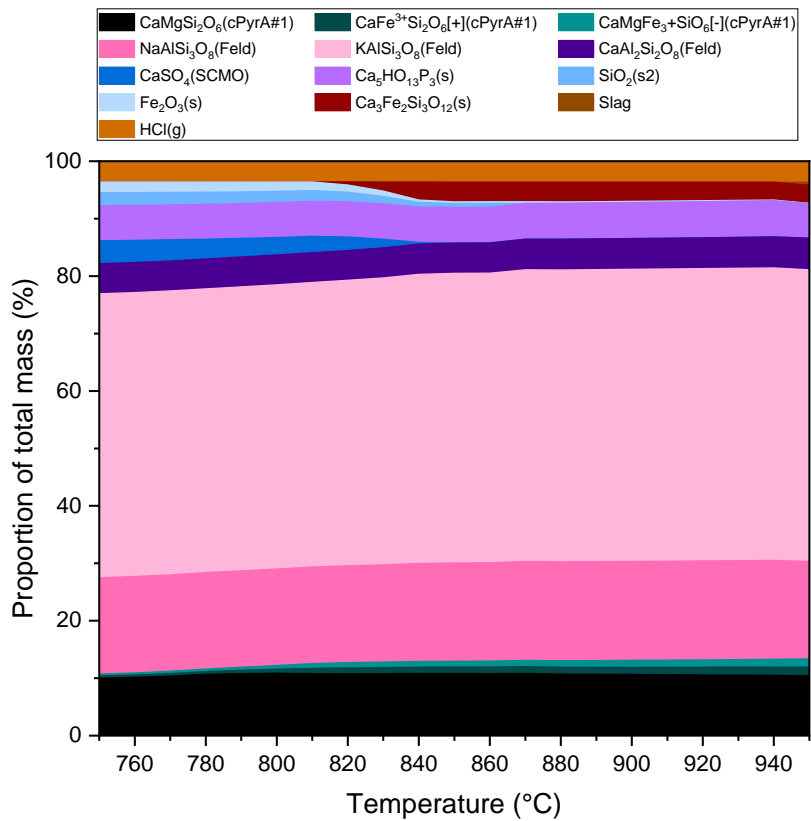
Figure 6.12: *Phase chemistry for miscanthus & 50% kaolin case.*
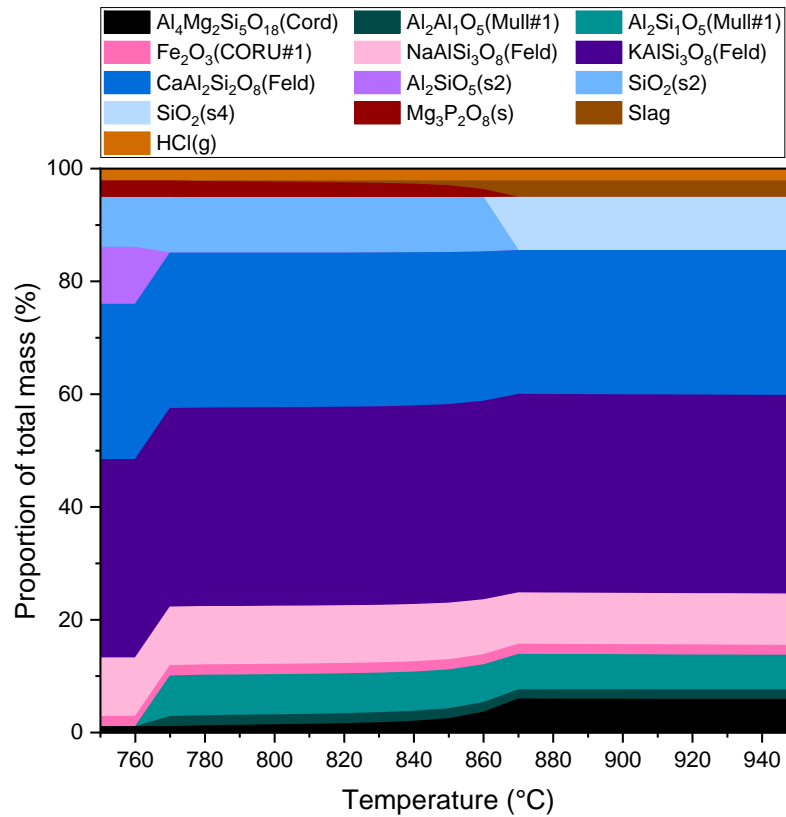
Figure 6.13: Phase chemistry for miscanthus & 150% kaolin case.

6.2.4   Comparison and Discussion

From Figure 6.1 and Figure 6.8, it is evident that when using no additive, both wheat straw and miscanthus are predicted to produce similar amounts of a slag plus liquid phase. Both show quantities of around $3g/kW_{th}$ at 800°C, and $7g/kW_{th}$ at 950°C, with similar intermediary temperature trends. This would suggest that on a purely chemical basis, both fuels should be "equally bad" with regards to agglomeration. In Chapter 3 section 3.8.1 it can be seen that both fuels have similar ash contents, and whilst miscanthus does have almost half the K_2O content of the wheat straw, the K/Ca ratio is similar between the two fuels which is suggested in literature to be an indicator of agglomeration propensity [171]. However, even without additive use in Chapter 5, the wheat straw was observed to be a far worse fuel than the miscanthus, with much shorter defluidization times. With kaolin, neither fuel is predicted to produce more than $1.25g/kW_{th}$ of slag plus liquid; this upper value being the wheat straw with 300% kaolin case. Dolomite with wheat straw is predicted to perform substantially worse than with miscanthus. The 50% case is predicted to perform as poorly as the no additive case, and the 150% case, whilst producing $<1g/kW_{th}$ below 900°C, rapidly increases to around $4g/kW_{th}$ slag plus liquid by 950°C.

With the miscanthus however, the worst dolomite case according to the model (50% dosage) produces no more than 2.5g/kW$_{th}$ by 950°C. Whilst both fuels contain around 6wt.% ash content, they have significant material differences within this ash content (e.g. 19.8wt.% K$_2$O in wheat straw versus 11.7wt.% in miscanthus, or 21.1wt.% CaO in wheat straw versus 13.5wt.% in miscanthus). Therefore, it is expected that they would respond differently to additive use, and this is apparent here. Miscanthus was seen to respond very well to additive use in Chapter 5 (section 5.3.1.1), avoiding defluidization issues, and this behaviour is reflected here in the model. Wheat straw, comparably, is predicted to have similar quantities of slag plus liquid to miscanthus in the no additive case, kaolin cases, and the 150% dolomite case. On this basis, FactSage does not reflect the poor experimental performance of the wheat straw. This would suggest that physical behaviours are having a bigger role in propagating agglomeration issues when using the wheat straw pellets than for the miscanthus, as FactSage only consider the system chemical equilibrium. This therefore adds further support to the theory that it is pellet breakdown and ash release mechanisms that are particularly problematic for the wheat straw as proposed in Chapter 5 section 5.4.

For the miscanthus, it was noted the 50% dolomite case was predicted to produce the most slag plus liquid content with a peak of 2g/kW$_{th}$ across the 800-850°C temperature range. This temperature range was typical of the bed during testing (see Chapter 5 section 5.3.1.2). During testing, this condition did not undergo any bed defluidization, therefore this value of 2g/kW$_{th}$ slag plus liquid may be considered acceptable in the bed whilst avoiding agglomeration issues. Another consideration is that the "no additive" test, which did undergo defluidization in Chapter 5 section 5.3.1.1, operated across the 800-850°C range (see Chapter 5 section 5.3.1.2). This case is predicted to form between 3.5-5.5g/kW$_{th}$ of slag plus liquid. Therefore, if attempting to optimise dolomite dosage with miscanthus via FactSage, it would be recommended to keep far below this lower bound of 3.5g/kW$_{th}$, and as close to the 2g/kW$_{th}$ slag plus liquid limit as can be achieved. Determining the exact point at which defluidization becomes an issue would necessitate further experimental testing of lower dolomite dosages.

As can be seen across sections 6.2.2 and 6.2.3, there was good general alignment between the predicted solid phases from the FactSage models, and those seen in fundamental XRD studies of ash and ash/additive blends by other groups. There were some differences, though these appear to be in part due to different conditions and ash

compositions modelled here versus those used in literature comparisons. This would suggest that when using FactSage to predict biomass ash melting behaviour, users can be reasonably confident that the predicted solid phases are reasonable. However, it is difficult to assess if the predicted phase quantities are realistic due to a lack of quantitative XRD experimental studies for ash and additive blend in the literature. It is important to state that the most important factor, from the perspective of agglomeration prediction or estimation, is the prediction of the quantity of molten slag and liquid that would form in the bed [75]. Therefore, whilst the accurate prediction of solid phases is not of direct importance, it is a consequence of having predicted the correct quantities and composition of the slag phase. It is difficult to assess the accuracy of these melt quantity predictions, aside from on a qualitative basis as done here, i.e. longer operational times were seen to correlate with a lower melt quantity prediction. It is important to draw the distinction that these predicted melt quantities may be entirely correct for both wheat straw and miscanthus – i.e. that it is simply the physical factors of the wheat straw particle that caused its severe agglomeration issues, as proposed in Chapter 5 section 5.4. This means that whilst chemically this approach may be entirely correct, the approach cannot be used to predict overall agglomeration severity.

For both fuels, kaolin was seen to be the superior additive in modelling, producing lower quantities of slag plus liquid across all dosages versus the dolomite, with even a 50% dosage of kaolin sufficient to reduce the quantity of slag plug liquid to near negligible amounts. Furthermore, there was a clear reduction in KCl gas content with successive increases to kaolin dosage, as KCl reacted to form alkali aluminosilicates. As mentioned, this would have clear benefits downstream of the bed in a FBC boiler by reducing corrosion of boiler metalwork. As the 50% kaolin dosage was sufficient to minimise ash melt formation, something seen experimentally with the miscanthus defluidization time performance in Chapter 5 section 5.3.1.1, there would appear to be little reason to go beyond this dosage point.

Given the kaolin behaviour of removing alkali metal content from the bed and flue gas, as well as the prediction of it leading to lower bed slag plus liquid quantities, kaolin would appear to be the superior additive to dolomite. In sourcing materials for the test campaign, kaolin was available at around £500 per tonne versus dolomite at around £160 per tonne. These prices would no doubt be open to negotiation for power station operators ordering far larger quantities on a regular basis, but it does give an indicate

the potential of a ~3x cost delta between the two. Therefore, on a cost/performance trade-off basis, commercial operators may still wish to consider dolomite if it provides a sufficient performance improvement to meet their plant operation targets whilst limiting cost.

6.3   Modelling of EDX Data

6.3.1   Objectives & Modelling Matrix

In Chapter 5, a substantial amount of SEM/EDX analysis was performed to determine the composition of agglomerates at different common features and spatial locations. One thermochemical modelling approach that is far less common for agglomeration studies in the literature is to use EDX compositional data as the model input, to determine the phases that would have been present when the sample was in-situ. To the authors' knowledge only two other groups have published a study using this approach for bed agglomeration with biomass fuels [122, 151]. Elled, et al. [151] modelled up to 15 discrete EDX measurements across several agglomerate samples for tests with wood, straw, bark, and solid recovered fuels. He, et al. [122] used averaged EDX data for woody fuels to construct a model of coating layer formation. In this chapter, the average EDX data analysed in Chapter 5 sections 5.3.4-5.3.5 was used to model phase formations. This would aid in deepening understanding of the phases, behaviours, and mechanisms of agglomeration when the agglomerates were in the bed at temperatures of 800-900°C. This approach has never been performed in the literature with this type of spatial EDX data nor with additive use. It is also an approach that would be difficult to replicate experimentally. Moreover, it mitigates some of the weaknesses of FactSage, as physical behaviours influencing agglomerate composition would have been captured in the during experimentation and formation of the agglomerates.

The standard approach for FactSage modelling set out in Chapter 3 section 3.6 was applied. Table 6.3 lists the EDX data sets used. These are the same data sets that were analysed in Chapter 5 sections 5.3.4-5.3.5. Some minor components (e.g. chromium) were removed from the data set due to having no influence on agglomeration mechanisms but would otherwise significantly increase compute times for modelling. The solutions used in each modelling case are listed in Table 6.4. A 1000g mass of the EDX data was used as the sole input to the model. No gaseous environments were considered, as the objective was to model this "final state" EDX data at the operating

bed temperature. The cases were modelled from 500-1500°C, with a 10°C temperature stepping, at 1atm pressure. A narrower temperature range of 500-1000°C was chosen for discussion in the subsequent sections. This is slightly larger than that in section 6.2, as it would allow for a broader discussion of expected phase changes and reflect the fact that agglomerates will have undergone both testing and subsequent cooling of the bed.

Table 6.3: *EDX analysis data for different agglomerate regions across both fuels and additives, used as the modelling inputs.*

Component	Wheat Straw & Kaolin			Wheat Straw & Dolomite		Miscanthus & Kaolin			Miscanthus & Dolomite		
	Bulk ash melt around kaolin particles	Ash melt adjacent to additive	Additive adjacent to ash melt	Bulk ash melt around dolomite particles	Ash melt adjacent to dolomite particles	Bulk ash melt	Ash melt adjacent to kaolin particles	Kaolin particles adjacent to ash melt	Bulk ash melt	Ash melt adjacent to dolomite	Dolomite particles adjacent to ash melt
O (wt.%)	42.04	42.35	46.12	41.47	42.95	43.47	42.46	48.39	47.27	47.55	48.71
Na (wt.%)	0.76	0.57	0.30	0.61	1.03	7.58	6.44	0.92	4.48	3.14	2.18
Mg (wt.%)	1.32	1.07	0.24	5.74	4.04	0.85	0.87	0.16	2.00	6.74	29.31
Al (wt.%)	1.69	0.48	20.62	0.41	0.89	0.31	1.72	20.83	0.41	0.42	
Si (wt.%)	29.68	32.30	26.43	27.51	24.02	30.70	28.35	22.46	29.54	26.21	6.69
P (wt.%)	2.19	1.46	0.40	0.91	2.30	0.60	0.63	0.21	0.79	0.64	0.31
S (wt.%)	0.30	0.21			0.18	0.38	0.54			0.16	0.30
Cl (wt.%)			0.19	0.12	0.25	0.36	0.45	0.11	0.26	0.35	0.49
K (wt.%)	14.24	16.26	5.01	7.94	9.39	12.00	13.13	5.94	7.83	7.45	1.31
Ca (wt.%)	8.22	5.34	1.09	16.64	14.53	2.86	2.77		5.92	6.81	9.99
Fe (wt.%)	0.63	0.49	0.91	0.68	0.77	0.88	0.64	0.98	0.94	0.55	0.72

Table 6.4: FactSage solutions enabled for each EDX data set modelling case.

Fuel	Kaolin			Dolomite		
	Bulk ash melt	**Ash adjacent to kaolin**	**Kaolin adjacent to ash**	**Bulk ash melt**	**Ash adjacent to dolomite**	**Dolomite adjacent to ash**
Wheat Straw[1]	FToxid: SLAGA (I), cPyrA (I), WOLLA (+), Feld (+)	FToxid: SLAGA (I), cPyr (I), WOLLA (+), Feld (+)	FToxid: SLAGA (I), Feld, (+) FTsalt: PRVKA (J)	FToxid: SLAGA (I), cPyrA (I), WOLLA (+), Mel_A (+), NCSO (+) Ftpulp: ACL (J)	FToxid: SLAGA (I), cPyrA (I), WOLLA (+), Feld (+) FTpulp: ACL (J) FTsalt: CSOB (J), KSO_ (I)	*Not modelled; insufficient experimental data for averaging.*
Miscanthus[1]	FToxid: SLAGA (I), SPINA (I), cPyrA (I), Feld (+) FTpulp: ACL (J) FTsalt: CSOB (J)	FToxid: SLAGA (I), SPINA (I), cPyrA (I), OlivA (I), CORU (I), Feld (+) FTpulp: ACL (J) FTsalt: CSOB (J)	FToxid: SLAGA (I), Cord (+), CORU (I), Feld (+)	FToxid: SLAGA (I), cPyrA (I), LcPy (+), WOLLA (+), Feld (+) FTpulp: ACL (J)	FToxid: SLAGA (I), cPyrA (I), LcPy (+), OlivA (I), Feld (+) FTpulp: ACL (J) FTsalt: CSOB (J)	FToxid: SLAGA (I), SPINA (+), MeO_A (I), OlivA (I) FTpulp: ACL (J) FTsalt: CSOB (J), KSO_ (I), LCSO (I)

[1] *Refer to Appendix D for further detail on each solution used.*

6.3.2   Phase Formations: Wheat Straw with Additives

6.3.2.1   Melt Formation

Figure 6.14 shows the combined slag plus liquid quantities predicted for each agglomerate location when using wheat straw and additives. A few trends are evident. The overall quantity of slag plus liquid does not change to a significant degree in any of the cases between 800-900°C. For most locations, there is a rapid rise in slag plus liquid content over the 600-800°C temperature range. This is the result of the formation of various ash melt components, such as potassium silicate eutectics which melt from around 750°C [91]. With kaolin use, both the bulk ash melt region and the ash adjacent to kaolin particles region are predicted to have upwards of 40% more melt content over the 750-950°C temperature range than the equivalent dolomite case. This significant difference is likely due to dolomite interactions with ash releasing magnesium and calcium content, which would lead to elevated melting temperatures as discussed in section 6.2.4 and speculated previously by Steenari & Lindqvist [165]. It can be seen in Table 6.3 that with dolomite, there is twice as much calcium (16.64wt.% versus 8.22wt.%) and three times as much magnesium (5.74wt.% versus 1.32wt.%) in the bulk ash melt phase than with kaolin and wheat straw. This provides clear evidence of the benefit of the dolomite behaviour in reducing ash melt formation.

Regions of ash adjacent to kaolin and ash adjacent to dolomite are both predicted as having greater quantities of molten ash than the bulk melt regions. For both additives, as can be seen in Table 6.3, these regions have slightly higher potassium contents, but perhaps more importantly have lower magnesium and calcium contents. This leaves the composition of these regions dominated by K-Si-O, as was observed in Chapter 5 sections 5.3.4.2 and 5.3.5.2, which form a more molten potassium silicate "leading edge of attack" against additive particles. This again is in-line with expectations, as potassium silicate eutectics with greater silica contents generally have lower melting points [91, 268]; e.g. for $K_2O.SiO_2$ the melting point is 976°C, whereas for $K_2O.3SiO_2$ the melting point is 740°C. Bulk melt regions have higher quantities of calcium and magnesium, which have formed stable solid calcium/magnesium silicates as would be expected, reducing the overall melt quantity. The lowest melting points in the $CaO-SiO_2$ and $CaO-MgO-SiO_2$ systems are 1436°C and 1357°C respectively [269, 270].

From the analysis of the kaolin particle region adjacent to ash, a small degree of melting is expected at around 980°C. This temperature is far in excess of those seen in the bed during experimentation in Chapter 5 section 5.3.1.2 (no more than 950°C during brief periods of operation). Therefore, there would be no melting of kaolin expected in reality, which aligns with the experimental observation of distinct boundaries between kaolin and ash from the SEM/EDX work in Chapter 5 section 5.3.4.1, with no evidence of changes to the morphology of kaolin particles. This prediction also aligns with other studies of kaolin with biomass ash, which have found no evidence of kaolin melting below 1000-1100°C [249, 264], lending further credibility to the FactSage prediction. In a commercial BFB boiler however, the freeboard can be exposed to temperatures up to around 1100°C [235]. Therefore, any entrained fine fragments of kaolin may contribute to the formation of molten slag deposits on the boiler wall tubes.

An equivalent modelling case of dolomite particle regions adjacent to wheat straw ash was not possible, as there was insufficient EDX data to find a conclusive average composition. This was due to the high degree of heterogeneity seen in the dolomite structure, as discussed in Chapter 5 section 5.3.4.3.
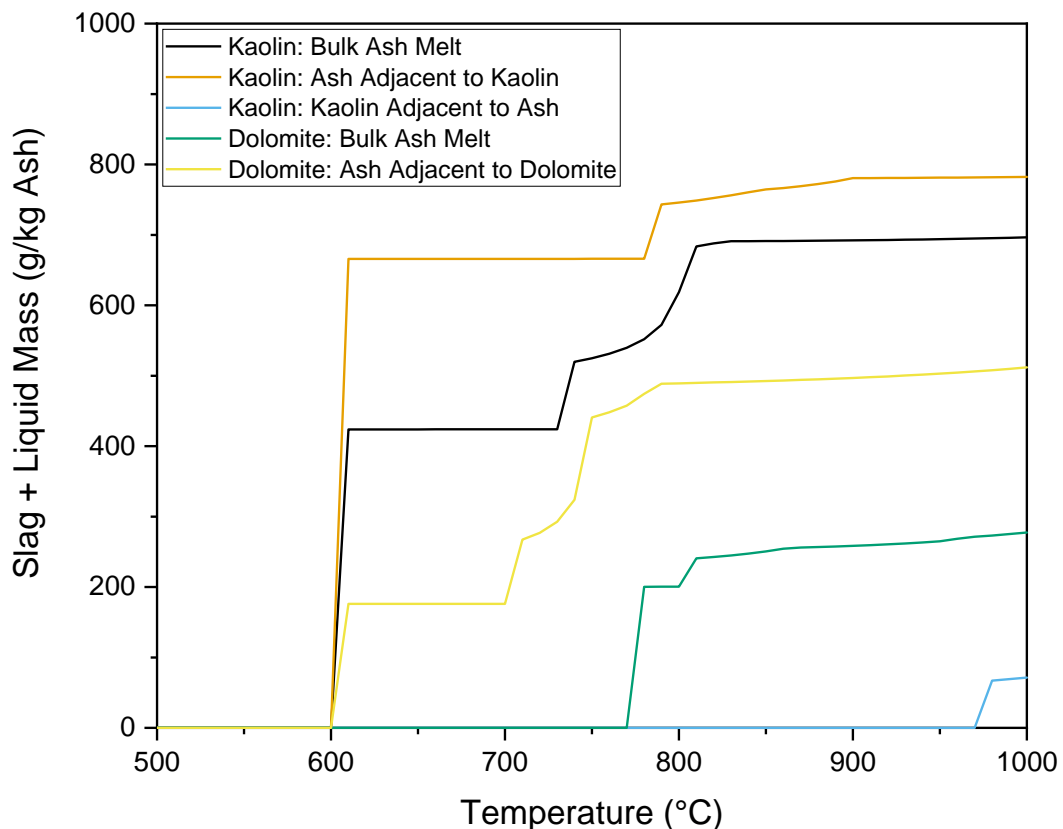
Figure 6.14: Combined slag plus liquid mass for wheat straw and additives EDX data cases, at the different agglomerate locations as listed.

6.3.2.2   Phase Formations

The predicted phase composition for wheat straw with each additive at 850°C is shown in Figure 6.15. A temperature of 850°C was selected as this is the typical bed target operating temperature. Components with a mass <10g have not been shown, due to representing <1% of the total system mass. Several key similarities and differences are evident. Across all the cases, aside from kaolin particles adjacent to ash, K_2O and SiO_2 are the major slag components. This is as would be expected given that both are responsible for fundamental agglomeration behaviours [111]. Calcium silicates ($CaSiO_3$) and calcium magnesium silicates ($CaMgSi_2O_6$) are major solid components in all the ash regions. In the ash adjacent to kaolin case, a liquid potassium silicate phase ($K_2Si_4O_9$) accounts for over 50% of the mass, with the solid phase making up a much smaller proportion of the mass (~20%). As mentioned previously, this highly molten region would form a leading edge of attack against the kaolin. This molten region is likely to be highly viscous, as $K_2Si_4O_9$ has a viscosity of 1700 poise at 1200°C [271]. The kaolin particle region adjacent to ash is the most unique of the cases, with no molten region. This primarily comprises of $KAlSi_3O_8$ and Al_2SiO_5, which is as would be anticipated given that kaolin is an aluminosilicate that reacts with potassium to form a potassium aluminosilicate. Lower order alkali aluminosilicates ($KAlSiO_4$) have been found in XRD studies of ash and kaolin blends [253].
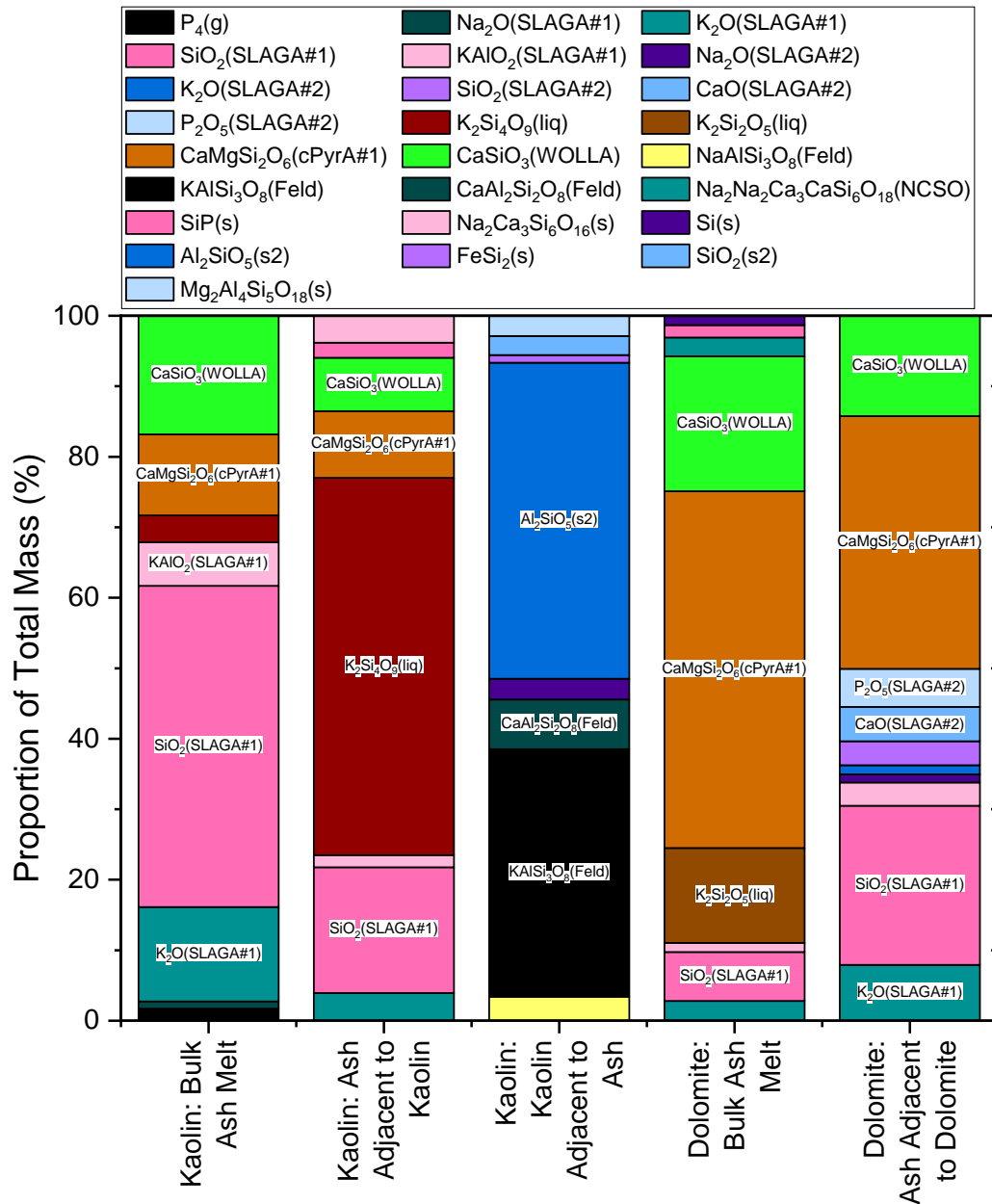
Figure 6.15: Phase composition for wheat straw and additive EDX data cases at 850°C.

6.3.3 Phase Formations: Miscanthus with Additives

6.3.3.1 Melt Formation

Figure 6.16 shows the combined slag plus liquid mass for miscanthus and additives at different agglomerate locations. Looking at the bulk ash melt regions in comparison to regions of ash adjacent to additive particles, it is seen that for both additives, the bulk ash melt region is more molten over the 750-950°C range. In the case of miscanthus and kaolin, this delta is very small, around 7% at most. For kaolin in the 700-770°C temperature range, the behaviour is briefly reversed, i.e., the bulk ash melt region is less

molten than the ash adjacent to kaolin particles. This behaviour again is broadly as would be expected from the input EDX data (Table 6.3). In the kaolin case, the bulk ash melt region and ash adjacent to kaolin region compositions are very similar, though the ash adjacent to kaolin region does have 1.4wt.% more aluminium content and almost 2.5wt.% less silicon content. Aluminium is known to increase melt temperatures, as seen experimentally by others [164, 272]. From a separate analysis of the slag components (Figure 6.17), it is apparent that this lower silicon content led to less silica in the slag melt and accounted for the slag formation difference between the bulk ash melt and ash adjacent to kaolin regions. In the dolomite cases, ash adjacent to dolomite has three and half times as much magnesium content, and less sodium content (Table 6.3). These would appear to be the drivers of the lower melt quantity versus the bulk ash melt region, given that magnesium is known to increase melt temperatures whereas sodium is known to contribute to biomass ash melting issues [164, 176, 273].

The overall quantity of molten ash is lower when using dolomite versus kaolin, both for the bulk ash melt and the ash adjacent to additive regions. As with wheat straw, this is again likely down to release of calcium and magnesium into these regions, as seen in Table 6.3, both of which are known to reduce ash melting issues [164].

Another interesting behaviour seen in Figure 6.16 regards dolomite particle regions adjacent to ash. There is the prediction of around 10% of the total system mass forming a melt over the 800-900°C range, slowly increasing with elevated temperatures. This melt is comprised of a slag of SiO_2, K_2O, MgO, and P_2O_5, plus a smaller (~10%) liquid fraction of KCl (Figure 6.17). Aside from MgO, none of these components are present in dolomite (see Chapter 3 section 3.8.3), suggesting that there was some intrusion of molten ash into the outer dolomite structure that was picked up during EDX analysis. It is possible that this molten ash in the outer regions of the dolomite particle acts as the diffusion medium for magnesium and calcium in the dolomite to migrate into the ash melt and then move outwards into the wider bulk ash melt. Note that this does not appear to be a crystal substitution mechanism, as was proposed for the formation of calcium layers on olivine in Chapter 4 section 4.3.7.2. This calcium/magnesium diffusion theory could be studied further in a controlled laboratory test with a synthetic mixture of biomass ash with dolomite.
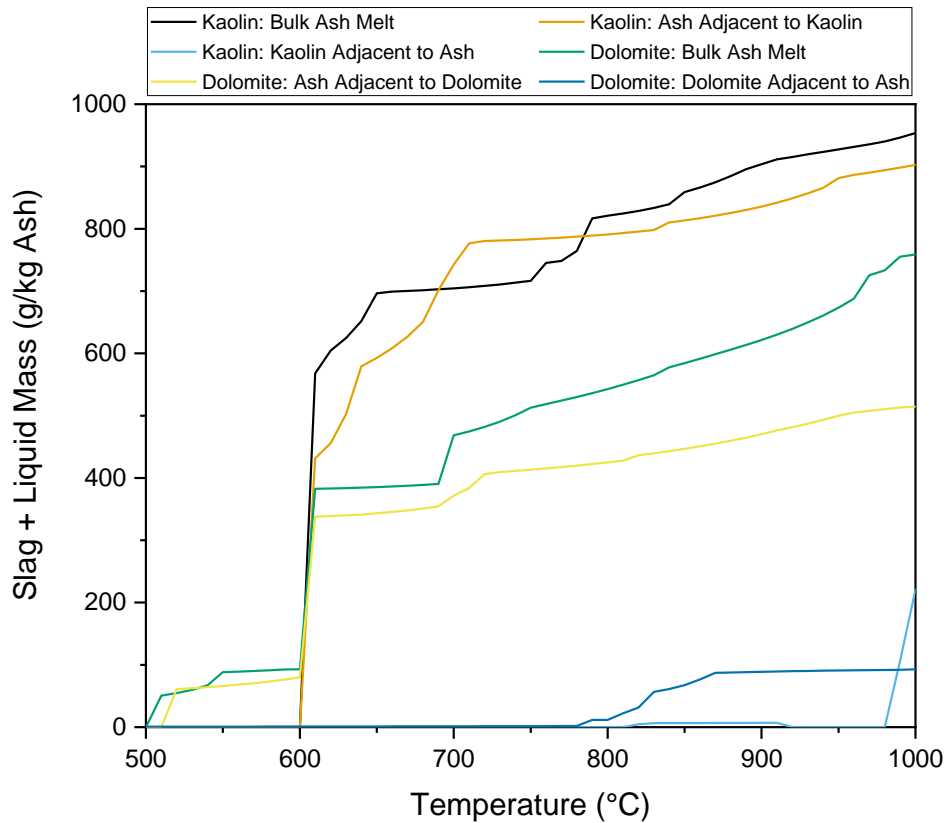
Figure 6.16: *Combined slag plus liquid mass for miscanthus and additives EDX data cases, at the different agglomerate locations as listed.*

6.3.3.2   Melt Formation Comparison with Wheat Straw

The main similarity seen for both fuels with additives when comparing melt formation is that with dolomite, there is a lower quantity of melt present in the bulk melt and ash adjacent to additive regions than with kaolin usage. As discussed in sections 6.3.2-6.3.3, this is as expected given that dolomite was seen to release calcium and magnesium into the wider ash melt in Chapter 5 section 5.3.4.3 and both of these are known to increase ash melting points [164, 264]. It is worth noting that this lower quantity of melt with dolomite does not imply that dolomite is the better additive, as the modelling of EDX data only considers localised melt formation on an agglomerate. To determine the total ash melt formation, the approach taken in section 6.2 would be required as this considers the entire fuel ash and additive input.

A second visible trend is that when comparing the kaolin additive cases for each fuel, the use of miscanthus resulted in a higher melt quantity than when using wheat straw, when comparing like-for-like ash regions. This difference was generally around 100-200g/kg of melt. For example, when looking at the bulk ash melt region with kaolin when using wheat straw (Figure 6.14), from 600°C to 1000°C, total melt quantity

increased from around 400g/kg ash to around 700g/kg ash. With miscanthus on the other hand (Figure 6.16), for the same region and temperature range (600-1000°C for the bulk ash melt region with the kaolin data set), total melt quantity varied from around 550g/kg ash to around 950g/kg ash. This trend was also seen in with dolomite use in the bulk ash melt region. This suggests that wheat straw agglomerates were able to bind together with a lower quantity of melt than equivalent miscanthus agglomerates. Such a behaviour would support the theory proposed in Chapter 5 section 5.4 and supported by findings in this chapter: physical behaviours surrounding the lack of breakdown of the wheat straw pellet and the release of ash to its surface allow it to act as a "ready-made" platform for agglomerate formation, and thus are a major cause of the poor performance of the fuel. Experimental validation would be required to confirm the different minimum quantities of melt needed to form agglomerates under these circumstances. Some investigations have been made along these lines, though none are applicable for comparison here, nor consider the impact of agglomerate shape on the required amount of ash melt [175, 176, 274].

6.3.3.3   Phase Formation

Figure 6.17 shows the predicted phase formations for miscanthus and each of the additive cases at 850°C. Once again, components with a mass <10g have been removed due to representing <1% of the total system mass. K_2O and SiO_2 in slag form are both major components of each ash case, with Na_2O also present in notable amounts. In the dolomite ash cases, solid phases comprise mostly of $CaMgSi_2O_6$, along with smaller quantities of a variety of other calcium and magnesium silicate compounds, e.g. $Na_2Mg_2Si_6O_{15}$. This is result of the release of calcium and magnesium from dolomite into ash as previously discussed. The additive particles again appear distinct versus the ash cases. Kaolin adjacent to ash, as with wheat straw, is mostly $KAlSi_3O_8$ and Al_2SiO_5, reflecting it being both an aluminosilicate, and its reaction with potassium. Dolomite adjacent to ash is shown to be formed of mostly three compounds: MgO, $CaMgSiO_4$, and $Ca_3MgSi_2O_8$. The presence of these calcium magnesium silicates may be due to the intrusion of the ash melt into the outer region of the dolomite, as discussed previously (section 6.3.3.1). Ordinarily, dolomite itself does not have any silica content (see Chapter 3 section 3.8.3).
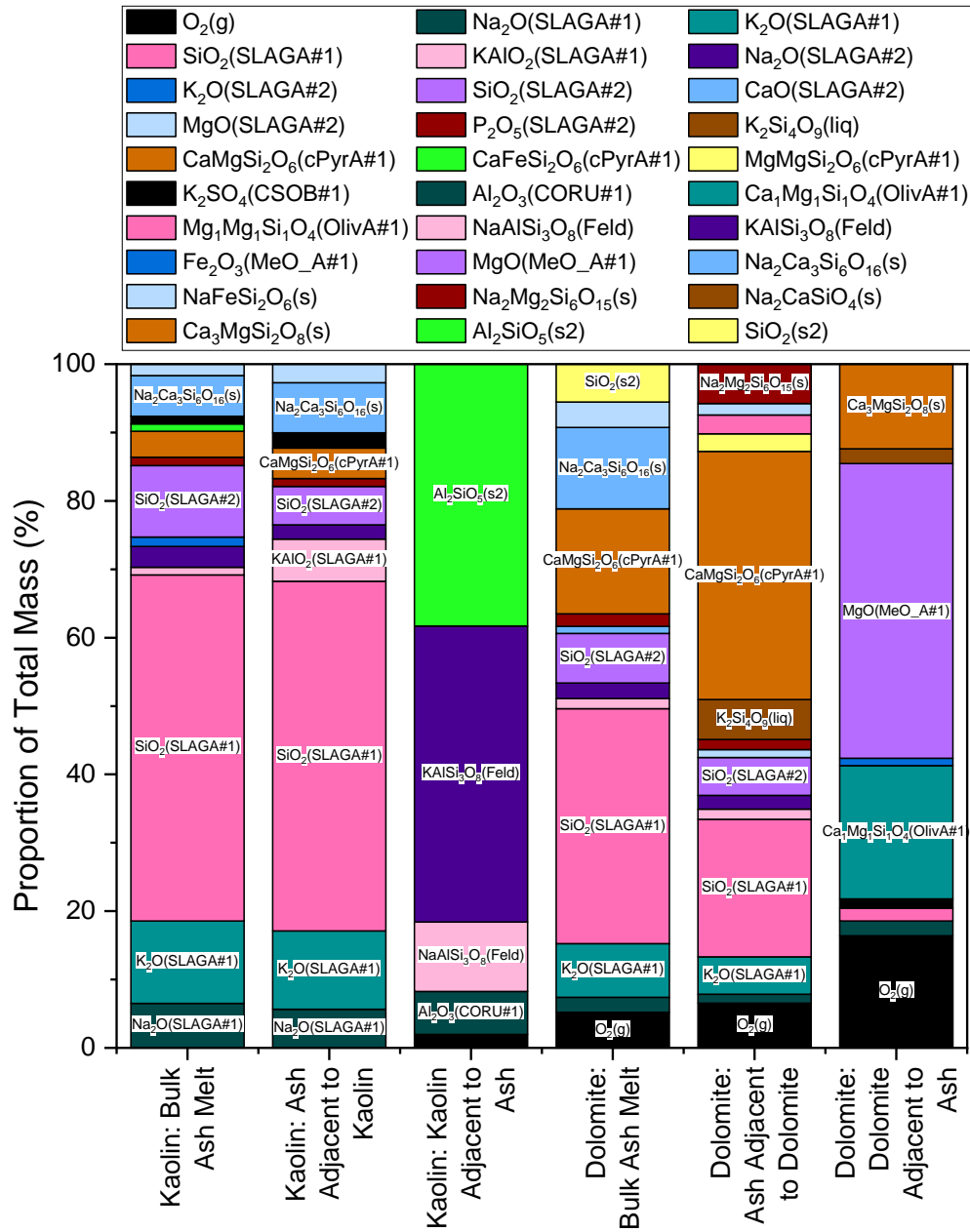
Figure 6.17: *Phase composition for miscanthus and additive EDX data cases at 850°C.*

A final aspect of note across Figure 6.17 is the prediction of varying amounts of gaseous O_2 in some cases. The samples that were analysed via EDX and thus produced the EDX data modelled here were in solid form, however the Equilib module of FactSage used for modelling predicts phase composition at equilibrium. This would suggest that the samples did not reach equilibrium. This could be for a variety of reasons such as insufficient operational time (up to ~4 hours maximum), the exposure of the samples to varying temperatures during tests and cool down, and changes to the bed chemical system over time with the continual addition of fresh fuel. This highlights the potential shortcomings of using a chemical equilibrium modelling tool, and the potential

benefits of incorporating some chemical kinetics modelling capabilities. An additional possible reason for this O_2 content may be instrument error and/or over-reporting of oxygen content when taking the EDX measurement. The potential for EDX measurement error was discussed in Chapter 3 section 3.4.2. However, as this presence of O_2 did not arise in all cases modelled here, and as the data used is an average of many data points taken over a period of months, this is less likely to be the main cause.

6.3.4 Comparison with Fuel Ash Modelling Approach

The modelling of real EDX data from bed agglomerates is a unique approach with few similar works. The approach has different strengths and weaknesses compared to the fuel ash approach applied in section 6.2, and these will be evaluated here. To enable a quantitative comparison between data sets for the predicted quantity of slag plus liquid have been transformed into units of the molten fraction of the system as a proportion of the total ash input at three temperatures, 800°C, 850°C, and 900°C in Table 6.5.

Table 6.5 reveals a picture of the overall condition of the bed and agglomerates, as predicted by FactSage. With kaolin, under the fuel ash approach, melting is generally very low for both fuels except in higher kaolin dosage cases where it is up to 8.9%. In some kaolin cases, there is the prediction of no melt formation at all. This prediction does not reflect experimental experience, as agglomerates were found in the bed for all fuel and additive conditions (see Chapter 5 section 5.3.2), which would suggest again some weaknesses to the fuel ash modelling approach, as was discussed in detail across sections 6.2.2-6.2.4. With dolomite under the fuel ash modelling approach, there is notably more total melt formation predicted, again for both fuels. Melt formation is as high as 19% of the input ash mass, significantly greater than the largest melt formation predicted with kaolin under the fuel approach of 8.9%. As can also be seen, the quantity of melt formed in the whole bed in the fuels approach has no relationship to the amount of melting predicted under the EDX approach for agglomerate samples. This again highlights the fact that agglomeration severity, and/or the usefulness of an additive, cannot be determined by modelling EDX data alone.

When considering the results of both approaches, and the experimental findings in Chapter 5, kaolin is likely to be the preferred additive. Whilst the prediction of little to no melt formation with kaolin is erroneous, as it is known that ash melting and agglomeration did occur with kaolin, it does give a qualitative indication that a more

detailed or smaller scale experimental study would show kaolin to have a lower total melt formation than dolomite. The higher quantity of melt formation with kaolin predicted for agglomerate samples via the EDX modelling approach should not pose an issue, as this is localised to individual agglomerates and does not reflect the total bed melt formation. A further advantage of kaolin would be the removal of gaseous KCl, which would aid in corrosion mitigation [81], as discussed across section 6.2.

Table 6.5: *Comparison between the molten proportion (total slag plus liquid mass) of input ash mass, for both the fuel-additive modelling approach taken in section 6.2 and the EDX layer data modelling approach taken in section 6.3.*

Modelling Case			Molten proportion of 1000g ash input (%)		
			800°C	**850°C**	**900°C**
Fuel Approach	Wheat Straw	Kaolin 50%	0.0	0.0	0.6
		Kaolin 150%	0.0	0.0	0.0
		Kaolin 300%	1.0	5.0	8.9
		Dolomite 50%	28.3	30.0	35.0
		Dolomite 150%	1.3	1.6	15.0
	Miscanthus	Kaolin 50%	0.0	0.0	0.0
		Kaolin 150%	0.5	2.1	7.4
		Dolomite 50%	9.3	17.3	19.0
		Dolomite 150%	8.1	8.9	10.2
EDX Layer Approach	Wheat Straw	Bulk Ash Melt with Kaolin	61.9	69.1	69.2
		Ash Adjacent to Kaolin	74.6	76.4	78.1
		Bulk Ash Melt with Dolomite	20.0	25.1	25.8
		Ash Adjacent to Dolomite	48.9	49.3	49.7
	Miscanthus	Bulk Ash Melt with Kaolin	82.1	85.9	90.4
		Ash Adjacent to Kaolin	79.1	81.4	83.6
		Bulk Ash Melt with Dolomite	54.3	58.4	62.2
		Ash Adjacent to Dolomite	42.5	44.7	47.0

6.4 Accuracy and Validity of FactSage for Biomass Ash Melt Modelling

As highlighted in Chapter 2 section 2.4 there are several potential issues and shortcomings in using FactSage for biomass ash melt modelling. This section discusses the validity and accuracy of FactSage for modelling key biomass ternary ash systems, in the context of the impact on the results presented in sections 6.2 and 6.3.

6.4.1 K_2O-CaO-SiO_2 System

The K_2O-CaO-SiO_2 system is integral to ash melt behaviour, as has been seen both in experimental studies within this thesis, and the numerous other biomass ash works discussed in Chapter 2 section 2.4. Documentation for the FToxid database as of FactSage version 7.0, which was used in this study, states that whilst the binary K_2O-SiO_2 system is fully optimized, higher order systems (e.g. ternary) containing K_2O are not, leading to potentially inaccurate predictions. The primary source of data on the K_2O-CaO-SiO_2 system is the work of Morey, at al. [93] published in 1930. Little subsequent work explored this system until around 2010, due to a greater interest in other alkali metal ternary systems such as Na_2O-CaO-SiO_2 that are of importance for glass making [275]. Morey, et al. [93] explored the silica rich region of the K_2O-CaO-SiO_2 phase diagram, due to the volatility of K_2O, and tested mixtures with maximums of ~60wt.% K_2O, ~40wt.% CaO, and ~80wt.% SiO_2. These ranges would encapsulate the biomass ashes and additive cases modelling and tested in this work, as has been plotted on Figure 6.18.

In the last 5-10 years, several groups have re-investigated this ternary system and found conflicting results versus those of Morey, et al. [93]. In 2009, Berjonneau, et al. [186] performed experimental liquidus temperature studies of a K_2O-CaO-SiO_2 system in comparison to FactSage predictions and found that they differed by up to 200°C. In 2011, Arroyabe, et al. [276] determined that one solid phase compound on the ternary phase diagram of Morey, et al. [93], K_2CaSiO_4, was in fact a misidentification of $K_2Ca_2SiO_7$. Chen, et al. [277] performed fundamental studies in similar parts of the K_2O-CaO-SiO_2 system to Morey, et al. [93], identifying new solid phases and highlighting phase field inaccuracies. The work of Schmidmair, et al. [278] discovered a new potassium calcium silicate compound ($K_2CaSi_4O_{10}$) in the 800-900°C temperature range. A recent study by Santoso, et al. [279] performed further experimental study into

the K_2O-CaO-SiO_2 system, and validated some of the findings of Morey, et al. [93] and Chen, et al. [277].
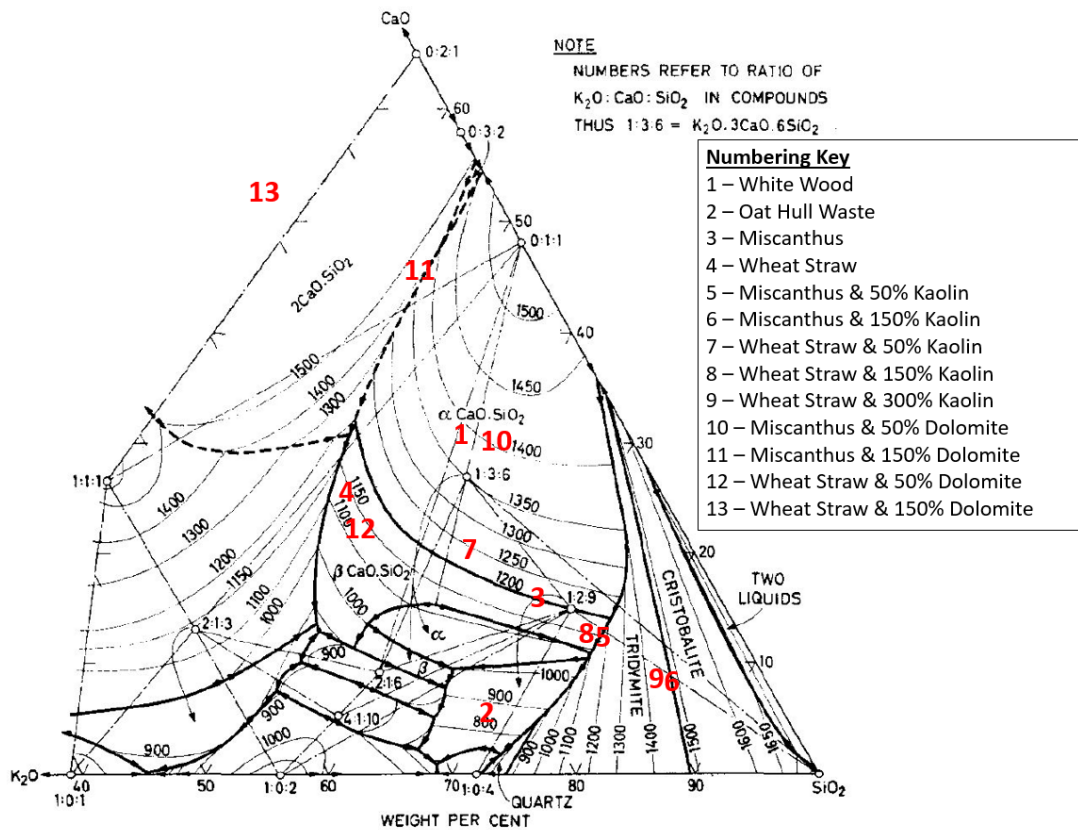
Figure 6.18: *K_2O-CaO-SiO_2 ternary liquidus projection diagram annotated with the positions of the four fuel ashes and the combined ash/additive mixtures, labelled 1-13. Note that only point 13 is in a region where there is no data available. Diagram reproduced and adapted from the work of Roedder [104] with the permission of copyright holder Elsevier. Originally presented by Morey, et al. [93].*

As these works highlight, and as reviews have discussed [181], there is a clear need for further fundamental experimental studies on this system. Figure 6.18 plots the different fuel ashes and additive combinations modelled and or/experimentally tested within this thesis. Only the wheat straw with 150% dolomite case is outside of the range of experimental data provided by Morey, et al. [93], due to its high calcium content, meaning that the vast majority of cases modelled in this work lie in ranges over which there is thermochemical data, even if there is degree of inaccuracy to this data. It should also be noted that the changelog for a recent release of FactSage, version 7.3 (2019), states that there has been optimization of K_2O containing binary and ternary systems, likely using data from some of the aforementioned recent studies [280]. However, as FactSage is a "black box", it is difficult to tell by what degree this accuracy has improved, outside of the user manually plotting experimental literature onto phase

diagrams drawn in FactSage. The work of Santoso, et al. [279], published in 2020, used FactSage 7.3 and showed a good alignment between the FactSage predictions and their experimental results at 1000°C and 1100°C, with a few exceptions. Ultimately, there should be understanding by the user that modelling of ash melts across the K_2O-CaO-SiO_2 system may suffer from some inaccuracy due to a lack of fully validated data, and that applies to the work performed in this chapter.

6.4.2 K_2O-CaO-P_2O_5 System

The K_2O-CaO-P_2O_5 system is important for modelling and understanding high phosphorous content biomass fuels. As discussed in the work of Billen, et al. [94, 184] and others [95, 281, 282], where fuels have high a phosphorous content, more thermodynamically stable calcium phosphates preferentially form instead of calcium silicates. This prevents the formation of stable K-Ca-silicates. Low melting point K-silicates can then more easily form, with the additional phosphorous content forming potassium phosphates that react with silica, again forming problematic potassium silicate melts. As discussed in the review of Lindberg, et al. [181], the primary issue with modelling in this system is again the lack of fundamental experimental data for the thermodynamic properties of compounds within the system. As Lindström, et al. [282] state, some very limited ternary data does exist from a small series of papers published in the 1970's, though this covers a limited compositional range with respect to that expected in biomass fuels. The thesis of Sandström [283] also highlights this lack of fundamental data and performs investigations into the structure of several Ca-K-phosphate crystals. During examination of agglomerate samples in Chapter 4 section 4.3.7.3, there was some evidence of phosphorous involvement in some oat hull waste agglomerates, but only a small portion of the total agglomerates analysed. The oat hull waste does have the highest P_2O_5 content within its ash (5.3wt.%), though only marginally more so than the wheat straw (4.8wt.%) for which no phosphorous involvement was observed in agglomeration processes. Therefore, it is difficult to conclude whether the lack of data surrounding the K_2O-CaO-P_2O_5 system, and its weakness in FactSage, would have impacted modelling of the miscanthus and wheat straw fuel ashes.

6.4.3 K₂O-Al₂O₃-SiO₂

Whilst none of the biomass ashes have significant quantities of Al_2O_3, modelling of ashes with kaolin as performed in section 6.2 introduced significant amounts of Al_2O_3, which increases ash melt temperatures by the reaction of K_2O with Al_2O_3 [164]. Therefore, this would place a greater importance onto the accuracy of the K_2O-Al_2O_3-SiO_2 system in modelling. The four fuels and the five fuel and kaolin mixtures that were modelled and/or tested experimentally are plotted Figure 6.19, showing that all are within the range for which there is fundamental experimental data. As of FactSage 7.0, FToxid documentation states that the K_2O-Al_2O_3-SiO_2 system has been re-evaluated and re-optimized. This was detailed in the work of Kim, et al. [284], with the model used in comparisons to experimental data from literature and these results found to be favourable. This would therefore suggest a good level of accuracy for this system in the models with kaolin, albeit with the caveats surrounding other ash systems (e.g. K_2O-CaO-SiO_2) as previously discussed. The related quaternary system Na_2O-Al_2O_3-CaO-SiO_2 is also quoted as being fully optimised in FToxid documentation.
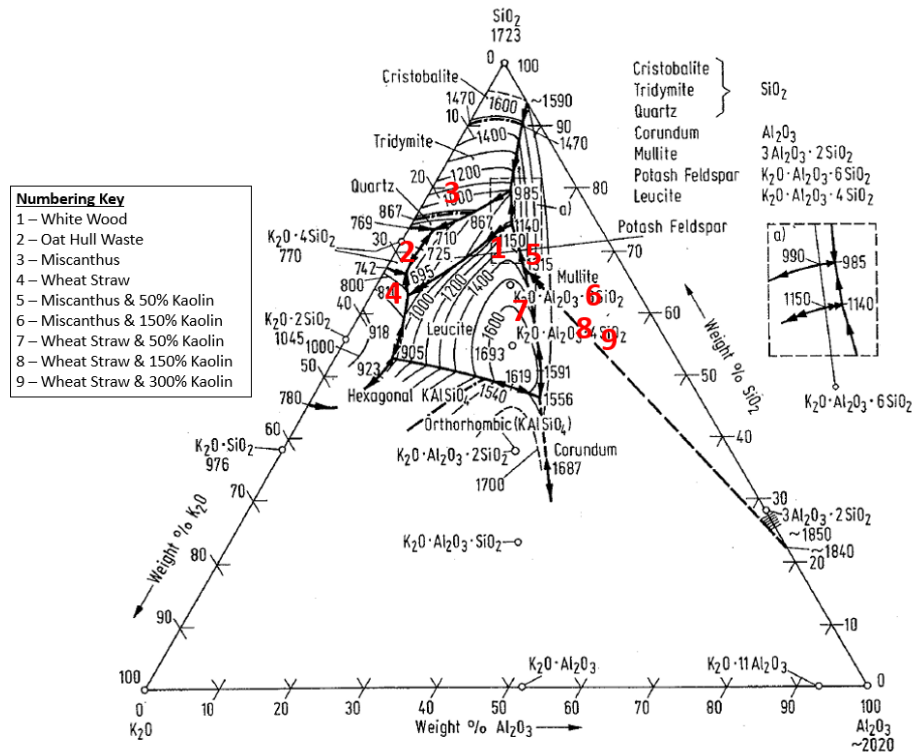
Figure 6.19: *K_2O-Al_2O_3-SiO_2 ternary liquidus projection diagram annotated with the positions of the four fuel ashes and the ash/kaolin cases, labelled 1-9. Diagram reproduced and adapted from the work of Roedder [104] with the permission of copyright holder Elsevier. Phase diagram originally presented in the works of Schairer & Bowen [285, 286].*

6.4.4   Physical Behaviours

As is evident from discussions in section 6.2, and discussions around FactSage in Chapter 2 section 2.4 and Chapter 3 section 3.6, FactSage purely considers the equilibrium chemistry of an input system, regardless of the physical realities of a system (e.g. division of elements across physical components, degree of mixing, temperature gradients, surface area of a particle available for reaction etc.). These limitations are unlikely to be resolved, as FactSage at its core is a tool for thermochemical equilibrium modelling. An understanding of their potential impact is however needed.

As was discussed in Chapter 5 section 5.4, physical behaviours for wheat straw pellets surrounding pellet breakdown and ash release appear integral to agglomeration severity. This was further supported by the modelling work in section 6.2 of this chapter, which suggested that on a purely chemical basis, additives would significantly reduce slag melt formation. Experimentally, interaction between both ashes and both additives was seen in Chapter 5, though this did not result in a performance benefit for wheat straw. Therefore, a user with no experimental results that solely relies FactSage may draw the incorrect conclusions, and such an approach should be avoided.

The Equilib module of FactSage used in this work assumes that the input system reaches chemical equilibrium, a process which may take upwards of several hours for some solid phases to fully form. In testing however, agglomerate samples were exposed to elevated temperatures for a maximum of around 5 hours, depending on the fuel/additive combination. They were then slowly cooled down, as opposed to rapid cooling which is performed in experimental thermochemical studies. Therefore, there is likely to be some divergence in experimentally observed solid phases and degree of melting, versus that predicted via an idealised equilibrium model. The inclusion of a chemical kinetics model or functions would allow for a more accurate prediction of resultant components, e.g. through the user specifying exposure time. However, this would substantially increase the complexity of FactSage as a software package, the development burden, and the computational requirement, with there already being software packages used for chemical kinetics simulation such as Cantera [287].

The second modelling approach considered in section 6.3, of using real EDX composition data as the model input, overcomes some of these weaknesses. As this uses averaged data from real agglomerate samples, exposed to the physical realities of FBC,

it gives a more representative basis for modelling. However, the arguments surrounding FactSage being a tool for equilibrium modelling, which is not strictly applicable, still apply. Furthermore, as noted in section 6.3.4, this modelling approach cannot provide a suggestion as to the total degree of melting across the complete bed-ash inventory, therefore is more of a complementary tool to SEM/EDX analysis.

6.4.5   Modelling of EDX Data

As discussed across section 6.3, EDX data was modelled in FactSage. This approach is beneficial, as the ash layers that were modelled had been formed in a real fluidized bed and were subject to actual agglomerate formation behaviour. However, the standardless EDX measurement, as used in this thesis, does itself carry some inaccuracy, which would consequently affect the results of FactSage modelling. This was discussed in greater detail in Chapter 3 section 3.4.2. For EDX analysis in this thesis, numerous measurements were taken from several locations on each sample, with an average of these then used for analysis and discussion. As noted in Chapter 3 section 3.4.2, this approach, which is commonly used in literature agglomeration studies, was used to mitigate the much larger inaccuracy of, for example, using only a single measurement from a single sample. The impact of minor compositional errors on model results, can be appraised from the analysis across section 6.3. For example, when using miscanthus and kaolin, the average EDX data for the "bulk ash melt" and "ash melt adjacent to kaolin" had similar compositions, with elemental differences of around 1-3wt.% (Table 6.3). The model results for this data showed broadly similar liquid plus slag masses (Figure 6.16) and phase formations (Figure 6.17). Therefore, assuming a similar degree of inaccuracy after the averaging of numerous sets of EDX data, the impact should not be of great concern in comparison to the broader uncertainties inherent to FactSage as discussed in sections 6.4.1-6.4.4. More broadly the advantage of tis EDX data modelling approach is significant, as the sample was exposed to real fluidized bed processes and it would otherwise be challenging to experimentally study agglomerate composition and phases at the operating bed temperature.

6.4.6   Evaluation of FactSage for Agglomeration Prediction

From the discussion of the accuracy of FactSage for modelling ternary systems across sections 6.4.1-6.4.3, for the K_2O-CaO-SiO_2 system, and systems with phosphorous, there is still a need for further fundamental experimental thermochemical studies. This

is needed to validate prior data, or in the case of phosphorous systems, to provide a greater quality and quantity of data for the FactSage developers to implement use. That said, on a qualitative basis the compound predictions made by FactSage did generally align with those seen experimentally by others, as was discussed in section 6.2-6.3. As was highlighted in section 6.4.4, FactSage does not model any physical behaviours of relevance to agglomeration, therefore predicted that wheat straw would see reduced slag formation with additives, which may lead a user to the incorrect conclusion that additives would be effective for agglomeration mitigation with wheat straw. This is equally the case for fuels without additives, as was seen in section 6.2 where both miscanthus and wheat straw had similar ash contents and thus were predicted to have similar amounts of slag formation, despite the far worse performance of the wheat straw in practice. The FactSage predictions may be entirely correct, but if physical factors are of more importance for a given fuel the evidently FactSage cannot be used as even an indicative tool for agglomeration prediction.

On this basis, FactSage is better suited as a complementary tool to experimental agglomeration studies, as used in this chapter, rather than as a guiding tool to evaluate the likelihood of agglomeration challenges with a fuel. There is potential for greater use of FactSage to model real agglomerate composition data, from EDX analysis or similar, as was done in section 6.3. Few groups have used this approach in literature, and it is of use in gaining a better understanding the chemistry of agglomerates at operational bed temperatures, an aspect that would otherwise be challenging to observe experimentally.

6.5   Chapter Summary

Two different thermochemical modelling approaches have been applied to further investigate additive usage with wheat straw and miscanthus. The first approach was to model the interactions between fuel ash, gas environment and additives. This predicted that both additives would substantially reduce slag formation with both fuels. This aligns with experimental experiences with miscanthus in Chapter 5, but not with wheat straw, where additives were found to be ineffective at extending bed defluidization time. This supports the theory that wheat straw pellet breakdown and ash release are integral to its severe agglomeration issues, as physical factors are not captured in FactSage models. It was also seen that kaolin is the superior additive to dolomite, with lower predicted slag formation than dolomite and the benefit of gaseous KCl capture to

mitigate against corrosion challenges. The predicted solid phases were compared qualitatively against available experimental XRD studies of ash and additive mixtures, and were found to have generally good agreement, lending confidence to the predictions.

In the second modelling approach, composition data from different agglomerate structural regions analysed in Chapter 5 sections 5.3.4-5.3.5 was modelled. Findings broadly aligned with what was expected from the EDX data. With wheat straw, regions of ash adjacent to kaolin were found to be more molten than the bulk ash melt, due to the formation of a liquid potassium silicate. Ash regions when using dolomite were less molten than their counterparts when using kaolin, due to the formation of solid calcium/magnesium silicates. Wheat straw agglomerates had lower overall total melt quantities than miscanthus agglomerates, again suggesting the importance of physical factors in wheat straw agglomeration.

The overall accuracy and validity of FactSage in the context of agglomeration modelling was also evaluated. Key ash ternary systems, notably K_2O-CaO-SiO_2 and K_2O-CaO-P_2O_5, require further fundamental experimentation and validation, as both are integral to agglomeration phenomena and accurate data is required to improve database quality and model predictions. As FactSage does not consider any physical behaviours, erroneous predictions arose with wheat straw and additives. Therefore, FactSage is better as a complimentary tool to experimental studies of agglomeration than as a predictor of overall agglomeration severity. Modelling of EDX data avoids several FactSage weaknesses, though cannot be used to predict overall agglomeration severity.

Chapter 7

Performance Improvement of the Wilton 10 CHP Station

7.1   Redaction Notice

Chapter 7 has been redacted in the online version of this thesis for commercial confidentiality reasons.

This chapter discussed a study of a 5-year fuel data set from a commercial biomass power station, including the application of principal component analysis and random forest regression machine learning.

Appendix E-Appendix K, which contain supplementary material in relation to Chapter 7, have also been redacted in the online version of this thesis.

This page has been redacted in the online version of this thesis. Please refer to page 224 for further information.

This page has been redacted in the online version of this thesis. Please refer to page 224 for further information.

This page has been redacted in the online version of this thesis. Please refer to page 224 for further information.

This page has been redacted in the online version of this thesis. Please refer to page 224 for further information.

This page has been redacted in the online version of this thesis. Please refer to page 224 for further information.

This page has been redacted in the online version of this thesis. Please refer to page 224 for further information.

This page has been redacted in the online version of this thesis. Please refer to page 224 for further information.

This page has been redacted in the online version of this thesis. Please refer to page 224 for further information.

This page has been redacted in the online version of this thesis. Please refer to page 224 for further information.

This page has been redacted in the online version of this thesis. Please refer to page 224 for further information.

This page has been redacted in the online version of this thesis. Please refer to page 224 for further information.

This page has been redacted in the online version of this thesis. Please refer to page 224 for further information.

This page has been redacted in the online version of this thesis. Please refer to page 224 for further information.

This page has been redacted in the online version of this thesis. Please refer to page 224 for further information.

This page has been redacted in the online version of this thesis. Please refer to page 224 for further information.

This page has been redacted in the online version of this thesis. Please refer to page 224 for further information.

This page has been redacted in the online version of this thesis. Please refer to page 224 for further information.

This page has been redacted in the online version of this thesis. Please refer to page 224 for further information.

This page has been redacted in the online version of this thesis. Please refer to page 224 for further information.

This page has been redacted in the online version of this thesis. Please refer to page 224 for further information.

This page has been redacted in the online version of this thesis. Please refer to page 224 for further information.

This page has been redacted in the online version of this thesis. Please refer to page 224 for further information.

This page has been redacted in the online version of this thesis. Please refer to page 224 for further information.

This page has been redacted in the online version of this thesis. Please refer to page 224 for further information.

This page has been redacted in the online version of this thesis. Please refer to page 224 for further information.

Chapter 8

Conclusion

8.1 Thesis Summary and Conclusions

This thesis has presented a thorough study into the use of different fuels, operating conditions, bed materials, and additives in a fluidized bed combustor. The investigation has encompassed both experimental and thermochemical modelling efforts, to deduce the fundamental underlying behaviours by which mitigative measures interact with agglomeration mechanisms. This work has been further expanded by a study into the quality of the fuel used in the Wilton 10 fluidized bed biomass boiler, operated by project sponsors Sembcorp Energy UK. Several important novel findings and new methodological approaches have been presented across Chapter 4-Chapter 7. This project has fulfilled its overall aim of deepening the understanding of agglomeration mechanisms and mitigation, with a focus on non-woody fuels.

Chapter 1 provided background and context to biomass power generation and fluidized bed combustion technology, with a focus on the UK market. This chapter highlighted the underlying ash issues inherent to biomass fuels: corrosion, fouling, slagging, and for fluidized bed boilers, bed agglomeration. In parallel to this, challenges facing the UK biomass power market were emphasised, notably the uncertain future of current government financial incentives for biomass fuel use (ROCs, non-domestic RHI), and the limited UK supply of wood biomass. These factors are encouraging operators to investigate the use of cheaper, lower quality biomass fuels as part of their fuel blend, which typically result in more severe agglomeration issues due to higher ash contents.

Chapter 2 presented a comprehensive analysis and critique of the current understanding of agglomeration mechanisms with biomass fuels, the effectiveness of different mitigation measures. In addition, it also considered the use of thermochemical modelling software such as FactSage to understand agglomeration issues and the use of the random forest machine learning algorithm in fuel studies. There is a wealth of literature that focuses on woody fuels and the coating-induced agglomeration

mechanism typical of woody fuels, where alkali metals in ash interact with silica in bed materials to form a melt. The melt-induced agglomeration mechanism has previously received less attention in the literature and occurs primarily with higher ash agricultural fuels, whereby alkali metals and silica within ash form a melt. A phenomenon observed by a few authors was the formation of agglomerates in the shape of fuel pellets or particles, though there was little discussion of the importance or causes of this behaviour. Alternative bed materials and additive use were seen to be effective agglomeration mitigation measures in the literature, though again these studies typically focused on their use with woody fuels. There were also few detailed studies into the mechanisms by which additives interact with ash in the context of agglomeration. Many authors in the literature had used FactSage and thermochemical modelling software for general biomass ash modelling, with a smaller subset applying the software to agglomeration challenges with varying degrees of success. With regards to the use of random forest machine learning with fuel data, whilst a handful of studies had applied the technique to fields adjacent to biomass fuel data (e.g. fuel drying), only one had applied the technique to the classification of fuel types. No studies were found that use the algorithm to predict fuel contaminant levels or to find underlying fuel relationships.

In Chapter 3, the approaches to the experimental and modelling studies performed in this thesis were explained. A focus was on the large pilot-scale bubbling fluidized bed combustor used for experimentation and its limitations in comparison to commercial BFB boilers. Also covered was the generic approach to FactSage, which was used for modelling Chapter 6, and the methodology behind the use of principal component and analysis and random forest regression as applied in Chapter 7. Details on the materials used in testing were also provided, contrasting the key differences between them.

In Chapter 4 an experimental study was performed into the use of four prospective biomass fuels, the impact of varying operating conditions, and the use of the non-silica bed material olivine. In addition, there was an extensive deposition probe trial with wheat straw and olivine. This fulfilled thesis objective 1: to determine the relative performance of different biomass fuels and the effect of different operational conditions; clarifying literature uncertainties. White wood was the only fuel that did not cause bed defluidization. Miscanthus and oat hull waste were moderately agglomerating fuels, whereas wheat straw underwent the most severe and rapid agglomeration. Olivine had not previously been tested with wheat straw in the literature and was seen to

lengthen defluidization times by 25%. This may be due to a combination of the far lower silica content of olivine and it being a borderline wettable/non-wettable material, though further investigation and confirmation is needed. This poor wettability likely helped mitigate against some of the physical agglomeration behaviours inherent to wheat straw, that were further explored in Chapter 5. Despite this substantial extension to defluidization time however, wheat straw remained a poor fuel in comparison to the others. With regards to bed height, an optimum bed height was found for the unit, with both higher and lower bed heights resulting in lower defluidization times, which may be the reason for conflicting trends in prior literature. A smaller bed particle size was also found to lengthen defluidization time but may result in greater bed material losses in commercial boilers. A new approach to agglomerate study was taken by dividing the bed into distinct vertical and lateral zones to evaluate spatial differences. With white wood and oat hull waste, locations closer to the landing point of fuel onto the bed had higher potassium contents and lower calcium contents. This suggests ash melting in these regions would be worse, and targeted agglomeration mitigation strategies may wish to consider these locations of initial fuel entry and mixing into the bed.

In Chapter 5, the use of varying dosages of the bed additives kaolin and dolomite with the fuels miscanthus and wheat straw was investigated. This fulfilled objective 2: determining the impact of these additives with non-traditional agricultural biomass fuels. There was no extension to defluidization time when using any additive with wheat straw, whereas additive use with miscanthus prevented bed defluidization entirely. In examining agglomerate composition and morphology, it was seen that despite these substantially different performance responses to additive usage, both additives chemically interacted with both fuel ashes. This was seen through a novel systematic SEM/EDX approach of classifying common agglomerate features and spatial zones, e.g. the outer layer of an additive particle adjacent to ash, to gain a deeper fundamental understanding of additive behaviours. Previous studies only examined a handful of discrete points on a sample. Dolomite released calcium and magnesium to the ash, from across the whole dolomite particle, which would raise ash melt temperatures and mitigate agglomeration. Kaolin absorbed potassium content from ash to depths of up to 60µm in the kaolin particle, forming stable alkali aluminosilicates, which would also mitigate agglomeration. Most interactions between kaolin and ash occurred in the outer 20µm region of kaolin particles, showing the degree to which

kaolin reacts with biomass ash. In testing, wheat straw was visually observed to be predisposed to forming fuel pellet shaped agglomerates, with bed particles binding to fuel pellets as they underwent char oxidation. It is suggested that this behaviour caused the lack of change to defluidization times when using additives with wheat straw, despite the clear chemical interaction between additives and wheat straw ash. The fuel pellets act as a "seed" for agglomerate formation, releasing ash content to the pellet surface and allowing the binding of bed particles to the pellet. As the pellet input to the boiler was constant across all tests ($65kW_{th}$), this would mean a constant input of "seed agglomerates", hence the lack of change to defluidization time with additives. This finding highlights a key behavioural difference between biomass fuels which previously was not previously evident in literature and is deserving of further study.

In Chapter 6, FactSage was used to model the fuel and additive combinations tested in Chapter 5 via two distinct approaches. This fulfilled objective 3, to determine the underlying chemical behaviour of additives and the usefulness of FactSage for agglomeration studies. The first modelling approach was to use fuel ash, additives, and flue gas composition as model inputs, to determine the theoretical performance of each additive on a chemical basis. Both additives were predicted to substantially reduce ash melt formation with both fuels. This aligns with the experimental result of no bed defluidization with miscanthus, but not that of wheat straw where there was no change to defluidization time. This again supports the theory that physical behaviours are the reason for the particularly poor performance of the wheat straw, as FactSage modelling approach only considers the chemical equilibrium of the system. This finding showed that the traditional FactSage approach of using fuel ash as a model input is not as useful for agglomeration studies, as here it could not give a reliable indication of fuel performance with additives. The second modelling approach was to model EDX data, which had only been attempted by two other groups, neither of which had the novel spatially classified additive-agglomerate data as was available here. With wheat straw, ash adjacent to kaolin was found to be more molten due to the formation of a liquid potassium silicate, in line with what was expected from experimental EDX data. All ash regions with dolomite were less molten than their counterparts with kaolin due to the release of calcium and magnesium forming stable high melting point Ca/Mg-silicates. Wheat straw agglomerates had a lower predicted melt quantity than their miscanthus counterparts, suggesting again that physical behaviours helped drive severe

agglomeration as FactSage only considers system equilibrium chemistry. With regards to the usefulness and accuracy of FactSage, fundamental experimental work is still required to improve thermochemical database and modelling accuracy. The second modelling approach of utilising EDX data was considered more accurate and applicable, as the data had a basis in physical reality, which partially mitigates the downside of FactSage only considering system chemistry.

In Chapter 7, a study was performed on a 5-year virgin and recycled wood fuel blend data set that was used at the Wilton 10 CHP station operated by Sembcorp Energy UK. This fulfilled objective 4, to improve the performance of a commercial BFB boiler. Only one other similar long-term study existed in the literature, which examined the fuel composition of a Swedish waste wood fired boiler. From the analysis in this chapter, it was seen that chlorine content, ash content and zinc content were all above boiler manufacturer design limits, which would worsen the existing corrosion and slagging issues. The use of principal component analysis and a machine learning technique (random forest regression) did not reveal any underlying relationships or usable predictive tools. It is suggested that this is because of the highly heterogeneous nature of the fuel data (many sources and suppliers constituting the blend, over a long timescale). Using representative figures for boiler tube leaks, it was highlighted that the poor-quality fuel could account for lost revenues in excess of £1.6m, which could be recovered in part with the fuel improvements areas noted in this study. The study also highlighted key points for the broader operator community, such as the general weakness of the PAS 111 guidance for waste wood grading and sampling, which may unintentionally cause misrepresentation of the quality of waste wood. It was also recommended to perform a detailed analysis of the non-woody elements in the waste wood, and quantify the types of waste wood present, all of which have a significant impact on contaminant quantities entering the boiler that are at present unmeasured and unaccounted for.

8.2   Contributions to Knowledge

As highlighted in section 8.1, this thesis has produced many findings through an original campaign of research. The major contributions to knowledge arising from this thesis are:

1. The use of olivine with wheat straw, a fuel susceptible to severe agglomeration, was found to extend operational time before bed defluidization. This is likely due to a combination of the lower silica content of olivine and it being less wettable, both of which minimise the formation of agglomerates. However, the use of olivine with wheat straw was not found to be so substantial a benefit that wheat straw would be viable as a primary fuel candidate in comparison to wood fuels.

2. The ineffectiveness of additives with wheat straw at lengthening operational times has been shown. It was proposed that this is due to the ash release to the pellet surface and general lack of pellet breakdown, allowing the pellet to act as a "ready-made" agglomerate platform. Both additives were seen to chemically interact with wheat straw ash, both in theory and in experimentation.

3. The use of a new spatial approach to agglomerate sampling across different vertical and lateral regions of the bed has revealed higher levels of potassium, and lower levels of calcium at regions closer to the landing point of fuel onto the bed. This is suggested to be due to a higher availability of fresh fuel ash in these areas. This may inform agglomeration mitigation approaches targeted at fuel landing locations, and this spatial analysis approach in general may be worthy of further study and application.

4. A new approach to classifying agglomerate composition measurements by common spatial zones and features has been applied. This has been used to clearly present the mechanisms and the extent to which kaolin and dolomite interact with biomass ashes to mitigate agglomeration.

5. The traditional FactSage approach of modelling a system from base inputs (ash, additives, gaseous environment) does not accurately reflect agglomeration behaviour, and is not useful for predicting fuel performance prior to experimental trials. This was shown when modelling wheat straw with additives, where predicted performance did not match experimental observations even on a qualitative basis.

6. Modelling of EDX data in FactSage provided a more accurate, detailed prediction of underlying chemistry due to its basis on real data. Moreover, the output of this exercise would otherwise be difficult to experimentally investigate (formation and composition of slag melt and agglomerates in-situ). However, this approach cannot be used to predict the overall extent or severity of

agglomeration as it does not include the whole bed-ash inventory and is a retroactive approach.

7. Analysis of the Wilton 10 blend-to-boiler fuel mixture highlighted the potential benefits of a more detailed approach to contaminant classification and quantification, as well proposing improvements to the PAS 111 fuel sampling approach. These suggestions could be applied to any biomass power station using waste wood.

8. The use of random forest regression and principal component analysis with the Wilton 10 fuel data did not reveal underlying fuel relationships, likely due to the high degree of heterogeneity inherent to the fuel blend, sourcing, and suppliers. These techniques have not previously been applied to commercial fuel blend data sets in published literature. It would be recommended that future studies focus on "narrower" fuel data sets, i.e. those of a singular fuel type, from the same source, over shorter timespans, and that are not blended.

8.3   Limitations

As with any research project, there are limitations to project scope, resources, and time, as well as external challenges outside of the authors control, which have constrained studies in some areas.

In Chapter 3, several shortcomings of the pilot-scale fluidized bed combustor were highlighted, notably the limitations of the fuel feeding system. These prevented pushing fuel thermal inputs higher and obtaining a combustion profile in the freeboard that is more representative of a commercial BFB boiler (i.e. freeboard temperatures greater than 950°C). This limited the usefulness of the emissions data and the deposition probe study. However, it would not have an impact on agglomeration behaviours in the bed which were the core focus of this thesis, as bed temperatures and fluidization regimes were representative of those in a commercial bubbling fluidized bed boiler. The issues with the feeding system would have required a re-design and replacement, which were not viable with the available project resources.

The spatial study of agglomerates from different bed locations in Chapter 4 did show clear variances in agglomerate composition across the bed. In addition, these findings aligned with an earlier, far narrower study from the literature that examined different vertical locations. However, the study here was limited to just a selection of oat hull

waste samples and some white wood samples, with a study across the other fuels or bed locations not possible due to resource limitations for additional SEM/EDX analysis. The findings and level of detail here is sufficient to indicate that this is an area where further study would be worthwhile. Similarly, further investigation into the effects of bed height and particle size on defluidization time in Chapter 4 would have been beneficial to elucidate the underlying relationships. Such a study would have been more feasible on a smaller scale fluidized bed, with a far higher throughput of tests per day than was possible with the pilot-scale unit used here.

In Chapter 5, one obvious shortcoming was the lack of testing at lower additive dosages with miscanthus, to determine optimum additive dosages. However, a severe natural flooding of experimental facilities prevented further testing work. This event also resulted in the loss of bed samples and fuels. This sample loss prevented further XRD study of agglomerates, which was the most underdeveloped area of the thesis, and an area that would otherwise have contributed to detailed comparison and discussion in Chapter 6.

8.4   Recommendations for Future Work

The findings from this thesis have revealed numerous promising areas for further study. The first of these is further detailed study of bed agglomerate composition, morphology, and particle size fraction from different bed locations. The findings in Chapter 4 highlighted that there was bed scale variance to agglomerate composition. This was found with oat hull waste and white wood, fuels predisposed to coating-induced agglomeration. A similar study into other fuels, particularly those that mostly agglomerate via a melt-induced mechanism would be valuable to validate this behaviour for other fuels. In addition, a broader study of these factors in a commercial boiler would validate these findings. Moreover, it may reveal whether targeted agglomeration mitigation methods are beneficial, such as better management of fuel input location to the bed. Such a study could also be used to inform the optimal bed removal and replenishment strategies in commercial BFB boilers, and if certain zones should be more frequently replaced to mitigate against agglomeration. Bed replenishment strategies in fluidized bed are an area with little to no publicly available research. It would be recommended that bed particle size distribution before and after tests was also

measured at different regions of the bed, to provide further qualitative data as to the bed condition.

Another area of the work from Chapter 4 suitable for expansion would be to perform a wider study on the impact of bed particle size and bed height on defluidization time. The findings here added clarity to the literature and suggested reasons for possible prior contradictions. However, a greater volume of testing would help to elucidate the underlying phenomena and would likely be best accomplished with smaller scale equipment.

The main area for future work arising from Chapter 5 would be investigations into the fundamental ash release and fuel particle breakdown behaviours of different fuels in the context of fluidized bed combustion. A detailed study into this would likely lead to a better understanding of underlying structural and compositional factors inherent to the wheat straw which caused its poor performance. This could also lead to identification of other fuels that should be avoided due to such qualities. There are several other smaller areas of work arising from Chapter 5 that would be worthy of further experimentation. These include studies of variable additive dosages, additive blends, or quantification of the effective additive lifetime within the bed until there is no further reaction with ash, would all aid commercial operators in optimising additive use and bed replenishment rates, and improve understanding of agglomeration behaviours at the bed-scale.

In Chapter 6, it was identified that key chemical ternary systems, such as K_2O-CaO-SiO_2 are still require experimental validation of their phases to feed into thermochemical databases. This would significantly enhance the accuracy and credibility of predictions. Another potential area of improvement would be to combine the equilibrium modelling capabilities of FactSage with some degree of chemical kinetic modelling, to gain a more accurate insight into what compounds would form over a given timescale. However, this would significantly increase the software development burden. Opening up FactSage to be less of a black box, for example by directly showing reaction pathways from input reactions to resultant products, would be welcomed to aid analysis. At present this can only approximated by the user via lengthy manual comparison methods. With regards to the work performed here, the approach of using EDX data as a model input was noted as being more realistic for the purpose of

agglomeration studies but is rarely performed in agglomeration studies in the literature. It is recommended that other authors consider this approach.

With regards to the fuels study in Chapter 7, the analysis approaches and considerations utilised within the chapter may be of use to operators performing similar fuel studies. Fundamental studies into the release of components such as chlorine and zinc from contaminants such as plastics, metals and nails would all aid commercial operators, as would a better general understanding of the occurrence and management of non-combustible contaminants in waste wood streams. It was also notable that only one other similar study was found in the literature for a commercial fluidized bed boiler and its fuel input quality. Whilst companies are keen to maintain confidentiality of their plant operating and analysis data, they do possess significant quantities of data that engineering teams often do not have the time to analyse in addition to day-to-day duties. With larger data sets available from industry, advanced statistical analysis techniques such as PCA and machine learning, as applied here, become viable and may lead to new fundamental insights. Whilst new insights were not attained here, they have been made in the works of others, therefore remain a large area for continued, mutually beneficial, collaboration between industry and academia.

On the challenges of biomass fuels and bed agglomeration in general, one area originally planned for investigation as part of this thesis was the effect of different fuel blends on bed agglomeration and operational characteristics. Wilton 10 uses a mixed waste wood and virgin wood fuel blend. As noted throughout this thesis, commercial operators in the UK face a high level of competition for limited wood supplies and are increasingly considering alternate fuels such as the agricultural types investigated in this work. The limited works on biomass-biomass fuel blends that do exist in literature have shown complex non-linear behaviours as discussed in Chapter 2 section 2.3.6.2. Therefore, future work in this area would be useful to operators and academia, and would likely lead to the discovery of new fundamental fuel behaviours and characteristics.

References

[1]   Frankfurt School of Finance and Management, "Global Trends in Renewable Energy Investment 2016," Frankfurt School of Finance and Management, 2016.

[2]   EPA, "Overview of Greenhouse Gases," 2015. [Online]. Available: https://www.epa.gov/ghgemissions/overview-greenhouse-gases. [Accessed 31 May 2017].

[3]   European Commission, "Paris Agreement," 2016. [Online]. Available: https://ec.europa.eu/clima/policies/international/negotiations/paris_en. [Accessed 3 September 2020].

[4]   A. Pandey, T. Bhaskar, M. Stöcker and R. Sukumaran, Recent Advances in Thermochemical Conversion of Biomass, Elsevier, 2015.

[5]   J. Timperley, "Biomass subsidies 'not fit for purpose', says Chatham House," 2017. [Online]. Available: https://www.carbonbrief.org/biomass-subsidies-not-fit-for-purpose-chatham-house. [Accessed 31 May 2017].

[6]   F. Johnsson, "Fluidized Bed Combustion for Clean Energy," Vancouver, Canada, 2007.

[7]   A. Khan, W. de Jong, P. Jansens and H. Spliethoff, "Biomass combustion in fluidized bed boilers: Potential problems and remedies," *Fuel Processing Technology,* vol. 90, pp. 21-50, 2009.

[8]   D. Kunii and O. Levenspiel, Fluidization Engineering, 1st ed., John Wiley & Sons, 1969.

[9]   D. Kunii and O. Levenspiel, Fluidization Engineering, 2nd Edition, Butterworth-Heinemann, 1991.

[10]   IEA-CCC, "Understanding fluidised bed combustion," November 2003. [Online]. Available: http://www.iea-coal.org.uk/documents/81082/5448/Understanding-fluidised-bed-combustion. [Accessed 30 May 2017].

[11]   B. Leckner, "Fluidized Bed Combustion: Mixing and Pollutant Limitation," *Progress in Energy and Combustion Science,* vol. 24, pp. 31-61, 1998.

[12]   J. Grace, "Contacting modes and behaviour classification of gas—solid and other two-phase suspensions," *The Canadian Journal of Chemical Engineering,* vol. 64, no. 3, p. 353–363, 1986.

[13]   S. Bañales-López and V. Norberg-Bohn, "Public policy for energy technology innovation: A historical analysis of fluidized bed combustion development in the USA," *Energy Policy,* vol. 30, pp. 1173-1180, 2002.

[14]   B. Leckner, "Developments in Fluidized Bed Conversion of Solid Fuels," in *Thermal Science*, Turku, Finland, 2015.

[15]   F. Winkler, "Process for the production of water gas". Germany Patent DE437970, 1922.

[16]   W. Watson, Constructing Success in the Electric Power Industry - Combined Cycle Gas Turbines and Fluidised Beds, University of Sussex, 1998.

[17]   W. Patterson, "To bed betimes," *New Scientist,* pp. 180-181, 20 July 1978.

[18]   Industrial Environmental Research Laboratory, "Technology Overview: Circulating Fluidized-Bed Combustion," US Environmental Protection Agency, 1982.

[19]   National Research Council, "Coal: Energy for the Future," National Academies Press, 1995.

[20]   E. Vakkilainen, Steam Generation from Biomass: Construction and Design of Large Boilers, Butterworth-Heinemann, 2016.

[21]   P. Basu, Combustion and Gasification in Fluidized Beds, 1st ed., Taylor & Francis, 2006.

[22]   B. Leckner, P. Szentannai and F. Winter, "Scale-up of fluidized-bed combustion – A review," *Fuel,* vol. 90, no. 10, pp. 2951-2964, 2011.

[23]   F. Scala and B. Leckner, "Atmospheric (non-circulating) fluidized bed (FB) combustion," in *Fluidized Bed Technologies for Near-Zero Emission Combustion and Gasification*, Woodhead Publishing, 2013, pp. 641-668.

[24]   J. Koornneef, M. Junginger and A. Faaij, "Development of fluidized bed combustion - An overview of trends, performance and cost," *Progress in Energy and Combustion Science,* vol. 33, pp. 19-55, 2007.

[25]   IEA-CCC, "Pressurized Fluidized Bed Combustion (PFBC)," 2010. [Online]. Available: http://www.iea-coal.org.uk/site/2010/database-section/ccts/pressurized-fluidized-bed-combustion-pfbc?. [Accessed 23 1 2017].

[26]   J. Peña, "Bubbling Fluidized Bed (BFB), When to use this technology?," in *Industrial Fluidization South Africa*, Johannesburg, South Africa, 2011.

[27]   A. Hotta, "Circulating Fluidized Bed Technology - 4th EU South Africa Clean Coal Working Group Meeting," 5 November 2012. [Online]. Available: http://www.energy.gov.za/files/4thEUSouthAfricaCleanCoalWorkingGroup/EU_SA_Workshop_20121105.pdf. [Accessed 1 June 2017].

[28]   R. Cai, X. Ke, J. Lyu, H. Yang, M. Zhang, G. Yue and W. Ling, "Progress of circulating fluidized bed combustion technology in China: a review," *Clean Energy,* vol. 1, no. 1, pp. 36-49, 2017.

References

[29]   Sumitomo SHI FW, "BFB BOILERS," Sumitomo SHI FW, 2018. [Online].
        Available: http://www.shi-fw.com/clean-energy-solutions/bfb-boilers/.
        [Accessed 11 October 2018].

[30]   K. Nuortimo, E. Timo and N. Teemu, "Large Scale Utility CFB Technology
        in Worlds Largest Greenfield 100% Biomass Power Plant," in *25th European
        Biomass Conference and Exhibition*, Stockholm, Sweden, 2017.

[31]   Sumitomo SHI FW, "CFB BOILERS," Sumitomo SHI FW, 2018. [Online].
        Available: http://www.shi-fw.com/clean-energy-solutions/cfb-boilers/.
        [Accessed 11 October 2018].

[32]   Valmet, "HYBEX boilers - using BFB technology," Valmet, 2018. [Online].
        Available: https://www.valmet.com/energyproduction/bfb-boilers/. [Accessed
        11 October 2018].

[33]   Valmet, "CYMIC boilers - using CFB technology," Valmet, 2018. [Online].
        Available: https://www.valmet.com/energyproduction/cfb-boilers/. [Accessed
        11 October 2018].

[34]   GE, "Circulating Fluidized Bed (CFB) Boilers," GE, 2018. [Online].
        Available: https://www.ge.com/power/steam/boilers/circulating-fluidised-bed.
        [Accessed 11 October 2018].

[35]   GE, "GE Recently Acquired Boiler Technology to Help Pakistan Meet Power
        Demand with Domestic Coal," GE Newsroom, 2016. [Online]. Available:
        https://www.genewsroom.com/press-releases/ge-recently-acquired-boiler-
        technology-help-pakistan-meet-power-demand-domestic-coal. [Accessed 18
        January 2019].

[36]   Andritz, "EcoFluid bubbling fluidized bed boilers," Andritz, [Online].
        Available: https://www.andritz.com/products-en/pulp-and-
        paper/environmental-solutions/ecofluid-boilers. [Accessed 11 October 2018].

[37]   Andritz, "Andritz Power Systems Brochure," 2018. [Online]. Available:
        https://www.andritz.com/products-en/pulp-and-paper/environmental-
        solutions/ecofluid-boilers. [Accessed 19 January 2019].

[38]   Andritz, "PowerFluid circulating fluidized bed boilers," Andritz, 2018.
        [Online]. Available: https://www.andritz.com/products-en/pulp-and-
        paper/environmental-solutions/powerfluid-boilers. [Accessed 11 October
        2018].

[39]   Babcock & Wilcox, "Bubbling Fluidized-Bed Boilers," Babcock & Wilcox,
        2018. [Online]. Available: https://www.babcock.com/en/products/bubbling-
        fluidized-bed-boilers. [Accessed 11 October 2018].

[40]   Babcock & Wilcox, "Circulating Fluidized-Bed Boilers," Babcock & Wilcox,
        2018. [Online]. Available: https://www.babcock.com/en/products/fluidized-
        bed-boiler. [Accessed 11 October 2018].

[41]   Doosan Lentjes, "Circulating Fluidised Bed Technologies: Benefits," Doosan
        Lentjes, 2018. [Online]. Available:

http://www.doosanlentjes.com/en/cfbt/benefits/. [Accessed 17 December 2018].

[42]   B. Jenkins, L. Baxter, T. Miles Jr. and T. Miles, "Combustion properties of biomass," *Fuel Processing Technology,* vol. 54, pp. 17-46, 1998.

[43]   R. Saidur, E. Abdelaziz, A. Demirbas, M. Hossain and S. Mekhilef, "A review on biomass as a fuel for boilers," *Renewable and Sustainable Energy Reviews,* vol. 15, no. 5, pp. 2262-2289, 2011.

[44]   S. Vassilev, D. Baxter, L. Andersen and C. Vassileva, "An overview of the chemical composition of biomass," *Fuel,* vol. 89, no. 5, pp. 913-933, 2010.

[45]   P. Xing, P. Mason, S. Chilton, S. Lloyd, J. Jones, A. Williams, W. Nimmo and M. Pourkashanian, "A comparative assessment of biomass ash preparation methods using X-ray fluorescence and wet chemical analysis," *Fuel,* vol. 182, pp. 161-165, 2016.

[46]   S. Vassilev, D. Baxter and C. Vassileva, "An overview of the behaviour of biomass during combustion: Part II. Ash fusion and ash formation mechanisms of biomass types," *Fuel,* vol. 117, pp. 152-183, 2014.

[47]   E. Johnson, "Goodbye to carbon neutral: Getting biomass footprints right," *Environmental Impact Assessment Review,* vol. 29, no. 3, pp. 165-168, 2009.

[48]   J. Goldemberg, T. Johansson and D. Anderson, "World energy assessment: overview : 2004 update," United Nations Development Programme, New York, 2004.

[49]   International Energy Agency, "World Energy Balances: Overview," International Energy Agency, Paris, France, 2020.

[50]   S. Yılmaz and H. Selim, "A review on the methods for biomass to energy conversion systems design," *Renewable and Sustainable Energy Reviews,* vol. 25, pp. 420-430, 2013.

[51]   N. Samiran, M. Jaafar, J. Ng, S. Lam and C. Chong, "Progress in biomass gasification technique – With focus on Malaysian palm biomass for syngas production," *Renewable and Sustainable Energy Reviews,* vol. 62, pp. 1047-1062, 2016.

[52]   Department for Business, Energy & Industrial Strategy, "Electricity Generation Costs," UK Government, 2016.

[53]   UK Government, "National Renewable Energy Action Plan for the United Kingdom," UK Government, 2010.

[54]   Department for Business, Energy & Industrial Strategy (BEIS), "Chapter 6 Renewable Sources of Energy," in *Digest of United Kingdom Energy Statistics 2020 (DUKES)*, London, HM Government, 2020, pp. 106-128.

[55]   Renewable Energy Association, "Bioenergy Strategy Phase 1: Bioenergy in the UK - the state of play," Renewable Energy Association, 2019.

References

[56]   L. Walsh, "Plug could be pulled on Port Clarence biomass-fired plant," ENDS Waste & Bioenergy, 2018.

[57]   Tolvik Consulting, "UK Dedicated Biomass Statistics - 2017," Tolvik Consulting, 2017.

[58]   Power Technology, "Wood Burning Power Station at Wilton 10," 2007. [Online]. Available: https://www.power-technology.com/projects/wood-burning/. [Accessed 2 August 2018].

[59]   M. Bolhar-Nordenkampf, "Utilization of Biomass residues for Energy production in Pulp and Paper Industry," Italy, 2014.

[60]   Valmet, "Valmet's technology helps to reduce CO2 emissions in UK," 2016. [Online]. Available: https://www.valmet.com/about-us/references/energy-references/long-cooperation-key-to-successful-upgrade/. [Accessed 2 August 2018].

[61]   Valmet, "Metso supplies power boiler to UPM Caledonian for green energy production in Scotland," 2007. [Online]. Available: https://www.valmet.com/media/news/news-archive-1999-2013/pulp-and-paper-news/metso-supplies-power-boiler-to-upm-caledonian-for-green-energy-production-in-scotland/. [Accessed 2 August 2018].

[62]   ANDRITZ, "Reference story: New biomass boiler at Iggesund Workington, UK," 2014. [Online]. Available: https://www.andritz.com/resource/blob/223620/26ca43c981b83e6ba8cf05ec2ea832a5/pp-refstory-iggesund-data.pdf. [Accessed 2 August 2018].

[63]   Valmet, "Valmet delivered biomass boiler handed over to RWE Innogy in the UK," Valmet, 2014. [Online]. Available: https://www.valmet.com/media/news/press-releases/2014/valmet-delivered-biomass-boiler-handed-over-to-rwe-innogy-in-the-uk-/. [Accessed 11 October 2018].

[64]   M. Wickham, "Biomass to power," *Bioenergy Insight,* p. 70, May/June 2017.

[65]   R. Giglio and T. Jäntti, "Tees Renewable Energy Plant," *Modern Power Systems,* pp. 21-26, November 2017.

[66]   D. Brack, "The Impacts of the Demand for Woody Biomass for Power and Heat on Climate and Forests," Chatham House, 2017.

[67]   T. Beeley, "Extending Fuel Specifications and Plant Limits to Increase Flexibility," 2019. [Online]. Available: https://www.tferf.org/past-meetings. [Accessed 19 February 2020].

[68]   D. Sanderson, "The Importance of Flexibility in Biomass Supply Chains," 2019. [Online]. Available: https://www.tferf.org/past-meetings. [Accessed 19 February 2020].

[69]   M. Lackner, F. Winter and A. Agarwal, "Agglomeration in Fluidized Bed Combustion: Mechanisms, Detection, and Counteraction," in *Handbook of Combustion Vol. 4*, John Wiley & Sons, 2010, pp. 471-491.

[70]   M. Hupa, O. Karlström and E. Vainio, "Biomass combustion technology development – It is all about chemical details," *Proceedings of the Combustion Institute,* vol. 36, no. 1, pp. 113-134, 2017.

[71]   R. Brown, M. Dawson and J. Smeenk, "Bed Material Agglomeration During Fluidized Bed Combustion," U.S. Department of Energy, Pittsburgh, PA, 1996.

[72]   E. Zabetta, V. Barišić, K. Peltola and A. Hotta, "Foster Wheeler Experience with biomass and waste in CFBs," in *33rd International Technical Conference on Coal Utilization and Fuel Systems*, Clearwater, Florida, 2008.

[73]   A. Giramonti, R. Lessard, D. Merrick and M. Hobson, "Technical and Economic Assessment of Fluidized Bed Augmented Compressed Air Energy Storage System," Battelle Memorial Institute, 1991.

[74]   N. Kumar, P. Besuner, S. Lefton, D. Agan and D. Hilleman, "Power plant cycling costs," National Renewable Energy Laboratory, Sunnyvale, California, 2012.

[75]   M. Bartels, W. Lin, J. Nijenhuis, F. Kapteijn and J. van Ommen, "Agglomeration in fluidized beds at high temperatures: Mechanisms, detection and prevention," *Progress in Energy and Combustion Science,* vol. 34, no. 5, pp. 633-666, 2008.

[76]   P. Basu, C. Kefa and L. Jestin, "Corrosion and Fouling of Heat Transfer Surfaces," in *Boilers and Burners: Design and Theory*, Springer, 2000, pp. 385-425.

[77]   Y. Niu, Y. Zhu, H. Tan, S. Hui, Z. Jing and W. Xu, "Investigations on biomass slagging in utility boiler: Criterion numbers and slagging growth mechanisms," *Fuel Processing Technology,* vol. 128, pp. 499-508, 2014.

[78]   A. Stam, K. Haasnnot and G. Brem, "Superheater fouling in a BFB boiler firing wood-based fuel blends," *Fuel,* vol. 135, pp. 322-331, 2014.

[79]   Y. Niu, H. Tan and S. Hui, "Ash-related issues during biomass combustion: Alkali-induced slagging, silicate melt-induced slagging (ash fusion), agglomeration, corrosion, ash utilization, and related countermeasures," *Progress in Energy and Combustion Science,* vol. 52, pp. 1-61, 2016.

[80]   P. Henderson, P. Szakálos, R. Pettersson, C. Andersson and J. Högberg, "Reducing superheater corrosion in wood-fired boilers," *Materials and Corrosion,* vol. 57, no. 2, pp. 128-134, 2006.

[81]   H. Kassman, M. Broström, M. Berg and L. Åmand, "Measures to reduce chlorine in deposits: Application in a large-scale circulating fluidised bed boiler firing biomass," *Fuel,* vol. 60, no. 4, pp. 1325-1334, 2011.

[82]   A. Demirbas, "Potential applications of renewable energy sources, biomass combustion problems in boiler power systems and combustion related environmental issues," *Progress in Energy and Combustion Science,* vol. 31, no. 2, pp. 171-192, 2005.

References

[83] H. Nielsen, F. Frandsen, K. Dam-Johansen and L. Baxter, "The implications of chlorine-associated corrosion on the operation of biomass-fired boilers," *Progress in Energy and Combustion Science,* vol. 26, no. 3, p. 2000, 283-298.

[84] K. Davidsson, L.-E. Åmand, B.-M. Steenari, A.-L. Elled, D. Eskilsson and B. Leckner, "Countermeasures against alkali-related problems during combustion of biomass in a circulating fluidized bed boiler," *Chemical Engineering Science,* vol. 63, no. 21, pp. 5314-5329, 2008.

[85] Sembcorp Energy UK, "Wilton International," Sembcorp Energy UK, 2018. [Online]. Available: https://www.wiltoninternational.com/. [Accessed 6 March 2018].

[86] Sembcorp Energy UK, "Sembcorp Utilities UK," Sembcorp Energy UK, 2018. [Online]. Available: https://www.sembcorp.co.uk/. [Accessed 11 October 2018].

[87] J. Morris, S. Daood, S. Chilton and W. Nimmo, "Mechanisms and Mitigation of Agglomeration during Fluidized Bed Combustion of Biomass: A Review," *Fuel,* Vols. Submitted, under review, 2018.

[88] A. Khadlikar, P. Rozelle and S. Pisupati, "Models of agglomerate growth in fluidized bed reactors: Critical review, status and applications," *Powder Technology,* vol. 264, pp. 216-228, 2014.

[89] V. Mettanant, P. Basu and J. Butler, "Agglomeration of biomass fired fluidized bed gasifier and combustor," *The Canadian Journal of Chemical Engineering,* vol. 87, no. 5, pp. 656-684, 2009.

[90] F. Scala, "Particle agglomeration during fluidized bed combustion: Mechanisms, early detection and possible countermeasures," *Fuel Processing Technology,* vol. 171, pp. 31-38, 2018.

[91] G. Olofsson, Z. Ye, I. Bjerle and A. Andersson, "Bed Agglomeration Problems in Fluidized-Bed Biomass Combustion," *Industrial & Engineering Chemistry Research,* vol. 41, no. 12, pp. 2888-2894, 2002.

[92] M. Radovanovic, Fluidized Bed Combustion, Taylor & Francis, 1986.

[93] G. Morey, F. Kracek and N. Bowen, "The Ternary System K2O-CaO-SiO2," *Journal of the Society of Glass Technology,* vol. 14, pp. 149-187, 1940.

[94] P. Billen, B. Creemers, J. Costa, J. Van Caneghem and C. Vandecasteele, "Coating and melt induced agglomeration in a poultry litter fired fluidized bed combustor," *Biomass and Bioenergy,* vol. 69, pp. 71-79, 2014.

[95] V. Barišić, L.-E. Åmand and E. Zabetta, "The role of limestone in preventing agglomeration and slagging during CFB combustion of high-phosphorous fuels," in *World Bioenergy 2008*, Jönköping, Sweden, 2008.

[96] C. Sevonius, P. Yrjas, D. Lindberg and L. Hupa, "Agglomeration tendency of a fluidized bed during addition of different phosphate compounds," *Fuel,* vol. 268, p. 117300, 2020.

[97]   K. Wagner, G. Häggström, N. Skoglund, J. Priscak, M. Kuba, M. Öhman and H. Hofbauer, "Layer formation mechanism of K-feldspar in bubbling fluidized bed combustion of phosphorus-lean and phosphorus-rich residual biomass," *Applied Energy,* vol. 248, pp. 545-554, 2019.

[98]   A. Ghaly, A. Ergüdenler and E. Laufer, "Agglomeration characteristics of alumina sand-straw ash mixtures at elevated temperatures," *Biomass and bioenergy,* vol. 5, no. 6, p. 467–480, 1993.

[99]   A. Ghaly, A. Ergüdenler and E. Laufer, "Study of agglomeration characteristics of silica sand-straw ash mixtures using scanning electronic microscopy and energy dispersion X-ray techniques," *Bioresource technology,* vol. 48, no. 2, p. 127–134, 1994.

[100]   A. Nordin, M. Öhman, B. Skrifvars and M. Hupa, Applications of Advanced Technology to Ash-Related Problems in Boilers, Springer International Publishing, 1996.

[101]   B. Skrifvars, M. Hupa, R. Backman and M. Hiltunen, "Sintering mechanisms of FBC ashes," *Fuel,* vol. 73, no. 2, pp. 171-176, 1994.

[102]   B. Skrifvars, R. Backman and M. Hupa, "Characterization of the sintering tendency of ten biomass ashes in FBC conditions by a laboratory test and by phase equilibrium calculations," *Fuel Processing Technology,* vol. 56, no. 1, pp. 55-67, 1998.

[103]   B. Skrifvars, M. Öhman, A. Nordin and M. Hupa, "Predicting bed agglomeration tendencies for biomass fuels fired in FBC boilers: a comparison of three different prediction methods," *Energy & Fuels,* vol. 13, no. 2, pp. 359-363, 1999.

[104]   E. Roedder, "Silicate melt systems," *Physics and Chemistry of the Earth,* vol. 3, pp. 224-297, 1959.

[105]   W. Hosford, Materials Science: An Intermediate Text, Cambridge University Press, 2006.

[106]   M. Öhman, A. Nordin, B.-J. Skrifvars, R. Backman and M. Hupa, "Bed Agglomeration Characteristics during Fluidized Bed Combustion of Biomass Fuels," *Energy & Fuels,* vol. 14, pp. 169-178, 2000.

[107]   M. Öhman and A. Nordin, "A new method for quantification of fluidized bed agglomeration tendencies: a sensitivity analysis," *Energy & Fuels,* vol. 12, no. 1, p. 90–94, 1998.

[108]   J. Silvennoinen, "A new method to inhibit bed agglomeration problems in fluidized bed boilers," Jacksonville, Florida, 2003.

[109]   L. Nuutinen, M. Tiainen, M. Virtanen, S. Enestam and R. Laitinen, "Coating Layers on Bed Particles during Biomass Fuel Combustion in Fluidized-Bed Boilers," *Energy & Fuels,* vol. 18, no. 1, pp. 127-139, 2004.

References

[110] H. Visser, "The Influence of Fuel Composition on Agglomeration Behaviour in Fluidised-Bed Combustion," Energy Research Centre of the Netherlands (ECN), 2004.

[111] E. Brus, M. Öhman and A. Nordin, "Mechanisms of Bed Agglomeration during Fluidized-Bed Combustion of Biomass Fuels," *Energy & Fuels,* vol. 19, no. 3, pp. 825-832, 2005.

[112] M. Öhman, L. Pommer and A. Nordin, "Bed Agglomeration Characteristics and Mechanisms during Gasification and Combustion of Biomass Fuels," *Energy & Fuels,* vol. 19, no. 4, pp. 1742-1748, 2005.

[113] M. Zevenhoven-Onderwater, M. Öhman, B. Skrifvars, R. Backman, A. Nordin and M. Hupa, "Bed Agglomeration Characteristics of Wood-Derived Fuels in FBC," *Energy & Fuels,* vol. 20, no. 2, pp. 818-824, 2006.

[114] A. Grimm, M. Öhman, T. Lindberg, A. Fredriksson and D. Boström, "Bed Agglomeration Characteristics in Fluidized-Bed Combustion of Biomass Fuels Using Olivine as Bed Material," *Energy & Fuels,* vol. 26, no. 7, pp. 4550-4559, 2012.

[115] J. Kaknics, R. Michel and J. Poirier, "Miscanthus ash transformation and interaction with bed materials at high temperature," *Fuel Processing Technology,* vol. 141, pp. 178-184, 2016.

[116] J. Kaknics, R. Michel, A. Richard and J. Poirier, "High-Temperature Interactions between Molten Miscanthus Ashes and Bed Materials in a Fluidized-Bed Gasifier," *Energy & Fuels,* vol. 29, no. 3, pp. 1785-1792, 2015.

[117] F. Kirnbauer and H. Hofbauer, "Investigations on Bed Material Changes in a Dual Fluidized Bed Steam Gasification Plant in Güssing, Austria," *Energy & Fuels,* vol. 25, no. 8, pp. 3793-3798, 2011.

[118] M. Kuba, H. He, F. Kirnbauer, N. Skoglund, D. Boström, M. Öhman and H. Hofbauer, "Mechanism of Layer Formation on Olivine Bed Particles in Industrial-Scale Dual Fluid Bed Gasification of Wood," *Energy & Fuels,* vol. 30, no. 9, pp. 7410-7418, 2016.

[119] H. He, D. Boström and M. Öhman, "Time Dependence of Bed Particle Layer Formation in Fluidized Quartz Bed Combustion of Wood-Derived Fuels," *Energy & Fuels,* vol. 28, no. 6, pp. 3841-3848, 2014.

[120] B. Gatternig and J. Karl, "Investigations on the Mechanisms of Ash-Induced Agglomeration in Fluidized-Bed Combustion of Biomass," *Energy & Fuels,* vol. 29, pp. 931-941, 2015.

[121] F. Scala and R. Chirone, "Characterization and Early Detection of Bed Agglomeration during the Fluidized Bed Combustion of Olive Husk," *Energy & Fuels,* vol. 20, no. 1, pp. 120-132, 2006.

[122] H. He, X. Ji, D. Boström, R. Backman and M. Öhman, "Mechanism of Quartz Bed Particle Layer Formation in Fluidized Bed Combustion of Wood Derived Fuels," *Energy & Fuels,* vol. 30, no. 3, pp. 2227-2232, 2016.

[123] B. Gatternig and J. Karl, "The Influence of Particle Size, Fluidization Velocity, and Fuel Type on Ash-Induced Agglomeration in Biomass Combustion," *Frontiers in Energy Research,* vol. 2, 2014.

[124] W. Lin, K. Dam-Johansen and F. Frandsen, "Agglomeration in bio-fuel fired fluidized bed combustors," *Chemical Engineering Journal,* vol. 96, no. 1-3, pp. 171-185, 2003.

[125] R. Chirone, F. Miccio and F. Scala, "Mechanism and prediction of bed agglomeration during fluidized bed combustion of a biomass fuel: Effect of the reactor scale," *Chemical Engineering Journal,* vol. 123, no. 3, pp. 71-80, 2006.

[126] H. Liu, Y. Feng, S. Wu and D. Liu, "The role of ash particles in the bed agglomeration during the fluidized bed combustion of rice straw," *Bioresource Technology,* vol. 100, no. 24, pp. 6505-6513, 2009.

[127] C. Lin and M. Wey, "The effect of mineral compositions of waste and operating conditions on particle agglomeration/defluidization during incineration," *Fuel,* vol. 83, no. 17-18, pp. 2335-2343, 2004.

[128] R. Chirone, P. Salatino, F. Scala, R. Solimene and M. Urciuolo, "Fluidized bed combustion of pelletized biomass and waste-derived fuels," *Combustion and Flame,* vol. 155, no. 1-2, pp. 21-36, 2008.

[129] F. Scala and R. Chirone, "An SEM/EDX study of bed agglomerates formed during fluidized bed combustion of three biomass fuels," *Biomass and Bioenergy,* vol. 32, no. 3, pp. 252-266, 2008.

[130] C. Yu, J. Qin, H. Nie, M. Fang and Z. Luo, "Experimental research on agglomeration in straw-fired fluidized beds," *Applied Energy,* vol. 88, no. 12, pp. 4534-4543, 2011.

[131] C. Zhou, C. Rosen and K. Engvall, "Biomass oxygen/steam gasification in a pressurized bubbling fluidized bed: Agglomeration behavior," *Applied Energy,* vol. 172, pp. 230-250, 2016.

[132] P. Chaivatamaset, P. Sricharoon and S. Tia, "Bed agglomeration characteristics of palm shell and corncob combustion in fluidized bed," *Applied Thermal Engineering,* vol. 31, no. 14-15, pp. 2916-2927, 2011.

[133] C. Lin, T. Peng and W. Wang, "Effect of particle size distribution on agglomeration/defluidization during fluidized bed combustion," *Powder Technology,* vol. 207, no. 1-3, pp. 290-295, 2011.

[134] J. Howard, Fluidized Bed Technology: Principles and Applications, Adam Hilger Ltd., 1989.

[135] S. Oka, Fluidized Bed Combustion, CRC Press, 2003.

[136] J. Kuo, W. Hsu and T. Yo, "Effect of air distribution on solid fuel bed combustion," *Transactions - American Society of Chemical Engineers Journal of Energy Resources Technology,* vol. 119, pp. 120-128, 1997.

References

[137] S. Chilton, The Combustion of Low Grade Fuels in Fluidised Bed Combustors, University of Leeds, 2017.

[138] R. Darton, "Bubble growth due to coalescence in fluidised beds," *Transactions of the Institute of Chemical Engineers,* vol. 55, pp. 274-280, 1977.

[139] B. Gudka, J. Jones, A. Lea-Langton, A. Williams and A. Saddawi, "A review of the mitigation of deposition and emission problems during biomass combustion through washing pre-treatment," *Journal of the Energy Institute,* vol. 89, no. 2, pp. 159-171, 2016.

[140] M. Hupa, "Interaction of fuels in co-firing in FBC," *Fuel,* vol. 80, no. 10, pp. 1312-1319, 2005.

[141] M. Sami, K. Annamalai and M. Wooldridge, "Co-firing of coal and biomass fuel blends," *Progress in energy and combustion science,* vol. 27, no. 2, pp. 171-214, 2001.

[142] E. Agbor, X. Zhang and A. Kumar, "A review of biomass co-firing in North America," *Renewable and Sustainable Energy Reviews,* vol. 40, pp. 930-943, 2014.

[143] S. Sahu, N. Chakraborty and P. Sarkar, "Coal–biomass co-combustion: An overview," *Renewable and Sustainable Energy Reviews,* vol. 39, pp. 575-586, 2014.

[144] M. Kopczyński, J. Lasek, A. Iluk and J. Zuwała, "The co-combustion of hard coal with raw and torrefied biomasses (willow (Salix viminalis), olive oil residue and waste wood from furniture manufacturing)," *Energy,* vol. 140, pp. 1316-1325, 2017.

[145] R. Isemin, A. Mikhalev, V. Konyakhin, S. Kuzmin, O. Milovanov and D. Klimov, "Combustion of Different Type Biopellets in a Fixed – Turbulent Fluidized Bed," *Procedia Engineering,* vol. 117, pp. 132-141, 2015.

[146] T. Yang, F. Lü, X. Kai, Y. He and R. Li, "Mechanism of coal and biomass co-combustion: Deposition characteristics," *Journal of Fuel Chemistry and Technology,* vol. 40, no. 3, pp. 273-278, 2012.

[147] C. Badour, A. Gilbert, C. Xu, H. Li, Y. Shao, G. Tourigny and F. Preto, "Combustion and air emissions from co-firing a wood biomass, a Canadian peat and a Canadian lignite coal in a bubbling fluidised bed combustor," *The Canadian Journal of Chemical Engineering,* vol. 90, no. 5, pp. 1170-1177, 2012.

[148] D. Salour, B. Jenkins, M. Vafaei and M. Kayhanian, "Control of in-bed agglomeration by fuel blending in a pilot scale straw and wood fueled AFBC," *Biomass and Bioenergy,* vol. 4, no. 2, pp. 117-133, 1993.

[149] S. Link, P. Yrjas and L. Hupa, "Ash melting behaviour of wheat straw blends with wood and reed," *Renewable Energy,* pp. In press, corrected proof, 2017.

[150]   P. Thy, B. Jenkins, R. Williams, C. Lesher and R. Bakker, "Bed agglomeration in fluidized combustor fueled by wood and rice straw blends," *Fuel Processing Technology,* vol. 91, no. 11, pp. 1464-1485, 2010.

[151]   A. Elled, L. Åmand and B. Steenari, "Composition of agglomerates in fluidized bed reactors for thermochemical conversion of biomass and waste fuels," *Fuel,* vol. 111, pp. 696-708, 2013.

[152]   N. Skoglund, A. Grimm, M. Öhman and D. Boström, "Effects on Ash Chemistry when Co-firing Municipal Sewage Sludge and Wheat Straw in a Fluidized Bed: Influence on the Ash Chemistry by Fuel Mixing," *Energy & Fuels,* vol. 27, no. 10, pp. 5725-5732, 2013.

[153]   J. Silvennoinen and M. Hedman, "Co-firing of agricultural fuels in a full-scale fluidized bed boiler," *Fuel Processing Technology,* vol. 105, pp. 11-19, 2013.

[154]   M. Becidan, E. Houshfar, R. Khalil, Ø. Skreiberg, T. Løvås and L. Sørum, "Optimal Mixtures to Reduce the Formation of Corrosive Compounds during Straw Combustion: A Thermodynamic Analysis," *Energy & Fuels,* vol. 25, no. 7, pp. 3223-3234, 2011.

[155]   A. Burton and H. Wu, "Influence of biomass particle size on bed agglomeration during biomass pyrolysis in fluidised bed," *Proceedings of the Combustion Institute,* vol. 36, no. 2, pp. 2199-2205, 2017.

[156]   H. Li, Q. Chen, X. Zhang, K. Finney, V. Sharifi and J. Swithenbank, "Evaluation of a biomass drying process using waste heat from process industries: A case study," *Applied Thermal Engineering,* vol. 35, pp. 71-80, 2012.

[157]   P. Knutsson, G. Schwebel, B. Steenari and H. Leion, "Effect of bed materials mixing on the observed bed sintering," Beijing, China, 2014.

[158]   A. Corcoran, J. Marinkovic, F. Lind, H. Thunman, P. Knutssun and M. Seemann, "Ash Properties of Ilmenite Used as Bed Material for Combustion of Biomass in a Circulating Fluidized Bed Boiler," *Energy & Fuels,* vol. 28, pp. 7672-7679, 2014.

[159]   A. Corcoran, P. Knutsson, F. Lind and H. Thunman, "Mechanism for Migration and Layer Growth of Biomass Ash on Ilmenite Used for Oxygen Carrier Aided Combustion," *Energy & Fuels,* vol. 32, no. 8, pp. 8845-8856, 2018.

[160]   L. Bierlein and B. Fredriksson-Moeller, "New Industrial Development in Fluidised Bed Combustion of Waste and Biomass," in *25th Euopean Biomass Conference and Exhibition*, Stockholm, Sweden, 2017.

[161]   R. Symonds, R. Hughes and M. Obras Loscertales, "Oxy-pressurized fluidized bed combustion: Configuration and options analysis," *Applied Energy,* vol. 262, p. 114531, 2020.

[162]   D. Geldart, "Types of Gas Fluidization," *Powder Technology,* vol. 7, pp. 285-292, 1973.

References

[163]   F. Duan, C.-S. Chyang, L.-H. Zhang and S.-F. Yin, "Bed agglomeration characteristics of rice straw combustion in a vortexing fluidized-bed combustor," *Bioresource Technology,* vol. 183, pp. 195-202, 2015.

[164]   L. Wang, J. Hustad, Ø. Skreiberg, G. Skjevrak and M. Grønli, "A Critical Review on Additives to Reduce Ash Related Operation Problems in Biomass Combustion Applications," *Energy Procedia,* vol. 20, pp. 20-29, 2012.

[165]   B.-M. Steenari and O. Lindqvist, "High-temperature reactions of straw ash and the anti-sintering additives kaolin and dolomite," *Biomass and Bioenergy,* vol. 14, no. 1, p. 67–76, 1998.

[166]   M. Öhman and A. Nordin, "The Role of Kaolin in Prevention of Bed Agglomeration during Fluidized Bed Combustion of Biomass Fuels," *Energy & Fuels,* vol. 14, no. 3, pp. 618-624, 2000.

[167]   D. Vamvuka, D. Zografos and G. Alevizos, "Control methods for mitigating biomass ash-related problems in fluidized beds," *Bioresource Technology,* vol. 99, no. 9, pp. 3534-3544, 2008.

[168]   V. Barišić, K. Peltola and E. Coda Zabetta, "Role of Pulverized Coal Ash against Agglomeration, Fouling, and Corrosion in Circulating Fluidized-Bed Boilers Firing Challenging Biomass," *Energy & Fuels,* vol. 27, no. 10, pp. 5706-5713, 2013.

[169]   C. Lin, J. Kuo, M. Wey, S. Chang and K. Wang, "Inhibition and promotion: The effect of earth alkali metals and operating temperature on particle agglomeration/defluidization during incineration in fluidized bed," *Powder Technology,* vol. 189, no. 1, pp. 57-63, 2009.

[170]   D. Clery, P. Mason, C. Raynor and J. Jones, "The effects of an additive on the release of potassium in biomass combustion," *Fuel,* vol. 214, pp. 647-655, 2018.

[171]   H. Chi, M. Pans, C. Sun and H. Liu, "An investigation of lime addition to fuel as a countermeasure to bed agglomeration for the combustion of non-woody biomass fuels in a 20kWth bubbling fluidised bed combustor," *Fuel,* vol. 240, pp. 349-361, 2019.

[172]   J. Seville and R. Clift, "The Effect of Thin Liquid Layers on Fluidisation Characteristics," *Powder Technology,* vol. 37, pp. 117-129, 1984.

[173]   E. Brus, M. Öhman, A. Nordin, B. Skrifvars and R. Backman, "Bed Material Consumption in Biomass Fired Fluidised Bed Boilers Due to Risk of Bed Agglomeration - Coating Formation and Possibilities for Regeneration," *IFRF Combustion Journal,* 2003.

[174]   H. Visser, S. van Lith and J. Kiel, "Biomass Ash-Bed Material Interactions Leading to Agglomeration in FBC," *Journal of Energy Resources Technology,* vol. 130, no. 1, p. 011801, 2008.

[175]   C. Sevonius, P. Yrjas and M. Hupa, "Defluidization of a quartz bed – Laboratory experiments with potassium salts," *Fuel,* vol. 127, pp. 161-168, 2014.

[176] C. Sevonius, P. Yrjas, D. Lindberg and L. Hupa, "Impact of sodium salts on agglomeration in a laboratory fluidized bed," *Fuel,* vol. 245, pp. 305-315, 2019.

[177] B. Anicic, W. Lin, K. Dam-Johansen and H. Wu, "Agglomeration mechanism in biomass fluidized bed combustion – Reaction between potassium carbonate and silica sand," *Fuel Processing Technology,* vol. 173, pp. 182-190, 2018.

[178] R. Michel, J. Kaknics, E. de Bilbao and J. Poirier, "The mechanism of agglomeration of the refractory materials in a fluidized-bed reactor," *Ceramics International,* vol. 42, no. 2, pp. 2570-2581, 2016.

[179] C. Bale, E. Bélisle, P. Chartrand, S. Decterov, G. Eriksson, A. Gheribi, K. Hack, I.-H. Jung, Y.-B. Kang, J. Melançon, A. Pelton, S. Petersen, C. Robelin, J. Sangster, P. Spencer and M.-A. Van Ende, "FactSage thermochemical software and databases, 2010–2016," *Calphad,* vol. 54, pp. 35-53, 2016.

[180] T. Rizvi, P. Xing, M. Pourkashanian, L. Darvell, J. Jones and W. Nimmo, "Prediction of biomass ash fusion behaviour by the use of detailed characterisation methods coupled with thermodynamic analysis," *Fuel,* vol. 141, pp. 275-284, 2015.

[181] D. Lindberg, R. Backman, P. Chartrand and M. Hupa, "Towards a comprehensive thermodynamic database for ash-forming elements in biomass and waste combustion — Current situation and future developments," *Fuel Processing Technology,* vol. 105, pp. 129-141, 2013.

[182] M. Blander, T. Milne, D. Dayton, R. Backman, D. Blake, V. Kühnel, W. Linak, A. Nordin and A. Ljung, "Equilibrium Chemistry of Biomass Combustion: A Round-Robin Set of Calculations Using Available Computer Programs and Databases," *Energy & Fuels,* vol. 15, no. 2, pp. 344-349, 2001.

[183] N. Saunders and A. Miodownik, CALPHAD: Calculation of Phase Diagrams - A Comprehensive Guide, Elsevier, 1998.

[184] P. Billen, J. Van Carneghem and C. Vandecasteele, "Predicting Melt Formation and Agglomeration in Fluidized Bed Combustors by Equilibrium Calculations," *Waste and Biomass Valorization,* vol. 5, no. 5, pp. 879-892, 2014.

[185] A. Grimm, N. Skoglund, D. Boström and M. Öhman, "Bed Agglomeration Characteristics in Fluidized Quartz Bed Combustion of Phosphorus-Rich Biomass Fuels," *Enery & Fuels,* vol. 25, no. 3, pp. 937-947, 2011.

[186] J. Berjonneau, L. Colombel, J. Poirier, M. Pichavant, F. Defoort and J.-M. Seiler, "Determination of the Liquidus Temperatures of Ashes from the Biomass Gazification for Fuel Production by Thermodynamical and Experimental Approaches," *Energy & Fuels,* vol. 23, no. 12, pp. 6231-6241, 2009.

[187] L. Fryda, K. Panopoulos and E. Kakaras, "Agglomeration in fluidised bed gasification of biomass," *Powder Technology,* vol. 181, no. 3, pp. 307-320, 2008.

References

[188]   M. Zevenhoven-Onderwater, R. Backman, B.-J. Skrifvars and M. Hupa, "The ash chemistry in fluidised bed gasification of biomass fuels. Part I: predicting the chemistry of melting ashes and ash–bed material interaction," *Fuel,* vol. 80, no. 10, pp. 1489-1502, 2001.

[189]   M. Zevenhoven-Onderwater, R. Backman, B.-J. Skrifvars, M. Hupa, T. Liliendahl, C. Rosén, K. Sjöström, K. Engvall and A. Hallgren, "The ash chemistry in fluidised bed gasification of biomass fuels. Part II: Ash behaviour prediction versus bench scale agglomeration tests," *Fuel,* vol. 80, no. 10, pp. 1503-1512, 2001.

[190]   D. Boström, N. Skoglund, A. Grimm, C. Boman, M. Öhman, M. Broström and R. Backman, "Ash Transformation Chemistry during Combustion of Biomass," *Energy & Fuels,* vol. 26, no. 1, pp. 85-93, 2012.

[191]   L. Breiman, "Random Forests," *Machine Learning,* vol. 45, pp. 5-32, 2001.

[192]   Elsevier, "Scopus," Elsevier, 2020. [Online]. Available: https://www.scopus.com. [Accessed 15 October 2020].

[193]   G. James, D. Witten, T. Hastie and R. Tibshirani, An Introduction to Statistical Learning, Springer Texts in Statistics, 2013.

[194]   T. Hastie, R. Tibshirani and J. Friednman, The Elements of Statistical Learning, Springer, 2008.

[195]   H. Ge, X. Li, Y. Li, G. Lu and Y. Yan, "Biomass fuel identification using flame spectroscopy and tree model algorithms," *Combustion Science and Technology,* pp. 1-18, 2019.

[196]   W. Zhang, X. Cheng, Y. Hu and Y. Yan, "Online prediction of biomass moisture content in a fluidized bed dryer using electrostatic sensor arrays and the Random Forest method," *Fuel,* vol. 239, pp. 437-445, 2019.

[197]   F. Elmaz, B. Büyükçakır, Ö. Yücel and A. Mutlu, "Classification of solid fuels with machine learning," *Fuel,* vol. 266, p. 117066, 2020.

[198]   B. Gatternig and J. Karl, "Prediction of ash-induced agglomeration in biomass-fired fluidized beds by an advanced regression-based approach," *Fuel,* vol. 161, pp. 157-167, 2015.

[199]   ECN, "Phyllis2 Database for Biomass and Waste," ECN, 2019. [Online]. Available: https://phyllis.nl/. [Accessed 5 July 2019].

[200]   Fuji Electric, "Single-Beam NDIR Gas Analyzer <ZRE>," 2018. [Online]. Available: http://www.fujielectric.com/products/instruments/ products/anlz_gas/ZRE.html. [Accessed 5 March 2018].

[201]   Fuji Electric, "Double Beam NDIR Gas Analyzer <ZKJ>," 2018. [Online]. Available: http://www.fujielectric.com/products/instruments/ products/anlz_gas/ZKJ.html. [Accessed 5 March 2018].

[202]   Signal Group, "Signal Group Home," Signal Group, 2018. [Online]. Available: http://www.signal-group.com/. [Accessed 11 April 2018].

[203]   EMStec, "An In-Service Emissions Test for Spark Ignition Petrol Engines - Appendix 1 Technologies available for measuring NOx," EMStec Ltd., Oxford, UK, 2002.

[204]   F. Sher, M. A. D. Pans, C. Sun and H. Liu, "Experimental investigation of woody and non-woody biomass combustion in a bubbling fluidised bed combustor focusing on gaseous emissions and temperature profiles," *Energy,* vol. 141, pp. 2069-2080, 2017.

[205]   P. Grammelis and E. Kakaras, "Biomass Combustion Modeling in Fluidized Beds," *Energy & Fuels,* vol. 19, no. 1, pp. 292-297, 2005.

[206]   J. Saastamoinen, "Release Profile of Volatiles in Fluidised Bed Combustion of Biomass," *Journal of Fundamentals of Renewable Energy and Applications,* vol. 5, no. 1, 2014.

[207]   E. Zabetta, M. Hupa and K. Saviharju, "Reducing NOx Emissions Using Fuel Staging, Air Staging, and Selective Noncatalytic Reduction in Synergy," *Industrial & Engineering Chemistry Research,* vol. 44, pp. 4552-4561, 2005.

[208]   G. Olofsson, W. Wang, Z. Ye, I. Bjerle and A. Andersson, "Repressing NOx and N2O Emissions in a Fluidized Bed Biomass Combustor," *Energy & Fuels,* vol. 16, no. 4, pp. 915-919, 2002.

[209]   E. Vakkilainen, "Fluidized Bed Boilers for Biomass," in *Steam Generation from Biomass*, Elsevier, 2017, pp. 211-236.

[210]   Buehler, "Epoxy Mounting Systems," Buehler, 2018. [Online]. Available: https://www.buehler.co.uk/epoxy-mounting-systems.php. [Accessed 12 April 2018].

[211]   Struers, "SECOTOM-15/-50," 2018. [Online]. Available: https://www.struers.com/en-GB/Products/ Cutting/Cutting-equipment/Secotom. [Accessed 10 October 2018].

[212]   Buehler, "AutoMet™ 250 Pro Grinder-Polisher," 2019. [Online]. Available: https://www.buehler.co.uk/automet-250-pro-grinder-polisher-touch-screen-programmable.php. [Accessed 26 March 2019].

[213]   Edwards Vacuum, "Edwards Vacuum," 2018. [Online]. Available: https://www.edwardsvacuum.com/. [Accessed 16 April 2018].

[214]   Quroum Technologies, "Q150T Plus - Turbomolecular pumped coater," 2019. [Online]. Available: https://www.quorumtech.com/quorum-product/q150t-turbo-pumped-sputter-coatercarbon-coater. [Accessed 3 December 2019].

[215]   J. Goldstein, D. Newbury, D. Joy, C. Lyman, P. Echlin, E. Lifshin, L. Sawyer and J. Michael, Scanning Electron Microscopy and X-Ray Microanalysis, 3rd Edition, New York: Springer, 2003.

[216]   H. He, Layer Formation on Bed Particles during Fluidized Bed Combustion and Gasification of Woody Biomass, Luleå, Sweden: Luleå University of Technology, 2017.

References

[217]   V. Pecharsky and P. Zavalij, Fundamentals of powder diffraction and structural characterization of materials, New York: Springer, 2005.

[218]   Malvern Panalytical, "X'Pert³ Powder," Malvern Panalytical, 2020. [Online]. Available: https://www.malvernpanalytical.com/en/products/product-range/xpert3-range/xpert3-powder. [Accessed 24 February 2020].

[219]   S. D. Gates-Rector and T. N. Blanton, "The Powder Diffraction File: A Quality Materials Characterization Database," *Powder Diffraction,* vol. 34, no. 4, pp. 352-60, 2019.

[220]   T. Ekvall, K. Andersson, T. Leffler and M. Berg, "K–Cl–S chemistry in air and oxy-combustion atmospheres," *Proceedings of the Combustion Institute,* vol. 36, no. 3, pp. 4011-4018, 2017.

[221]   I. Jolliffe, Principal Component Analysis, Second Edition, London: Springer, 2012.

[222]   Mathworks, "MATLAB R2019b," Mathworks, Natick, Massachusetts, 2019.

[223]   Mathworks, "Help Centre - pca," Mathworks, 2020. [Online]. Available: https://www.mathworks.com/help/stats/pca.html. [Accessed 17 March 2020].

[224]   Scikit-Learn, "4.2 Permutation feature importance," 2020. [Online]. Available: https://scikit-learn.org/stable/modules/permutation_importance.html. [Accessed 21 October 2020].

[225]   Scikit-Learn, "3.3. Metrics and scoring: quantifying the quality of predictions," Scikit-Learn, 2020. [Online]. Available: https://scikit-learn.org/stable/modules/model_evaluation.html. [Accessed 21 October 2020].

[226]   M. Olszak-Humienik and M. Jablonski, "Thermal behavior of natural dolomite," *Journal of Thermal Analysis and Calorimetry,* vol. 119, no. 3, pp. 2239-2248, 2015.

[227]   H. Wang, C. Li, Z. Peng and S. Zhang, "Characterization and thermal behavior of kaolin," *Journal of Thermal Analysis and Calorimetry,* vol. 105, no. 1, pp. 157-160, 2011.

[228]   A. Guatame-García, M. Buxton, F. Deon, C. Lievens and C. Hecker, "Toward an on-line characterization of kaolin calcination process using short-wave infrared spectroscopy," *Mineral Processing and Extractive Metallurgy Review,* vol. 39, no. 6, pp. 420-431, 2018.

[229]   M. Bai, L. Reddy and T. Hussain, "Experimental and thermodynamic investigations on the chlorine-induced corrosion of HVOF thermal sprayed NiAl coatings and 304 stainless steels at 700 °C," *Corrosion Science,* vol. 135, pp. 147-157, 2018.

[230]   thyssenkrupp Materials UK, "Stainless Steel 304 1.4301," thyssenkrupp Materials UK, 2017. [Online]. Available: https://www.thyssenkrupp-materials.co.uk/stainless-steel-304-14301.html. [Accessed 5 June 2019].

[231] Exocor, "Stellite 6 Alloy Technical Data," 2012. [Online]. Available: http://exocor.com/downloads/product-datasheets/Stellite-6-Datasheet.pdf. [Accessed 5 June 2019].

[232] J. Morris, S. Daood and W. Nimmo, "Agglomeration and the effect of process conditions on fluidized bed combustion of biomasses with olivine and silica sand as bed materials: Pilot-scale investigation," *Biomass and Bioenergy,* vol. 142, p. 105806, 2020.

[233] S. De Geyter, M. Öhman, D. Boström, M. Eriksson and A. Nordin, "Effects of Non-Quartz Minerals in Natural Bed Sand on Agglomeration Characteristics during Fluidized Bed Combustion of Biomass Fuels," *Energy & Fuels,* vol. 21, no. 5, pp. 2663-2668, 2007.

[234] K. Davidsson, L. Åmand, A. Elled and B. Leckner, "Effect of Cofiring Coal and Biofuel with Sewage Sludge on Alkali Problems in a Circulating Fluidized Bed Boiler," *Energy & Fuels,* vol. 21, no. 6, pp. 3180-3188, 2007.

[235] M. Huttunen, J. Peltola, S. Kallio, L. Karvonen, T. Niemi and V. Ylä-Outinen, "Analysis of the processes in fluidized bed boiler furnaces during load changes," *Energy Procedia,* vol. 120, pp. 580-587, 2017.

[236] J. Ribeiro, E. Vicente, C. Alves, X. Querol, F. Amato and L. Tarelho, "Characteristics of ash and particle emissions during bubbling fluidised bed combustion of three types of residual forest biomass," *Environmental Science and Pollution Research,* vol. 24, no. 11, pp. 10018-10029, 2017.

[237] G. Stubenberger, R. Scharler and I. Obernberger, "Nitrogen Release Behaviour of Different Biomass Fuels Under Lab-Scale and Pilot-Scale Conditions," in *15th European Biomasss Conference and Exhibition*, Berlin, 2007.

[238] A. J. Elshout and S. Beilke, "Oxidation of No to No2 in Flue Gas Plumes of Power Stations," in *Physico-Chemical Behaviour of Atmospheric Pollutants - Proceedings of the Third European Symposium held in Varese, Italy, 10–12 April*, Spring, 1984, pp. 535-536.

[239] European Parliament, *Directive 2010/75/EU of the European Parliament and of the Council on Industrial Emissions,* Brussels, Belgium: Eruopean Union, 2010.

[240] A. Keppel, J. Finnan, B. Rice, P. Owende and K. MacDonnell, "Cereal grain combustion in domestic boilers," *Biosystems Engineering,* vol. 115, no. 2, pp. 136-143, 2013.

[241] M. Mladenović, M. Paprika and A. Marinković, "Denitrification techniques for biomass combustion," *Renewable and Sustainable Energy Reviews,* vol. 82, pp. 3350-3364, 2018.

[242] R. Beetstra, J. Nijenhuis, N. Ellis and J. van Ommen, "The influence of the particle size distribution on fluidized bed hydrodynamics using high-throughput experimentation," *AIChE Journal,* vol. 55, no. 8, pp. 2013-2023, 2009.

References

[243]   L. Shartsis and S. Spinner, "Surface tension of molten alkali silicates," *Journal of Research of the National Bureau of Standards,* vol. 46, no. 5, pp. 385-390, 1951.

[244]   S. Sharma and W. Philbrook, "Improved Values of Surface Tension of Calcium Silicate Melts," *Scripta Metallurgica,* vol. 4, no. 2, pp. 107-109, 1970.

[245]   P. Thy, C. Lesher and B. Jenkins, "Experimental determination of high-temperature elemental losses from biomass slag," *Fuel,* vol. 79, pp. 693-700, 2000.

[246]   Cigre, Understanding and mitigating corrosion, Paris, France: Cigre (International Council on Large Electric Systems), 2019.

[247]   M. Fernández Llorente, P. Díaz Arocas, L. Gutiérrez Nebot and J. Carrasco García, "The effect of the addition of chemical materials on the sintering of biomass ash," *Fuel,* vol. 87, no. 12, pp. 2651-2658, 2008.

[248]   L. Wang, Ø. Skreiberg and M. Becidan, "Investigation of additives for preventing ash fouling and sintering during barley straw combustion," *Applied Thermal Engineering,* vol. 70, no. 2, pp. 1262-1269, 2014.

[249]   L. Roberts, P. Mason, J. Jones, W. Gale, A. Williams, A. Hunt and J. Ashman, "The impact of aluminosilicate-based additives upon the sintering and melting behaviour of biomass ash," *Biomass and Bioenergy,* vol. 127, p. 105284, 2019.

[250]   Scottish Environmental Protection Agency, "SEPA Monitoring Quick Guide 5 version 1.0," 2012. [Online]. Available: https://www.sepa.org.uk/media/156002/ qg5_monitoring_nox_sepa_version_1.pdf. [Accessed 20 May 2020].

[251]   C. Forsberg, M. Broström, R. Backman, E. Edvardsson, S. Badiei, M. Berg and H. Kassman, "Principle, calibration, and application of the in situ alkali chloride monitor," *Review of Scientific Instruments,* vol. 80, no. 2, p. 023104, 2009.

[252]   K. Davidsson, B.-M. Steenari and D. Eskilsson, "Kaolin Addition during Biomass Combustion in a 35 MW Circulating Fluidized-Bed Boiler," *Energy & Fuels,* vol. 21, no. 4, pp. 1959-1966, 2007.

[253]   F. Li, B. Yu, J. Li, Z. Wang, M. Guo, H. Fan, T. Wang and Y. Fang, "Exploration of potassium migration behavior in straw ashes under reducing atmosphere and its modification by additives," *Renewable Energy,* vol. 145, pp. 2286-2295, 2020.

[254]   M. Uberoi, W. Punjak and F. Shadman, "The kinetics and mechanism of alkali removal from flue gases by solid sorbents," *Progress in Energy and Combustion Science,* vol. 16, no. 4, pp. 205-211, 1990.

[255]   M. Tiainen, J. Daavitsainen and R. Laitinen, "The Role of Amorphous Material in Ash on the Agglomeration Problems in FB Boilers. A Powder XRD and SEM-EDS Study," *Energy & Fuels,* vol. 16, pp. 871-877, 2002.

[256] A. Strandberg, N. Skoglund, M. Thyrel, T. Lestander, M. Broström and R. Backman, "Time-Resolved Study of Silicate Slag Formation During Combustion of Wheat Straw Pellets," *Energy & Fuels,* vol. 33, no. 3, pp. 2308-2318, 2019.

[257] A. Strandberg, M. Thyrel, N. Skoglund, T. Lestander, M. Broström and R. Backman, "Biomass pellet combustion: Cavities and ash formation characterized by synchrotron X-ray micro-tomography," *Fuel Processing Technology,* vol. 176, pp. 211-220, 2018.

[258] Z. He, W. Saw, P. van Eyk, G. Nathan and P. Ashman, "Effect of Calcium and Phosphorus on Interactions between Quartz Sand and K-Salt-Doped Wood under Both Steam Gasification and Combustion Atmospheres," *Energy & Fuels,* vol. 34, no. 3, pp. 3210-3222, 2020.

[259] N. Eustathopoulos, M. Nicholas and B. Drevet, Wettability at High Temperatures, London: Elsevier Science, 1999.

[260] H. Risnes, J. Fjellerup, U. Henriksen, A. Moilanen, P. Norby, K. Papadakis, D. Posselt and L. Sørensen, "Calcium addition in straw gasification," *Fuel,* vol. 82, pp. 641-651, 2003.

[261] P. Billen, J. Costa, L. van der Aa, L. Westdorp, J. Van Caneghem and C. Vandecasteele, "An Agglomeration Index for CaO Addition (as CaCO3) to Prevent Defluidization: Application to a Full-Scale Poultry Litter Fired FBC," *Energy & Fuels,* vol. 28, no. 8, pp. 5455-5462, 2014.

[262] A. Stam and G. Brem, "Fouling in coal-fired boilers: Biomass co-firing, full conversion and use of additives – A thermodynamic approach," *Fuel,* vol. 239, pp. 1274-1283, 2019.

[263] P. Sommersacher, T. Brunner, I. Obernberger, N. Kienzl and W. Kanzian, "Application of Novel and Advanced Fuel Characterization Tools for the Combustion Related Characterization of Different Wood/Kaolin and Straw/Kaolin Mixtures," *Energy & Fuels,* vol. 27, no. 9, pp. 5192-5206, 2013.

[264] F. Li, H. Fan, M. Guo, Q. Guo and Y. Fang, "Influencing Mechanism of Additives on Ash Fusion Behaviors of Straw," *Energy & Fuels,* vol. 32, no. 3, pp. 3272-3280, 2018.

[265] F. Moradian, P. Tchoffor, K. Davidsson, A. Pettersson and A. Backman, "Thermodynamic equilibrium prediction of bed agglomeration tendency in dual fluidized-bed gasification of forest residues," *Fuel Processing Technology,* vol. 154, pp. 82-90, 2016.

[266] P. Richet and Y. Bottinga, "Anorthite, andesine, wollastonite, diopside, cordierite and pyrope: thermodynamics of melting, glass transitions, and properties of the amorphous phases," *Earth and Planetary Science Letters,* vol. 67, no. 3, pp. 415-432, 1984.

[267] J. Dodson, A. Hunt, V. Budarin, A. Matharu and J. Clark, "The chemical value of wheat straw combustion residues," *RSC Advances,* vol. 1, no. 3, pp. 523-530, 2011.

References

[268] R. Gupta, T. Wall and L. Baxter, "Ash behaviour in biomass-fluidised bed gasification," in *Impact of Mineral Impurities in Solid Fuel Combustion*, Kluwer Academic Publishers, 2002, pp. 555-567.

[269] J. White, J. Lee, O. Hessling and B. Glaser, "Reactions Between Liquid CaO-SiO2 Slags and Graphite Substrates," *Metallurgical and Materials Transactions B,* vol. 48, no. 1, pp. 506-515, 2017.

[270] J. Ferguson and H. Merwin, "The Ternary System CaO-MgO-SiO2," *Proceedings of the National Academy of Sciences of the United States of America,* vol. 5, no. 1, pp. 16-18, 1919.

[271] J. Dickinson, C. Scarfe and P. McMillan, "Physical properties and structure of K2Si4O9 melt quenched from pressures up to 2.4 GPa," *Journal of Geophysical Research,* vol. 95, no. B10, p. 15675, 1990.

[272] F. Miccio, A. Murri, V. Medri and E. Landi, "Utilization of Fireclay for Preventing Fluidized-Bed Agglomeration during Biomass Thermochemical Processing," *Industrial & Engineering Chemistry Research,* vol. 58, no. 51, pp. 23498-23507, 2019.

[273] C. Ronchi and M. Sheindlin, "Melting point of MgO," *Journal of Applied Physics,* vol. 90, no. 7, 2001.

[274] A. Montes, M. Hamidi, C. Briens, F. Berruti, H. Tran and C. Xu, "Study on the critical amount of liquid for bed material agglomeration in a bubbling fluidized bed," *Powder Technology,* vol. 284, pp. 437-442, 2015.

[275] V. Kahlenberg, M.-P. Mayerl, D. Schmidmair, H. Krüger and M. Tribus, "First investigations on the quaternary system Na2O-K2O-CaO-SiO2: synthesis and crystal structure of the mixed alkali calcium silicate K1.08Na0.92Ca6Si4O15," *Mineralogy and Petrology,* vol. 112, no. 2, pp. 219-228, 2018.

[276] E. Arroyabe, R. Tessadri, D. Többens and V. Kahlenberg, "Does K2CaSiO4 Exist? A Phase-Analytical Study in the System K2O-CaO-SiO2 with Implications for the Characterization of Residual Materials," *Journal of the American Ceramic Society,* vol. 94, no. 8, pp. 2652-2655, 2011.

[277] M. Chen, X. Hou, J. Chen and B. Zhao, "Phase Equilibria Studies in the SiO2-K2O-CaO System," *Metallurgical and Materials Transactions B,* vol. 47, no. 3, pp. 1690-1696, 2016.

[278] D. Schmidmair, V. Kahlenberg and A. Grießer, "K2CaSi4O10: A novel phase in the ternary system K2O-CaO-SiO2 and member of the litidionite group of crystal structures," *Journal of the American Ceramic Society,* vol. 101, no. 2, pp. 919-927, 2018.

[279] I. Santoso, P. Taskinen, A. Jokilaakso, M.-K. Paek and D. Lindberg, "Phase equilibria and liquid phase behavior of the K2O-CaO-SiO2 system for entrained flow biomass gasification," *Fuel,* vol. 265, p. 116894, 2020.

[280]   FactSage, "What's New in FactSage 7.3," CRCT/GTT, March 2019. [Online]. Available: http://www.factsage.com/facthelp/FS73New.htm#FToxid. [Accessed 21 October 2019].

[281]   E. Zabetta, V. Barišć, K. Peltola, J. Sarkki and T. Jantti, "Advanced technology to co-fire large shares of agricultural residues with biomass in utility CFBs," *Fuel Processing Technology,* vol. 105, pp. 2-10, 2013.

[282]   E. Lindström, M. Sandström, D. Boström and M. Öhman, "Slagging Characteristics during Combustion of Cereal Grains Rich in Phosphorus," *Energy & Fuels,* vol. 21, no. 2, pp. 710-717, 2007.

[283]   M. Sandström, Structural and Solid State EMF Studies of Phases in the CaO–K2O–P2O5 System with Relevance for Biomass Combustion, Umeå Universitet, 2006.

[284]   D.-G. Kim, B. Konar and I.-H. Jung, "Thermodynamic optimization of the K2O-Al2O3 -SiO2 system," *Ceramics International,* vol. 44, no. 14, pp. 16712-16724, 2018.

[285]   J. Schairer and N. Bowen, "Melting relations in the systems Na2O-Al2O3-SiO2 and K2O-Al2O3-SiO2," *American Journal of Science,* vol. 245, no. 4, pp. 193-204, 1947.

[286]   J. Schairer and N. Bowen, "The system K2O-Al2O3-SiO2," *American Journal of Science,* vol. 253, pp. 681-746, 1955.

[287]   D. Goodwin, R. Speth, H. Moffat and B. Weber, "Cantera," 2020. [Online]. Available: https://cantera.org/. [Accessed 12 February 2020].

[288]   Sembcorp Utilities UK, "Our Services - Energy: Power and Steam," 2016. [Online]. Available: http://www.sembcorp.co.uk/ourservicesenergy.aspx. [Accessed 1 5 2017].

[289]   Ofgem, "About the RO," 2017. [Online]. Available: https://www.ofgem.gov.uk/environmental-programmes/ro/about-ro. [Accessed 27 4 2017].

[290]   L. Vallely, "Edie explains: Renewables Obligation Certificates (ROCs)," 2014. [Online]. Available: https://www.edie.net/library/Edie-explains-Renewables-Obligation-Certificates-ROCs/6538. [Accessed 27 4 2017].

[291]   Department for Business, Energy and Industrial Strategy, "Simple Guide to the CHP Quality Assurance (CHPQA) Programme," UK Government, London, 2019.

[292]   Department for Business, Energy & Industrial Strategy, "GN10 Defining Good Quality CHP - Criteria for Good Quality CHP," 2017. [Online]. Available: https://www.gov.uk/guidance/chpqa-guidance-notes. [Accessed 27 4 2017].

[293]   Ofgem, "Energy suppliers," 2019. [Online]. Available: https://www.ofgem.gov.uk/environmental- programmes/ro/energy-suppliers. [Accessed 19 December 2019].

References

[294] CMS Law, "Renewables Obligation certificate (ROC) values – Brexit and beyond," CMS Law, 2016. [Online]. Available: https://www.cms-lawnow.com/ealerts/2016/07/renewables-obligation-certificate-roc-values-brexit-and-beyond?cc_lang=en. [Accessed 12 December 2019].

[295] M. Edo, E. Björn, P.-E. Persson and S. Jansson, "Assessment of chemical and material contamination in waste wood fuels – A case study ranging over nine years," *Waste Management,* vol. 49, pp. 311-319, 2016.

[296] N. Saqib and M. Bäckström, "Trace element partitioning in ashes from boilers firing pure wood or mixtures of solid waste with respect to fuel composition, chlorine content and temperature," *Waste Management,* vol. 34, no. 12, pp. 2505-2519, 2014.

[297] Y. Alipour, P. Viklund and P. Henderson, "The analysis of furnace wall deposits in a low-NOx waste wood-fired bubbling fluidised bed boiler," *VGB PowerTech,* vol. 12, pp. 96-100, 2012.

[298] Y. Alipour, P. Henderson and P. Szakálos, "The effect of a nickel alloy coating on the corrosion of furnace wall tubes in a waste wood fired power plant: The effect of a nickel alloy coating on waterwalls," *Materials and Corrosion,* vol. 65, no. 2, pp. 217-225, 2014.

[299] M. Huron, S. Oukala, J. Lardière, N. Giraud and C. Dupont, "An extensive characterization of various treated waste wood for assessment of suitability with combustion process," *Fuel,* vol. 202, pp. 118-128, 2017.

[300] E. Cesprini, G. Resente, V. Causin, T. Urso, R. Cavalli and M. Zanetti, "Energy recovery of glued wood waste – A review," *Fuel,* vol. 262, p. 116520, 2020.

[301] J. Dibdiakova, L. Wang and H. Li, "Characterization of Ashes from Pinus Sylvestris forest Biomass," *Energy Procedia,* vol. 75, pp. 186-191, 2015.

[302] S. Vassilev, C. Vassileva, Y.-C. Song, W.-Y. Li and J. Feng, "Ash contents and ash-forming elements of biomass and their significance for solid biofuel combustion," *Fuel,* vol. 208, pp. 377-409, 2017.

[303] S. Enestam, R. Backman, K. Mäkelä and M. Hupa, "Evaluation of the condensation behavior of lead and zinc in BFB combustion of recovered waste wood," *Fuel Processing Technology,* vol. 105, pp. 161-169, 2013.

[304] B. Ouvrard, J. Abildtrup, G. Bostedt and A. Stenger, "Determinants of forest owners attitudes towards wood ash recycling in Sweden - Can the nutrient cycle be closed?," *Ecological Economics,* vol. 164, p. 106293, 2019.

[305] Y. Yan, T. Mattisson, P. Moldenhauer, E. Anthony and P. Clough, "Applying machine learning algorithms in estimating the performance of heterogeneous, multi-component materials as oxygen carriers for chemical-looping processes," *Chemical Engineering Journal,* vol. 387, p. 124072, 2020.

[306] J. Yan, A. Karlsson, Z. Zou and U. Edlund, "Contamination of heavy metals and metalloids in biomass and waste fuels: Comparative characterisation and

trend estimation," *Science of The Total Environment,* vol. 700, p. 134382, 2020.

[307]   G. Sawyer and M. Irle, "Development of colour indicator techniques to detect chemical contamination in wood waste for recycling," The Waste & Resources Action Programme, 2005.

[308]   British Standards Institution, "Specification for the requirements and test methods for processing waste wood - PAS 111: 2012.," British Standards Institution, London, 2012.

[309]   M. Junginger, C. Hennig, T. Mai-Moulin, M. Edo and I. Johansson, "Transboundary flows of woody biomass waste streams in Europe," IEA Bioenergy, 2018.

[310]   British Standards Institution, "BS EN ISO 18135:2017 Solid Biofuels - Sampling," British Standards Institution, London, 2017.

[311]   S. Pfeuffer, "Benchmarking Boiler Tube Failures," POWER, 2009. [Online]. Available: https://www.powermag.com/update-benchmarking-boiler-tube-failures/. [Accessed 21 January 2020].

[312]   Ofgem, "Wholesale Market Indicators," Ofgem, 2020. [Online]. Available: https://www.ofgem.gov.uk/data-portal/wholesale-market-indicators. [Accessed 21 January 2020].

[313]   Waste & Resources Action Programme (WRAP), "Market Situation Report - Summer 2011: Realising the value of recovered wood," 2011. [Online]. Available: http://www.wrap.org.uk/sites/files/wrap/Wood%20Market%20Situation%20Report_0.pdf. [Accessed 21 January 2020].

[314]   Waste & Resources Action Programme (WRAP), "Recovered Wood Gate Fees," Waste & Resources Action Programme (WRAP), [Online]. Available: http://www.wrap.org.uk/content/recovered-wood-gate-fees. [Accessed 21 January 2020].

[315]   European Commission, "Best Available Techniques (BAT) Reference Document for Large Combustion Plants - Industrial Emissions Directive 2010/75/EU (Integrated Pollution Prevention and Control)," Joint Research Centre of the European Union, 2017.

[316]   European Commission, "Best Available Techniques (BAT) Reference Document for Waste Incineration - Industrial Emissions Directive 2010/75/EU (Integrated Pollution Prevention and Control) (Draft)," Joint Research Centre of the European Union, 2018.

[317]   British Standards Institution, "ISO 6976 Natural gas — Calculation of calorific values, density, relative density and Wobbe indices from composition," British Standards Institution, 2016.

[318]   M. Fernández Llorente, R. Escalada Cuadrado, J. Murillo Laplaza and J. Carrasco García, "Combustion in bubbling fluidised bed with bed material of

limestone to reduce the biomass ash agglomeration and sintering," *Fuel,* vol. 85, no. 14-15, pp. 2081-2092, 2006.

[319] R. Liu, B. Jin, Z. Zhong and J. Zhao, "Reduction of Bed Agglomeration in CFB Combustion Biomass with Aluminium-Contain Bed Material," *Process Safety and Environmental Protection,* vol. 85, no. 5, pp. 441-445, 2007.

[320] P. Chaivatamaset and S. Tia, "The characteristics of bed agglomeration during fluidized bed combustion of eucalyptus bark," *Applied Thermal Engineering,* vol. 75, pp. 1134-1146, 2015.

[321] S. Enestam, "Ash related challenges from a boiler manufacturer's point of view," Valmet Technologies, 2016. [Online]. Available: http://www.users.abo.fi/maengblo/FPK_II_2016/Ash%20related%20challenges%202016%20SE.pdf. [Accessed 31 May 2017].

Appendix A
Publications & Dissemination

Outputs and content from this thesis have been published and disseminated in the following journal articles, conferences, and seminars.

A.1　　Peer-Reviewed Journal Articles

1. Mechanisms and mitigation of agglomeration during fluidized bed combustion of biomass: A review. **Morris, J.D.**, Daood, S.S., Chilton, S., Nimmo, W. 2018, Fuel, Vol. 230, pp. 452-473.

2. Agglomeration and the effect of process conditions on fluidized bed combustion of biomasses with olivine and silica sand as bed materials: Pilot-scale investigation. **Morris, J.D.**, Daood, S.S., Nimmo, W. 2020. Biomass and Bioenergy, Vol. 142, Article No. 105806.

A.2　　Manuscripts

The following manuscripts have been prepared based upon this thesis:

1. The effect of using kaolin and dolomite additives to mitigate agglomeration with challenging agricultural biomass fuels. **Morris, J.D.**, Daood, S.S., Nimmo, W. Unpublished manuscript under submission.

A.3　　Conference Oral Presentations

Bold text denotes presenter.

1. The effects of operational conditions on agglomeration in a fluidized bed combustor using biomass. **Morris, J.D.**, Daood, S.S., Chilton, S., Ng, B.J., Nimmo, W. 14-17th May 2018. European Biomass Conference and Exhibition (26th EUBCE 2018), Copenhagen, Denmark.

2. The effects of operational variables on defluidization in a fluidized bed biomass combustor. **Morris, J.D.**, Daood, S.S., Chilton, S., Ng, B.J., Nimmo, W. 30-31st May 2018. International Flame Research Foundation Conference (IFRF 2018), Sheffield, UK.

3. Pilot-scale operational study of biomass usage in a fluidized bed combustor. **Morris, J.D.**, Daood, S.S., Chilton, S., Ng, B.J., Nimmo, W. 5-7th September 2018. The European Conference on Fuel and Energy Research and its Applications (12th ECCRIA 2018), Cardiff, UK.

4. *Accepted.* Pilot-Scale Fluidized Bed Agglomeration Mitigation for Agricultural Fuels with Kaolin and Dolomite Bed Additives. **Morris, J.D.**, Daood, S.S., Nimmo, W. 6-8th September 2021. The European Conference on Fuel and Energy Research and its Applications (1st FERIA), Nottingham, UK.

A.4   Conference Poster Presentations

Bold text denotes presenter.

1. Mechanisms and mitigation of agglomeration during fluidized bed combustion of biomass. Morris, J.D., Daood, S.S., **Nimmo, W.** 18-21st October 2019. International Conference on Alternative Fuels, Energy and Environment (ICAFEE 2019). Taichung, Taiwan.

A.5   Seminar/Workshop Oral Presentations

Bold text denotes presenter.

1. Mechanisms and mitigation of agglomeration during fluidized bed combustion of biomass. **Morris, J.D.**, Daood, S.S., Nimmo, W. 7th October 2019. The Fuel & Energy Research Forum - Workshop on Combustion-Related Work. London, UK.

2. *Accepted.* Use of additives to prevent fluidized bed agglomeration with biomass fuels. **Morris, J.D.**, Daood, S.S., Nimmo, W. 23rd June 2021. The Fuel & Energy Research Forum – Combustion Interest Group Seminar. Swindon, UK.

A.6   Other Dissemination

Presentations or posters arising from this thesis have also been delivered at the following events to students, academia, and industry.

1. EngD Winter School 2017. Carbon Capture, Storage and Cleaner Fossil Energy CDT. The University of Nottingham, 13-16th February 2017. Nottingham, UK.
2. Presentation on Project Progress to Sembcorp. Sembcorp Energy UK HQ, 11th January 2018. Middlesbrough, UK.
3. EngD Winter School 2018. Carbon Capture, Storage and Cleaner Fossil Energy CDT. The University of Nottingham, 12-14th February 2018. Nottingham, UK.
4. Presentation on Project Options to Sembcorp. Sembcorp Energy UK HQ, 21st February 2018. Middlesbrough, UK.
5. Engineering PGR Research Symposium. The University of Sheffield, 26th June 2018. Sheffield, UK.
6. EngD Winter School 2019. Carbon Capture, Storage and Cleaner Fossil Energy CDT. The University of Sheffield, 12-14th February 2019. Sheffield, UK.
7. Department of Mechanical Engineering PhD Poster Showcase. The University of Sheffield, 27th June 2019. Sheffield, UK.
8. EngD Research Showcase 2020 (Virtual). Carbon Capture, Storage and Cleaner Fossil Energy CDT. The University of Nottingham, 26th May 2020. Nottingham, UK.

Appendix B

Training Modules Completed

Table B. 1 lists the 180 credits of mandatory and optional training modules completed during the Engineering Doctorate project.

Table B. 1: Training modules completed.

Module Code	Module Title	Credits	Host Institution *
CIC6006	Application Programming using C/C++	5	UoS
CIC6007	Application Programming using MATLAB	5	UoS
CIC6010	Introduction to Programming using Python	5	UoS
F84CSS	International Placement	10	UoN
FCE6100	Professional Behaviour and Ethical Conduct	0	UoS
H84FPT	Pilot-scale Facilities Training	20	UoS
H84RP4	Research Project Portfolio Part 2	20	UoN
MAT6005	X-ray Experimental Techniques	5	UoS
MEC6008	Graphical Programming with LabView	10	UoS
MEC6408	Industrial Marketing: Basics and Cases	10	UoS
MEC6909	Commercialisation of Research	10	LU
MEC6912	Industrial Case Studies	10	LU
MEC6913	Industrial Mini-Project	10	UoS
MEC6914	Research Project Portfolio Part 1	10	UoN
MEC6920	Power Generation & Carbon Capture	10	UoN
MEC6921	Energy Systems and Policy	20	UoN
MEC6922	Research and Professional Skulls	10	UoN
MEC6923	Communication & Public Engagement Skills for Energy Researchers	10	UoN

* UoN – University of Nottingham; UoS – The University of Sheffield; LU – Loughborough University.

Appendix C
Phyllis2 Data Utilised in FactSage Models

Chlorine composition data for the miscanthus and wheat straw fuels modelled in Chapter 6 was unavailable. Therefore, an average chlorine value for miscanthus and wheat straw was taken from the Phyllis2 biomass fuel database [199]. This database is operated by TNO (formerly ECN) and contains a mixture of peer reviewed literature sources and internal fuel data sets. Information on the chlorine fuel data from Phyllis2 that was used in the FactSage modelling activities is listed across Table C. 1-Table C. 3.

***Table C. 1:** Chlorine information for wheat straw extracted from Phyllis2 database [199].*

Quantity	Value
Fuel	Wheat Straw
Data Retrieval Date	18 June 2019
Average Ash (wt.% dry)	6.44
No. of Data Sets Used for Ash Average	48
Average Chlorine (mg/kg daf)	4335.7
No. of Data Sets Used for Cl Average	32
Total Data Sets Retrieved	63
Data Sets Retrieved (reference no.)	wheat straw (#424); wheat straw (#425); wheat straw (#426); wheat straw (#427); wheat straw (#454); wheat straw (#455); wheat straw (#456); wheat straw (#457); wheat straw (#458); wheat straw (#459); wheat straw (#460); wheat straw (#461); wheat straw (#462); wheat straw (#463); wheat straw (#464); wheat straw (#465); wheat straw (#466); wheat straw (#467); wheat straw (#468); wheat straw (#469); wheat straw (#470); wheat straw (#471); wheat straw (#472); wheat straw (#475); wheat straw (#476); wheat straw (#703); wheat straw (#712); wheat straw (#713); wheat straw (#760); wheat straw (#799); wheat straw (#800); wheat straw (#801); wheat straw (#802); wheat straw (#945); wheat straw (#977); wheat straw (#990); wheat straw (#991); wheat straw (#992); wheat straw (#1022); wheat straw (#1026); wheat straw (#1098); wheat straw (#1271); wheat straw (#1438); wheat straw (#1814); wheat straw (#1819); wheat straw (#1903); wheat straw (#1933); wheat straw (#1965); wheat straw (#2141); wheat straw (#2266); wheat straw (#2390); wheat straw (#2391); wheat straw (#2392); wheat straw (#2548); wheat straw (#2599); wheat straw (#2601); wheat straw (#2602); wheat straw (#2609); wheat straw (#2620); wheat straw (#3201); wheat straw (#3202); Wheat straw (#3071); Wheat straw (#3161)

Table C. 2: *Chlorine information for miscanthus extracted from Phyllis2 database [199].*

Quantity	Value
Fuel	Miscanthus
Data Retrieval Date	18 June 2019
Average Ash (wt.% dry)	3.74
No. of Data Sets Used for Ash Average	39
Average Chlorine (mg/kg daf)	2149.1
No. of Data Sets Used for Cl average	45
Total Data Sets Retrieved	51
Data Sets Retrieved (reference no.)	miscanthus (#568); miscanthus (#569); miscanthus (#570); miscanthus (#571); miscanthus (#572); miscanthus (#573); miscanthus (#574); miscanthus (#575); miscanthus (#576); miscanthus (#577); miscanthus (#578); miscanthus (#579); miscanthus (#580); miscanthus (#581); miscanthus (#582); miscanthus (#583); miscanthus (#584); miscanthus (#585); miscanthus (#586); miscanthus (#587); miscanthus (#588); miscanthus (#589); miscanthus (#590); miscanthus (#591); miscanthus (#592); miscanthus (#593); miscanthus (#594); miscanthus (#595); miscanthus (#596); miscanthus (#597); miscanthus (#598); miscanthus (#599); miscanthus (#600); miscanthus (#601); miscanthus (#602); miscanthus (#603); miscanthus (#604); miscanthus (#605); miscanthus (#606); miscanthus (#607); miscanthus (#608); miscanthus (#609); miscanthus (#610); miscanthus (#1040); miscanthus (#1743); miscanthus (#1744); miscanthus (#1821); miscanthus (#1931); miscanthus (#1976); miscanthus (#2532); miscanthus (#2744)

Table C. 3: *Conversion of chlorine content from mg/kg to a proportion of fuel ash content on a weight basis. This was used to calculate the chlorine content input, then used together with the 1000g ash input in FactSage modelling activities in Chapter 6.*

Quantity	Miscanthus	Wheat Straw
Chlorine (mg/kg daf) (Phyllis2)	2149.1	4335.7
Ash (wt.% dry) (Phyllis2)	3.74	6.44
Chlorine (wt.% daf) (calculated)	0.215	0.434
Chlorine (wt.% dry) (calculated)	0.207	0.407
Chlorine (as % of ash wt.) (calculated)	5.54	6.33

Appendix D
FactSage Solution Phases Summary

This appendix contains an abridged extract of key solution information taken directly from the FactSage 7.0 software documentation files for ease of reference [179]. Table D. 1 lists key information for all solutions used in the FactSage modelling activities that were discussed in Chapter 6. Specifically, Table D. 1 is a listing of the compound(s) that are modelled for each solution. Descriptions for the FactSage solution miscibility settings are given in Table D. 2.

Full documentation for each solution phase is available in the documentation files for FactSage 7.0. Alternatively, solution information for the current release of FactSage is available online at: www.crct.polymtl.ca/fact/documentation.

Table D. 1: Key information summary for all solutions used in the FactSage modelling activities, taken as direct extract from FactSage 7.0 software documentation files for ease of reference [179]. Refer to FactSage software documentation files for complete information.

Solution	Information Summary
	FToxid
aC2SA	A-a-$(Ca,Sr)_2SiO_4$. Ca_2SiO_4 + (Mg_2SiO_4, Fe_2SiO_4, Mn_2SiO_4, Ba_2SiO_4, $Ca_3B_2O_6$ in dilute amounts).
Brau	Braunite. Non-stoichiometric Mn_7SiO_{12} with excess Mn_2O_3.
Cord	Cordierite. $Al_4Fe_2Si_5O_{18} - Al_4Mg_2Si_5O_{18}$ solution.
CORU	Corundum. Al_2O_3-Cr_2O_3-Fe_2O_3 + (Mn_2O_3, Ti_2O_3 in dilute amounts) corundum structure solution.
cPyrA	A-Clinopyroxene. $MSiO_3 - MAl_2SiO_6 - MFe_2SiO_6$ solution (where: M = Fe(II), Ca, Mg)
Feld	Feldspar. $NaAlSi_3O_8 - KAlSi_3O_8 - CaAl_2Si_2O_8$ solution.
KASH	$KAlSiO_4$-HT. Non-stoichiometric high-temperature kalsilite, $KAlSiO_4$, with excess SiO_2, Na and Ca.
LcPy	Low clinopyroxene. $CaMgSi_2O_6 - Mg_2Si_2O_6$ solid solution (low clinopyroxene structure)
Mel_A	A-Melilite. $(Ca,Pb)_2[Mg,Fe(II),Fe(III),Al,Zn]\{Al,Fe(III),Si\}_2O_7$.
MeO_A	A-Monoxide. Fe(II)O,CaO,MgO,Mn(II)O,NiO,CoO at all compositions + (Al,Fe(III),Cr(III),Ti(IV),Zn,Zr in dilute amounts).
Mull	Mullite. $3Al_2O_32SiO_2$, $2Al_2O_3SiO_2$.
NCA2	Na2CaAl4O8. $Na_2CaAl_4O_8$ solid solution $Na_2(Na_2,Ca)Al_4O_8$.
NCSO	Combeite. $(Na_2,Ca)Na_2(Ca,Na_2)_3CaSi_6O_{18}$.
Neph	Nepheline. Non-stoichiometric low-temperature $NaAlSiO_4 - KAlSiO_4$ solid solution, dissolving excess SiO2 and Ca.
OlivA	A-Olivine. Mg_2SiO_4-Ca_2SiO_4-Fe_2SiO_4-Mn_2SiO_4-Co_2SiO_4-Ni_2SiO_4-Zn_2SiO_4 solution.

Solution	Information Summary
FToxid	
oPyr	Orthopyroxene. $MSiO_3 – MAl_2SiO_6 – MFe_2SiO_6$ solution (where: M = Fe(II), Ca, Mg).
Rhod	Rhodonite. $MnSiO_3$ + ($CaSiO_3$, $CoSiO_3$, $FeSiO_3$, $MgSiO_3$ in dilute amounts).
aC2SA	A-a-$(Ca,Sr)_2SiO_4$. Ca_2SiO_4 + (Mg_2SiO_4, Fe_2SiO_4, Mn_2SiO_4, Ba_2SiO_4, $Ca_3B_2O_6$ in dilute amounts).
Brau	Braunite. Non-stoichiometric Mn_7SiO_{12} with excess Mn_2O_3.
Cord	Cordierite. $Al_4Fe_2Si_5O_{18} – Al_4Mg_2Si_5O_{18}$ solution.
CORU	Corundum. Al_2O_3-Cr_2O_3-Fe_2O_3 + (Mn_2O_3, Ti_2O_3 in dilute amounts) corundum structure solution.
cPyrA	A-Clinopyroxene. $MSiO_3 – MAl_2SiO_6 – MFe_2SiO_6$ solution (where: M = Fe(II), Ca, Mg)
Feld	Feldspar. $NaAlSi_3O_8 – KAlSi_3O_8 – CaAl_2Si_2O_8$ solution.
KASH	$KAlSiO_4$-HT. Non-stoichiometric high-temperature kalsilite, $KAlSiO_4$, with excess SiO_2, Na and Ca.
LcPy	Low clinopyroxene. $CaMgSi_2O_6 – Mg_2Si_2O_6$ solid solution (low clinopyroxene structure)
Mel_A	A-Melilite. $(Ca,Pb)_2[Mg,Fe(II),Fe(III),Al,Zn]\{Al,Fe(III),Si\}_2O_7$.
MeO_A	A-Monoxide. Fe(II)O,CaO,MgO,Mn(II)O,NiO,CoO at all compositions + (Al,Fe(III),Cr(III),Ti(IV),Zn,Zr in dilute amounts).
Mull	Mullite. $3Al_2O_32SiO_2$, $2Al_2O_3SiO_2$.
NCA2	$Na_2CaAl4O8$. $Na_2CaAl_4O_8$ solid solution $Na_2(Na_2,Ca)Al_4O_8$.
NCSO	Combeite. $(Na_2,Ca)Na_2(Ca,Na_2)_3CaSi_6O_{18}$.
Neph	Nepheline. Non-stoichiometric low-temperature $NaAlSiO_4 – KAlSiO_4$ solid solution, dissolving excess SiO2 and Ca.
OlivA	A-Olivine. Mg_2SiO_4-Ca_2SiO_4-Fe_2SiO_4-Mn_2SiO_4-Co_2SiO_4-Ni_2SiO_4-Zn_2SiO_4 solution.
oPyr	Orthopyroxene. $MSiO_3 – MAl_2SiO_6 – MFe_2SiO_6$ solution (where: M = Fe(II), Ca, Mg).
Rhod	Rhodonite. $MnSiO_3$ + ($CaSiO_3$, $CoSiO_3$, $FeSiO_3$, $MgSiO_3$ in dilute amounts).
SLAGA	Slag liquid. Oxides of: Al, As, B, Ba, Ca, Co, Cr(II), Cr(III), Cu(I), Fe(II), Fe(III), Ge, K, Mg, Mn(II), Mn(III), Na, Ni, P, Pb, Si, Sn, Ti(III), Ti(IV), Zn, Zr + (S in dilute solution (<10%)).
SPINA	Spinel. AB_2O_4-type cubic spinel solution containing Al-Co-Cr-Fe-Mg-Ni-Zn-O (2+ and 3+ oxidation states only).
WOLLA	Wollastonite. $CaSiO_3$ with $MgSiO_3$, $FeSiO_3$, $MnSiO_3$ and $BaSiO_3$ in solution.
FTsalt	
ACL_B	Solid chloride solution.
CSOB	Solid alkali sulphate/carbonate solution.
KCOH	KCl-KOH solid solution.
KSO_	Solid alkali sulphate/carbonate solution.
LCSO	Molten carbonate/sulphate solution.
PRVKA	Solid chloride solution with perovskite structure.
SCMO	MgSO4-CaSO4 solid solution.
FTpulp	
ACL	Solid chloride solution.

Table D. 2: *FactSage solution miscibility settings. These were enabled as required when configuring FactSage models and are viewable in the solution settings tables in Chapter 6.*

Solution Setting	Description
(+)	Single phase solution.
(I)	Two-phase immiscibility.
(J)	Three-phase immiscibility.

Appendix E

Wilton 10 Blend-to-Boiler Fuel Data: Data Features

E.1   Redaction Notice

Appendix E has been redacted in the online version of this thesis for commercial confidentiality reasons.

This appendix listed information regarding the data subject to analysis within Chapter 7, which was also redacted for commercial confidentiality reasons.

Appendix F

Random Forest Model Script

F.1   Redaction Notice

Appendix F has been redacted in the online version of this thesis for commercial confidentiality reasons.

This appendix showed the script used to perform random forest regression, a method applied in Chapter 7, which was also redacted for commercial confidentiality reasons.

Appendix F

This page has been redacted in the online version of this thesis. Please refer to page 295 for further information.

This page has been redacted in the online version of this thesis. Please refer to page 295 for further information.

This page has been redacted in the online version of this thesis. Please refer to page 295 for further information.

This page has been redacted in the online version of this thesis. Please refer to page 295 for further information.

Appendix G

Random Forest Modelling of Synthetic Fuel Data Set

G.1 Redaction Notice

Appendix G has been redacted in the online version of this thesis for commercial confidentiality reasons.

This appendix described a model calibration exercise, in which a synthetic fuel data set was used to prove the validity of the random forest regression model and the potential benefits of the method as applied in Chapter 7, which was also redacted for commercial confidentiality reasons.

This page has been redacted in the online version of this thesis. Please refer to page 300 for further information.

This page has been redacted in the online version of this thesis. Please refer to page 300 for further information.

This page has been redacted in the online version of this thesis. Please refer to page 300 for further information.

This page has been redacted in the online version of this thesis. Please refer to page 300 for further information.

This page has been redacted in the online version of this thesis. Please refer to page 300 for further information.

Appendix H
Random Forest Model Tuning

H.1   Redaction Notice

Appendix H has been redacted in the online version of this thesis for commercial confidentiality reasons.

This appendix described a hyperparameter tuning of the random forest regression model, as applied in Chapter 7, which was also redacted for commercial confidentiality reasons.

This page has been redacted in the online version of this thesis. Please refer to page 306 for further information.

This page has been redacted in the online version of this thesis. Please refer to page 306 for further information.

This page has been redacted in the online version of this thesis. Please refer to page 306 for further information.

Appendix I

Principal Component Analysis Script

I.1   Redaction Notice

Appendix I has been redacted in the online version of this thesis for commercial confidentiality reasons.

This appendix showed the script used to perform principal component analysis, a method applied in Chapter 7, which was also redacted for commercial confidentiality reasons.

This page has been redacted in the online version of this thesis. Please refer to page 310 for further information.

Appendix I

This page has been redacted in the online version of this thesis. Please refer to page 310 for further information.

Appendix J
Wilton 10 Emissions Study

J.1   Redaction Notice

Appendix J has been redacted in the online version of this thesis for commercial confidentiality reasons.

This appendix described a study of Wilton 10 plant emissions over several years, in support of the fuel study performed in Chapter 7, which was also redacted for commercial confidentiality reasons

This page has been redacted in the online version of this thesis. Please refer to page 313 for further information.

This page has been redacted in the online version of this thesis. Please refer to page 313 for further information.

This page has been redacted in the online version of this thesis. Please refer to page 313 for further information.

This page has been redacted in the online version of this thesis. Please refer to page 313 for further information.

This page has been redacted in the online version of this thesis. Please refer to page 313 for further information.

This page has been redacted in the online version of this thesis. Please refer to page 313 for further information.

Appendix J

This page has been redacted in the online version of this thesis. Please refer to page 313 for further information.

Appendix K

Engineering Projects Performed with Sembcorp Energy UK

K.1   Redaction Notice

Appendix K has been redacted in the online version of this thesis for commercial confidentiality reasons.

This appendix briefly described other projects performed with Sembcorp Energy UK during the EngD project.

This page has been redacted in the online version of this thesis. Please refer to page 321 for further information.

This page has been redacted in the online version of this thesis. Please refer to page 321 for further information.

This page has been redacted in the online version of this thesis. Please refer to page 321 for further information.

This page intentionally left blank.